Durham E-Theses

A theoretical Study of Spectroscopic Properties of van der Waals Trimers

Adam Cooper

How to cite:

Use policy

Abstract of Thesis for Ph.D.,

"A Theoretical Study of Spectroscopic Properties of van der Waals Trimers."

Adam Cooper, Durham University, 26 September 1992.

A method for performing calculations on the lower bound states of van der Waals trimers is developed, which models atom-atom-diatom trimers with basis functions in all five degrees of freedom. Spherical harmonic and distributed Gaussian functions and solutions of one-dimensional adiabatic Hamiltonians are used as basis functions. Ar_3 was examined as a precursor system. No spectroscopy has been performed on Ar_3, nor is this currently feasible. For the systems considered, most experimental data exists for $v_{HCl} = 0$ Ar_2HCl so this is the main target of the work. Predictions are made for Ar_2DCl, for $v_{HCl} = 1$ Ar_2HCl, and for $v_{HF} = 0, 1$ Ar_2HF ; experiments are currently in progress on some of these systems.

The current state of knowledge of the pair potentials of the Ar-Ar, and Ar-HF/Cl systems is summarised. Physical models for important three-body potential terms are suggested; these arise from dipoles induced on the argon atoms, dispersion effects, orbital deformation and the Ar_2 overlap-induced field. The parameters in the models come from the literature, where possible, and otherwise from a fit to some *ab-initio* data points for the Ar_3 and Ar_2HCl trimers (Chałasinski *et al.*).

Calculations on Ar_3 with various two- and three-body potentials are presented and discussed in the context of earlier work. For Ar_2HCl a comparison is made with earlier, approximate, work (Hutson, Halberstadt and Beswick). The possible effects of Hamiltonian approximations are discussed before addressing the effects of individual three-body components. Two sets of three-body parameters are assessed, and indicate that the physical models used are substantially appropriate, although deficient in detail; agreement with experiment is good, with changes in frequencies of about 1.5cm^{-1} arising from the best three-body model. The most important three-body component is found to be the interaction of the overlap-induced field with the HCl permanent multipoles, with the dispersion effects slightly less important and other terms much less so.

1 6 APR 1993

Acknowledgements.

Statement.

No part of this thesis has previously been submitted by me for a degree to any university. Every effort has been made to ensure that all work which is not original to the author has been properly credited. I place no restriction upon access to, or copying of, this thesis.

Contents

Contents

1: Introduction.

This thesis is divided into ten chapters. Following the introductory remarks of this chapter, chapters 2 to 4 describe the basis-set methods which have been used, chapters 5 and 6 discuss intermolecular potential models, and chapters 7 to 9 set out and discuss the results obtained. A summary of the main conclusions is given in chapter 10.

I shall now briefly discuss the factors which influenced the methods employed and motivated the work presented in the following chapters. In particular, I shall indicate the significance of examining van der Waals trimers, the extent of the experimental data available, and the current knowledge of pertinent intermolecular forces.

Much of the subtlety of Chemistry, Physics and Biology cannot be understood without an understanding of intermolecular potentials. Reaction kinetics, phase behaviour, crystal structure, thermodynamic properties of matter, transport kinetics and much more besides are all important potential dependent phenomena. In addition, the theoretical determination of accurate intermolecular potentials by fitting calculations to known experimental results may allow the prediction of behaviour under conditions inaccessible to experiment, for example in the interstellar medium.

Spectroscopy of the vibrations of molecules, clusters, or solids provides an important method of measuring the effects of intermolecular forces; it is not possible to directly measure these forces. The aim of this thesis is to explore theoretical methods for the study of the vibrations of trimeric van der Waals systems, and hence to perform calculations on such systems.

Weakly bound molecules, such as the ones I have investigated, are important because they exhibit large amplitude motions and tunnelling effects in the vibrations; much of the potential surface affects the vibrational energy levels. Thus we can obtain a potential energy surface for a wide range of geometries. The wide range of a potential surface may allow the different contributions to the intermolecular potential to be separated out since each will have its own form of coordinate dependence. The physics of large amplitude motion has motivated a substantial experimental [1] [2] [3] [4] [5] and theoretical [6] effort

to determine complete intermolecular potentials. Before about ten years ago bulk gas properties were the common source of data for determining intermolecular potentials, but, following progress in experimental methods, spectroscopic and scattering results are currently used to greater effect. Classical bulk gas properties, such as viscosity and second virial coefficients, provide the least information as their interpretation usually leads only to a radial distribution function, which is in some sense averaged over angular orientation. Transport properties can sometimes give more information, particularly for molecular systems, where the Senftleben-Beenakker effect can be used to gain information on anisotropic interactions. Within the framework of this thesis these methods are of historical interest only, and are reviewed in the literature [7] [8]. The previous two references also survey a substantial body of knowledge on the subject of intermolecular forces, the formalisms of which are dealt with more rigorously by Grey and Gubbins [9].

In some special cases scattering experiments in molecular beams can lead to 'good' intermolecular potentials ('good' implies that the results allow a wide range of properties to be accurately calculated). Following the development of laser technology and of spectroscopy, measurements of the rotation–vibration spectra of complexes have been of greater utility, and it is the comparison of these with the calculated rotation–vibration energy levels of weakly bound molecules that forms the basis for the analysis of my results. This is done for trial potentials, which are assessed by the correlation of the calculated quantities with the spectroscopic transitions and properties that are measured. A review of the determination of intermolecular forces from spectroscopy of van der Waals molecules has been published by Hutson [10].

Van der Waals (VDW) molecules are a common example of weakly bound species, which therefore execute wide amplitude motion, although all molecules in highly excited states execute wide amplitude motion similar to VDW molecules [11]. VDW molecules are a preferred system of study, however, because wide amplitude motion occurs for small numbers of vibrational quanta. Large amplitude dynamical behaviour is not as easily modelled as the more rigid vibrations of most chemically bound molecules; many alternative formulations of the theory of floppy molecules are to be found in the literature [12] [13] [14]. The classical normal mode approach, while appropriate for everyday

1: Introduction.

molecules like water in all but their highest vibrational states, becomes increasingly inappropriate as the amplitudes of motion get larger. For instance, a bending mode of a rigid molecule becomes almost an intra–molecular rotation when the amplitude of the motion is large so that a completely different description of the motion is required. The traditional practice of assigning normal mode quantum numbers to vib-rotational eigenstates, while justifiable in a rigid molecule régime can become meaningless as floppyness increases; a different set of quantum numbers becomes appropriate. This can often be seen by inspection of the computed eigenvectors of a basis-set calculation. However, single quantum excitations in a floppy molecule often display motion similar to a normal mode. Large amplitude motions also preclude the analysis of spectroscopic results using the static equilibrium molecular geometry as a model for physical observables [15]. Substantial differences exist between, for example, a rotational constant predicted from the molecular geometry at the intermolecular potential minimum and that which is actually observed. Instead a rotational constant should be predicted by the expectation value of an element of the inverted inertia tensor of the complex.

The coupled channel propagator method and full basis-set matrix method form two distinct ways of solving the vib-rotational problem. The propagator method has been developed over a number of years [16] into a very efficient method of solution that is quick and does not require excessive computer memory [17]. The disadvantage of the propagator method is that it does not give explicit wavefunctions so that many observables cannot be extracted in a straightforward manner [18], such as spectral line intensities and moments of inertia. Since I wish to pursue such properties I will concentrate on full basis-set methods.

Ar_2HCl has been the subject of recent spectroscopic investigations in the microwave region by pulsed nozzle FT spectroscopy [19] and in the far infrared using a continuous supersonic jet with a tunable probe [20]. Previous theoretical calculations [21] have shown that Ar_2HCl is a system with spectroscopic observables which show sensitivity to non-additive forces. That treatment involved fixing the two argon atoms and performing calculations on the dynamics of HCl in their field using the BOUND program [17] to solve the coupled equations. This approximation has been shown to be too drastic by the more

recent far infrared work.

Ar$_2$HF has also been studied in both the microwave [22] and far infrared experiments are in progress by the Nesbitt group.

Several more complicated Ar$_n$HX species have also been spectroscopically observed by the microwave work of the Gutowsky group: Ar$_3$HCl [23], Ar$_3$HF [24] and Ar$_4$HF [25]. Ar$_n$HF complexes have also been studied in the near infrared [26]. Species with more than two argon atoms in the cluster are rather too complicated for the current state of theoretical methods, other than qualitative treatments.

Reliable intermolecular potentials are known for Ar–Ar, Ar–HCl and for Ar–HF interactions. In all cases, the potential surface is supported by accurate modelling of physical and spectroscopic parameters. Both of the Ar$_2$HX molecules are floppy so that the complex dynamics sample a large part of the potential hypersurface; this is essential if meaningful information relating to intermolecular forces is to be elucidated.

In general, the intermolecular potential between more than two atoms or molecules is not simply the sum of interactions between all pairs [27]. This arises from the fact that each monomer affects the electron distribution in all the others. For example, only half of the third virial coefficient of argon arises from two–body interactions. The properties of condensed media are therefore poorly modelled by pairwise sum potentials.

Currently, very little is known about real three–body forces, despite considerable effort on the part of *ab-initio* theoreticians. Supermolecule calculations are notoriously inaccurate, while the application of perturbative methods allows various contributions to be calculated. The calculations are still computationally very expensive and there may be many significant terms in third and fourth order perturbative corrections. Developments in the *ab-initio* field are current. The sensitivity of spectroscopic parameters to the intermolecular potential can, in principle, be used to refine a potential which is based upon *ab-initio* calculations.

In my work basis-set methods are used with argon motions included to model the cluster dynamics more accurately than previously, when argon motions were neglected. Using a model which has full dynamical freedom, the effect of changes in the intermolec-

1: Introduction.

ular potential is investigated, particularly with focus on plausible three-body effects. The quality of agreement between theoretical and spectroscopic observables allows an assessment of the accuracy of the intermolecular potential and by having a potential function with terms based on physical effects can give insight into these effects.

The objective of the work to be described is to assess the magnitude and effect of realistic three-body forces by studying model systems, such as Ar_3, Ar_2HCl and Ar_2HF, and comparing with experiment, where possible.

2: Basis-set Methods For Modelling Molecular Motions

In this chapter I assess the suitability of a variety of choices of basis-function types for describing wide-amplitude motion. The applicability of a basis-set of distributed Gaussians is reviewed, and calculations are performed using three possible candidates for modelling angular motions with differing rigidity. The background terminology and algebra, which is built upon in the following two chapters, is laid out in the first half of this chapter.

Basis-set methods have been dominated by the Rayleigh-Ritz variational principle [28], although other methods have been used [29]. If an exact wavefunction, Ψ is approximated by a basis-set expansion $\Psi_{\text{app}} = \sum_i^{N_\phi} c_i \phi_i$ then we need to solve the secular equations:

$$\sum_j c_j \langle \phi_i | \widehat{H} - E_{\text{app}} | \phi_j \rangle = 0. \tag{1}$$

In matrix form the secular equations are of the form

$$(\mathbf{H} - E_{\text{app}} \mathbf{S})c = 0, \tag{2}$$

where $\mathbf{H}$ is a matrix of elements $H_{ij} = \langle \phi_i | \widehat{H} | \phi_j \rangle$ and $\mathbf{S}$ is an overlap matrix with elements $S_{ij} = \langle \phi_i | \phi_j \rangle$.

The quality of the approximation depends on the suitability of the ϕ_i to describe the system and N_ϕ; N_ϕ may be smaller as the ϕ_i are made more like the real wavefunction and may have no sensible value if the ϕ_i are not physically suitable.

2.1 Choice of Basis Function

In the field of interest the basis functions commonly used are Legendre Polynomials and distributed Gaussians. Legendre Polynomials are suitable for wide amplitude bending coordinates since these functions are rotational eigenfunctions. Distributed Gaussians are suitable for wide amplitude stretching type coordinates. Harmonic oscillator functions are of less utility, for van der Waals complexes, since they rely on the existence of a well defined equilibrium structure about which small vibrations are executed, but they may

find use where this is the case. Legendre Polynomials suffer from not being a very flexible basis-set; they have no variational parameters. An extension of the Legendre function is the Jacobi function, which is as a special case identical to the Legendre function. The Jacobi function has two parameters, which can be fitted to place basis function emphasis at the angle required and to control its width. Jacobi polynomials have been little used so far, perhaps due to the existence of simpler functions. They have been successfully applied to excited states in water [30].

The distributed Gaussian basis (DGB) method models a function in one coordinate by a number of Gaussians with centres distributed on that coordinate. There is a co-efficient in the exponential chosen, or varied, to optimise the solution. There are also various ways of spacing the Gaussian centres. One limitation of this method is that a function which extends over an infinite space can only be flexibly defined over the finite range of the distribution; points outside this are forced to have function values given only by the 'tails' of the Gaussians. The DGB does, however, posses a great deal of flexibility over the range of the distribution, and moreover the degree of flexibility is controllable by the size of the basis.

Harmonic oscillator and Legendre functions and the DGB all have the advantage that the kinetic energy terms in the coordinate of the function can be analytic, whereas quadrature integration is required for Jacobi polynomials. All of these, except the DGB, are orthogonal polynomials, over the range $(-1,+1)$ for Jacobi and Legendre, whereas the DGB set is never orthogonal, although the overlap integrals are analytic. Since the DGB is used in secular equation methods of solution, non-orthogonality slows down the eigenvalue-finding step since the non-unit overlap matrix must be decomposed and the Hamiltonian matrix transformed [31]. The use of distributed Gaussians has in some ways revolutionised the field since it eases the direct calculation of eigenfunctions as well as eigenvalues. The DGB approach is substantially documented in the literature, having been applied to Morse potentials approximating C–H and H–H bonds [32] [33], but was popularised by Bačić, Hamilton, Light and coworkers [34], and applied to LiCN/LiNC [35] and HCN/HNC [36]. The DGB method has been variously extended to other systems, and has been used to also model an angular coordinate in Ar—CO_2 [37]. In some of these

calculations [35][38] a discrete variable representation (DVR) of the angular motion has been used where angular and radial motions are strongly coupled. In contrast I shall use a conventional finite basis representation (FBR).

2.2 The Distributed Gaussian Basis (DGB).

The use of a Gaussian basis has the advantage that kinetic energy and overlap integrals are analytic. Defining the distributed Gaussian basis as a set of real Gaussians on $(-\infty < x < +\infty)$,

$$\psi_i(x) = \left(\frac{2A_i}{\pi}\right)^{\frac{1}{4}} \exp\left[-A_i(x - x_i)^2\right], \tag{3}$$

we need to choose the centres x_i and scaling factors A_i. If we define the following terms, for a pair of Gaussians,

$$P_{ii'} = \frac{A_i R_i + A_{i'} R_{i'}}{A_i + A_{i'}}, \tag{4}$$

$$Q_1 = \left(\frac{4A_i A_{i'}}{\pi^2}\right)^{\frac{1}{4}}, \tag{5}$$

$$Q_2 = \sqrt{A_i + A_{i'}}, \tag{6}$$

$$Q_3 = \frac{A_i A_{i'}}{A_i + A_{i'}}, \tag{7}$$

$$Q_4 = Q_3(R_i - R_{i'})^2, \tag{8}$$

and

$$N_{ii'} = Q_1 e^{-Q_4}, \tag{9}$$

then the overlap matrix elements are:

$$S_{ii'} = N_{ii'}\frac{\sqrt{\pi}}{Q_2}, \tag{10}$$

and the kinetic energy matrix elements are:

$$K_{ii'} = N_{ii'}\frac{\hbar^2}{\mu}Q_3(1 - 2Q_4)S_{ii'}. \tag{11}$$

Hamilton and Light [39] showed that the exact method used for finding the A_i is not critical and give the prescription:

$$A_i = \frac{4c^2}{(x_{i+1} - x_{i-1})^2}; \quad A_1 = \frac{c^2}{(x_2 - x_1)^2}; \quad A_N = \frac{c^2}{(x_N - x_{N-1})^2} \tag{12}.$$

I shall use this throughout. The parameter c is still a variable, and needs to be small enough that the basis-set adequately covers the space of the function the DGB is modelling, yet large enough to describe sharply changing parts of a wavefunction. The value of c may be found according to the variational principle.

Hamilton and Light [39]proposed that the x_i are best determined by finding the positions of the $N-1$ nodes of a function Ψ_N. They did this semi-classically by satisfying the conditions:

$$\int_{x_{\min}}^{x_1} p(x)dx = \frac{\pi}{4}, \quad \int_{x_i}^{x_{i+1}} p(x)dx = \pi, \tag{13}$$

where $x_{\min}$ is the inner classical turning point for the highest energy of interest and $p(x)$ is the classical momentum. However, other workers have elected to use equally spaced Gaussian functions [40] [41]. An equally-spaced DGB needs to be slightly larger than following [42] for high accuracy but can offer substantial savings in matrix element calculations, and is the preferred method in my calculations.

2.3   A Comparison Of Some Angular Basis Functions

The choice of basis function is determined by the shape of the potential. Comparisons are made for potentials of the form $V(\theta) = \sum_i V_i P_i(\cos\theta)$, where $P_i(x)$ is a Legendre polynomial and the sum over i is very short. In terms of an atom–diatom system, the coefficients in this potential provide a measure of the angular rigidity of the potential. The computational effort involved in the calculations of a matrix element for different types of basis functions is quite different (table 1), and in marginal cases may lead to choosing a basis type which requires a slightly larger basis-set size. The great speed of the Legendre basis matrix setup in this example is due to the fact that the potential is modelled in terms of Legendre polynomials, making the matrix elements completely analytic 3–j symbols [43]. A longer expansion of $V(\theta)$ would increase the times for this method by a greater proportion than for the others, more so for a realistic potential. A realistic potential would either have matrix elements evaluated by quadrature, or the coefficients in a polynomial expansion of the potential would be evaluated by quadrature; both of these tasks are of similar computational effort to the calculation of H.O. matrix integrals. A real system would have similar setup times for H.O. and Legendre basis-sets

of the same size.

Table 1. Some approximate timings for a SUN 3/60 (timed to limited precision).

Basis Size	H.O. Setup Time/s	Legendre Setup Time/s	Jacobi Setup Time/s	Diagonalise Time/s
10	0.06	0.003	0.30	0.06
20	0.24	0.008	1.4	0.25
30	0.6	0.013	4.0	0.65
40	1.4	0.022	8.5	1.4
50	2.9	0.026	16.0	2.4

The matrix setup for a Jacobi function basis-set is seen (table 1) to take between five and six times as long as the H.O. function case (or for Legendre functions in a real system). This great time discrepancy is due to extensive recursion relationships necessary to evaluate the function and its derivatives, which are required to calculate the (non-analytic) Jacobi function kinetic matrix elements. Bearing in mind the diagonalisation times given it will not be worth using Jacobi functions unless an incredibly smaller basis-set is required if time, rather than storage, is a restricting computational factor.

2.4 Legendre Polynomial Basis and Hamiltonian Matrix Elements.

For the set of basis functions, $\bar{P}_k$, which are Legendre polynomials normalised on $(-1,1)$,

$$\bar{P}_k(\cos\theta) = \sqrt{\frac{2k+1}{4\pi}} P_k(\cos\theta), \qquad (14)$$

the atom-diatom bender Hamiltonian for $J = 0$ is written:

$$\hat{H} = b\hat{j}^2 + V(\theta), \qquad (15)$$

where the rotational constant of the molecular complex is

$$b = \frac{\hbar^2}{2\mu R_{eq}^2}. \qquad (16)$$

It is preferred to scale the Hamiltonian to measure the degree of bender localisation by a single variable equal to V_2/b, giving:

$$\hat{H}_s = \hat{j}^2 + \frac{V_2}{b} P_2(\cos\theta), \qquad (17)$$

where the potential expansion $V(\theta)$ is taken only to a single term for simplicity.

The matrix elements between basis functions are simple:

$$\langle m|\hat{H}_s|n\rangle = \langle m|\hat{j}^2|n\rangle + \frac{V_2}{b}\langle m|P_2(\cos\theta)|n\rangle \tag{18}$$

where

$$\langle m|\hat{j}^2|n\rangle = \delta_{nm}n(n+1) \tag{19}$$

and the final integral evaluates as a 3–j symbol [43]:

$$\langle m|P_2(\cos\theta)|n\rangle = \sqrt{(2m+1)(2n+1)}\begin{pmatrix} m & 2 & n \\ 0 & 0 & 0 \end{pmatrix}^2. \tag{20}$$

The form of the 3–j symbol leads to non–zero matrix elements only for cases where $(m+n+2)$ is even and $(m,n,2)$ satisfy a triangle relationship.

2.5 Harmonic Oscillator Basis and Hamiltonian Matrix Elements.

A harmonic oscillator basis function in $\cos\theta$, for an equilibrium at $\cos\theta = 0$, is defined as

$$\phi_v(\cos\theta) = N_v H_v(\gamma^{\frac{1}{2}}\cos\theta)\exp\left(-\frac{\gamma}{2}\cos^2\theta\right), \tag{21}$$

where $H_v(x)$ is a Hermite Polynomial and N_v a normalisation factor,

$$N_v = \left(\frac{1}{2^v v!}\right)^{\frac{1}{2}}\left(\frac{\gamma}{\pi}\right)^{\frac{1}{4}}, \tag{22}$$

and γ is the H.O. scale factor. Defining $\mu = \cos\theta$, and using the single term potential expansion, the b–scaled Hamiltonian for $J = 0$ is written, with $\hat{j}^2$ expressed explicitly, as:

$$\hat{H}_s = -\frac{\partial}{\partial\mu}(1-\mu^2)\frac{\partial}{\partial\mu} + \frac{V_2}{b}P_2(\cos\theta). \tag{23}$$

The solutions of the harmonic oscillator equation (i.e. with a kinetic term $bd^2/d\mu^2$), with potential $V = V_q\cos^2\theta$, have $\gamma = \sqrt{V_q/b}$. Thus an estimate of γ can be made by approximating the potential as quadratic and assuming that the kinetic term is numerically similar. This estimate is poor, and in practice γ is a variational parameter. If the first, kinetic, term in $\hat{H}_s$ is denoted $\hat{K}$, there are matrix elements:

$$\langle m|\hat{K}|n\rangle = -\langle m|\frac{\partial^2}{\partial\mu^2}|n\rangle - (2n-1)\gamma\langle m|\mu^2|n\rangle + \gamma^2\langle m|\mu^4|n\rangle +$$

$$2\langle m|\mu\frac{\partial}{\partial\mu}|n\rangle, \tag{24}$$

where the identity [44]

$$\frac{\partial^2}{\partial x^2}\left[\exp\left(-\frac{x^2}{2}\right)H_n(x)\right] = -(2n+1-x^2)\exp\left(-\frac{x^2}{2}\right)H_n(x) \tag{25}$$

has been used. If the integral range of $\cos\theta$ of $(-1,1)$ is approximated as $(-\infty,+\infty)$ then we have a kinetic energy term with known analytic integrals [45]. This approximation is clearly valid only if the potential is strongly anisotropic. Since the H.O. basis functions are solutions for small amplitude motion, this approximation is not expected to be the limit on the quality of the solutions.

The potential integrals must be evaluated by Gauss–Hermite quadrature. Gauss–Hermite quadrature is not limited to the range $(-1,+1)$ so similar restrictions apply to the potential anisotropy as for the kinetic term if the potential integral is to be meaningful. The position of the extreme quadrature points should be monitored and a judgement made as to whether the integration is good, inaccurate to some degree, or invalid (quadrature points with $\cos\theta$ outside $(-1,1)$).

In a highly anisotropic system, the Hamiltonian may be approximated by setting $(1-\mu^2)\approx 1$ in the classically allowed region. I call this the 'Highly Rigid' approximation. If the potential is separated into a quadratic part and a residual the matrix element, evaluation of

$$\hat{H}_s = -\frac{\partial^2}{\partial\mu^2} + \frac{V_{\text{harmonic}}}{b}\mu^2 + V_{\text{residual}} \tag{26}$$

is simplified since the first two terms are the harmonic oscillator operator equation. The matrix elements are then just integrals over the residual potential plus the harmonic oscillator energies,

$$E_v = 2(v+\tfrac{1}{2})\sqrt{\frac{V_{\text{harmonic}}}{b}}, \tag{27}$$

which appear in diagonal matrix elements only due to the orthogonality of the basis. Such an approximation finds little validity in Van der Waals molecular complexes since they are not rigid enough to justify it.

2.6 Jacobi Polynomial Basis and Hamiltonian Matrix Elements.

The Jacobi polynomials, $P_n^{(\alpha,\beta)}(x)$, are a set of orthogonal polynomials on $(-1,1)$ which can be considered to be an extension of Legendre Polynomials insomuch as they contain the Legendre Polynomials as a special set, when $\alpha = 0$ and $\beta = 0$. Orthogonality is obtained through a weight function:

$$\int_{-1}^{1} (1-x)^{\alpha}(1+x)^{\beta} P_n^{(\alpha,\beta)}(x) P_m^{(\alpha,\beta)}(x) dx = 0; \qquad n \neq m \qquad \text{and} \qquad \alpha, \beta > -1. \quad (28)$$

The Jacobi basis functions are therefore defined to be

$$B_n^{(\alpha,\beta)}(x) = (1-x)^{\alpha/2}(1+x)^{\beta/2} P_n^{(\alpha,\beta)}(x). \quad (29)$$

The parameters α and β are varied so as to make the basis functions appropriate for the potential. Estimates of these parameters can be made by consulting plots of the basis functions, but the variational principle is the best way to determine their values. This adds an additional computation time over Legendre and H.O. bases with zero and one variational parameters respectively. However, in a multidimensional problem these parameters may be evaluated for a single degree of freedom and hence can add little to the total computational effort. An inspection of the form of the weighted Jacobi polynomials, depicted in figure 1, indicates their suitability for wide amplitude motions with equilibrium geometries of arbitrary angle.

The spread of these functions is controlled by the size of α and β and the equilibrium position by their ratio.

For the same Hamiltonian as for the harmonic oscillator basis, a set of nine basic integrals for the kinetic energy operator are obtained (i.e. integrals with simple operators such as $x^l \frac{d^m}{dx^m}$), which do not seem to have analytic solutions in the general case despite much effort to this end. The explicit form of Jacobi polynomials is cumbersome, so not amenable to efficient computation, and numerically difficult to calculate accurately. It is therefore necessary to use a recursion relation in n for $B_n^{(\alpha,\beta)}(x)$ and for derivatives $d^m(B_n^{(\alpha,\beta)}(x))/dx^m$ to perform the quadrature. This makes the evaluation of Jacobi basis matrix elements quite time-consuming relative to the harmonic oscillator and Legendre
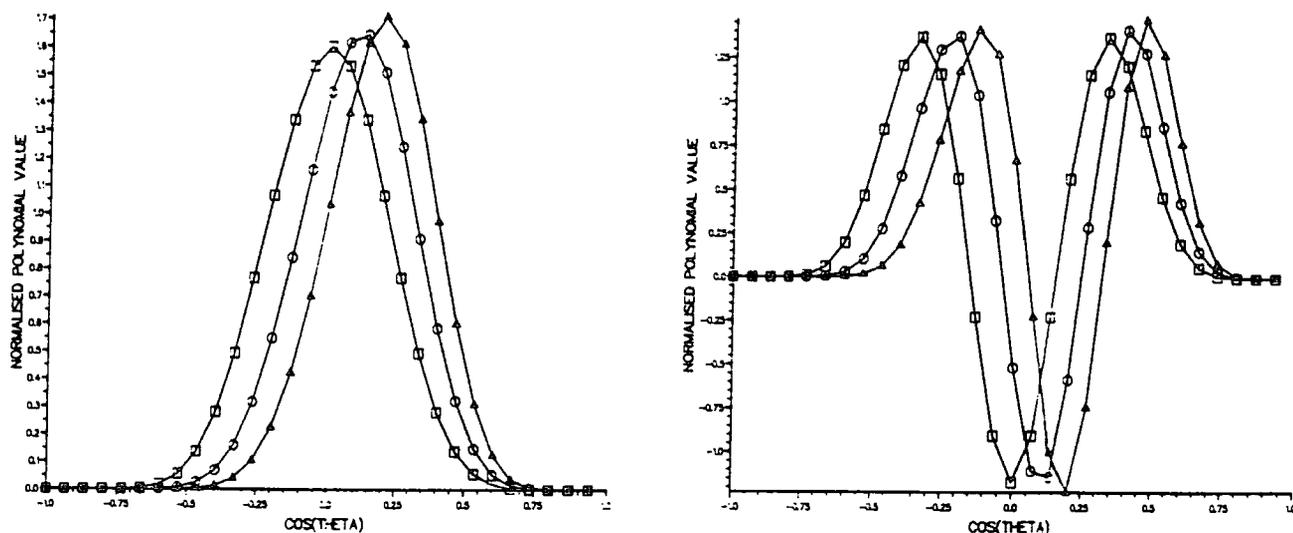
Fig. 1. Weighted Jacobi Polynomials for Three Choices of α and β; $\alpha = 20, \beta = 20$ ⊡ ,

$\alpha = 20, \beta = 25$ ⊙ , $\alpha = 20, \beta = 30$ ▲ for $n = 0$ and $n = 2$.

cases. In some potentials however, as already mentioned, these other two basis-sets may

not converge for sensible basis-sizes.

2.7 Comparative Results for Angular Basis Functions.

2.7. 1 When Is the 'Highly Rigid' Approximation Good?

The ground state energy for varying rigidity of the angular potential is shown in

figure 2, where A and B are for the 'Highly Rigid' Approximation and C for the exact

Hamiltonian; A and C are for an eight function basis and B for a ten function one.

From figure 2 it is clear that the error due to approximating the Hamiltonian is much

larger than any convergence error. From the graph there is observed to be an approx-

imately inverse relationship between the relative energy and V_2/b. Extrapolating to

greater anisotropy leads to the conclusion that the approximate curve will only have

reached 1×10^{-6} from the abscissa for $V_2/b \approx 8 \times 10^5$, which represents a highly rigid

system. For states higher than the ground state the error will become progressively worse,

so that the 'Highly Rigid' approximation is not valid.
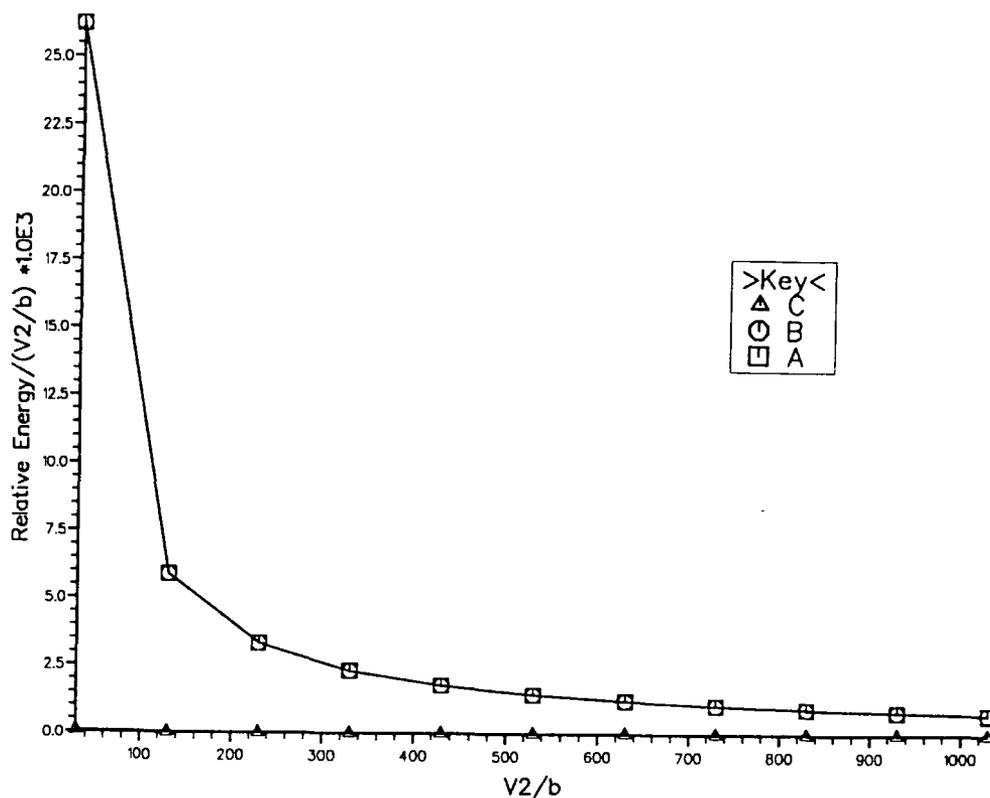
Fig. 2. Comparison of 'Highly Rigid' vs. Exact Hamiltonian Ground State Energies.

7. 2 Harmonic Oscillator or Legendre Polynomial?

Calculations were performed for the potential $V(\theta) = V_2 P_2(\cos\theta)$. Convergence of a H.O. basis is depicted graphically (figure 3) and compared with an unconverged Legendre polynomial basis.

The inadequacies of each type of basis function at low V_2/b for H.O. and high V_2/b for Legendre are clearly seen, larger basis-sets being required in these limits. H.O. results for lower V_2/b are not calculable since the quadrature scheme starts to place points outside the valid range of integration, a caution mentioned earlier. For equal basis-sizes of 15 functions, the 'crossover' point in accuracy for the ground state is at $V_2/b \approx 90$.

The graph (figure 4) for the $n = 2$ eigenvalue does not show an appreciable change in the location of the 'crossover' point, indicating that the $n = 0$ and $n = 2$ state are of

2: Basis-set Methods For Modelling Molecular Motions
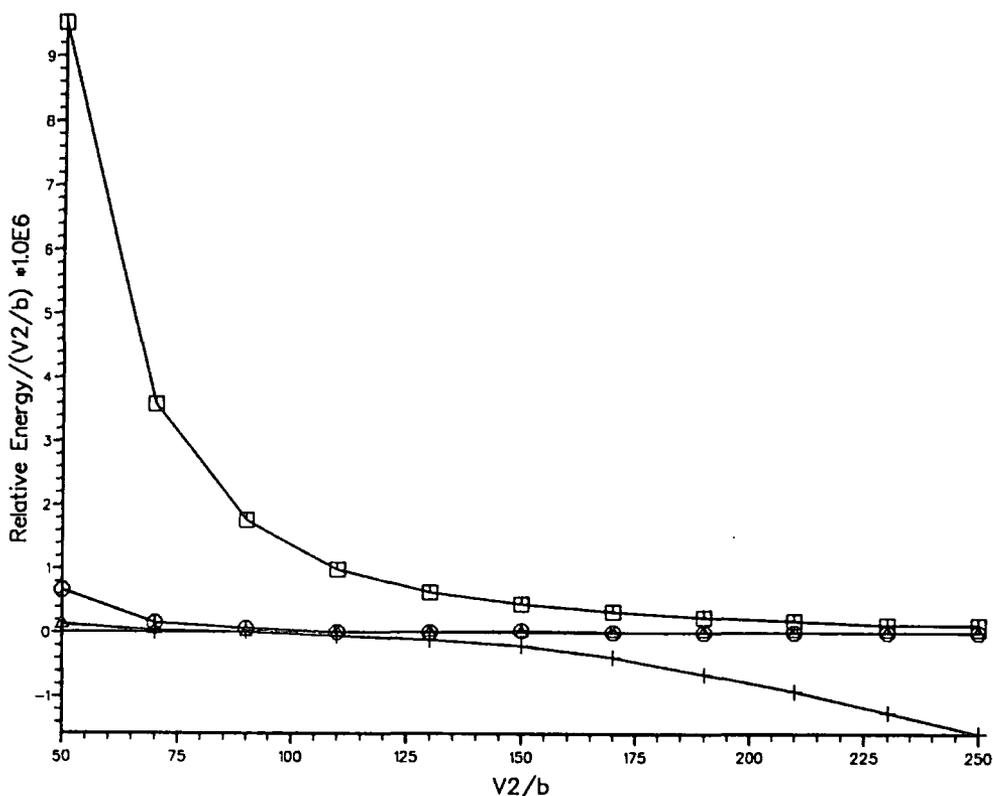
Fig. 3. Results of H.O. Basis Calculation with 7 (□), 10 (⊙) and 15 (▲) Functions and Legendre Basis with 15 Functions (+) for the Ground State, Relative to a Converged Calculation.

similar rigidity.

Although care should be exercised in extending observations from a fictional system to real ones, it is apparent that for anisotropies V_2/b less than about 100 the Legendre basis is more compact, and above this an H.O. basis is better. This is lower than might be estimated by arguments about small displacements being required for the H.O. basis to be appropriate. In these calculations it is apparent that at the 'crossover' point there is still quite a large difference between the results from the two basis-set calculations. Thus there will be some systems which fall into the region where neither basis-set provides a good description, for limited basis-sizes. Such cases might be better described using a Jacobi polynomial basis. Additionally, the results presented may give a misleading
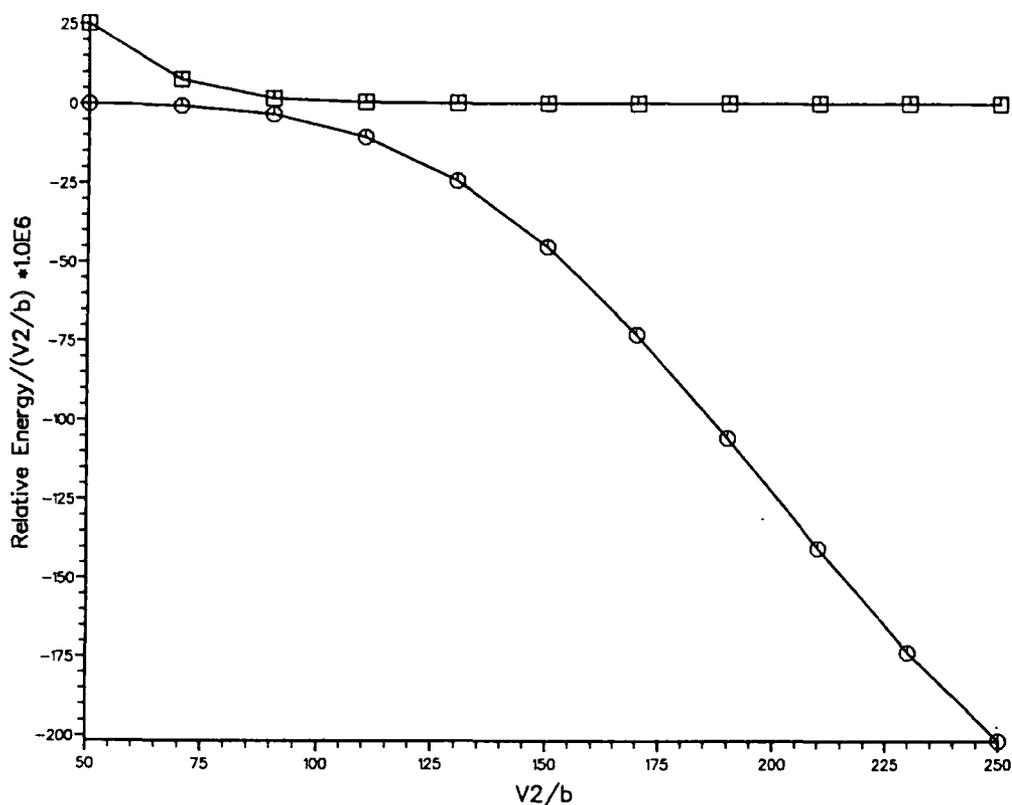
Fig. 4. The $n = 2$ Eigenvalue for 15 Basis Functions for H.O. ($\square$) and Legendre ($\odot$) bases.

impression about the suitability of H.O. basis functions in real potentials which do not have a quadratic–looking potential. In such cases, small numbers of H.O. functions may no longer provide reasonable approximations to the wavefunction, even when the motion is sufficiently localised that we might otherwise expect them to. This may arise since H.O's are the eigenfunctions of a quadratic potential, admittedly with a slightly different kinetic energy term. This qualification would need to be tested for a real system.

7. 3   Legendre or Jacobi Polynomial?

To evaluate the advantages of the Jacobi basis a potential $V = V_1 P_1(\cos\theta) + V_2 P_2(\cos\theta)$ was used, with the V_2 coefficient fixed. In addition to examining the expression of wavefunctions for arbitrary equilibrium angle in this section, calculations

described in the previous section showed the need for a basis-set which has an angular range which is suitable for the potential. Jacobi basis functions should satisfy both of these requirements.
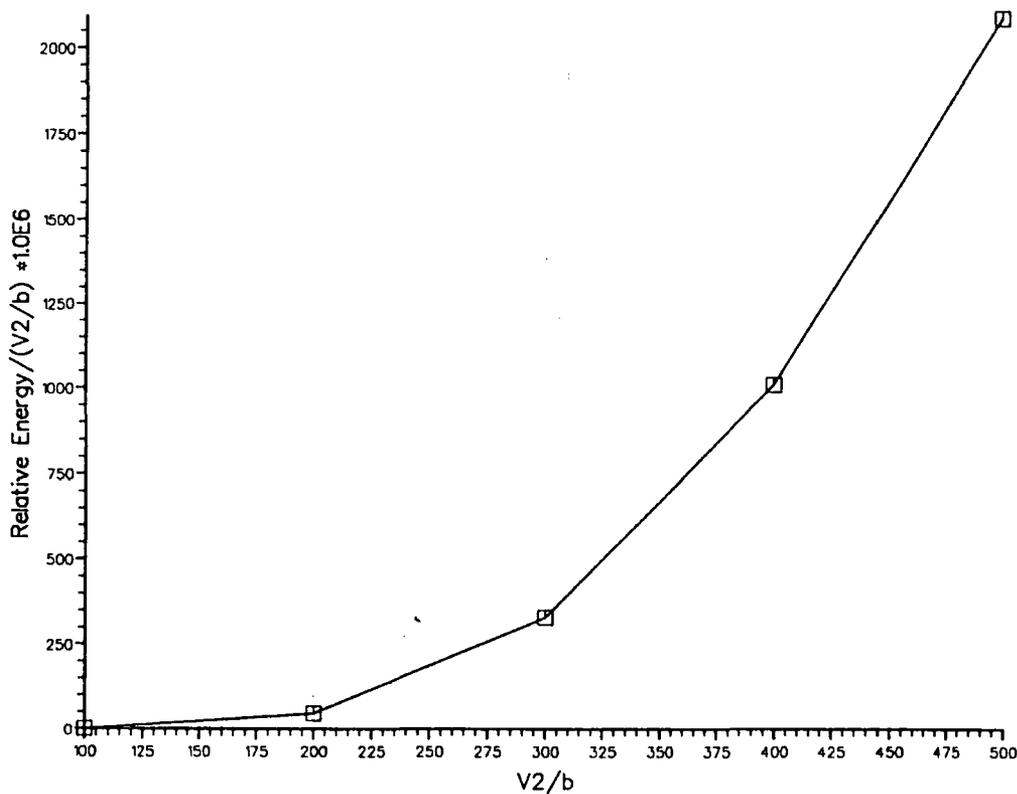
Fig. 5. Difference Between $n = 2$ Eigenvalue for 15 Legendre and Jacobi Basis Functions.

From the plot of the difference between results for Legendre and Jacobi polynomial basis functions (figure 5) it can be seen that for $V_2/b \approx 100$ there is less than 10^{-5} difference, indicating that the Jacobi basis is not able to improve on the errors relative to a H.O basis in the previous section. Comparing the graphs indicates that the Jacobi basis becomes better as the anisotropy increases, and is always at least as good as the Legendre. This progressive improvement, with V_2/b, parallels an increase in the optimal values of the parameters α and β; the smaller the parameter, the more the function looks

like a Legendre polynomial. The values for α and β are determined variationally for each different basis-set size, although the values obtained for small basis-set size are generally adequate for large sets. For values of V_2/b in the region of a few hundred, the optimal parameters lead to functions which are sufficiently similar to Legendre polynomials and change the ground state energy sufficiently slowly that finding the minimum of this with respect to the parameters is quite hard. Computationally the NAG algorithm E04JAF is often unable to locate a minimum. Consequently I choose to perform calculations with $V_2/b = 1500$ when I vary V_1/b and conclude that in the 'crossover' region noted in the previous section Jacobi basis functions are not able to bridge the gap between H.O and Legendre functions.

Three graphs (figure 7) are reproduced for $V_2/b = 1500$ which compare Legendre and Jacobi bases relative to a Jacobi basis-set which is converged to better than 10^{-7} (V_2/b reduced units) for the lowest 10 eigenvalues. All three of the basis-sets presented have ground states identical to better than 10^{-7}. The reasons for the greater number of Legendre basis functions were discussed in the previous section. It can be seen (table 2) that the movement of the potential minimum affects the Jacobi parameters in the expected way; the parameters listed move the function centre from very close to 90° to about 95°.

Table 2. The effect on optimal α and β of varying V_1/b for ten Jacobi polynomials and $V_2/b = 1500$.

V_1/b	α	β
50.0	40.300	39.600
100.0	40.394	39.629
150.0	40.394	39.629
200.0	41.694	38.343
250.0	41.694	38.343
300.0	43.735	36.317

The Jacobi results are clearly rather good , certainly being comparable to the H.O. basis discussed previously. The oscillating behaviour of the results for Legendre poly-
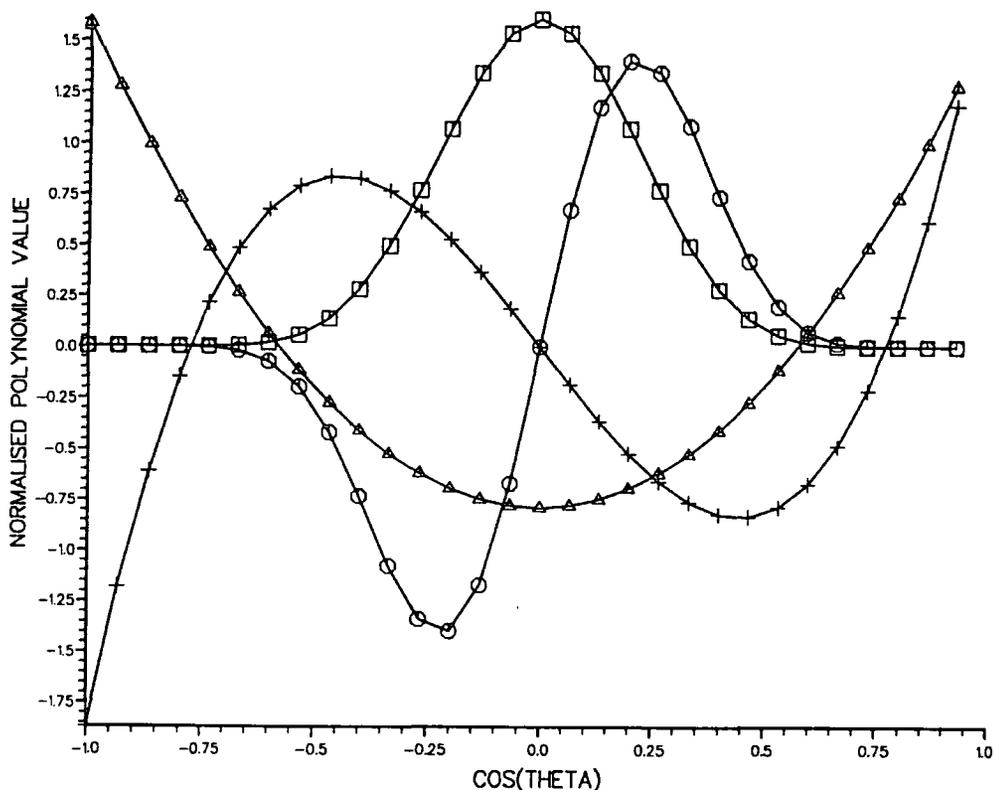
Fig. 6. The Legendre Polynomials of Small Order.

nomial basis-sets is due to the potential minimum moving through points where there are either zeroes or stationary points in the Legendre polynomials. Where a stationary point coincides with the potential minimum even-order wavefunctions (i.e. those with a maximum value at the potential minimum) will be better expressed than odd-order ones, and vice–versa. Such a case appears to occur at $V_1/b \approx 200$. The reason for the great improvement obtained by using Jacobi polynomials over Legendre ones for expressing localised wavefunctions is easily seen from plots of the Legendre functions (figure 6), by comparison with the previously presented plots of Jacobi functions.
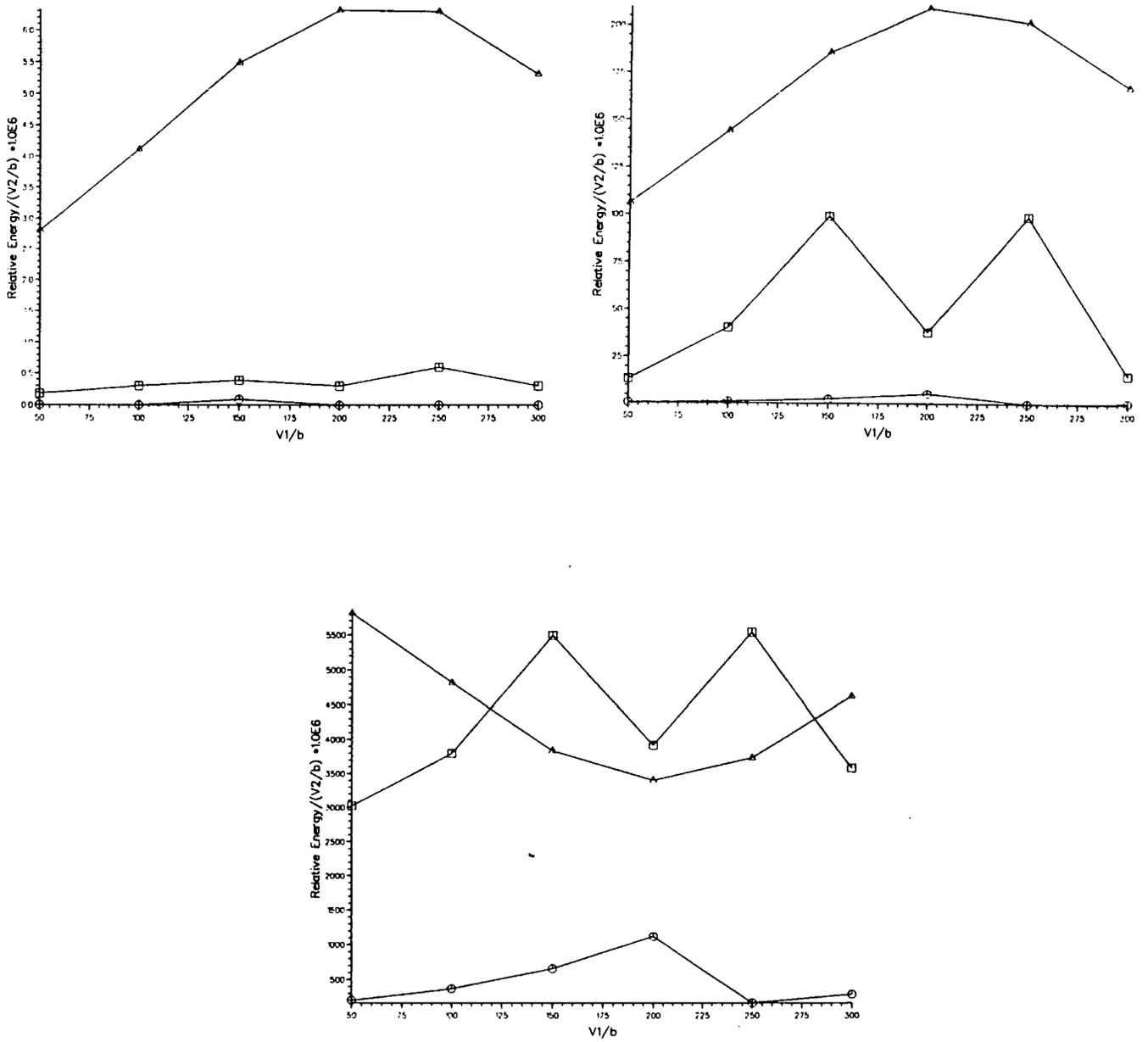
Fig. 7. Results Using Jacobi Bases of size 10 ⊓ and 15 ⦶ and a Legendre basis of size 30 ▲ for the $n = 3$, $n = 5$ and $n = 8$ eigenstates.

3: Some Theoretical Methods for Floppy Triatomics.

Using the groundwork laid out in the preceding chapter, I now formulate a number of three-dimensional models, and apply them to Ar_3 in chapter 8. The methods which I describe are designed for floppy triatomics; much earlier work has been published for more rigid systems [46] [47]. The Ar_3 system is a suitable prototype trimer as it is one step below Ar_2HX, for which experimental data are available, on the conceptual and computational ladder. Forward references to Ar_2HCl (chapter 4) are made to indicate some of the areas where extensions to the trimer models will be required.

I have investigated three methods of calculating triatomic eigenstates as applied to Ar_3. Two of these use a Jacobi coordinate system and so treat the system in the $C_{2v}(M)$ subgroup of its full molecular symmetry, $D_{3h}(M)$ (since it has an equilateral triangle equilibrium geometry). The full D_{3h} symmetry is used in a normal mode treatment using harmonic oscillator functions (H.O's) as a basis. All three methods perform $J = 0$ (rotationless) calculations. In purely vibrational calculations it is appropriate to classify the molecular symmetry by the nuclear permutation groups S_2 and S_3 rather than $C_{2v}(M)$ and $D_{3h}(M)$. This is done for one method which uses Jacobi coordinates. The Jacobi coordinates appropriate are as described for Ar_2HX except that θ and ϕ are no longer relevant since the HX is 'reduced' to an Ar atom. This leaves a conceptual atom pair with separation ρ and a centre of mass R away from the third atom. The angle between R and ρ is defined as χ. Figure 8 shows the coordinate system graphically.

Both Jacobi methods use a DGB for the R coordinate but differ in the ρ and χ functions used and in the use of symmetrisation of basis functions in Method II. Calculations using hyperspherical coordinates in a coupled channel method [48] are available for comparison. Results of other methods utilising hyperspherical coordinates with different potentials [49] [50] may also be compared with mine. The suitability of the methods described below, ranked in terms of degree of molecular floppiness goes: normal mode – Jacobi schemes – hyperspherical.

The normal mode method assumes that the system is rigid enough that all displace-
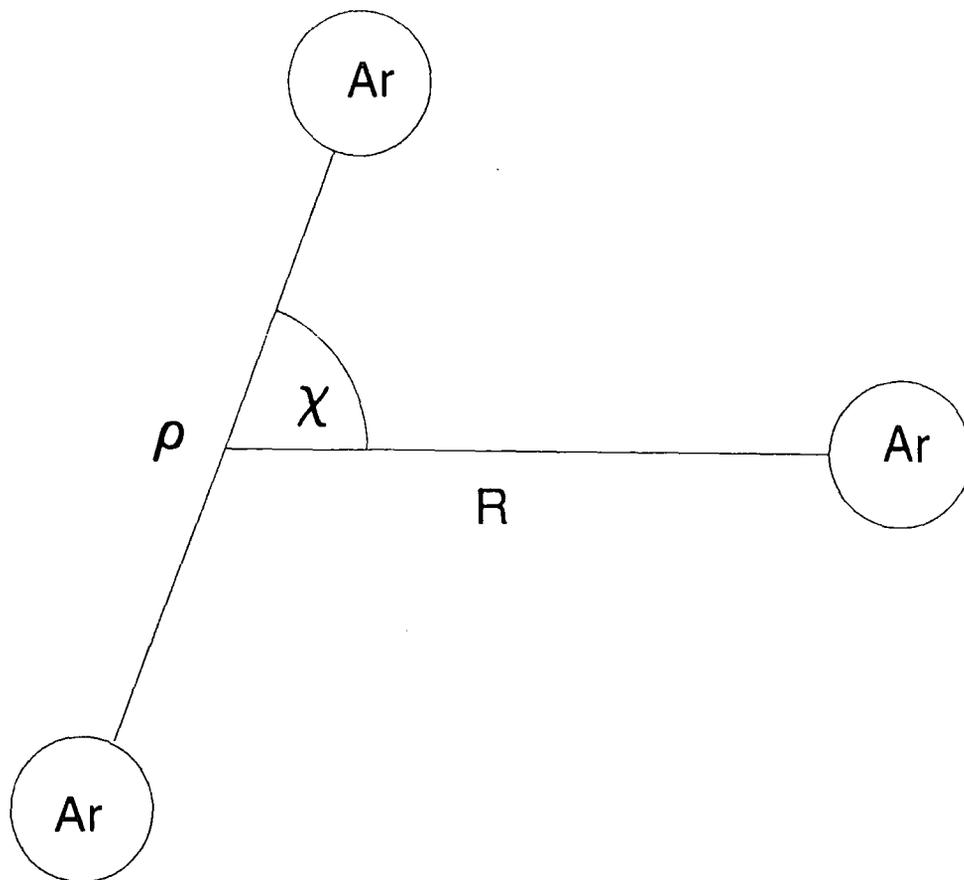
Fig. 8. The Triatomic Jacobi Coordinates.

ments are small, and is likely to provide poor solutions to the Ar_3 problem, the errors increasing rapidly with increasing eigenstate energy. The Jacobi methods are more suitable for non-rigid systems as they permit limited large amplitude motion. The first Jacobi method ('Method I') uses H.O.'s in ρ and χ and is of debatable validity: inspection of the potential plots (see appendix A) indicates that the use of H.O. functions in ρ is possibly unwise. Indeed, it is found that many more functions are required in ρ than χ for convergence. More specialised functions in ρ than χ are used in the second Jacobi method ('Method II') and it is found that much fewer functions in ρ and χ are needed. In addition, in Method II, the same number of functions in ρ as in χ are required, a good indicator that the tailored functions are effective. All of these methods are unsuitable for cases where the amplitudes of motion are sufficient to 'rearrange' a molecule. This is because the basis functions are inappropriate for describing this type of motion in the coordinate systems used. This places a limit of $\chi = \pm 90°$ on the range of rotation of the 'diatom'. Hyperspherical methods allow naturally for such motions, but I am limited to calculating eigenstates which do not extend into such a régime. The implementation of a hyperspherical method for trimeric species to give exact results via a close coupling

calculation has been described for H_3^+, $(H_2)_3$ and Ne_3 [48]and has also been applied to Ar_3 by the same authors [51].

3.1 Methods of Solution – Normal Coordinate Method

The lower energy levels of a chemically bound triatomic molecule would usually be obtained from a normal-mode calculation. However, this method has several potential disadvantages for a floppy molecule such as Ar_3; the vibrations are highly anharmonic, requiring a large basis set to represent them, and there are configurations that can be represented by more than one set of normal coordinate values. Nevertheless, it is interesting to investigate how well a normal mode calculation can manage in practice for a molecule of this type.

The normal coordinates for a D_{3h} molecule may be derived from symmetry rules in the traditional manner [52]. They have symmetries A_1 and E. The transformation from normal coordinates, Q_j, to an x-y plane of cartesian atomic displacements in the plane of the molecule, $\{\Delta x_i, \Delta y_i\}$ is:

$$\Delta x_1 = \frac{Q_3}{\sqrt{3m}}, \quad \Delta y_1 = \frac{Q_1 + Q_2}{\sqrt{3m}}, \tag{30}$$

$$\Delta x_2 = \frac{\sqrt{3}(Q_1 - Q_2) - Q_3}{2\sqrt{3m}}, \quad \Delta \dot{y}_2 = -\frac{Q_1 + Q_2 - \sqrt{3}Q_3}{2\sqrt{3m}}, \tag{31}$$

$$\Delta x_3 = -\frac{\sqrt{3}(Q_1 - Q_2) + Q_3}{2\sqrt{3m}}, \quad \Delta y_3 = -\frac{Q_1 + Q_2 + \sqrt{3}Q_3}{2\sqrt{3m}}. \tag{32}$$

Mass scaling results in the factors $(3m)^{-\frac{1}{2}}$, where m is the atomic mass. Q_1 represents the totally symmetric vibration; Q_2 and Q_3 represent the E orthogonal degenerate pair.

The vibrational wavefunction is expanded in an unsymmetrised product basis:

$$\Psi(Q_1, Q_2, Q_3) = \sum_j^N \sum_k^N \sum_l^N c_{ijk} \phi_j(Q_1) \phi_k(Q_2) \phi_l(Q_3), \tag{33}$$

where the ϕ are normalised harmonic oscillator functions:

$$\phi_j(Q_i) = N_{ji} H_j(\gamma_i^{\frac{1}{2}} Q_i) \exp\left(-\frac{1}{2}\gamma_i Q_i^2\right). \tag{34}$$

Here j is the quantum number and i labels the mode so that $H_j(x)$ is a Hermite Polynomial and N_{ji} a normalisation factor,

$$N_{ji} = \left(\frac{1}{2^j j!}\right)^{\frac{1}{2}} \left(\frac{\gamma_i}{\pi}\right)^{\frac{1}{4}}. \tag{35}$$

3: Some Theoretical Methods for Floppy Triatomics.

The γ_i are scale factors and determine the units of the Q_i, Δx_i and Δy_i. The values of the scale factors are determined by a variational calculation using a single function, minimising the ground state energy for each normal coordinate with a one-dimensional Hamiltonian using NAG routine E04JAF,

$$\widehat{H}_i = -\frac{\hbar^2}{2}\frac{\partial^2}{\partial Q_i^2} + V(Q_i). \tag{36}$$

The potential function $V(Q_i)$ is the full system potential evaluated with the other normal coordinates set equal to zero. The full vibrational Hamiltonian

$$\widehat{H} = -\frac{\hbar^2}{2}\sum_{j=1}^{3}\frac{\partial^2}{\partial Q_j^2} + V(Q_1, Q_2, Q_3), \tag{37}$$

may then be diagonalised, in the basis described, using the above transformations to evaluate the potential.

A Hamiltonian matrix is set up in the orthodox manner. The potential integrals are evaluated by Gauss-Hermite quadrature using NAG routine D01BBF, and the kinetic energy integrals are analytic [53]:

$$\langle \phi_i(Q_1)\phi_j(Q_2)\phi_k(Q_3)| - \sum_{l=1}^{3}\frac{\partial^2}{\partial Q_l^2}|\phi_{i'}(Q_1)\phi_{j'}(Q_2)\phi_{k'}(Q_3)\rangle =$$

$$\left((i+\frac{1}{2})\gamma_1 - \frac{1}{2}\sqrt{i'(i+1)}\gamma_1\delta_{ii'-2} - \frac{1}{2}\sqrt{i(i'+1)}\gamma_1\delta_{ii'+2}\right)\delta_{jj'}\delta_{kk'}$$

$$+ \left((j+\frac{1}{2})\gamma_2 - \frac{1}{2}\sqrt{j'(j+1)}\gamma_2\delta_{jj'-2} - \frac{1}{2}\sqrt{j(j'+1)}\gamma_2\delta_{jj'+2}\right)\delta_{ii'}\delta_{kk'}$$

$$+ \left((k+\frac{1}{2})\gamma_3 - \frac{1}{2}\sqrt{k'(k+1)}\gamma_3\delta_{kk'-2} - \frac{1}{2}\sqrt{k(k'+1)}\gamma_3\delta_{kk'+2}\right)\delta_{ii'}\delta_{jj'}. \tag{38}$$

3.2 Jacobi Coordinate Method I.

The Hamiltonian in Jacobi coordinates is:

$$\hat{H} = -\frac{\hbar^2}{2\mu R}\left(\frac{\partial^2}{\partial R^2}\right)R + \frac{\hbar^2}{M_{Ar}\rho^2}\hat{j}_{Ar}^2$$

$$-\frac{\hbar^2}{M_{Ar}\rho}\left(\frac{\partial^2}{\partial \rho^2}\right)\rho + \frac{\hbar^2}{2\mu R^2}(\hat{J} - \hat{j}_{Ar})^2 + V(R, \rho, \chi), \tag{39}$$

where

$$\mu = \frac{2M_{Ar}}{3} \quad \text{and} \quad \hat{j}_{Ar}^2 = -\frac{\partial}{\partial \cos\chi}\left((1 - \cos^2\chi)\frac{\partial}{\partial \cos\chi}\right), \tag{40}$$

i.e. the reduced mass, μ, is that of the 'atom–diatom' complex.

The basis-set used is a product basis of a DGB in R and H.O. functions in $\cos\chi$ and ρ:

$$\Psi(\cos\chi,\rho,R) = \sum_{i=0}^{N_\rho}\sum_{j=0}^{N_\chi}\sum_{k=0}^{N_R} c_{ijk}\phi_i(\cos\chi)\phi_j(\rho-\rho_0)\psi_k(R), \quad i+j \le q_{max}; \qquad (41)$$

the sum being restricted in this way allows a more size efficient basis. The ϕ are normalised harmonic oscillator functions, as previously described, having three variable parameters, ρ_0, γ_ρ and γ_χ The H.O. point of zero displacement in the real coordinates is ρ_0, and may be approximately determined from the minimum on the potential energy surface. Since the potential is not symmetric this is not the optimum value, as for the ground state $\langle\rho\rangle$ is greater than the value of ρ at the potential minimum. The optimal value of ρ_0 may be determined variationally. The potential is symmetric in χ, with an equilibrium at $\cos\chi = 0$, so that there is no choice in the function centre. The DGB consists of equally spaced functions $\psi_k(R)$, with parameters determined as discussed earlier.

The problem is solved in two stages. First, it is necessary to determine good values for the harmonic oscillator scale factors, γ_χ and γ_ρ, and maybe the zero–point of the ρ function, ρ_0. This is done by freezing R at its equilibrium value and diagonalising the Hamiltonian matrix with the basis

$$\Psi_{H.O.}(\cos\chi,\rho) = \sum_i\sum_j c_{ij}\phi_i(\cos\chi)\phi_j(\rho-\rho_0), \quad i+j \le q_{max}, \qquad (42)$$

varying the parameters to minimise the ground state energy using the NAG routine E04JAF. Once these parameters are determined, the full Hamiltonian is diagonalised in the basis Ψ.

3.3 Jacobi Coordinate Method II.

This method is a simplification of the theoretical method used for Ar_2HX trimers; only the triatom-specific details are given here.

Functions are chosen to model the motion in each coordinate according to the extent of freedom and boundary conditions.

- A set of gaussians $\psi_i(R)$ distributed equally on R (i.e. a DGB) is used to model the large amplitude stretch. The spread of each gaussian is calculated in terms of a variational parameter, 'c', and the range of distribution is convergence determined.

- Orthonormal one-dimensional functions $\Upsilon_w(\rho)$ and $\Phi_v(\cos\chi)$, determined as eigenfunctions of effective potentials, are used for the ρ and χ degrees of freedom. The method of calculating these functions is described later.

The basis function is now:

$$\Psi_a = \psi_i(R)\Phi_v(\cos\chi)\Upsilon_w(\rho), \tag{43}$$

the collection of the index i and the quantum numbers $\{v, w\}$ are denoted a. The basis-set is described by the DGB size, $N_{DGB} \geq i \geq 1$, and the quantum number restrictions $v_{max} \geq v \geq 0$, $w \geq 0$ and $q_{max} \geq v + w$. Symmetrisation following the method described in the section dealing with Ar_2HX theory is applied. In contrast to Ar_2HX, where the alternating symmetry of the HX rotational functions with respect to space inversion, E^*, allows for both values of the parity, ϵ, vibrational wavefunctions of triatomic complexes must have ϵ even. That is to say E^* is only a symmetry operation on an Ar_3 ro-vibrational wavefunction; here only the vibrational wavefunction is determined, so that symmetry group is the permutation group, S_2, rather than $C_{2v}(M)$. Hence the symmetry labels are A' and A''; A_1 and B_2 in C_{2v} map to A' and A'' in S_2, respectively. The symmetry with respect to argon permutation, η, is found to impose the restriction that $(v + \eta)$ must be even; symmetry separates calculations with odd and even functions in χ vibrations.

For Ar_3, the exchange of two particles must leave the sign of the total wavefunction unchanged, since Ar nuclei are bosons. Rotational functions alternate in symmetry with respect to argon permutation. This may be shown by noting that the D_{MK}^{J*} rotational functions transform with character $(-1)^K$ under (12) permutation, hence vibrational states with a given η will only exist if $(-1)^\eta = (-1)^K$ since the argon nuclei are spinless, and hence must have a symmetric nuclear spin wavefunction. Since I am calculating vibrational, rather than $J = 0$ states I require both values of η to be used (I distinguish between a $J = 0$ and vibrational calculation since I calculate $\eta = 1$ states, which do not exist for $J = 0$). States which are symmetric under (12) permutation have $\eta = 0$ and are

labelled A' and states which are antisymmetric have $\eta = 1$ and are labelled A''. The A_1 label in $D_{3h}(M)$ maps to A' in S_2, while the E pair are formed from the representation $A' \oplus A''$. The energetic difference between the two components of the E pair will indicate the degree of convergence of the basis-set.

3.3. 1   The Calculation of $\Upsilon_w(\rho)$ and $\Phi_v(\cos\chi)$

$\Upsilon_w(\rho)$ and $\Phi_v(\cos\chi)$ are calculated as eigenstates of a part of the Hamiltonian operator which relates to the coordinate of interest. This contains an one-dimensional effective potential V_{eff} which is a cut on the full potential energy surface. This is an adiabatic Hamiltonian. Some criteria are required to determine appropriate values for the coordinates of the cut. It is important to examine the forms of trimer potentials in general to get some indication of the relative importance of any coordinate by itself. In particular, we do not wish to use a cut which unduly restricts Υ or Φ nor one which gives them too great a spread. Some numerical results of the method described here are presented in chapter 7.

Examination of potential cuts for triangular trimers (plots for Ar_3 and Ar_2HCl/F are given in appendices A, B and C) shows that there is strong dependence of $V(\chi)$ with respect to R. To pick a value of R_{cut} as being that for equilibrium is clearly unsuitable as $\Phi(\cos\chi)$ will be too restricted. We wish to allow freedom in χ in the presence of excitation in R and so select $R_{cut} = \langle R\rangle_1$, where $\langle R\rangle_1$ is the expectation value of R for the first state excited in R of a calculation with ρ and χ clamped at their equilibrium values. $\rho_{cut} = \langle\rho\rangle_1$ is used, where $\langle\rho\rangle_1$ is the expectation value of ρ of $\Upsilon_1(\rho)$. The choice of ρ_{cut} is likely to be less critical due to the rather square appearance ρ versus $\cos\chi$ potentials.

For $V(\rho)$, $\cos\chi_{cut} = 0$ is used as the only rational choice. An inspection of ρ versus R plane cuts on the potentials of interest shows that there is a minimum for R_{cut} below which $\Upsilon(\rho)$ will be too restricted, in general. Using the same recipe as for $\Phi(\cos\chi)$ will avoid this and should provide a suitable value on the basis of the same arguments.

3: Some Theoretical Methods for Floppy Triatomics.

The one-dimensional adiabatic Hamiltonians are simply:

$$\hat{H}_{1D,\rho} = -\frac{\hbar^2}{M_{Ar}\rho}\left(\frac{\partial^2}{\partial\rho^2}\right)\rho + V(R_{cut},\rho,\cos\chi_{cut}) \tag{44}$$

and

$$\hat{H}_{1D,\chi} = \left(\frac{\hbar^2}{M_{Ar}\rho_{cut}^2} + \frac{\hbar^2}{2\mu R_{cut}^2}\right)\hat{j}_{Ar}^2 + V(R_{cut},\rho_{cut},\cos\chi). \tag{45}$$

.3. 2   The Matrix Elements.

The vibrational Hamiltonian is as above for the Jacobi I method, with $J = 0$, since it is only coordinate-dependent. Much of the kinetic part of the Hamiltonian, $\hat{H}$, can be evaluated analytically, whereas the potential part must be evaluated using numerical methods. It is appropriate to rearrange $\hat{H}$ by defining:

$$\hat{K}_\rho = \hat{K}_{\rho,0} + \hat{K}_{\rho,r} = -\frac{\hbar^2}{M_{Ar}\rho}\left(\frac{\partial^2}{\partial\rho^2}\right)\rho, \tag{46}$$

$$\hat{K}_\chi = \hat{K}_{\chi,0} + \hat{K}_{\chi,r} = \left(\frac{\hbar^2}{M_{Ar}\rho^2} + \frac{\hbar^2}{2\mu R^2}\right)\hat{j}_{Ar}^2 \tag{47}$$

and

$$V(R,\rho,\chi) = V_0(\rho) + V_0(\chi) + V_r(R,\rho,\chi) \tag{48}$$

such that:

$$(\hat{K}_{\rho,0} + V_0(\rho) - E_w^\Upsilon)\Upsilon_w(\rho) = 0 \tag{49}$$

and

$$(\hat{K}_{\chi,0} + V_0(\chi) - E_v^\Phi)\Phi_v(\cos\chi) = 0. \tag{50}$$

That is $\hat{H}_{1D,\rho} = \hat{K}_{\rho,0} + V_0(\rho)$ and $\hat{H}_{1D,\chi} = \hat{K}_{\chi,0} + V_0(\chi)$. The Hamiltonian is now:

$$\hat{H} = -\frac{\hbar^2}{2\mu R}\left(\frac{\partial^2}{\partial R^2}\right)R + V_r(R,\rho,\chi)+$$

$$\hat{K}_{\rho,0} + \hat{K}_{\rho,r} + \hat{K}_{\chi,0} + \hat{K}_{\chi,r} + V_0(\rho) + V_0(\chi). \tag{51}$$

Thus only the residual potential V_r need be integrated over since we have the E_w^Υ and E_v^Φ and Υ_w and Φ_v are orthonormal functions. This is an advantage since less precision is demanded of the integration in ρ and $\cos\chi$.

We can also make savings in the R part of the potential integral evaluation. For an equally spaced DGB, products of pairs of DGB basis functions have centres at or exactly in between one of the basis function centres. If, at each of these $2N_{DGB} - 1$ centres, the potential in R is expanded as a Taylor series $V(x) = \sum_n C_n x^n$ we obtain an integral of form:

$$\int_0^\infty \psi_{i'}(R)V(R)\psi_i(R)dR = \sum_n C_{2n} \int_{-\infty}^\infty x^{2n}e^{-ax^2}dx, \tag{52}$$

where $x = R - R_{\text{centre}}$, R_{centre} is the centre of a product of two DGB basis functions and a is twice the DGB exponent. The integral is a well-known analytic one:

$$\int_{-\infty}^\infty x^{2n}e^{-ax^2}dx = \frac{(2n-1)(2n-3)...1}{(2a)^n}\sqrt{\frac{\pi}{a}}. \tag{53}$$

The Taylor expansion only needs to be carried out at $2N_{DGB} - 1$ points and can be performed from a grid of a small number points covering the whole range of R. I used a variant on CACM algorithm 416 [54] for this.

The analytic DGB basis-function overlap-integral is defined as

$$S_{i'i} = \int_0^\infty \psi_{i'}(R)\psi_i(R)dR = e^{-g(R_i - R_{i'})/2}, \tag{54}$$

where g is the DGB exponent, and the R kinetic term is defined as

$$K_{i'i}^R = -\frac{\hbar^2}{2\mu}\int_0^\infty \psi_{i'}(R)\left(\frac{1}{R}\frac{\partial^2}{\partial R^2}\right)R\psi_i(R)dR = \frac{\hbar^2}{2\mu}S_{i'i}g[1 - g(R_i - R_{i'})^2]. \tag{55}$$

The kinetic energy term in $\cos\chi$ is analytic if the $\Phi_v(\cos\chi)$ are expressed as an expansion of harmonic oscillators. It can be shown that if

$$\hat{K} = \frac{\partial}{\partial\cos\chi}(1 - \cos^2\chi)\frac{\partial}{\partial\cos\chi} \tag{56}$$

then integrals between harmonic oscillator functions,

$$\varphi_n(x) = \left(\frac{\gamma}{\pi}\right)^{\frac{1}{4}}\left(\frac{1}{2^n n!}\right)^{\frac{1}{2}}H_v(\gamma^{\frac{1}{2}}x)\exp(-\gamma x^2/2), \tag{57}$$

where $H_n(y)$ is a Hermite polynomial, are:

$$\langle n|\hat{K}|n\rangle = -\gamma(n + \frac{1}{2}) + \frac{n(n+1)}{2} + \frac{3}{4}$$

3: Some Theoretical Methods for Floppy Triatomics.

$$\langle n+2|\hat{K}|n\rangle = \frac{\gamma\sqrt{(n+1)(n+2)}}{2}$$

$$\langle n+4|\hat{K}|n\rangle = -\frac{\sqrt{(n+1)(n+2)(n+3)(n+4)}}{4}. \tag{58}$$

If $\Phi_v(\cos\chi) = \sum_n c_n^{(v)}\varphi_n(\cos\chi)$ then

$$K_{v'v}^\chi = \sum_n c_n^{(v')} \sum_m c_m^{(v)}\langle m|\hat{K}|n\rangle. \tag{59}$$

The symmetry of the $\Phi_v(\cos\chi)$ and the properties of the $\langle m|\hat{K}|n\rangle$ ensure that $K_{v'v}^\chi = 0$ unless $v - v'$ is even. This is also guaranteed by the basis-set symmetrisation used.

The numerically evaluated terms are defined by

$$T_{i'i}^{\ddagger} = \frac{\hbar^2}{2\mu}\int_0^\infty \psi_{i'}(R)\frac{(R_{\text{cut}}^2 - R^2)}{R_{\text{cut}}^2 R^2}\psi_i(R)dR, \tag{60}$$

$$T_{i'i} = \frac{\hbar^2}{2\mu}\int_0^\infty \psi_{i'}(R)\frac{1}{R^2}\psi_i(R)dR \tag{61}$$

and

$$U_{w'w} = \frac{\hbar^2}{M_{\text{Ar}}}\int_0^\infty \Upsilon_{w'}(\rho)\frac{(\rho_{\text{cut}}^2 - \rho^2)}{\rho_{\text{cut}}^2\rho^2}\Upsilon_w(\rho)d\rho. \tag{62}$$

The Hamiltonian matrix element is then:

$$H_{a'a} = \delta_{w'w}\left[\delta_{v'v}\left(K_{i'i}^R + S_{i'i}(E_v^\Phi + E_w^\Upsilon)\right) - T_{i'i}^{\ddagger}K_{v'v}^\chi\right] - S_{i'i}U_{w'w}K_{v'v}^\chi +$$

$$\int_0^\infty dR\int_0^\infty d\rho\int_{-1}^1 d(\cos\chi)\psi_{i'}(R)\Phi_{v'}(\cos\chi)\Upsilon_{w'}(\rho)V(R,\rho,\chi)\psi_i(R)\Phi_v(\cos\chi)\Upsilon_w(\rho). \tag{63}$$

3.4 A Note on the Symmetries of Overtone States of Ar$_3$.

Overtone levels of a doubly degenerate state have degeneracy $v + 1$, where v is the sum of quantum numbers in each component of the pair. For example, there is a set of degenerate wavefunctions $\Psi_{3,0}$, $\Psi_{2,1}$, $\Psi_{1,2}$ and $\Psi_{0,3}$ for a total of three quanta.

The procedure for establishing the symmetry labels of these overtones is well established [53] and is expounded below. If the degenerate pair of functions are denoted Q_a and Q_b, a operator $\hat{R}$ will transform among this pair: $\hat{R}(Q_a) = R_a a Q_a + R_a b Q_b$ and $\hat{R}(Q_b) = R_b a Q_a + R_b b Q_b$. Using a set of normal coordinates it is possible to arrange for

$\hat{R}(Q_a) = R_a Q_a$ and $R(Q_b) = R_b Q_b$ since the character under a transformation is not coordinate dependent. Hence the character of a degenerate set of states with v quanta under the application of $\hat{R}$ w times, $\chi_v(R^w)$, can be written:

for $v = 2$ we have

$$\hat{R}(Q_a^2) = R_a^2 Q_a^2, \tag{64}$$

$$\hat{R}(Q_a Q_b) = R_a R_b Q_a Q_b \tag{65}$$

and

$$\hat{R}(Q_b^2) = R_b^2 Q_b^2, \tag{66}$$

giving

$$\chi_2(R) = R_a^2 + R_a R_b + R_b^2 \tag{67}$$

and for $v = 3$ we have

$$\hat{R}(Q_a^3) = R_a^3 Q_a^3, \tag{68}$$

$$\hat{R}(Q_a^2 Q_b) = R_a^2 R_b Q_a^2 Q_b, \tag{69}$$

$$\hat{R}(Q_a Q_b^2) = R_a R_b^2 Q_a Q_b^2 \tag{70}$$

and

$$\hat{R}(Q_b^3) = R_b^3 Q_b^3, \tag{71}$$

giving

$$\chi_2(R) = R_a^3 + R_a^2 R_b + R_a R_b^2 + R_b^3. \tag{72}$$

Since $\chi_1(R^w) = R_a^w + R_b^w$, we can write $\chi_2(R) = \frac{1}{2}[\chi_1(R)\chi_2(R) + \chi_1(R^3)]$, and generalise to:

$$\chi_v(R) = \frac{1}{2}[\chi_1(R)\chi_{v-1}(R) + \chi_1(R^v)]. \tag{73}$$

This equation gives the character of any overtone of a doubly degenerate fundamental under an arbitrary operation R.

Using the equation for the character of an overtone, with the character table for symmetry group D_{3h}, it can be shown that for two quanta in an E fundamental $\chi_2(E) = \chi_2(\sigma_h) = 3$, $\chi_2(C_3) = \chi_2(S_3) = 0$ and $\chi_2(C_2) = \chi_2(\sigma_v) = 1$; i.e. the overtone has

The character table for D_{3h}:

	E	$2C_3$	$3C_2$	σ_h	$2S_3$	$3\sigma_v$
A_1	1	1	1	1	1	1
A_2	1	1	-1	1	1	-1
E	2	-1	0	2	-1	0
A_1'	1	1	1	-1	-1	-1
A_2'	1	1	-1	-1	-1	1
E'	2	-1	0	-2	1	0

symmetry $A_1 \oplus E$. The three quantum overtone has $\chi_3(E) = \chi_3(\sigma_h) = 4$, $\chi_3(C_3) = \chi_3(S_3) = 1$ and $\chi_3(C_2) = \chi_3(\sigma_v) = 0$ and has symmetry $A_1 \oplus A_2 \oplus E$.

The above has repercussions in the S_2 symmetrised treatment since E maps to $A' \oplus A''$ and A_2 also maps to A''. Hence for three quanta there will be two states of A' symmetry (an $\eta = 0$ calculation) and two states of A'' symmetry ($\eta = 1$); correlation of these results with D_{3h} labels will not be trivial.

4: The Theory Used to Model the Dynamics of Ar$_2$HX Systems.

Building on the Jacobi II method, which was described in the previous chapter, and found to be the most efficient method tested in chapter 8, I now describe in detail the method which is used to calculate the lower bound-states of Ar$_2$HX trimers in chapter 9. The coordinate system is first described followed by the Hamiltonian operator in this coordinate system. Some angular momentum terms are neglected from the Hamitonian in order to make the resulting matrix of tractable size. Using previously described basis functions, a symmetrised basis-set is written down and the algebra involved in the calculation of matrix elements between these functions is explicitly laid out. The methods which have been used to improve the efficiency of matrix element evaluation are also explained. The method by which relative band intensities were calculated, using analytic integrals, is also described. Finally, the simplifications arising from clamping the argon atoms are summarised.

4.1 The Coordinate System.

As is commonplace in the study of the dynamics of weakly bound complexes, body-fixed Jacobi coordinates are extended. The Jacobi coordinates consist of the separation, ρ, of the two argon atoms, the distance between the Ar$_2$ centre-of-mass and the HX centre-of-mass, R, and the angle between the vectors along ρ and R. Extension of these coordinates is necessary to account for the structure of the HX; two angles, θ and ϕ, are defined in the convention of spherical-polar coordinates. θ is the angle between the vector along R and the HX bond-vector, with $\theta = 0$ defined at the geometry when the H atom is closer to the Ar$_2$ centre-of-mass than X is. ϕ orientates the HX about the vector along R, for a given θ, and is defined as a multiple of π when the HX bond-vector lies in the same plane as the Ar$_2$ nuclei. This coordinate system is illustrated in figure 9.

A full consideration of the ro-vibrational dynamics would then describe the orientation of the complex in space by three (Euler) orientation angles [55] [43]. This approach is complicated since it would almost fully quantise internal angular momentum on the Ar$_2$
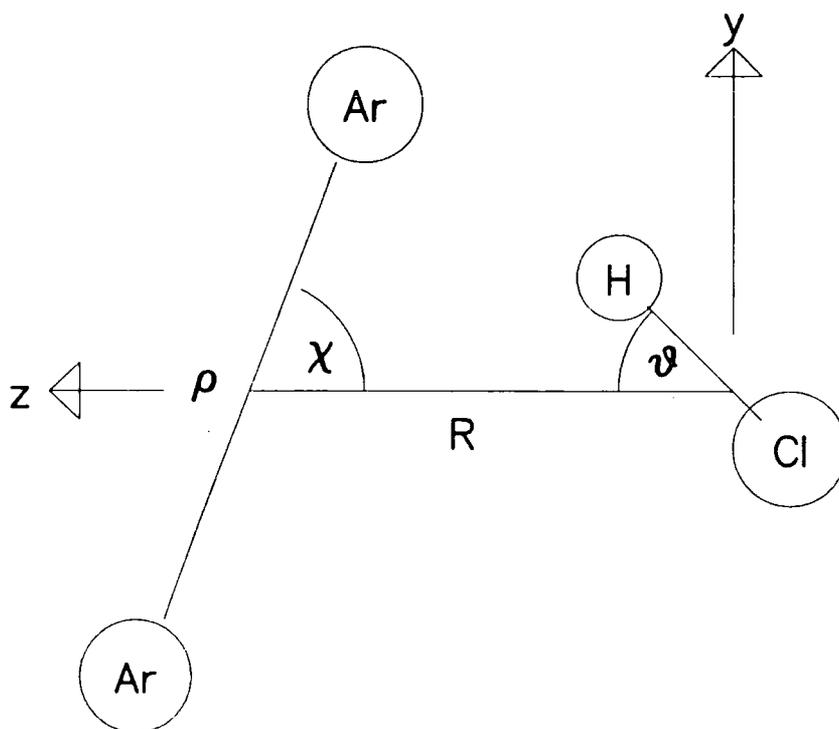
Fig. 9. The Body-fixed Jacobi-type coordinates for Ar_2HX.

to HX axis, while the complex is a near symmetric top with its top axis perpendicular to the molecular plane. The complications which arise in the consideration of angular momentum coupling are bypassed in this work by considering the purely vibrational problem. This does not preclude comparison of results with spectroscopy and so is not a drastic measure; rotational constants may be estimated from expectation value calculations.

4.2 The Hamiltonian.

The vibrational Hamiltonian in Jacobi coordinates, treating HX as a rigid rotor with rotational constant b_{HX}, is [21]:

$$
\hat{H}_{\text{vib}} = -\frac{\hbar^2}{2\mu R}\left(\frac{\partial^2}{\partial R^2}\right)R + b_{HX}\hat{\jmath}_{HX}^2 + \frac{\hbar^2}{M_{Ar}\rho^2}\hat{\jmath}_{Ar}^2
$$
$$
-\frac{\hbar^2}{M_{Ar}\rho}\left(\frac{\partial^2}{\partial\rho^2}\right)\rho + \frac{\hbar^2}{2\mu R^2}(\hat{\jmath}_{HX}+\hat{\jmath}_{Ar})^2 + V(R,\rho,\chi,\theta,\phi),
$$

(74)

4: The Theory Used to Model the Dynamics of Ar_2HX Systems.

where $\mu = 2M_{Ar}M_{HX}/(2M_{Ar} + M_{HX})$ is the collisional reduced mass of the complex, M_{Ar} is the argon atomic mass and $\hat{\jmath}_{HX}$ and $\hat{\jmath}_{Ar}$ are the body fixed angular momentum operators for HX and Ar$_2$ motions respectively.

$V(R, \rho, \chi, \theta, \phi)$ is the trimer intermolecular potential averaged over the HX internal vibration. This potential depends, at least in principle, on the HX vibrational quantum number.

The coupling of the angular motions of the Ar$_2$ and the HX through the cross term $\hat{\jmath}_{HX} \cdot \hat{\jmath}_{Ar}$ is neglected, giving the Hamiltonian:

$$
\hat{H} = -\frac{\hbar^2}{2\mu R}\left(\frac{\partial^2}{\partial R^2}\right)R + \left(b_{HX} + \frac{\hbar^2}{2\mu R^2}\right)\hat{\jmath}_{HX}^2 + \left(\frac{\hbar^2}{M_{Ar}\rho^2} + \frac{\hbar^2}{2\mu R^2}\right)\hat{\jmath}_{Ar}^2
$$
$$
- \frac{\hbar^2}{M_{Ar}\rho}\left(\frac{\partial^2}{\partial \rho^2}\right)\rho + V(R, \rho, \chi, \theta, \phi).
$$
(75)

4.3   The Basis Functions Used.

Functions are chosen to model the motion in each coordinate according to the extent of freedom and boundary conditions.

o   Spherical harmonics $Y_{jk}(\theta, \phi)$ in the phase convention of Condon and Shortley [56] are rotational eigenfunctions in free space and are chosen as a basis-set for HX motion since this is only weakly hindered.

o   A set of gaussians $\psi_i(R)$ distributed equally on R (i.e. a DGB) is used to model the large amplitude stretch. The spread of each gaussian is calculated in terms of a variational parameter, 'c', and the range of distribution is determined by convergence.

o   Orthonormal one-dimensional functions $\Upsilon_w(\rho)$ and $\Phi_v(\cos\chi)$, determined as eigenfunctions of effective potentials, are used for the ρ and χ degrees of freedom. The method of calculating these functions was described in the section on triatomic theory.

Symmetrised basis functions arising from a restricted direct product of functions in each body-fixed coordinate are used.

4: The Theory Used to Model the Dynamics of Ar$_2$HX Systems.

Ar$_2$HX has the molecular symmetry (MS) group $C_{2v}(M)$ [57]. Under the primitive symmetry operations of argon permutation, (12) and space fixed inversion, E^*, we have the character table:

	E	(12)	E^*	(12)*
A_1	1	1	1	1
A_2	1	1	-1	-1
B_1	1	-1	-1	1
B_2	1	-1	1	-1

In the Ar$_2$HX vibration-only problem, unlike Ar$_3$, E^* symmetrically transforms the vibrational wavefunction so that the character table of the ro-vibrational molecular symmetry group still applies. When considering the symmetry of the complete wavefunction, it must be borne in mind that rotational functions alternate in symmetry with respect to E^*.

The effect of each symmetry operation on the basis functions may be found from the transformation properties of the coordinates in them. With the coordinate system described above we may write:

$$(12)(\theta, \phi, \chi) \rightarrow (\theta, \pi + \phi, \pi - \chi);$$

$$E^*(\theta, \phi, \chi) \rightarrow (\theta, -\phi, \chi); \tag{76}$$

$$(12)^*(\theta, \phi, \chi) \rightarrow (\theta, -\pi - \phi, \pi - \chi),$$

from which it is possible to deduce the function transformation properties:

E	$\Phi_v(\cos\chi)$	$Y_{jk}(\theta, \phi)$
(12)	$(-)^v\Phi_v(\cos\chi)$	$(-)^k Y_{jk}(\theta, \phi)$
E^*	$\Phi_v(\cos\chi)$	$(-)^k Y_{j-k}(\theta, \phi)$
(12)*	$(-)^v\Phi_v(\cos\chi)$	$Y_{j-k}(\theta, \phi)$

With this information the primitive functions can be projected out to give symmetrised basis functions:

4: *The Theory Used to Model the Dynamics of Ar$_2$HX Systems.*

$$\Psi_a = \frac{1}{\sqrt{2(1+\delta_{k0})}}\psi_i(R)\Phi_v(\cos\chi)\Upsilon_w(\rho)\times$$
$$[Y_{jk}(\theta,\phi)+(-)^{k+\epsilon}Y_{j-k}(\theta,\phi)], \tag{77}$$

where the symbols ϵ and η determine the symmetry label which applies to the function: $(-1)^\epsilon$ gives the character with respect to space inversion, E^*, and $(-1)^\eta$ the character with respect to permutation, (12).

The collection of the index i, the quantum numbers $\{v, w, j, k\}$ and the symbols ϵ and η is denoted a. The basis-set is described by the DGB size, $N_{\mathrm{DGB}} \geq i \geq 1$, and the quantum number restrictions $v_{\max} \geq v \geq 0$, $w \geq 0$, $q_{\max} \geq v + w$, $j_{\max} \geq j \geq 0$. Two restrictions apply to k. Physically, $j \geq k \geq 0$ but the basis-set may be reduced by only using low k for high j.

Some quantum number combinations are eliminated by symmetry, so reducing the basis-set size; $(\eta + v + k)$ must be even and $k = 0$ functions are only included if $\epsilon = 0$.

Argon nuclei are bosons, however, so (12) permutation must not change the total wavefunction sign. In addition, argon nuclei are spinless, so that the nuclear spin part of the total wavefunction is symmetric, so that (12) permutation must not change the sign of the vibrational-rotational wavefunction. This symmetry restriction is not absolute, however, since the rotational functions alternate in symmetry under the operations (12) and E^*; all vibrational symmetries are represented in a ro-vibrational spectrum. Hence (vibration only) calculations should be performed for both values of η and the K selection borne in mind.

4.4 The Matrix Elements.

Much of the kinetic part of the Hamiltonian, $\hat{H}$, can be evaluated analytically, whereas the potential part must be evaluated using numerical methods. It is appropriate to rearrange $\hat{H}$ by defining:

$$\hat{K}_\rho = \hat{K}_{\rho,0} + \hat{K}_{\rho,r} = -\frac{\hbar^2}{M_{Ar}\rho}\left(\frac{\partial^2}{\partial\rho^2}\right)\rho, \tag{78}$$

$$\hat{K}_\chi = \hat{K}_{\chi,0} + \hat{K}_{\chi,r} = \left(\frac{\hbar^2}{M_{\mathrm{Ar}}\rho^2} + \frac{\hbar^2}{2\mu R^2}\right)\hat{j}_{\mathrm{Ar}}^2 \tag{79}$$

4: The Theory Used to Model the Dynamics of Ar_2HX Systems.

and

$$V(R,\rho,\chi,\theta,\phi) = V_0(\rho) + V_0(\chi) + V_r(R,\rho,\chi,\theta,\phi) \tag{80}$$

such that:

$$(\hat{K}_{\rho,0} + V_0(\rho) - E_w^\Upsilon)\Upsilon_w(\rho) = 0 \tag{81}$$

and

$$(\hat{K}_{\chi,0} + V_0(\chi) - E_v^\Phi)\Phi_v(\cos\chi) = 0. \tag{82}$$

That is $\hat{H}_{1D,\rho} = \hat{K}_{\rho,0} + V_0(\rho)$ and $\hat{H}_{1D,\chi} = \hat{K}_{\chi,0} + V_0(\chi)$. The Hamiltonian is now:

$$\hat{H} = -\frac{\hbar^2}{2\mu R}\left(\frac{\partial^2}{\partial R^2}\right)R + \left(b_{HX} + \frac{\hbar^2}{2\mu R^2}\right)\hat{j}_{HX}^2 +$$

$$V_r(R,\rho,\chi,\theta,\phi) + \hat{K}_{\rho,0} + \hat{K}_{\rho,r} + \hat{K}_{\chi,0} + \hat{K}_{\chi,r} + V_0(\rho) + V_0(\chi). \tag{83}$$

Thus only the residual potential V_r need be integrated over since we have the E_w^Υ and E_v^Φ and Υ_w and Φ_v are orthonormal functions. This is an advantage since less precision is demanded of the integration in ρ and $\cos\chi$.

Efficient evaluation of potential matrix elements is possible by expanding the residual potential as a series of spherical harmonics in θ and ϕ at a given $(R,\rho,\cos\chi)$ point. We may then take advantage of the analytic properties of an integral of three spherical harmonics. The potential is symmetric about $\phi = 0$ so that the expansion can be symmetrised:

$$V_r(R,\rho,\chi,\theta,\phi) = \sum_l \sum_{m=0}^l F_{lm}(R,\rho,\chi)[Y_{lm}(\theta,\phi) + (-1)^m Y_{l-m}(\theta,\phi)]/2. \tag{84}$$

Since spherical harmonics are orthogonal, the coefficients F_{pq} are evaluated by multiplying both sides of the expression for the series by $Y_{pq}^*(\theta,\phi)$ and integrating:

$$F_{pq}(R,\rho,\chi) = \frac{2}{(1+\delta_{q0})}\int_0^{2\pi} d\phi \int_0^\pi \sin\theta d\theta \; Y_{pq}^*(\theta,\phi)V_r(R,\rho,\chi,\theta,\phi). \tag{85}$$

Having reduced the potential to such a series, the (θ,ϕ) integrals reduce to sets of integrals which can be expressed in terms of 3-j symbols [43]:

$$\int_0^{2\pi} d\phi \int_0^\pi \sin\theta d\theta \; Y_{j'k'}Y_{lm}Y_{jk} = \sqrt{\frac{(2j'+1)(2l+1)(2j+1)}{4\pi}}\begin{pmatrix} j' & l & j \\ k' & m & k \end{pmatrix}\begin{pmatrix} j' & l & j \\ 0 & 0 & 0 \end{pmatrix}. \tag{86}$$

4: The Theory Used to Model the Dynamics of Ar_2HX Systems.

If this integral is denoted

$$\begin{bmatrix} j' & l & j \\ k' & m & k \end{bmatrix},$$
(87)

the properties of 3-j symbols give:

$$\begin{bmatrix} j' & l & j \\ k' & m & k \end{bmatrix} = \begin{bmatrix} j' & l & j \\ -k' & -m & -k \end{bmatrix},$$
(88)

$$\begin{bmatrix} j' & l & j \\ k' & m & k \end{bmatrix} = 0 \quad \text{unless} \quad k' + m + k = 0 \quad \text{and} \quad j' + l + j \quad \text{is even.}$$
(89)

The following numerically evaluated terms are also defined:

$$T_{i'i}^{\ddagger} = \frac{\hbar^2}{2\mu} \int_0^{\infty} \psi_{i'}(R) \frac{(R_{\text{cut}}^2 - R^2)}{R_{\text{cut}}^2 R^2} \psi_i(R) dR,$$
(90)

$$T_{i'i} = \frac{\hbar^2}{2\mu} \int_0^{\infty} \psi_{i'}(R) \frac{1}{R^2} \psi_i(R) dR$$
(91)

and

$$U_{w'w} = \frac{\hbar^2}{M_{\text{Ar}}} \int_0^{\infty} \Upsilon_{w'}(\rho) \frac{(\rho_{\text{cut}}^2 - \rho^2)}{\rho_{\text{cut}}^2 \rho^2} \Upsilon_w(\rho) d\rho.$$
(92)

The Hamiltonian matrix element is:

$$H_{a'a} = \delta_{j'j} \Bigg[\delta_{k'k} \Bigg[\delta_{w'w} \Bigg[\delta_{v'v} \Bigg(K_{i'i}^R + S_{i'i}(b_{\text{HCl}}j(j+1) + E_v^{\Phi} + E_w^{\Upsilon}) + $$

$$T_{i'i}j(j+1) \Bigg) - T_{i'i}^{\ddagger} K_{v'v}^{\chi} \Bigg] - S_{i'i}U_{w'w}K_{v'v}^{\chi} \Bigg] \Bigg] + $$

$$\frac{1}{(1+\delta_{k0})^{\frac{1}{2}}(1+\delta_{k'0})^{\frac{1}{2}}} \int_0^{\infty} dR \int_0^{\infty} d\rho \int_{-1}^{1} d(\cos\chi) \sum_l \sum_{m=0}^{l} F_{lm}(R,\rho,\chi)(-)^{k'}$$

$$\times \Bigg((-)^{\epsilon+k'} \begin{bmatrix} j' & l & j \\ k' & m & k \end{bmatrix} + (-)^{k+k'} \begin{bmatrix} j' & l & j \\ k' & m & -k \end{bmatrix} + \begin{bmatrix} j' & l & j \\ -k' & m & k \end{bmatrix} + (-)^{\epsilon+k} \begin{bmatrix} j' & l & j \\ -k' & m & -k \end{bmatrix} \Bigg).$$
(93)

4.5 Calculation of Band Intensities.

It is important to calculate transition intensities for comparison with experiment and to predict which other bands might be observable. The intensity of a transition between two vibrational states a and b, i.e. a band intensity, is proportional by a state-independent factor to:

$$I_{ab} = |I_{ab,-1}|^2 + |I_{ab,0}|^2 + |I_{ab,1}|^2,$$
(94)

where

$$I_{ab,q} = \langle a | Y_{1q} | b \rangle.$$
(95)

4: The Theory Used to Model the Dynamics of Ar$_2$HX Systems.

Parallel (*a*-type) transitions are identified by $I_{ab,\pm 1} = 0$; conversely perpendicular transitions have $I_{ab,0} = 0$. The vibration-only basis function is:

$$\Psi^{\dagger}_{ivwjk} = \frac{1}{\sqrt{2(1+\delta_{k0})}}\psi_i(R)\Phi_v(\cos\chi)\Upsilon_w(\rho)\times$$

$$[Y_{jk}(\theta,\phi) + (-)^{k+\epsilon}Y_{j-k}(\theta,\phi)]. \tag{96}$$

If $c^{(a;\epsilon\eta)}_{ivwjk}$ is an eigenvector component for a vibrational eigenfunction a, which has the given ϵ, η, then:

$$I_{ab,q} = \sum_{iwvjk}\sum_{i'j'k'}\frac{(-)^k}{4(1+\delta_{k0})(1+\delta_{k'0})}c^{(a;\epsilon\eta)}_{ivwjk}c^{(b;\epsilon'\eta')}_{i'vwj'k'}S_{i'i}\Gamma^{(\epsilon+\eta,\epsilon'+\eta')}_{jj'kk',q}, \tag{97}$$

where analytic expressions for integrals of the spherical harmonics Y_{lm} previously defined give us:

$$\Gamma^{(s,s')}_{jj'kk',q} = \begin{bmatrix} j & 1 & j' \\ -k & q & k' \end{bmatrix} + (-)^{s'}\begin{bmatrix} j & 1 & j' \\ -k & q & -k' \end{bmatrix} + (-)^{s}\begin{bmatrix} j & 1 & j' \\ k & q & k' \end{bmatrix} + (-)^{s+s'}\begin{bmatrix} j & 1 & j' \\ k & q & -k' \end{bmatrix}. \tag{98}$$

This provides a compact and efficient method of evaluating band intensities.

4.6 The Theory Used for Clamped Ar₂ Calculations.

In the same nomenclature as previously, the clamped Ar₂ Hamiltonian is:

$$\hat{H}_{\text{fix}} = -\frac{\hbar^2}{2\mu R}\left(\frac{\partial^2}{\partial R^2}\right)R + \left(b_{\text{HX}} + \frac{\hbar^2}{2\mu R^2}\right)\hat{j}^2_{\text{HX}} + V(R,\theta,\phi;\rho_{\text{fix}},\chi_{\text{fix}}). \tag{99}$$

$V(R,\theta,\phi;\rho_{\text{fix}},\chi_{\text{fix}})$ now depends parametrically on ρ_{fix} and χ_{fix}. For cases where $\chi \neq \frac{\pi}{2}$ the symmetry of the system is lower than the full dynamics case so that only E^* is a symmetry operation. The symmetrised basis functions are, following the same treatment as before:

$$\Psi_a = \frac{1}{\sqrt{2(1+\delta_{k0})}}\psi_i(R)[Y_{jk}(\theta,\phi) + (-)^{k+\epsilon}Y_{j-k}(\theta,\phi)]. \tag{100}$$

Now the only symmetry restriction is that $k = 0$ basis functions are excluded if ϵ is odd.

In the same nomenclature as the full dynamics case the Hamiltonian matrix element is then:

$$H_{a'a} = \delta_{j'j}\left[\delta_{k'k}\left((K^R_{i'i} + S_{i'i}(b_{\text{HX}}j(j+1))) + T_{i'i}j(j+1)\right)\right] +$$

4: The Theory Used to Model the Dynamics of Ar₂HX Systems.

$$\frac{1}{(1+\delta_{k0})^{\frac{1}{2}}(1+\delta_{k'0})^{\frac{1}{2}}} \int_0^\infty dR \sum_l \sum_{m=0}^l F_{lm}(R_{\text{fix}}, \rho_{\text{fix}}, \chi_{\text{fix}})(-1)^{k'} \times$$

$$\left((-)^{\epsilon+k'} \begin{bmatrix} j' & l & j \\ k' & m & k \end{bmatrix} + (-)^{k+k'} \begin{bmatrix} j' & l & j \\ k' & m & -k \end{bmatrix} + \begin{bmatrix} j' & l & j \\ -k' & m & k \end{bmatrix} + (-)^{\epsilon+k} \begin{bmatrix} j' & l & j \\ -k' & m & -k \end{bmatrix} \right). \quad (101)$$

This formalism is used to calculate the values of R_{cut} which are required in the calculation of Υ and Φ (see chapter 3 for a description of the scheme for determining Υ and Φ basis-sets, and chapter 7 for some results). The coupling of motion in different coordinates could, in principle, also be examined through a clamped Ar_2 calculation; calculations for non-equilibrium values of ρ and χ would be performed, and the perturbations to the stretch mode and HX bending states examined.

5: The Pair Intermolecular Potentials.

In this chapter I review the forms of some well-established pair potentials which are relevant to the trimers considered in this thesis; the pair potentials for Ar_2 and ArHX have been the subject of much previous study.

Rare gas atom interactions were probably the first to be studied quantitatively and a plethora of functional forms have been suggested, many being reviewed by Aziz [58]. The interactions of RgHX complexes other than ArHCl have been less extensively studied, although the methodology developed for one member of this group may, in principle, be extended routinely to the others.

5.1 The Argon-Argon Potential.

Aziz and Chen developed the variation on the Hartree-Fock Dispersion (HFD) potential, termed HFD-C [59], which I use; the HFD approach originates from the work of Scoles and coworkers [60] [61]. The HFD-C potential satisfactorily reproduces physical properties including the second virial coefficient, viscosity, thermal conductivity, diffusion, differential cross-sections, total cross-sections and dimer spectroscopic results. In addition the HFD-C potential has a simple form which can be physically interpreted.

$$V_{\text{HFD}-\text{C}}(\rho) = V_{\text{repulsive}}(\rho) + V_{\text{attractive}}(\rho) \tag{102}$$

$$V_{\text{repulsive}}(\rho) = \epsilon^* A^* x^\gamma e^{-\alpha^* x} \tag{103}$$

$$V_{\text{attractive}}(\rho) = -\epsilon^* F(x) \sum_{j=0}^{j=2} \frac{c_{2j+6}}{x^{2j+6}} \tag{104}$$

$$F(x) = \exp\left(-\left\{\frac{D}{x} - 1\right\}^2\right) \quad x < D$$
$$F(x) = 1 \quad x \geq D \tag{105}$$

where $x = \frac{\rho}{\rho_{\text{eq}}}$ and the parameters appear in table 3, where ϵ^* is the well depth.

$V_{\text{repulsive}}(\rho)$ is a modified Born-Mayer type potential and includes the effects of exchange repulsion and SCF deformation. $V_{\text{attractive}}(\rho)$ is a dispersion energy with the sum

taken to include dipole-dipole, dipole-quadrupole and quadrupole-quadrupole terms. At intermediate and short ranges orbital overlap reduces correlation and the dispersion energy is damped; $F(x)$ fulfills this rôle.

A variant on the HFD-C potential, termed HFD-B2, has been developed more recently by Aziz and Slaman [62]. It has

$$V_{\text{repulsive}}(\rho) = \epsilon^* A^* e^{-\alpha^* z + \beta^* z^2}, \tag{106}$$

and slightly modified coefficients. The HFD-B2 potential is also improved at long range, compared to the HFD-C. Comparison of the lowest few bound states of Ar_3 shows very little effect of the improvement of HFD-B2 over HFD-C.

Table 3. Parameters of the HFD-C and HFD-B2 potentials for Ar–Ar.

	HFD-C	HFD-B2
$\epsilon^*/k_B K$	143.224	143.224
$r_{\text{m}}/\text{Å}$	3.759	3.7565
α^*	16.345655	10.77874743
β^*	–	−1.8122004
γ	2	–
A^*	9.502720×10^6	2.26210716×10^5
c_6	1.0914254	1.10785136
c_8	0.6002595	0.56072459
c_{10}	0.3700113	0.34602794
D	1.4	1.36

5.2 The Argon-HX Potential.

The Ar–HCl potential has only been accurately determined much more recently than Ar_2, since much more sophisticated experimental techniques must be applied; typically individual clusters in a molecular beam must be spectroscopically probed in the infrared. The potential has largely been developed by Hutson and Howard [63] [64] and more recently refined by Hutson giving the H6(3) [65] and H6(4,3,0) potentials [66].

5: The Pair Intermolecular Potentials.

The same methods of parameterisation have also been applied to other Rg-HX complexes [67] [68].

As with the HFD-C potential the H6(3) potential is based on physically comprehensible contributions:

$$V_{\mathrm{H6(x)}}(R,\theta) = V_{\mathrm{short}}(R,\theta) + V_{\mathrm{ind}}(R,\theta) + V_{\mathrm{disp}}(R,\theta), \tag{107}$$

with exchange repulsion and SCF deformation modelled by

$$V_{\mathrm{short}}(R,\theta) = A(\theta)e^{-\beta(\theta)R}, \tag{108}$$

induction modelled by single centre dipole plus quadrupole on the HX polarising the argon

$$V_{\mathrm{ind}}(R,\theta) = -\alpha_{\mathrm{Ar}}\mu_{\mathrm{HX}}^2[1 + P_2(\cos\theta)]R^{-6}$$
$$- 6\alpha_{\mathrm{Ar}}\mu_{\mathrm{HX}}\Theta_{\mathrm{HX}}\cos^3\theta R^{-7} \tag{109}$$

and dispersion interactions described by

$$V_{\mathrm{disp}}(R,\theta) = -\sum_{n=6}^{8} C_n(\theta)D_n(R)R^{-n}, \tag{110}$$

where

$$D_n(R) = 1 - e^{-\beta R}\sum_{m=0}^{n}\frac{(\beta R)^m}{m!} \tag{111}$$

is a Tang and Toennies damping function [69] and is implicitly a function of θ through the dependence of β on θ.

The fitted parameters in the H6(3) potential are the Legendre co-efficients of the three functions β and the angular dependence of well depth, $\epsilon(\theta)$ and radial minimum position, $R_m(\theta)$, for example:

$$\epsilon(\theta) = \sum_{\lambda} \epsilon_\lambda P_\lambda(\cos\theta). \tag{112}$$

The other unknown parameters, such as $A(\theta)$, are calculated to reproduce the given well depth and radial minimum position.

More recent work, on ArHF [70], has lead to an improvement of the precision, utility and parameterisation of the functional form. The improved potential parameterisation

is known as H6(4,3,2) for ArHF and has also been applied to ArHCl [66], when it is called H6(4,3,0); the parenthetical numbers give the maximum order, λ_k, of the Legendre expansion for increasing power, k, of η. The H6(3) and H6(4,3,λ_2) potentials are quite similar, H6(4,3,λ_2) having dependence on the HX vibrational state included by a short power series in the Legendre expansions of the angular dependence of well depth and radial minimum position and β, for example:

$$\epsilon(\theta, \eta) = \sum_{\lambda k} \epsilon_{\lambda k} P_\lambda(\cos \theta) \eta^k. \tag{113}$$

The parameter η is the mass reduced vibrational quantum number of the HX,

$$\eta = (v + \frac{1}{2})/(\mu_{\text{HX}})^{1/2}. \tag{114}$$

Electrical properties, such as HX dipole and dispersion coefficients are written as a three term power series in η.

The modified potential terms are:

$$V_{\text{short}}(R, \theta, \eta) = A(\theta, \eta) e^{-\beta(\theta, \eta) R}, \tag{115}$$

$$V_{\text{disp}}(R, \theta, \eta) = -\sum_{n=6}^{10} C_n(\theta, \eta) D_n(R) R^{-n}, \tag{116}$$

and more strikingly

$$V_{\text{ind}}(R, \theta, \eta) = -\frac{1}{2} \alpha_{\text{Ar}} |F|^2, \tag{117}$$

where F is the electric field at the Ar atom due to a 'point charge plus quadrupole' (PCQ) charge distribution on the HX. The PCQ model compactly describes the field by placing charges on both of the nuclear centres and a quadrupole on the halide; higher order multipoles are implicitly accounted for so that the PCQ model is superior to a single centre dipole plus quadrupole model.

Plots of the two-body potentials for the trimers Ar_3, Ar_2HCl and Ar_2HF are given in appendices A, B and C.

5: The Pair Intermolecular Potentials.

6: A Discussion of Relevant Three-body Effects.

The current state of knowledge on the subject of three-body forces, which are relevant to Ar_3 and Ar_2HX systems, is rather poor, and mostly consists of suggestions, rather than broadly accepted fact.

Firstly, some recent work using *ab-initio* methods is described, in order to define terms used in the comparison of *ab-initio* and model data. A division of the most important three-body effects into four physical effects is made and the mathematical forms of these components is described. The four terms described arise from:

1. dispersion effects consisting of triple-dipole and higher order terms,

2. the interaction of dipoles induced on the argon atoms by HX permanent multipoles,

3. orbital deformation due to exchange and overlap repulsion,

and

4. the interaction of HX permanent multipoles with the electrostatic field which results from the overlap effects of the two argon atoms.

The parameters introduced in the mathematical models of the three-body effects are determined on the basis of monomer physical properties wherever possible, or varied to match model to *ab-initio* values. The comparison of the model three-body potential with the *ab-initio* data for both Ar_3 and Ar_2HCl forms the content of the last two sections of this chapter.

6.1 The *ab-initio* Perspective.

Ab-initio methods can take two routes to a determination of intermolecular forces; either a supermolecule approach or a perturbative approach may be used. The supermolecule method obtains the interaction energy as a difference between the sum of monomer energies and the energy of the complex. These two numbers are substantially greater than their difference and even when the monomer energies are evaluated using numerically consistent methods (e.g. Boys and Bernardi counterpoise method [71]) there

may be errors in the large energies of the same order as the interaction energy. In addition to this serious drawback the supermolecule method does not break down the components of the interaction, a desirable feature from the point of view of understanding intermolecular interactions.

A perturbative method to deal with calculations of intermolecular forces known as Intermolecular Møller-Plesset Perturbation Theory (IMMPT) has been developed by Warszawa theoreticians [72] [73]. Further work by Chałasiński *et al.* has firmly established the value this approach [74] [75] and it has been applied to a number of systems: Ar_3 and Ar_4 [76], $(HF)_2$ [75], $ArNH_3$ [77], $(HF)_3$ and $(HCl)_3$ [78] and Ar_2HCl [79].

In brief, the IMMPT method partitions the supermolecule hamiltonian to separate out the monomer terms. Both the interaction and electron correlation terms are treated as perturbations; that is we have a double perturbation expansion:

$$\hat{H} = \hat{H}^0 + \hat{W}_{\text{intra}} + \hat{V}. \tag{118}$$

$\hat{H}^0$ is the unperturbed hamiltonian and is a sum of Fock operators for the monomers; that is a sum of energy operators at the SCF level of theory, consisting of kinetic, Coulomb and exchange terms, which act on spin-orbit functions. $\hat{W}_{\text{intra}}$ is a sum of 'fluctuation potentials' for the monomers and handles the correlation effects and $\hat{V}$ is the interaction operator of the monomers. The intermolecular interaction energy corrections, $\epsilon^{(ij)}$, may then be categorised in terms of the order of perturbation with respect to $\hat{W}_{\text{intra}}$, j, and $\hat{V}$, i. Hence $\epsilon^{(k0)}$ is a correction term corresponding to the interaction of Hartree-Fock (i.e. uncorrelated) molecules at k^{th} order in $\hat{V}$ and $\epsilon^{(kl)}$ is the correction to $\epsilon^{(k0)}$ arising from changes intramolecular correlation at l^{th} order in $\hat{W}_{\text{intra}}$.

Defining $\Delta E^{(n)}$ as being the correction due to n^{th} order of IMMPT, the interaction energy for a trimer may be decomposed as follows:

$$\Delta E^{\text{SCF}} = \Delta E^{(0)} + \Delta E^{(1)} = \Delta E^{\text{HL}} + \Delta E^{\text{SCF}-\text{def}}. \tag{119}$$

ΔE^{HL} is the Heitler-London interaction energy between undeformed SCF monomers. $\Delta E^{\text{SCF}-\text{def}}$ is due to relaxation of the molecular orbitals in the electrostatic field

6: A Discussion of Relevant Three-body Effects.

caused by the other particles, subject to the Pauli principle. We may further decompose ΔE^{HL}:

$$\Delta E^{\text{HL}} = \epsilon_{\text{el}}^{(10)} + \epsilon_{\text{exch}}^{\text{HL}} = \epsilon_{\text{el}}^{(10)} + \epsilon_{\text{exch}}^{(10)} + \Delta_{\text{F}} + \Delta_{\text{W}}. \tag{120}$$

The terms Δ_{F} and Δ_{W} are small zeroth order exchange terms by which the $\epsilon_{\text{exch}}^{(10)}$ of IMMPT differs from $\epsilon_{\text{exch}}^{\text{HL}}$; no physical meaning is attributed to them. They account for the appearance of $\Delta E^{(0)}$ in the expression for ΔE^{SCF} above. Δ_{F} is zero for a complete basis and Δ_{W} is generally negligibly small. The $\epsilon_{\text{el}}^{(10)}$ term is of electrostatic origin and is additive. Non-additivity arises from $\epsilon_{\text{exch}}^{\text{HL}}$, which is always short-range and decays as $e^{-\alpha R}$ asymptotically, and from $\Delta E^{\text{SCF}-\text{def}}$, which for complexes containing a molecule with a permanent multipole has an R^{-n} asymptotic limit due to interactions of permanent with orbital deformation induced multipoles. An $e^{-\alpha R}$ asymptotic limit for $\Delta E^{\text{SCF}-\text{def}}$ applies in systems which do not contain a permanent multipole.

$$\Delta E^{(2)} = \epsilon_{\text{el,r}}^{(12)} + \epsilon_{\text{disp}}^{(20)} + \epsilon_{\text{ind}}^{(20)} + W_{\text{def}}^{(2)} + W_{\text{exch}}^{(2)}. \tag{121}$$

The electrostatic interaction of relaxed orbitals (i.e. trimer, rather than monomer, SCF orbitals), $\epsilon_{\text{el,r}}^{(12)}$, and the dispersion energy, $\epsilon_{\text{disp}}^{(20)}$, are additive whereas the induction interaction, $\epsilon_{\text{ind}}^{(20)}$, the intermolecular correlation correction to the SCF deformation energy, $W_{\text{def}}^{(2)}$ and the correlation energy correction allowing for exchange effects, $W_{\text{exch}}^{(2)}$ are not. The $\epsilon_{\text{ind}}^{(20)}$ term contains both straight-forward induced multipole-permanent multipole energies and terms arising from overlap effects. In the cases where $\epsilon_{\text{ind}}^{(20)}$ does not form the leading term, systems containing a permanent multipole moment will have non-additivity of $\Delta E^{(2)}$ dominated at long range by the $W_{\text{def}}^{(2)}$ term. Whichever of $\epsilon_{\text{ind}}^{(20)}$ or $W_{\text{def}}^{(2)}$ dominates, a R^{-n} long range character is expected. In the absence of a permanent moment $\epsilon_{\text{ind}}^{(20)}$ does not exist and both $W^{(2)}$ components asymptotically follow an exponential decay. The exchange component always dominates at very short-range.

$$\Delta E^{(3)} = \epsilon_{\text{el,r}}^{(13)} + \epsilon_{\text{disp}}^{(21)} + \epsilon_{\text{disp}}^{(30)} + \epsilon_{\text{ind}}^{(30)} + W_{\text{def}}^{(3)} + W_{\text{exch}}^{(3)}. \tag{122}$$

6: A Discussion of Relevant Three-body Effects.

Here non-additivity arises from the $W^{(3)}$ terms and the $\epsilon^{(30)}$ terms. $\epsilon_{\text{disp}}^{(30)}$ is dominated by the triple-dipole dispersion energy at long range, so decays as R^{-9} in this limit, but includes all three-body dispersion terms. The higher multipole dispersion terms have R^{-n} behaviour with $n > 9$ and so become more important as R is decreased. All other terms behave as do the analogous terms of lower perturbation order.

6.2 Dispersion Forces.

The importance of many-body potentials has been apparent for many years; work to resolve the failure of additive potentials to account for the lattice sums for rare gas solids was the first to address many-body effects. The first functional form was developed to describe three-body dispersion effects in such systems [80], the triple-dipole (Axilrod-Teller) term:

$$V_{\text{ddd}} = \nu_{123} \frac{(3\cos\Phi_1 \cos\Phi_2 \cos\Phi_3 + 1)}{R_{12}^3 R_{13}^3 R_{23}^3}, \tag{123}$$

where Φ_i is the angle subtended by vectors from particle i to the other two and R_{ij} is the $i - j$ interparticle separation (see figure 10).
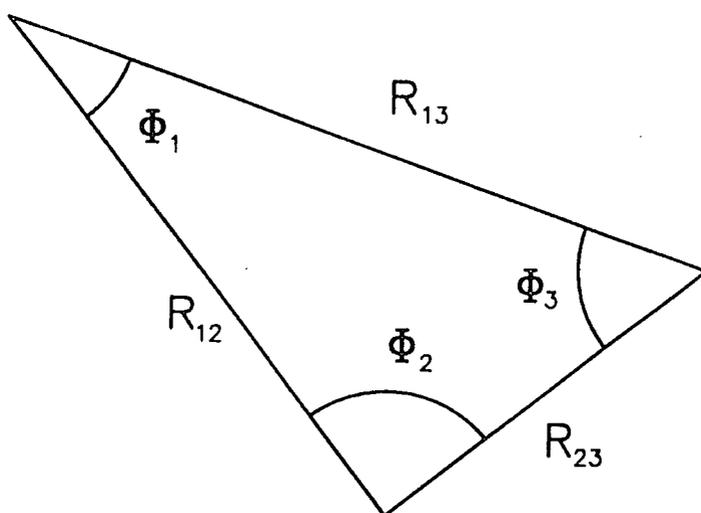
Fig. 10. Three Atom Coordinate System.

During the early 1970s much work was done on investigating the contribution of

6: A Discussion of Relevant Three-body Effects.

higher multipole-order dispersion forces [81] [82]. This work found that although the triple-dipole term was dominant the dipole-dipole-quadrupole term,

$$V_{ddq} = Z_{ddq}^{(3)} \frac{3}{16} \frac{[(9\cos\Phi_3 - 25\cos 3\Phi_3) + 6\cos(\Phi_1 - \Phi_2)(3 + 5\cos 2\Phi_3)]}{R_{12}^3 R_{13}^4 R_{23}^4}, \qquad (124)$$

accounted for about 20 % of the three-body dispersion energy for the rare gas lattices from Neon to Xenon. Higher terms than this amounted to only a few percent of the total when summed. The same conclusions are presented in the review of Meath & Koulis [83]. Note that the expression given is for a quadrupole on one of the atoms. The total energy is therefore a sum of three terms with permuted atom labels. Bell and Zucker [81] have summarised some double perturbation theory results for rare gas trimers, from which the values required for Ar_3 are $\nu_{123} = 3Z_{ddd}^{(3)} = 3.786 \times 10^5$ cm^{-1}Å^9 and $Z_{ddq}^{(3)} = 1.352 \times 10^5$ cm^{-1}Å^{11}.

More recently, using complex tensor representations of the various orders of polarisability and perturbation theory to high order, general equations for dispersion forces between any number of arbitrary molecules including hyperpolarisability effects have been derived [84] [85] [86]. The generality of these expressions hides the physics behind the interactions.

If the foundations upon which these derivations are built are used with the methods and symbolism of Buckingham [87], one can write expressions for three bodies for any order of dispersion multipole. Expressions already exist for the triple-dipole potential, V_{DDD} [88] [89], where the upper case 'D' indicates that the equation describes a molecular, rather than an atomic ('d'), system.

$$V_{DDD} = \frac{\nu_{123}}{3\bar\alpha_1 \bar\alpha_2 \bar\alpha_3} (\underline{T}_{\alpha\beta})_{ij} (\underline{T}_{\alpha\gamma})_{kl} (\underline{T}_{\gamma\beta})_{mn} (\underline{\alpha}_\alpha)_{ik} (\underline{\alpha}_\beta)_{jm} (\underline{\alpha}_\gamma)_{ln}, \qquad (125)$$

where the suffices α, β, γ denote the three bodies, $\underline{T}$ is an orientation tensor (symmetric) [87],

$$(T_{\alpha\beta})_{ij} = \frac{3(\hat{R}_{\alpha\beta})_i (\hat{R}_{\alpha\beta})_j - \delta_{ij}}{\mid R_{\alpha\beta} \mid^3}, \qquad (126)$$

where $(\hat{R}_{\alpha\beta})_i$ is the ith component of a particle to particle unit vector, $\underline{\alpha}$ is a polarisability tensor and ν_{123} is a grouping of parameters that depend only on the molecules.

6: A Discussion of Relevant Three-body Effects.

The explicit form of this expression simplifies slightly when it is made specific to the atom-atom-molecule case:

$$\underline{\alpha}_{\text{atom}} = \begin{pmatrix} \alpha_{\text{atom}} & 0 & 0 \\ 0 & \alpha_{\text{atom}} & 0 \\ 0 & 0 & \alpha_{\text{atom}} \end{pmatrix}, \tag{127}$$

$$\underline{\alpha}_{\text{axialmolecule}} = \begin{pmatrix} \alpha_\perp + \Delta_\alpha \sin^2\theta\cos^2\phi & \Delta_\alpha \sin^2\theta\sin\phi\cos\phi & \Delta_\alpha \sin\theta\cos\theta\cos\phi \\ \Delta_\alpha \sin^2\theta\sin\phi\cos\phi & \alpha_\perp + \Delta_\alpha \sin^2\theta\sin^2\phi & \Delta_\alpha \sin\theta\cos\theta\sin\phi \\ \Delta_\alpha \sin\theta\cos\theta\cos\phi & \Delta_\alpha \sin\theta\cos\theta\sin\phi & \alpha_\perp + \Delta_\alpha \cos^2\theta \end{pmatrix}, \tag{128}$$

where $\Delta_\alpha = \alpha_\| - \alpha_\perp$, and θ and ϕ are as defined for the molecular complex.

Hence the anisotropic triple-dipole energy may be evaluated by finding the tensor elements and evaluating the sums in the equation for V_{DDD}.

Literature values for polarisabilities are available. I used those summarised by Bulanin *et al.* [90], listed in table 4. The low anisotropy of the HCl polarisability suggests that to a first approximation an Axilrod-Teller term may correctly represent the triple-dipole potential for Ar_2HCl. The validity of such an expression is investigated later. The hydrogen fluoride molecule is less than a quarter as polarisable, so three-body dispersion effects in Ar_2HF will be correspondingly less significant, although more anisotropic.

Table 4. Relevant polarisabilities in $Å^3$ (Bulanin *et al.*).

α_{Ar}	1.6421
$\alpha_{\text{HCl}\perp}$	2.284
$\alpha_{\text{HCl}\|}$	2.554
$\alpha_{\text{HF}\perp}$	0.638
$\alpha_{\text{HF}\|}$	0.831

The principal features of a triple-dipole dispersion term are that it is repulsive for (equilateral) triangular geometries and attractive for linear geometries; electron correlation between particle pairs interferes for triangular geometries.

Kumar and Meath have evaluated isotropic dispersion energy coefficients for a wide range of combinations of rare gas and hydrogen halide systems [91]. They have a method which uses dipole oscillator strength distributions to obtain $\nu_{123} = 3.7015 \times 10^5 \text{cm}^{-1}\text{Å}^9$ for Ar_3, $\nu_{123} = 5.4155 \times 10^5 \text{cm}^{-1}\text{Å}^9$ for Ar_2HCl and $\nu_{123} = 2.7774 \times 10^5 \text{cm}^{-1}\text{Å}^9$ for

Ar_2HF. This is an isotropic coefficient so strictly is not the only parameter actually required for the Ar_2HX systems, but is the best estimate available. It does however represent a good starting point, which may be refined if necessary. Plots of V_{ddd} and V_{DDD} for Ar_3 and Ar_2HCl may be found in appendices A (Ar_3) and B (Ar_2HCl).

As for pairwise dispersion, exchange effects lead to a damping at short range. Tang and Toennies have investigated functional forms of two-body damping functions and conclude that a single form, $D_n(R)$, which has well-defined and physically reasonable behaviour, is of universal applicability [92].

$$D_n(R) = 1 - e^{-\beta R} \sum_{m=0}^{n} \frac{(\beta R)^m}{m!}. \tag{129}$$

The value of β here is assumed to be the same as to the exponent in the Born-Mayer term.

I propose that the form of the damping function for a three-centre problem is can be synthesised as a product of D_n functions in each inter-particle distance, although this is an extension which Tang and Toennies did not propose. For a triple-dipole potential D_3 functions are of the correct order in R, and we synthesise the triple-dipole damping function, D_{333}, where:

$$D_{lmn} = D_l(R_{12})D_m(R_{13})D_n(R_{23}). \tag{130}$$

The values of β_{ij} are taken as the exponent in the short-range terms of the two-body potentials. For the HFD-C Ar–Ar potential the exponent in the repulsive term evaluates as $\alpha^*/\rho_m = 4.348\text{Å}^{-1}$. The isotropic value of the exponent for the H6(3) potential (3.577Å^{-1} for ArHCl)) is used for β in the remaining two D_3 functions, irrespective of the whether the H6(3) or H6(4,3,0) potential is used. The importance of the damping term is investigated in calculations presented below. Analogous terms may be written by simple extension for higher order dispersion multipoles.

6.3 Electrostatic Induction Effects.

There is also a three-body energy arising from the interaction of multipoles induced on the argon atoms by the permanent multipoles on the HX. It has been found [90]that

a single-centre multipole expansion up to hexadecapole satisfactorily accounts for the dipole moment functions of the Ar–HX van der Waals complexes. The single-centre multipoles used are given in table 5. Although the more modern *ab-initio* technique of Distributed Multipole Analysis provides a more accurate description of the electrostatic field by distributing multipoles, the single centre expansion is good enough for the current application.

Table 5. HCl and HF centre-of-mass located multipoles.

| | Moment for | |
Multipole	HCl	HF
Q_1/D	1.0930	1.8022
$Q_2/D\text{Å}$	3.445	2.273
$Q_3/D\text{Å}^2$	2.446	1.699
$Q_4/D\text{Å}^3$	4.704	1.804

The potential at a point (r,θ) from the origin of a set of multipoles of a linear molecule is given by the expression:

$$V(r,\theta) = \sum_l \frac{Q_l}{r^{l+1}} P_l(\cos\theta), \qquad (131)$$

where Q_l is the magnitude of the multipole with rank l, $P_l(x)$ is a Legendre polynomial, and the coordinates are defined in figure 11.

The electric field vector, E, at (r,θ) induces a dipole vector, μ, in a particle (with polarisability tensor $\underline{\alpha}$) at that point:

$$E(r,\theta) = -\nabla V(r,\theta), \quad \mu(r,\theta) = \underline{\alpha}E(r,\theta). \qquad (132)$$

Since spherically symmetric systems have an $\underline{A}$ tensor with all elements zero there is no dipole component due to field gradient at a rare gas atom and no quadrupole induced by a uniform field. The small effects due to hyperpolarisabilities are neglected.

If the operator ∇ is applied through the chain rule, and E resolved into cartesian components, the following expressions are obtained:

$$E_x = \sum_l \frac{Q_l}{r^{l+2}} \sin\theta \cos\phi P'_{l+1}(\cos\theta), \qquad (133)$$

6: A Discussion of Relevant Three-body Effects.
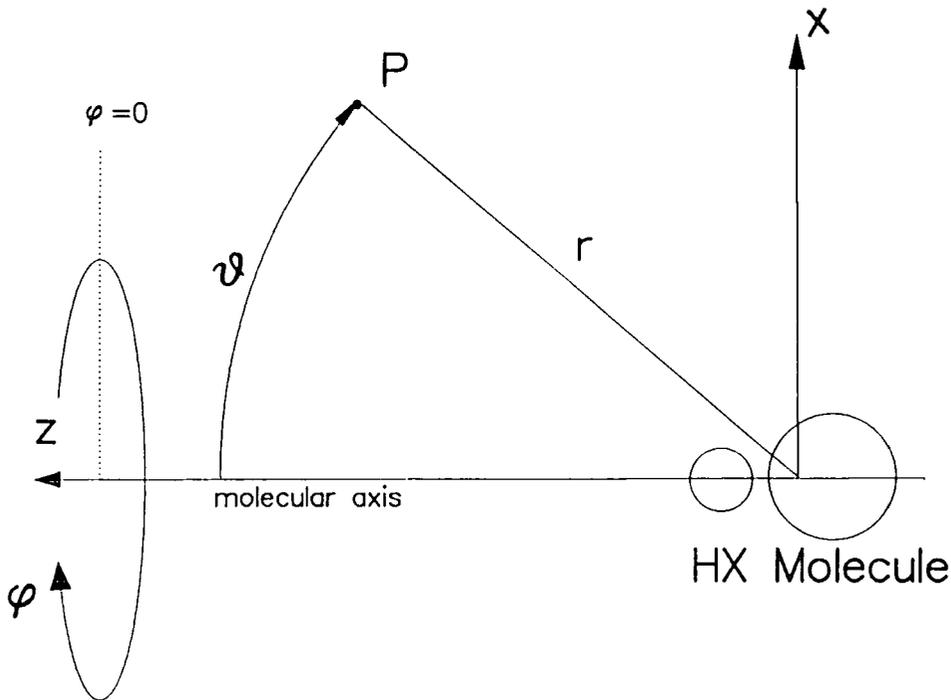
Fig. 11. Coordinates for Field Due to a Multipole.

$$E_y = \sum_l \frac{Q_l}{r^{l+2}} \sin\theta \sin\phi P'_{l+1}(\cos\theta), \tag{134}$$

$$E_z = \sum_l \frac{Q_l}{r^{l+2}} \left(P'_{l+1}(\cos\theta)\cos\theta - P'_l(\cos\theta) \right), \tag{135}$$

where [44]

$$P'_l(x) = \frac{dP_l(x)}{dx} = \frac{l}{1-x^2}(P_{l-1}(x) - xP_l(x)). \tag{136}$$

Induced dipoles have an interaction potential given by:

$$V_{dd} = -\frac{1}{\rho^3}(3(\hat{\rho}\cdot\mu_A)(\hat{\rho}\cdot\mu_B) - \mu_A\cdot\mu_B), \tag{137}$$

where A and B label induction centres (argon atoms) and $\hat{\rho}$ is the unit vector from A to B. This is the three-body component of induction energy which is due to the electrostatic field of the HX. Plots of V_{dd} for Ar_2HCl may be found in appendix B.

6.4 *Ab-initio* Calculations on Ar_2 Overlap Multipoles.

The electronic interaction of two argon atoms will result in displacement of the electron distribution from the atomic case: multipoles will be induced. For a homonuclear

pair of atoms, symmetry dictates that the lowest order multipole induced will be an axially symmetric quadrupole. There will be multipoles of higher order, however, and the electric field should properly be described by a Distributed Multipole Analysis [93].

An *ab-initio* analysis of the Ar_2 overlap multipoles was undertaken to determine both the scale and possible simple representations of the created field. A 26s/16p even tempered (no contraction) basis-set was obtained, with the Gaussian exponents, $\zeta_{i,l}$, generated according to [94]:

$$\ln \ln \beta_l = b_l \ln M + b'_l, \tag{138}$$

where M is the number of Gaussians to be used with angular quantum number l,

$$\ln \alpha_l = a_l \ln(\beta_l - 1) + a'_l, \tag{139}$$

and

$$\zeta_{i,l} = \alpha_l \beta_l^i \qquad i = 1, 2, 3....M. \tag{140}$$

Values for a_l and b_l are given by Schmidt & Ruedenberg and extended to d and f functions by Wells [95]; these generating parameters are given in table 6.

Table 6. Parameters for generating an even tempered $(2N)s/(N+3)p + N_d d + N_f f$ basis-set for argon.

$l =$	0	1	2	3
a_l	0.5262	0.9930	1.4598	1.9266
a'_l	−2.6897	−3.3397	−3.9897	−4.6396
b_l	−0.5428	−0.5086	−0.4744	−0.4402
b'_l	1.4224	1.1239	0.8254	0.5269

Using these parameters the tabulated 26s/16p even tempered basis-set was generated (table 7).

Table 7. 26s/16p even tempered basis-set for Ar.

s Functions		p Functions	
Primitive	Exponents	Primitive	Exponents
1	0.139832	27	0.084019
2	0.283692	28	0.178062
3	0.575554	29	0.377366
4	1.167685	30	0.799750
5	2.369001	31	1.694905
6	4.806234	32	3.592003
7	9.750897	33	7.612514
8	19.782639	34	16.133161
9	40.135056	35	34.190924
10	81.426077	36	72.460645
11	165.197379	37	153.565464
12	335.152755	38	325.450483
13	679.958543	39	689.725499
14	1379.501179	40	1461.731628
15	2798.734601	41	3097.840164
16	5678.078052	42	6565.236395
17	11519.695491		
18	23371.180000		
19	47415.494186		
20	96196.644284		
21	195163.933865		
22	395948.958149		
23	803301.995168		
24	1629740.607120		
25	3306420.826128		
26	6708072.825634		

With this basis-set, the CADPAC [96] program was used to perform a SCF calculation and Distributed Multipole Analysis [93]for four Ar-Ar internuclear distances. Multipole sites on the centre-of-mass, the nuclei, or all of the centre-of-mass and nulcei were used. The moments calculated for each of these schemes were calculated for an internuclear separation $\rho = 6.5a_0$, and are listed in table 8.

6: A Discussion of Relevant Three-body Effects.

Table 8. DMA description of Ar_2 for $\rho = 6.5a_0$, with three choices of multipole sites. Multipole moments are in atomic units.

Multipole Rank	C.O.M. Only	Nuclear Sites Only		Nuclear Sites and C.O.M.		
		Nucleus at $-z$	Nucleus at $+z$	Nucleus at $-z$	Nucleus at $+z$	Origin
0	0.00000000	0.00000000	0.00000000	−0.00566599	−0.00566599	0.0113319
1	0.00000000	0.01418851	−0.01418851	−0.00155434	0.00155434	0.00000000
2	−0.11890593	0.03277238	0.03277238	−0.00694488	−0.00694488	−0.0055286
3	0.00000000	0.09794836	−0.09794835	0.00663051	−0.00663051	0.00000000
4	−1.91979847	0.18474037	0.18474037	0.00674475	0.00674475	−0.0432253
5	−0.00000015	0.20219612	−0.20219612	0.00566530	−0.00566530	0.00000000
6	−37.16806442	−0.64003759	−0.64003759	0.00268010	0.00268010	−0.1500113

The single-centre multipoles only represent the field properly at long range whereas multiple sites will decrease the radius outside which the multipole series converges the field; high-order multipoles are implicitly described by lower order moments on a number of sites. In order to assess how many multipole centres, and how many moments, are required to model the field correctly for configurations of interest, a variety of multipole distributions were examined. An equilateral triangular geometry with side $\rho = 6.5a_0$ was used with argon atoms on two corners and the field evaluated at the third corner; the inner turning point of Ar_2 is close to $\rho = 6.5a_0$.

Table 9. Potential and field at the third corner of an equilateral triangle, table and energies in atomic units, described through various multipole distributions, for Ar_2.

Multipole Arrangement	Potential	Field
Up to rank 6 on Nuclear Sites and C.O.M.	2.486×10^{-4}	1.122×10^{-4}
Up to rank 6 on Nuclear Sites Only	2.484×10^{-4}	1.128×10^{-4}
Up to rank 2 on Nuclear Sites and C.O.M.	2.547×10^{-4}	1.164×10^{-4}
Up to rank 1 on Nuclear Sites and C.O.M.	3.064×10^{-4}	1.400×10^{-4}
Up to rank 2 on Nuclear Sites Only	3.056×10^{-4}	1.462×10^{-4}
Rank 1 on Nuclear Sites Only	3.358×10^{-4}	1.342×10^{-4}
Rank 2 on C.O.M. Only	3.333×10^{-4}	1.776×10^{-4}

6: A Discussion of Relevant Three-body Effects.

Table 9 gives the potential and field at the third corner, and shows that multipoles up to rank 2 on all three sites are required to get close to the converged field at this geometry; multipoles up to rank 6 on all three sites give a nearly converged field. Further reductions in the complexity of the multipole arrangement lead to rather larger errors. If a compact representation of the field is sought, the siting of dipole moments on the nuclear centres seems to offer the best trade-off between economy and precision. A single quadrupole is only 50% in error for the field and will be expected to be a better model for a small increase in ρ from the value given, which is close to the inner turning-point. Either nucleus centred dipoles or a centre-of-mass located quadrupole only require one multipole moment as a function of ρ to be known.

A model, which uses a single Gaussian effective electron in its derivation, for the quadrupole induced by overlap effects is known [97]:

$$\Theta_{\text{def}} = \frac{\rho^2}{2\left(1 - e^{\beta^2 \rho^2/2}\right)}, \qquad (141)$$

where the value of $\beta = 1.08\text{Å}^{-1}$ has been suggested for a pair of Argon atoms [98]. In view of the existence of this equation I will compare its results with *ab-initio* results using the basis-set given above with a view to using it as a simple model for the Ar_2 overlap field.

Table 10. *Ab-initio* and model values for Ar_2 (single centre) overlap quadrupole in atomic units.

ρ/a_0	*Ab-initio* $Q_{2(c)}$ with 26s/16p Basis	Θ_{def} Model with $\beta = 1.08\text{Å}^{-1}$	Θ_{def} Model with $\beta = 0.936\text{Å}^{-1}$
5.8	−0.291	−0.0695	−0.276
6.5	−0.119	−0.0595	−0.119
7.0	−0.0598	−0.0082	−0.0602
7.7	−0.0209	−0.0019	−0.0206

If the centre-of-mass quadrupole moments (table 10) calculated using CADPAC are used and a plot of $\ln(1 - \rho^2/2Q_{2(c)})$ vs. ρ^2 is made, where $Q_{2(c)}$ is the value of the single centre quadrupole, the *ab-initio* points are seen to lie close to the model and a value of

$\beta = 0.936\text{Å}^{-1}$ is obtained. This is rather smaller than the value of $\beta = 1.08\text{Å}^{-1}$, which was based on calculations of Ar-Kr collision induced dipoles: but rather larger than the value originally suggested by Jansen [97]. The ratio of quadrupole moments between these two choices of β ranges from about four to ten, for the range of ρ calculated, so it is clearly important to use the revised value of β in the current work.

The modelling of the overlap field of a pair of argon atoms will be important in three-body effects in Ar_2HX and the calculation of transition dipole moments in Ar_3.

6.5 Short Range Effects.

Three-body components also arise in short-range parts of potentials due to exchange, $\epsilon_{\text{exch}}^{\text{HL}} + \sum_{n>1} W_{\text{exch}}^{(n)}$, an overlap component of $\epsilon_{\text{ind}}^{(20)}$ and SCF orbital deformation, $\Delta E^{\text{SCF-def}} + \sum_{n>1} W_{\text{def}}^{(n)}$. In molecular systems permanent multipoles produce long range effects due to SCF deformation, however. More *ab-initio* results are required to assess the validity of proposed mathematical models for short-range three-body effects, particularly in view of the importance of the three-body SCF deformation term, which is about twice that of the exchange repulsion term for Ar_2HCl in the vicinity of the equilibrium geometry [79]. This is in contrast to atomic systems where three-body terms in $\epsilon_{\text{exch}}^{\text{HL}}$ dominate. The non-additive contribution to $\Delta E^{\text{SCF-def}}$ for an atomic system arises from cooperative or contra-operative orbital displacement and so is negative for a triangular geometry and positive for a linear geometry; the presence of a permanent multipole moment will introduce a term, of either sign, which is due to interaction of permanent multipoles with multipoles induced on a pair of other particles by SCF deformation.

For Ar_2HX, an inspection of the multipole moments of HX and a pair of argon atoms, and the multipole-quadrupole interaction equations [99] suggests that limiting consideration to the interactions of the deformation quadrupole with the permanent dipole and quadrupole moments on the HX will be adequate. A model for the quadrupole induced by overlap effects was introduced in the previous section:

$$\Theta_{\text{def}}/\text{DÅ} = 4.8032082 \frac{(\rho/\text{Å})^2}{2(1 - e^{\beta_{\Theta-\text{def}}^2 \rho^2/2})}, \tag{142}$$

where the factor 4.8032082 arises from unit conversion.

6: A Discussion of Relevant Three-body Effects.

Table 11. The overlap-induced quadrupole and interaction energy for varying argon separation for selected $\beta_{\Theta-\mathrm{def}}$ (for $\mathrm{Ar_2HCl}$, $R = 3.5\text{Å}$, $\cos\chi = 0$, $\cos\theta = 1$, $\phi = 0$).

$\rho/\text{Å}$	$\Theta_{\mathrm{def}}/\mathrm{D\text{Å}}$				$V_{\Theta-\mathrm{def}\mu}/\mathrm{cm^{-1}}$	$V_{\Theta-\mathrm{def}\Theta}/\mathrm{cm^{-1}}$
$\beta_{\Theta-\mathrm{def}}/\text{Å}^{-1} =$	0.936	0.965	1.000	1.080	(	0.965)
3.0	−0.428	−0.332	−0.243	−0.114	18.273	32.911
3.1	−0.348	−0.266	−0.191	−0.085	14.632	26.353
3.2	−0.280	−0.211	−0.148	−0.063	11.593	20.880
3.3	−0.224	−0.165	−0.113	−0.046	9.089	16.370
3.4	−0.177	−0.128	−0.086	−0.033	7.051	12.699
3.5	−0.138	−0.098	−0.064	−0.023	5.412	9.747
3.6	−0.107	−0.075	−0.048	−0.016	4.110	7.402
3.7	−0.082	−0.056	−0.035	−0.011	3.088	5.562
3.8	−0.062	−0.042	−0.025	−0.008	2.296	4.136
3.9	−0.047	−0.031	−0.018	−0.005	1.689	3.042
4.0	−0.035	−0.022	−0.013	−0.003	1.230	2.215
4.1	−0.026	−0.016	−0.009	−0.002	0.886	1.596
4.2	−0.019	−0.011	−0.006	−0.001	0.632	1.138
4.3	−0.013	−0.008	−0.004	−0.001	0.446	0.803
4.4	−0.010	−0.006	−0.003	−0.001	0.311	0.560

The interaction energy of Θ_{def} and an HX dipole, μ, is given by [87]

$$V_{\Theta-\mathrm{def}\mu} = \frac{3\Theta_{\mathrm{def}}\mu}{2R^4}[\cos\theta(3\cos^2\chi - 1) + 2\sin\theta\cos\phi\cos\chi\sin\chi] \qquad (143)$$

and for an HX quadrupole, Θ, is

$$V_{\Theta-\mathrm{def}\Theta} = \frac{3\Theta_{\mathrm{def}}\Theta}{4R^5}[1 - 5(\cos^2\chi + \cos^2\theta) + 17\cos^2\chi\cos^2\theta +$$

$$2\sin^2\chi\sin^2\theta\cos^2\phi + 16\sin\chi\sin\theta\cos\chi\cos\theta\cos\phi]. \qquad (144)$$

Plots of $V_{\Theta-\mathrm{def}\mu}$ and $V_{\Theta-\mathrm{def}\Theta}$ for $\mathrm{Ar_2HCl}$ may be found in appendix B.

Table 11 lists values of the overlap-induced quadrupole for four choices of $\beta_{\Theta-\mathrm{def}}$, as well as the interaction energy between the quadrupole and the HCl (multipole moments as quoted elsewhere). The value of the induced quadrupole is seen to be rather sensitive

6: A Discussion of Relevant Three-body Effects.

to the value of $\beta_{\Theta-\mathrm{def}}$. The quadrupole moment should be compared with a value of 3.445D$\mathring{A}$ for the HCl quadrupole.

Three-body deformation energetics which do not arise from the interaction of HX multipoles with overlap-induced multipoles are not accessible in such physically intelligible forms as the above potentials. Some *ab-initio* calculations have been performed, however [100]. Previous work on the exchange repulsion term has suggested that to a good approximation the potential is proportional to sums of the squares of terms similar to orbital overlap integrals [101] [102]. This approach does not lead to useful mathematical functions and instead I use the expressions of Jansen [97]. Jansen used a Gaussian effective-electron method and analytic perturbation Hamiltonian expressions to derive the three-body contribution to the interaction of three atoms at first and second-order perturbation including the effects of electron exchange. The second-order terms are very complicated and are not considered here.

Table 12. Integrals used in Gaussian electron calculations.

Integral	Value for Gaussian functions
Δ_{ab}^2	$\exp(-\beta^2 R_{ab}^2/2)$
Δ_{ac}^2	$\exp(-\beta^2 R_{ac}^2/2)$
Δ_{bc}^2	$\exp(-\beta^2 R_{bc}^2/2)$
Δ_{abc}^2	$\Delta_{ab}^2 + \Delta_{ac}^2 + \Delta_{bc}^2 - 2\Delta_{ab}\Delta_{ac}\Delta_{bc}$
$G_{aa(b)} = G_{bb(a)}$	$(2\beta/\sqrt{\pi})F(\beta^2 R_{ab}^2)$
$G_{ab(a)} = G_{ab(b)}$	$(2\beta/\sqrt{\pi})\Delta_{ab}F(\beta^2 R_{ab}^2/4)$
$G_{bc(a)}$	$(2\beta/\sqrt{\pi})\Delta_{bc}F(\beta^2 R_{a(bc)}^2)$
$G_{ac(b)}$	$(2\beta/\sqrt{\pi})\Delta_{ac}F(\beta^2 R_{b(ac)}^2)$
A_{abab}	$\beta(2/\pi)^{1/2}F(\beta^2 R_{ab}^2/2)$
A_{aabb}	$\beta(2/\pi)^{1/2}\Delta_{ab}^2$
A_{abac}	$\beta(2/\pi)^{1/2}\Delta_{bc}F(\beta^2 R_{a(bc)}^2/2)$
A_{abcb}	$\beta(2/\pi)^{1/2}\Delta_{ac}F(\beta^2 R_{b(ac)}^2/2)$
A_{aabc}	$\beta(2/\pi)^{1/2}\Delta_{ab}\Delta_{ac}F(\beta^2 R_{bc}^2/8)$
A_{abbc}	$\beta(2/\pi)^{1/2}\Delta_{ab}\Delta_{bc}F(\beta^2 R_{ac}^2/8)$

Labelling the atoms a, b and c, several analytic integrals arise in the Gaussian electron

6: A Discussion of Relevant Three-body Effects.

description; these are quoted in table 12, using the abbreviations:

$$F(x^2) = \frac{1}{2} \int_0^x \exp(-y^2)dy = \frac{\sqrt{(\pi)}}{2} \frac{\operatorname{erf} x}{x},$$ (145)

and $R_{b(ac)}$ is a Jacobi vector length.

If E_1 denotes the energy of the first-order Hamiltonian between the zeroth-order (anti-symmetrised Gaussian) wavefunction of an arbitrary triplet of atoms, and $E_1^{(0)}$ the same for the sum of the three isolated pairs then we are interested in the three-body energy, $E_1 - E_1^{(0)}$. The three particle perturbation Hamiltonian is expressible as a sum of pair Hamiltonians so that:

$$E_1 = E_1'(ab) + E_1'(ac) + E_1'(bc),$$ (146)

and expressions for E_1' are related to each other by permutation of indices.

$$E_1'(ab) = S_{\text{Jansen}} \left(\frac{1}{R_{ab}} - 2\frac{1 - (\Delta_{ac}^2 + \Delta_{bc}^2)/2}{1 - \Delta_{abc}^2} G_{aa(b)} \right.$$

$$+ 2\frac{\Delta_{ab} - \Delta_{ac}\Delta_{bc}}{1 - \Delta_{abc}^2} G_{ab(a)} + \frac{\Delta_{ac} - \Delta_{ab}\Delta_{bc}}{1 - \Delta_{abc}^2} G_{ac(b)}$$

$$+ \frac{\Delta_{bc} - \Delta_{ab}\Delta_{ac}}{1 - \Delta_{abc}^2} G_{bc(a)} + \frac{A_{abab} - A_{aabb}}{1 - \Delta_{abc}^2}$$

$$\left. + \frac{\Delta_{ac}(A_{abbc} - A_{abcb})}{1 - \Delta_{abc}^2} + \frac{\Delta_{bc}(A_{aabc} - A_{abac})}{1 - \Delta_{abc}^2} \right),$$ (147)

where S_{Jansen} is a factor, introduced in this work, which may be used to scale the energy to *ab-initio*, or other, data.

The first-order two-body energy of $a-b$ (i.e. the energy when c is removed to infinity) is:

$$E_1'^{(0)}(ab) = S_{\text{Jansen}} \left(\frac{1}{R_{ab}} - \frac{1}{1 - \Delta_{abc}^2}[2G_{aa(b)} - 2\Delta_{ab}G_{ab(a)} - A_{abab} + A_{aabb}] \right).$$ (148)

The energy correction due to three-body effects for three atoms is, therefore:

$$V_{\text{Jansen}} = E_1'(ab) - E_1'^{(0)}(ab) + E_1'(ac) - E_1'^{(0)}(ac) + E_1'(bc) - E_1'^{(0)}(bc).$$ (149)

A molecular system is somewhat more complicated to treat by this method. Instead of treating the electron distribution of the Ar_2HX in the Gaussian electron approximation,

6: A Discussion of Relevant Three-body Effects.

a crude adjustment is made which is applicable to the Ar_2HCl system only. Since the HCl molecule is isoelectronic with the Ar atom, the dipole-independent short-range effects are modelled assuming that the HCl electron distribution is identical to that of argon, but displaced a distance δ_{Jansen} from the HCl centre of mass, towards the H atom. The potential derived using this adjustment is denoted $\tilde{V}_{Jansen}$. The HF analogue is not so simple to deal with.

The parameters S_{Jansen}, β_{Jansen} and δ_{Jansen} for Ar_2HCl are are empirical. If the first-order energy for Ar_3 is the target then $S_{Jansen} = 1.2 \times 10^5 \text{Åcm}^{-1}$ and the value of β_{Jansen} should be close to that applicable to the induced quadrupole case. Since the Gaussian electron model is rather artificial, the value of β need not be the same in different applications; the model will be differently deficient depending upon the phenomenon which it is describes. In the Ar_2HCl case there is not the same guide for a suitable value for S_{Jansen} because of the introduction of the displacement δ_{Jansen}. In addition, β may be expected to be significantly different since it must approximate electron distributions for both Ar and HCl. The Argon trimer value is still a good point to start a fit, however. δ_{Jansen} must be determined with only physical commonsense as a guideline; δ_{Jansen} will be much less than half the HCl internuclear distance.

Although it must be stressed that the equations presented above are for a first-order perturbative hamiltonian and that the form of the second-order term is different, there is value in attempting to fit the functions to *ab-initio* sums of first and second-order energy corrections. In such cases the *a priori* estimates of the parameters become less appropriate. The view that the sum of first- and second-order *ab-initio* terms may be modelled by a first-order equation is supported, for the argon trimer in linear to triangular configurations, by the results of Jansen which show similar behaviour for first and second-order terms.

Plots of V_{Jansen} for Ar_3 and $\tilde{V}_{Jansen}$ for Ar_2HCl may be found in appendices A and B.

6: A Discussion of Relevant Three-body Effects.

6.6 Model and *ab-initio* Values for Ar₃ Three-body Potentials.

The *ab-initio* results presented in this section are from Chałasiński *el al.* [76], the breakdown of which appears in table 13.

Table 13. Breakdown of three-body *ab-initio* energies (in cm^{-1}) for various equilateral triangular configurations of side ρ. (Including the effect of neglecting BSSE [†] and including f polarisation functions [‡].)

$\rho/\text{Å}$	$\epsilon_{\text{exch}}^{\text{HL}}$	$\Delta E_{\text{def}}^{\text{SCF}}$	ΔE^{SCF}	$\Delta E^{(2)} = W^{(2)}$	$\Delta E^{(3)}$	$W^{(3)}$	$\epsilon_{\text{disp}}^{(30)}$	$\Sigma^{(3)}$	$\Sigma^{(3)} - \epsilon_{\text{disp}}^{(30)}$	$\Delta E^{(4)}$
2.646	−603.34	−30.51	−633.84	95.69	36.65	−46.97	83.62	−501.5	−585.1	−14.49
3.175	−46.73	−3.95	−50.68	15.49	12.58	−4.78	17.36	−22.61	−39.97	−3.47
3.704	−3.20	−0.31	−3.51	2.02	3.88	−0.42	4.30	2.46	−1.84	−1.08
3.704†	–	–	0.29	5.75	3.75	–	–	9.81	–	−1.93
3.704‡	–	–	−3.47	2.37	4.78	–	–	3.69	–	−1.38
4.233	−0.20	−0.02	−0.22	0.24	1.21	−0.04	1.25	1.23	−0.02	−0.35

Using the *ab-initio* data, listed above, it is possible to assess some of the model three-body potential terms.

The damped sum of the dispersion terms $\Sigma_{\text{disp}}^{(\text{model})} = V_{\text{ddd}} D_{333} + V_{\text{ddq}} D_{344}$ should be compared with $\epsilon_{\text{disp}}^{(30)}$ (see table 14). Discrepancies of both sign occur between these two quantities. If the undamped sum of the dispersion terms V_{ddd} and V_{ddq} is compared with $\epsilon_{\text{disp}}^{(30)}$, greater deviations from the *ab-initio* values are observed. Damping is thus seen to be important at the shorter ranges quoted. The discrepancy between $\Sigma_{\text{disp}}^{(\text{model})}$ and $\epsilon_{\text{disp}}^{(30)}$ is greater at short-range, where either higher order R^{-n} terms or greater damping than is modelled may account for the difference.

Table 14. Comparison of three-Body *ab-initio* and model dispersion terms.

$\rho/\text{Å}$	V_{ddd}	D_{333}	V_{ddq}	D_{344}	$\Sigma_{\text{disp}}^{(\text{model})}$	$\epsilon_{\text{disp}}^{(30)}$
2.646	81.80	0.990	9.78	0.975	90.52	83.62
3.175	15.87	0.998	1.32	0.995	17.15	17.36
3.704	3.97	1.000	0.24	0.999	4.21	4.30
4.233	1.19	1.000	0.06	1.000	1.25	1.25

6: A Discussion of Relevant Three-body Effects.

Since there are no physical parameters V_{Jansen}, the results of using three pairs of parameters, S_{Jansen} and β_{Jansen}, are shown. The parameters in V_{Jansen} were chosen to approximately model three sets of *ab-initio* data. From left to right, in table 15, the model potential is designed to describe ΔE^{SCF}, $\Delta E^{\text{SCF}} + \Delta E^{(2)}$ and $\Sigma^{(3)} - \epsilon_{\text{disp}}^{(30)}$.

Deviations of the three model potentials from the corresponding *ab-initio* term occur due to the inadequacy of the equation for V_{Jansen}, which is clearly of slightly the wrong shape. As stated earlier, the Jansen equations are only meant to model the first-order term, ΔE^{SCF}. However, we know that the second-order effects predicted by Jansen have the same behaviour as the first-order ones so we may fit the first-order equations to $\Delta E^{\text{SCF}} + \Delta E^{(2)}$ with good reason. However, caution should be taken with regard to the fit to $\Sigma^{(3)} - \epsilon_{\text{disp}}^{(30)}$ since the behaviour of the third order terms is not known; the agreement between so few data-points is not enough to support such an extension.

Table 15. Comparison of three-body *ab-initio* and model short-range (Jansen) terms.

$\rho/\text{Å}$	*ab-initio*			V_{Jansen}		
				$S/\text{Åcm}^{-1} =$ 4.3 × 10^5	7.5 × 10^5	8.0 × 10^5
	ΔE^{SCF}	$\Delta E^{\text{SCF}} + \Delta E^{(2)}$	$\Sigma^{(3)} - \epsilon_{\text{disp}}^{(30)}$	$\beta/\text{Å}^{-1} =$ 1.230	1.310	1.305
2.646	−633.84	−538.15	−585.1	−571.69	−525.77	−584.72
3.175	−50.68	−35.19	−39.97	−55.34	−36.00	−40.93
3.704	−3.51	−1.49	−1.84	−3.26	−1.43	−1.67
4.233	−0.22	0.02	−0.02	−0.12	−0.03	−0.04

Wells [95] has calculated three-body energies for Ar$_3$ at the Hartree-Fock level for an equilateral triangular geometry and some isosceles distortions. Table 16 shows the comparison of V_{Jansen} ($S/\text{Åcm}^{-1} = 4.3 \times 10^5$ and $\beta/\text{Å}^{-1} = 1.230$) with the Wells results. The equilateral geometry energy is consistent with the results of Chałasiński *el al.*, so V_{Jansen} agrees also. The change in sign of both model and *ab-initio* data occurs at about the same distortion, although the magnitude of the model effect is much greater in this region. How much this disagreement is due to model inadequacy and how much to *ab-initio* errors is not known; the effect of basis-set superposition makes small energies of low reliability, while the model for V_{Jansen} is based on rather simplistic assumptions. Without

6: A Discussion of Relevant Three-body Effects.

disregarding the discrepancies, the results of Wells support the use of V_{Jansen}.

Table 16. Comparison of three-body *ab-initio* (due to Wells) and model short range (Jansen) terms for isosceles distortions, showing the effect of function counterpoise (FC).

$R/\text{Å}$	$\rho/\text{Å}$	Hartree-Fock Interaction in cm^{-1}		
		No FC	Site-site FC	Model
3.253	3.756	−2.56	−2.66	−2.40
2.656	5.311	0.0081	−0.0419	−0.435
1.878	6.506	0.0937	0.0599	0.347
0.0	7.512	0.142	0.141	0.377

More *ab-initio* data is really required for Ar_3, for geometries other than equilateral triangular at shorter range than Wells used, to verify that the Jansen equations have the correct behaviour. Contour plots of the model three-body potential with parameters based on matching with *ab-initio* points are given in appendix A.

6.7 Model and *ab-initio* Values for Ar_2HCl Three-body Potentials.

The *ab-initio* results given are unpublished results by Chałasiński *et al.* [79]; tables 17 and 18 give a breakdown of the *ab-initio* components.

Table 18. Breakdown of three-body *ab-initio* energies (in cm^{-1}) for varied HCl orientation ($R = 3.509\text{Å}$, $\rho = 3.861\text{Å}$, $\phi = 0°$ $\cos\chi = 0$).

$\theta/°$	$\epsilon_{\text{exch}}^{\text{HL}}$	$\Delta E_{\text{def}}^{\text{SCF}}$	$\epsilon_{\text{ind}}^{(20)}$	$W^{(2)}$	ΔE^{SCF}	$\Delta E^{(2)}$	$\Delta E^{(3)}$	$\epsilon_{\text{ind}}^{(30)} + W^{(3)}$	$\epsilon_{\text{disp}}^{(30)}$	$\Sigma^{(3)}$
10	0.89	2.15	−1.96	3.72	3.04	1.76	5.57	−0.89	6.46	10.37
20	0.47	1.19	−1.60	3.20	1.66	1.60	5.05	−0.74	5.79	8.32
30	−0.13	0.18	−1.11	2.54	0.04	1.43	4.39	−0.55	4.94	5.86
40	−0.81	−0.50	−0.65	1.97	−1.32	1.32	3.75	−0.41	4.16	3.75
50	−1.54	−0.75	−0.27	1.61	−2.28	1.34	3.29	−0.32	3.61	2.35

The model potentials use the mathematical models described elsewhere is this chapter with the parameters documented in the appropriate section of text, except the vari-

Table 17. Breakdown of three-body *ab-initio* energies (in cm^{-1}) for various triangular configurations ($\phi = 0°$, $\cos\chi = 0$).

$R/\text{Å}$	$\rho/\text{Å}$	$\cos\theta$	ϵ_{exch}^{HL}	ΔE_{def}^{SCF}	$\epsilon_{ind}^{(20)}$	$W^{(2)}$	ΔE^{SCF}	$\Delta E^{(2)}$	$\Delta E^{(3)}$	$\epsilon_{ind}^{(30)} + W^{(3)}$	$\epsilon_{disp}^{(30)}$	$\Sigma^{(3)}$
3.640	3.175	1	15.18	5.84	−15.99	23.81	21.01	7.82	9.05	−3.18	12.23	37.88
3.605	3.332	1	9.27	5.04	−10.18	15.91	14.31	5.73	8.25	−2.40	10.64	28.28
3.472	3.861	1	1.04	2.52	−2.10	3.92	3.57	1.82	5.77	−0.95	6.72	11.16
3.290	4.458	1	−0.19	1.17	−0.33	0.79	0.99	0.45	3.63	−0.34	3.97	5.07
3.083	5.021	1	−0.08	0.66	−0.05	0.18	0.58	0.13	2.21	−0.13	2.34	2.92
2.795	5.664	1	0.04	0.35	0.00	0.03	0.39	0.03	1.13	−0.04	1.16	1.55
2.869	5.664	−1	0.05	0.03	0.00	0.05	0.07	0.05	0.82	0.00	0.82	0.97
3.157	5.021	−1	0.02	0.05	0.00	0.14	0.07	0.14	1.42	−0.03	1.46	1.57
3.546	3.861	−1	−0.04	0.12	−0.18	0.70	0.08	0.51	3.20	−0.19	3.39	3.79

able parameters: $\beta_{\Theta-def} = 0.965\text{Å}^{-1}$, $\beta_{Jansen} = 1.24\text{Å}^{-1}$, $S_{Jansen} = 200000\text{cm}^{-1}\text{Å}$ and $\delta_{Jansen} = 0.15\text{Å}$. The set of parameters, $\beta_{\Theta-def}$, β_{Jansen}, S_{Jansen} and δ_{Jansen} will be called "Model # 1" when the whole set is to be referred to. These parameters were chosen to match the model potential to the *ab-initio* points, the sum $\Sigma^{(model)} = \tilde{V}_{Jansen} + V_{\Theta-def\mu} + V_{\Theta-def\Theta} + V_{dd}$ correlating with the sum $\Delta E^{SCF} + \Delta E^{(2)}$. Although the $\Delta E^{(3)}$ term is seen to be of similar magnitude to the $\Delta E^{(2)}$ term this was not included in the values fitted to. This approach was used since the model used covers only effects taken into account in the sum $\Delta E^{SCF} + \Delta E^{(2)}$, with the same justifications supporting the use of $\tilde{V}_{Jansen}$ as applied to Ar_3. The value of $\beta_{\Theta-def}$ is slightly larger than that which was obtained from an analysis of the *ab-initio* multipole field for Ar_2, and appears to underestimate the induced quadrupole (see earlier table) by about 25%. It should be noted, however, that the value of 0.965Å^{-1} was obtained by fitting the effect of the overlap induced field to a model quadrupole and therefore implicitly averages the effects of higher order moments which were neglected in the model.

The model parameters were chosen by manual variation to give an approximate fit. Clearly the model is sensibly describing the features of the *ab-initio* data, but leaves noticeable gaps (see tables 20 and 21). It was quite easy to fit either the set of points

6: A Discussion of Relevant Three-body Effects.

with $\cos\theta = 1$ or the set with fixed R, but much harder to fit to the complete set; this is probably related to a deficiency in the θ dependence of $\widetilde{V}_{\text{Jansen}}$. The breakdown of the sum which was matched with the *ab-initio* data shows components with sensible magnitudes. In addition, the dispersion coefficient quoted from the literature earlier, and used for V_{ddd} and V_{DDD}, appears to be giving energies too small by a factor of about two, when compared with the *ab-initio* results (table 19). This is surprising, especially since the Ar_3 dispersion was so closely modeled, and surely cannot imply that only 50% of the three-body dispersion effect is due to the triple-dipole (this certainly was not the finding for Ar_3). Contour plots of the model three-body potential with parameters based on matching with *ab-initio* points are given in appendix B.

Table 19. Model three-body dispersion (in cm^{-1}) with $\nu_{123} = 5.4155 \times 10^5 cm^{-1} Å^9$, compared with *ab-initio*, for various triangular configurations ($\phi = 0°$, $\cos\chi = 0$).

$R/Å$	$\rho/Å$	$\cos\theta$	V_{ddd}	V_{DDD}	$\epsilon_{\text{disp}}^{(30)}$
3.640	3.175	1	5.722	6.278	12.23
3.605	3.332	1	5.008	5.494	10.64
3.472	3.861	1	3.289	3.610	6.72
3.290	4.458	1	2.095	2.310	3.97
3.083	5.021	1	1.346	1.498	2.34
2.795	5.664	1	0.736	0.843	1.16
2.869	5.664	−1	0.708	0.806	0.82
3.157	5.021	−1	1.254	1.393	1.46
3.546	3.861	−1	2.981	3.271	3.39

Table 20. Model and *ab-initio* energies (in cm^{-1}) for varied HCl orientation ($R = 3.509$Å, $\rho = 3.861$Å, $\phi = 0°$, $\cos\chi = 0$).

$\theta/°$	$\widetilde{V}_{\text{Jansen}}$	$V_{\Theta-\text{def}\mu}$	$V_{\Theta-\text{def}\Theta}$	V_{dd}	$\Sigma^{(\text{model})}$	V_{ddd}	V_{DDD}	ΔE^{SCF}	$\Delta E^{(2)}$	$\Delta E^{\text{SCF}} + \Delta E^{(2)}$	$\epsilon_{\text{di}}^{(3}$
10	−0.482	1.876	3.248	1.687	6.329	3.165	3.456	3.04	1.76	4.80	6.
20	−0.470	1.790	2.727	1.124	5.171	3.165	3.405	1.66	1.60	3.26	5.
30	−0.451	1.649	1.929	0.468	3.595	3.165	3.327	0.04	1.43	1.47	4.
40	−0.428	1.459	0.950	−0.048	1.933	3.165	3.232	−1.32	1.32	0.00	4.
50	−0.401	1.224	−0.092	−0.314	0.417	3.165	3.130	−2.28	1.34	−0.94	3.

Table 21. Model three-body potentials (in cm^{-1}), compared with *ab-initio*, for various triangular configurations ($\phi = 0°$, $\cos\chi = 0$).

$R/$Å	$\rho/$Å	$\cos\theta$	$\widetilde{V}_{\text{Jansen}}$	$V_{\Theta-\text{def}\mu}$	$V_{\Theta-\text{def}\Theta}$	V_{dd}	$\Sigma^{(\text{model})}$	ΔE^{SCF}	$\Delta E^{(2)}$	$\Delta E^{\text{SCF}} + \Delta E^{(2)}$
3.640	3.175	1	−4.872	10.514	18.209	3.847	27.697	21.01	7.82	28.83
3.605	3.332	1	−2.692	7.454	13.034	3.294	21.090	14.31	5.73	20.04
3.472	3.861	1	−0.538	1.969	3.574	1.996	7.000	3.57	1.82	5.39
3.290	4.458	1	−0.261	0.322	0.617	1.150	1.828	0.99	0.45	1.44
3.083	5.021	1	−0.155	0.044	0.090	0.672	0.651	0.58	0.13	0.71
2.795	5.664	1	−0.058	0.003	0.008	0.342	0.295	0.39	0.03	0.42
2.869	5.664	−1	−0.019	−0.003	0.007	0.020	0.004	0.07	0.05	0.12
3.157	5.021	−1	−0.033	−0.040	0.080	0.019	0.026	0.07	0.14	0.21
3.546	3.861	−1	−0.181	−1.809	3.217	0.022	1.248	0.08	0.51	0.59

6: A Discussion of Relevant Three-body Effects.

7: Calculation of Υ and Φ - Results.

In the chapters on the theory and method used for Ar_3 and Ar_2HX complexes, the use of basis functions $\Upsilon_w(\rho)$ and $\Phi_v(\cos\chi)$, eigenfunctions of an adiabatic one-dimensional potential, was described. The purpose of this chapter is to summarise the variation in Υ and Φ between the different trimers considered, to justify the method used in their determination, and to set out some operational details.

The functions $\Upsilon_w(\rho)$ and $\Phi_v(\cos\chi)$ which are used are constructed as an expansion in harmonic oscillator functions. This allows the evaluation of kinetic energy terms by analytic methods in the final calculations, while the potential function is integrated using a pointwise representation. It is found that 16 harmonic oscillator functions are required to model Υ and Φ adequately. The computational effort in the full 5-dimensional calculation is but little influenced by this size. As a consequence of the use of harmonic oscillator functions, there are three variational parameters: two for the basis-set for Υ and one for Φ. These parameters are identical to those described for the Jacobi Method I (Ar_3). In this context, however, the effect of minimising a sum of some of the lowest eigenvalues in the automatic numerical determination of the variational parameters, rather than just the ground state, is explored.

Although the variational principle strictly applies only to the ground state, it is empirically observed that all of the eigenstates which are well described by that basis lower in energy as the quality of the wavefunction is improved. To test this quantitatively, sets of calculations were performed where the variational parameters were selected on the basis of automatic (numerical) minimisation of the energy of each of the lowest four eigenvalues of Ar_2 and of sums of these energies. The difference between the lowest eigenvalue of a given index n, and those generated by the other minimisation sums is presented in figure 12.

From these results is is seen that finding the basis-set parameters by minimising the ground state energy only, while clearly the best for the ground state, gives poor results for the $n = 2$ and $n = 3$ levels. By minimising a sum of energies it is possible
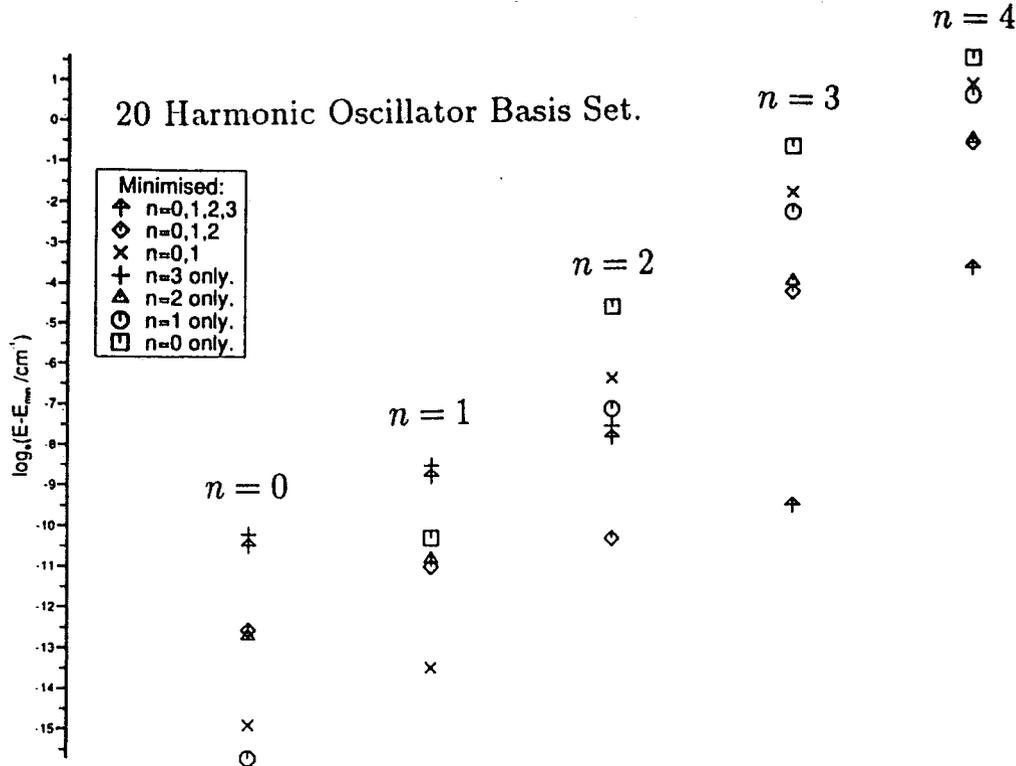
Fig. 12. Energy Level Errors for Ar_2 for Various Methods of Determining the Variational Parameters in Υ and Φ.

to bring successively higher levels down in energy without deteriorating the ground state unacceptably. On the basis of this observation, the basis-set parameters for Υ and Φ were determined by minimising the sum of the lowest four eigenvalues.

From the plots of the lowest energy Υ (figure 13), it is apparent that the presence of a third body significantly, but not greatly, affects the shape of the Ar_2 stretching wavefunction in a progressive manner: $Ar_2 < Ar_3 < Ar_2HCl < Ar_2HF$. For the Φ functions there is seen to be very little difference between the Ar_3 and Ar_2HF functions: whereas the Ar_2HCl functions are more localised. This must be due to variation in the Ar–third-body repulsion which will vary with χ as a function of the equilibrium values of R and ρ and the third body size.

It is interesting to note the variation in the energy level spacing: i.e. the anharmonicity of the potential cuts. The spacings are depicted graphically (figures 14 and 15) and essentially show that all of the systems considered behave similarly. The trimeric systems show a weaker anharmonicity in the stretching potential than Ar_2 itself, primarily due to a deepening of the potential well by the presence of the third body such that the dissociative tail is much higher than the energy of the fifth calculated level. The discontinuity in the Ar_2 curve arises from a poor description of a near-dissociative eigenstate by the

7: Calculation of Υ and Φ - Results.
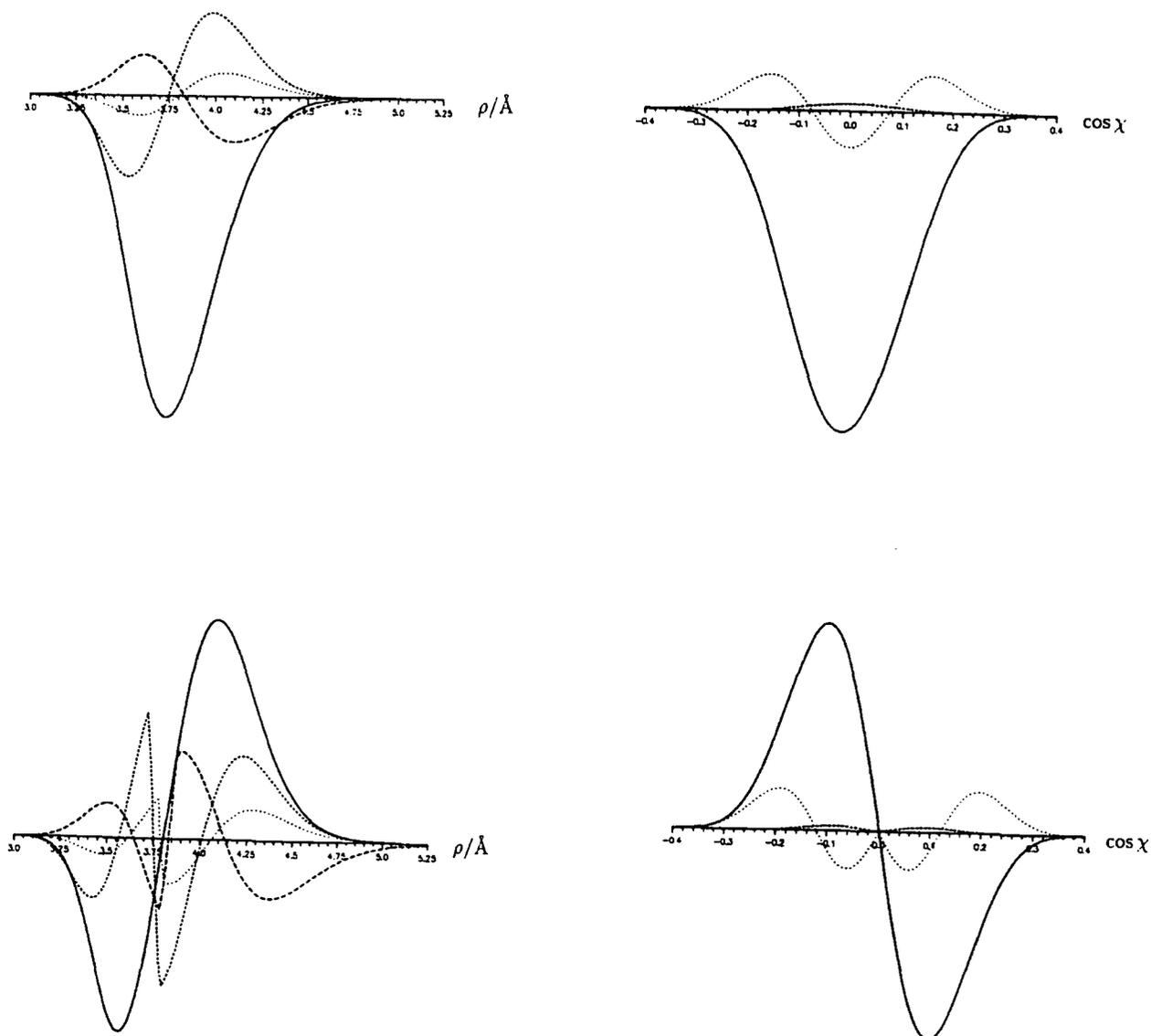
Fig. 13. Comparison of $\Upsilon_0(\rho)$, $\Upsilon_1(\rho)$, $\Phi_0(\cos\chi)$ and $\Phi_1(\cos\chi)$. The plots are for Ar$_3$ (——) and the deviations, $|$Ar$_3| - |$other$|$, from this for Ar$_2$HCl ($\cdots$), Ar$_2$HCl (– –) and Ar$_2$ (— —).

basis-set used. In contrast to the stretching potential, where the real potential gets wider than an harmonic approximation for increasing energy, the Ar$_2$ bending potential is seen to get narrower. This is probably over-emphasised in these calculations since R is frozen and cannot, therefore, increase as bending occurs. Some degree of coupling along these lines is expected in the real systems.

74
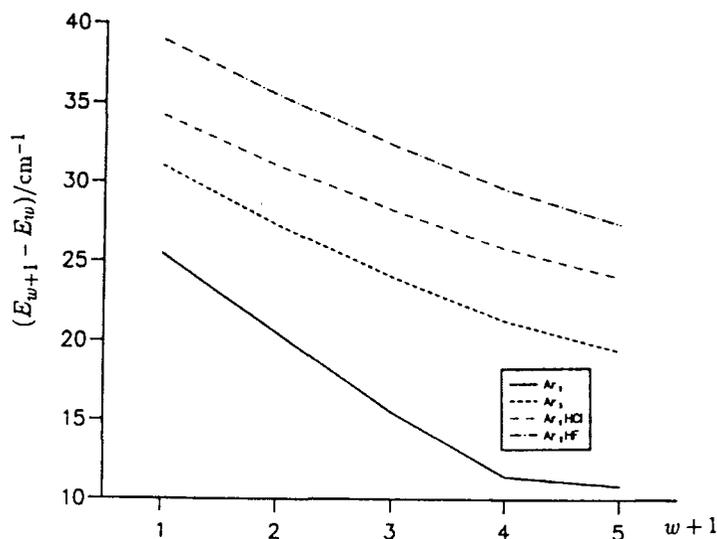
Fig. 14. Anharmonicity of the Functions Υ_w.
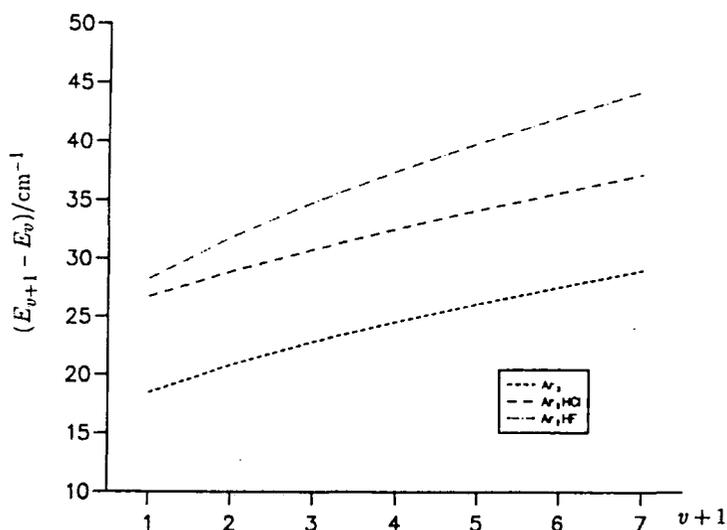
Fig. 15. Anharmonicity of the Functions Φ_v.

It is necessary to justify the recipe for determining the value of R_{cut}. A graphical representation of the frequencies of a fully dynamical calculation (figures 16 and 17) shows that the recipe for determining the value of R_{cut}, discussed in chapter 3, is close to optimal. Table 22 lists expectation values of ρ and R for all the systems considered;

7: Calculation of Υ and Φ - Results.

these are the relevant points on the graphs at which to assess the recipe. To perform calculations for atom-atom-diatom trimers similar to those presented for Ar_3 would be rather expensive and I am content to extend the results to the more complex Φ systems.

Table 22. Expectation values of R and ρ in Å from one-dimensional calculations.

potential:	Leitner	HFD-C	HFD-B2	HFD-C/H6(4,3,0)	HFD-C/H6(4,3,0)	HFD-C/H6(4,3,2)
		Ar_3		Ar_2HCl	Ar_2DCl	Ar_2HF
$\langle R\rangle_0/$Å	3.38	3.30	3.30	3.50	3.50	2.97
$\langle R\rangle_1/$Å	3.49	3.40	3.39	3.55	3.58	3.08
$\langle R\rangle_2/$Å	3.61	3.51	3.50	3.64	–	3.20
$\langle \rho\rangle_0/$Å	3.86	3.78	3.78	3.76	3.75	3.69
$\langle \rho\rangle_1/$Å	4.00	3.92	3.91	3.87	3.86	3.79
$\langle \rho\rangle_2/$Å	4.17	4.06	4.06	3.99	3.98	3.90
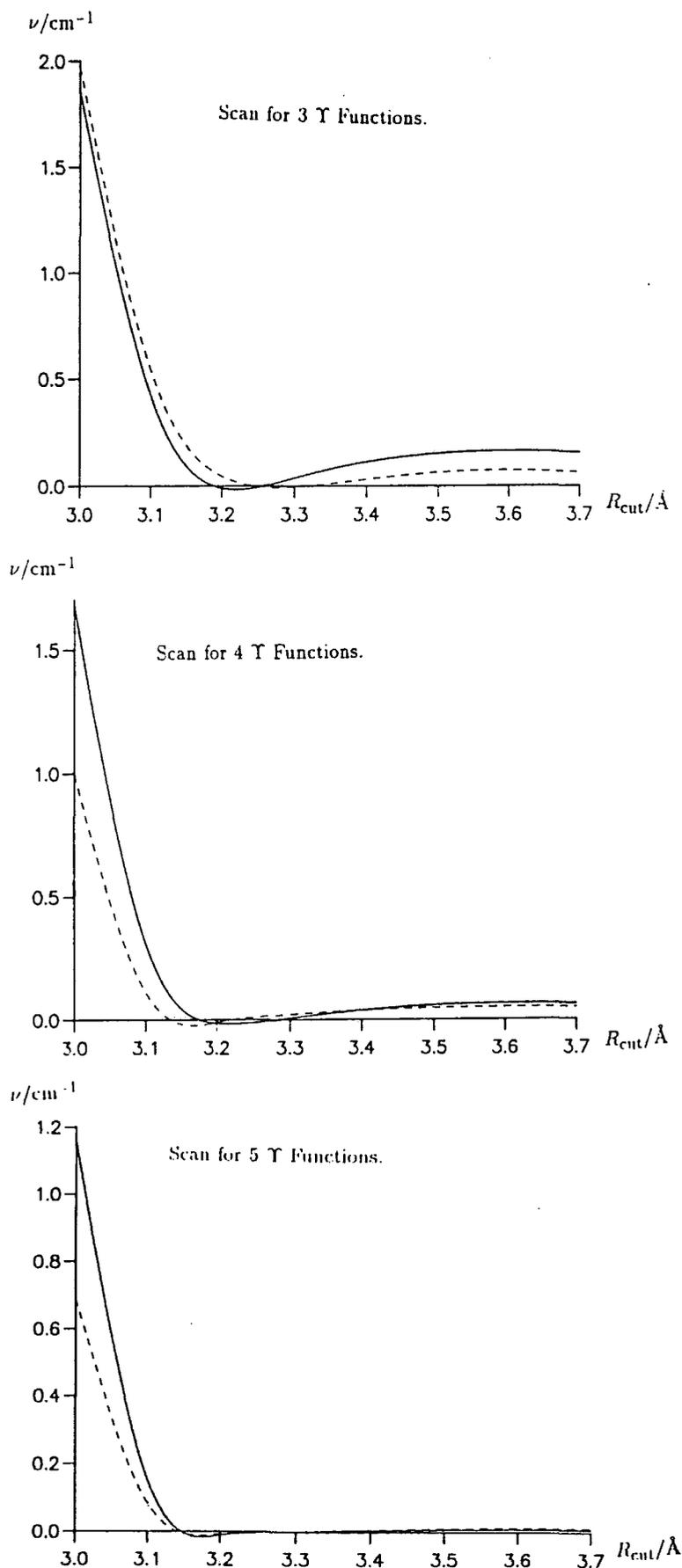
Fig. 16. Relative frequencies, $\nu_{1\leftarrow0}$(——) and $\nu_{3\leftarrow0}$(– –), of a Fully Dynamical Ar$_3$ Calculation for Varying Υ Basis Set Size with Respect to the Value of R_{cut}.

7: Calculation of Υ and Φ - Results.
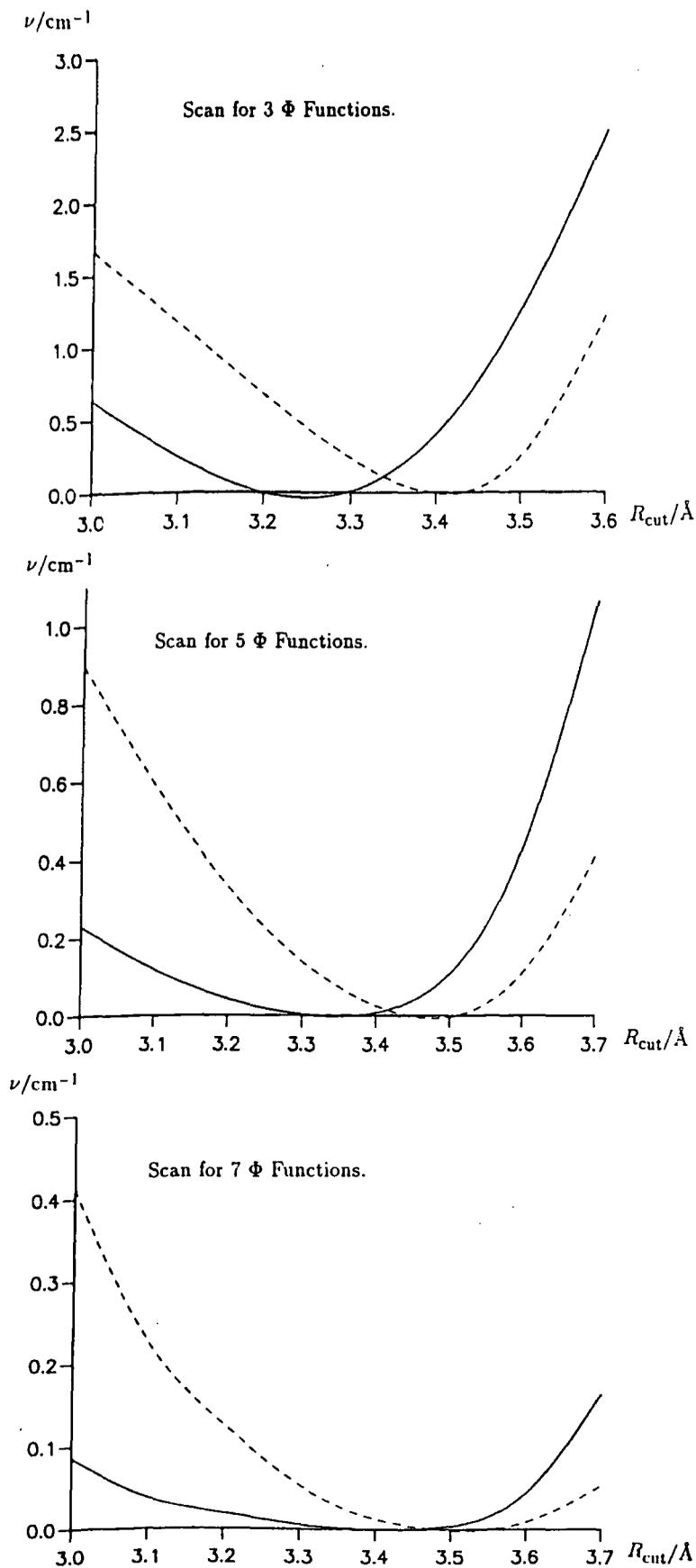
Fig. 17. Relative frequencies, $\nu_{1\leftarrow0}$(——) and $\nu_{3\leftarrow0}$(— —), of a Fully Dynamical Ar$_3$ Calculation for Varying Φ Basis Set Size with Respect to the Value of R_{cut}.

8: Triatom Calculations – Ar$_3$.

The Ar$_3$ system is a suitable prototype trimer as it is one step below Ar$_2$HX on the conceptual and computational ladder.

The first half of this chapter applies three different methods of calculating triatomic eigenstates, which were detailed in chapter 3, to Ar$_3$. Two of these methods use a Jacobi coordinate system and so treat the system in less than its full symmetry, which is D_{3h} since it has an equilateral triangle equilibrium geometry, which is used in a normal mode treatment. The results of these three methods are compared among themselves and to calculations using hyperspherical coordinates [48].

The second half of the chapter describes calculations on a variety of two- and three-body potentials; there are other calculations using different methods, in hyperspherical coordinates, which use a variety of two-body potentials [50][49][48]. Estimates of transition dipole moments for Ar$_3$ are also made. Finally, the symmetries of overtone states are briefly derived.

The HFD-C Ar-Ar potential, described in chapter 5, is used unless stated otherwise. From plots of the trimer potential, which may be found in appendix A, it is apparent that there is only quite a low barrier to either of two inversion modes. One involves the passage of an atom through the centre of the other pair and the other the rotation of a pair of atoms through 180°. The profiles of these two modes are illustrated (figure 18) with the conjugate coordinates adjusted to the minimum on the plane defined by the given coordinate; i.e. these are plots along the inversion path.

These inversion plots allow information on the absolute classical limits on any coordinate for an eigenvalue of given energy, and with conventional contour plots are useful for determining whether the molecule is stiff or floppy in a particular coordinate, and for estimating limits of the DGB in R in two of the methods. The inversion energy of $\approx -201 \text{cm}^{-1}$ flags an energy region where care needs to be taken since inversion cannot be properly described using Jacobi or normal coordinates. It is not true that this is a rigorous limit. Vibrational modes with excitation along the inversion coordinate will have

Centre of Mass Co—ordinate Inversion   Chi Inversion Path
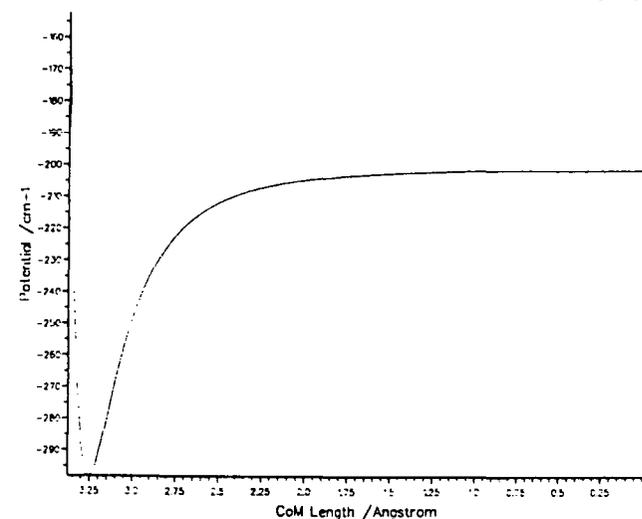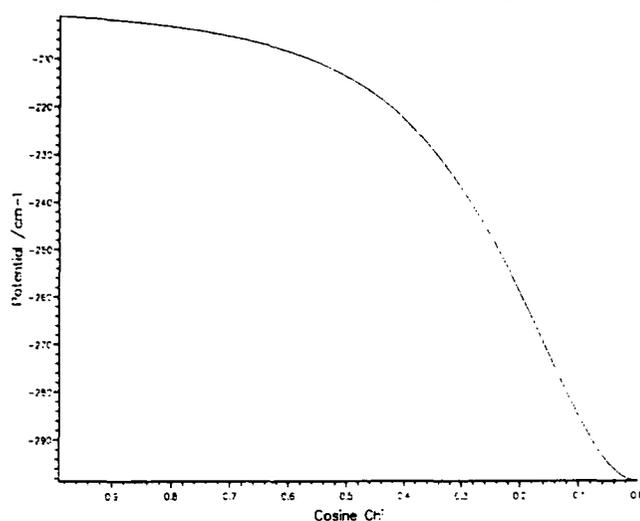
Fig. 18. Potential Plots for Ar_3 Inversion Modes.

tails extending out to the saddle point for energies below this due to tunneling; whereas a highly excited breathing mode, for example, may have an energy greatly above −201 cm^{-1} and is model-limited only by the dissociation limit.

8.1 Convergence – Normal Coordinate Method

Using the method described in chapter 3, the scale factors for masses expressed in atomic mass units for the three normal modes were found to be:

$$\gamma_1 = 1.203\text{Å}^{-\frac{1}{2}}, \quad \gamma_2 = \gamma_3 = 0.850\text{Å}^{-\frac{1}{2}}. \tag{150}$$

Finding these parameters by solving a one dimensional problem with only one function is believed to lead to these parameters being near to optimal, and is in keeping with the general ethos of the method. The calculations themselves are now very straightforward, the only parameters being the size of the H.O. basis in each mode. Since there is no justification for having different numbers of functions from each mode, they are always equally sized.

It is quite apparent, from table 23, that the eigenvalues are converging slowly, but are providing reasonable approximate values for the basis sizes used. A product basis-set with 9 functions in each normal mode is used.

8: Triatom Calculations – Ar_3.

Table 23. Convergence of Normal Mode calculations for energy levels $n = 0$ to $n = 15$.

n	3	4	5	6	7	8
			Basis Size in Each Mode			
0	−254.11528	−254.48177	−254.63728	−254.67461	−254.69132	−254.69743
1	−229.27296	−231.37773	−231.72231	−232.08737	−232.14840	−232.21158
2	−229.01888	−230.95004	−231.70860	−231.98155	−232.12822	−232.18573
3	−217.90869	−220.22680	−222.30179	−223.21426	−223.73604	−223.94258
4	−203.79093	−208.25331	−209.42315	−210.59803	−211.10382	−211.41895
5	−203.18782	−204.80113	−209.07085	−209.80673	−210.83860	−211.21481
6	−202.63980	−204.62073	−207.99799	−209.33263	−210.25037	−210.81540
7	−188.49978	−196.83492	−199.48259	−202.31336	−203.17596	−204.12367
8	−188.30676	−196.40403	−199.38294	−201.92188	−203.15663	−203.87677
9	−177.24309	−182.59306	−186.80149	−189.43085	−192.87313	−194.15248
10	−176.94646	−179.99536	−186.37184	−188.68541	−189.80730	−191.68804
11	−162.86673	−179.39439	−185.63645	−187.53352	−189.53077	−190.38825
12	−155.51764	−179.37544	−180.47569	−187.11960	−187.92662	−189.62861
13	−155.32564	−176.53614	−180.26306	−184.57296	−186.79901	−188.54958
14	−151.77950	−171.77645	−175.89716	−181.13377	−182.87546	−184.69395
15	−148.12973	−165.64011	−174.92801	−177.60571	−181.98838	−183.25858

8.2 Convergence – Jacobi Coordinate Method I.

In some ways the the two-stage nature of the Jacobi method makes the determination of convergence somewhat easier, since with the lower-dimension basis-set of the first stage calculation it is possible to perform calculations for basis-set sizes quite a bit larger than those that will actually be used in the final calculation, where the matrix size is a limiting factor. In this way, the distance from convergence for the basis-size which is actually used may be quite accurately determined, bearing in mind that the inclusion of an extra degree of freedom will slightly modify the optimal basis. The determination of the H.O. scale factors is, however, found to be quite a difficult process for basis-sets with many functions, both because of the dimension of the matrix to be solved and as a result of the rather gentle relief on the ground state energy surface (of the two dimensional calculation) as a

8: Triatom Calculations – Ar$_3$.

function of these parameters. The minimisation was performed both with ρ_0 fixed at the values given by the minimum of the potential surface, and with this parameter a variable of the minimisation.

Table 24. Log_{10} eigenvalue differences in cm^{-1}, relative to $N_\rho, N_\chi = 14$ for the 2D calculation.

N_ρ	N_χ	$\Delta E(0)$	$\Delta E(1)$	$\Delta E(2)$	$\Delta E(3)$	$\Delta E(4)$
3	5	−0.924307	−0.676913	0.321358	0.673623	0.647986
3	6	−0.924307	−0.792797	0.321377	0.673623	0.643590
3	7	−0.924563	−0.788026	0.321076	0.662165	0.643575
3	8	−0.924563	−0.794741	0.321068	0.662165	0.643276
3	9	−0.924563	−0.794741	0.321062	0.661570	0.643272
5	3	−2.319664	−0.002684	−0.125994	0.534446	0.539950
6	3	−2.488117	−0.061455	−0.200908	0.494096	0.453401
7	3	−2.593460	−0.131891	−0.202435	0.469054	0.384154
8	3	−2.856985	−0.380031	−0.205421	−0.076652	0.230221
9	3	−2.879426	−0.397994	−0.205840	−0.180469	0.222251
10	3	−2.889410	−0.408057	−0.205637	−0.265344	0.217781
12	3	−2.903090	−0.430228	−0.205331	−0.907701	0.206300
13	3	−2.903090	−0.432139	−0.205449	−1.133063	0.205161
8	5	−3.657577	−1.296881	−1.316413	−0.094166	−0.762708
5	6	−2.390406	−1.776764	−0.130364	0.299734	0.528687
8	6	−3.657577	−2.809668	−1.316323	−0.094139	−0.880843
9	6	−3.795880	−2.903090	−1.503901	−0.203211	−1.028539
10	6	−3.795880	−3.008774	−2.081445	−0.448611	−1.424235
11	6	−4.045757	−3.086186	−2.551294	−1.076186	−1.948076
13	6	−4.096910	−3.107905	−2.987163	−1.626169	−2.337242
6	6	−2.677781	−2.008774	−0.300726	0.220981	0.447577
10	10	−4.096910	−3.677781	−2.107349	−0.448648	−1.450506

Although the computational expense greatly increases each time a variable is added, the difference in the eigenvalues obtained was significant enough to justify it. The effect of optimising ρ_0 is, as would be expected, much greater for less complete basis sets, just as

8: Triatom Calculations – Ar₃.

the selection of the scale factors is more critical in these cases. Since we pursue a minimal basis-set, it is necessary to use an incomplete basis and hence to use an optimised ρ_0.

The convergence is seen to be incomplete (table 24), but is nevertheless better than if a DGB of the same size is used; the inherent flexibility of the DGB would not be exploited here, since potential cuts in ρ have minima which are only weakly dependent on the other coordinates. Considering that the inversion barrier is about -201 cm^{-1} and that the Ar–Ar zero point energy is about 15 cm^{-1}, it is estimated that an eigenvalue from the two coordinate calculation may not support a good vibrational manifold in R if it is above about -216 cm^{-1}. It is found that $E(3) \approx -216.6$ cm^{-1} and $E(4) \approx -216.1$ cm^{-1}: therefore it seems of low priority to attempt to use a basis set which converges these eigenvalues since they are estimated to lead to final eigenvalues very close to the inversion energy. The degree to which inversion behaviour is a problem depends upon the vibrational mode, however.

The rather extensive set of results presented above for the two-coordinate calculation demonstrates that the convergence with respect to the size of basis in each coordinate is not strongly dependent on the basis-set size for the other. From this table I select 10 H.O. functions in ρ and 6 in $\cos\chi$ to provide an acceptable level of accuracy without producing an excessive basis size.

So far all the results presented have not restricted the number of quanta in the harmonic oscillators to less than the sum of the highest function quantum numbers. If the quantum-number sum is restricted, the product functions composed of highly excited motions in both coordinates can be removed; this allows a more size-efficient basis-set to be used.

On the basis of the results listed in table 15, it is apparent that the error introduced by restricting the number of quanta in the H.O. product basis is rather small, and restricting it to 9 is not inappropriate if one is prepared to accept the $N_\rho = 10, N_\chi = 6$ basis. The changes in the three parameters are small, also indicating the slight decrease in quality of the basis.

8: Triatom Calculations – Ar_3.

Table 25. The effect of limiting the product basis-set for $N_\rho = 10, N_\chi = 6$.

No. of Quanta	Eigenvalues in cm^{-1}					$\gamma_\rho/\text{Å}^{-\frac{1}{2}}$ $\gamma_\chi/\text{Å}^{-\frac{1}{2}}$ $\rho_0/\text{Å}$		
	$E(0)$	$E(1)$	$E(2)$	$E(3)$	$E(4)$			
9	−269.25415	−241.68779	−241.32240	−216.63907	−216.06953	18.7117	125.1376	3.8588
10	−269.25415	−241.68827	−241.32261	−216.64256	−216.08594	18.71097	125.1486	3.8588
11	−269.25416	−241.68829	−241.32264	−216.64432	−216.08800	18.71135	125.1359	3.8587
12	−269.25416	−241.68830	−241.32266	−216.64474	−216.08931	18.71448	125.1456	3.8587
13	−269.25416	−241.68830	−241.32266	−216.64498	−216.08933	18.66843	125.1333	3.8590
14	−269.25416	−241.68830	−241.32266	−216.64481	−216.08932	18.61280	125.1469	3.8603

Having established a basis-set and parameters for the ρ and χ motions, the full calculations may be carried out. As well as the size of the DGB, it is necessary to select a range for the distribution. The problem encountered with this is that the quality of a solution is dependent on the spacing of the Gaussians, so that the size and range are intimately linked in their effect on the eigenvalues. Additionally it is not justifiable to choose the parameters by minimising the ground state energy alone, so the convergence of a number of eigenvalues must be examined. Inspection of the classical turning points for various energies suggests that runs should be carried out for a DGB evenly spread from a minimum of from 1.6Å to 2.0Å to a maximum of between 4.8Å and 5.5Å. These trials suggested a range of $(1.9\text{Å}, 5.0\text{Å})$ is appropriate.

Given this choice of range, a systematic analysis of the change in eigenvalues with DGB size was carried out, and is illustrated in figure 19.

Although there are a few eigenstates which have quite erratic eigenvalues, it is apparent that the majority converge in an orderly fashion. Despite being unable to continue the trials for the chosen size of H.O. basis due to memory limits, it is felt that the graphs demonstrate that calculations with 25 Gaussians will provide results of adequate accuracy for the majority of eigenstates with energies below the barrier to inversion.

On the basis of previous calculations, the Gaussian parameter c was initially chosen to be 0.7. Some trial variation of this parameter about this value indicated that it seemed to be appropriate.
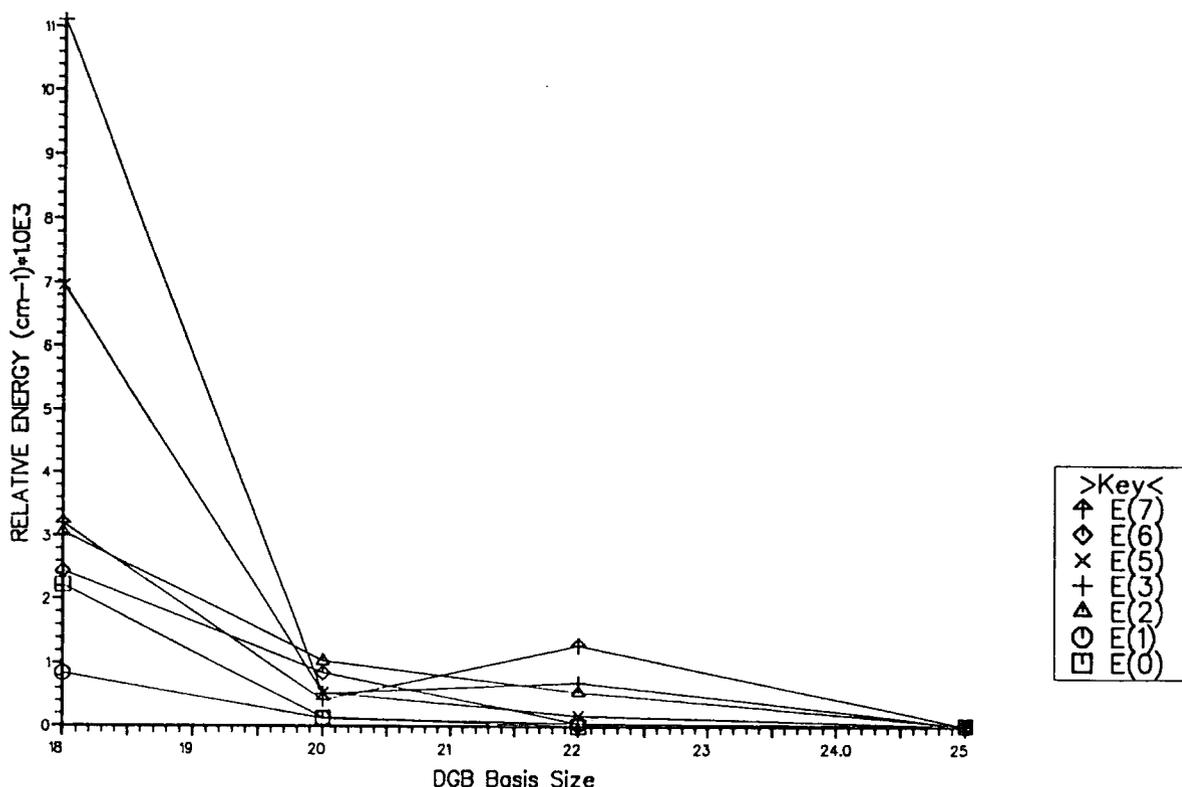
Fig. 19. DGB Size Convergence for Jacobi I Method.

8.3 Convergence – Jacobi Coordinate Method II.

If a basis-set is to be made as small as possible, it is important to ensure that the basis functions are not optimised for one vibrational state yet poor for other states of interest. This ethos is followed in the Jacobi Method II; the DGB is good in this respect and Υ and Φ are designed to be good also. The basis functions in ρ and $\cos\chi$ generated in this method are compromise functions; they are designed on a potential cut which is not biased to the ground state. Thus the error in description of excited states is reduced at the expense of the error in the ground state. The effect of including symmetry, albeit only in a subgroup of the full molecular symmetry group, added to the optimisation of Υ and Φ leads to a much smaller basis, than the other methods, for acceptable results. Details of the calculation of the ρ and $\cos\chi$ one-dimensional functions are given in a devoted chapter.

This is a one-step calculation, given Φ and Υ functions, for which convergence results are expressed graphically in figures 20-22. Trial calculations similar to those described in the previous section were used to determine a DGB range.

8: Triatom Calculations – Ar$_3$.

On the basis of the convergence calculations the basis-set used was:

$$\Psi(\eta) = \sum_{v=0}^{7} \sum_{w=0}^{3} \sum_{i=1}^{12} c_a \Psi_a, \tag{151}$$

with a DGB range of 2.60Å to 4.20Å and $c = 0.7$. q_{max} was $\cancel{5}^{6}$ for $\eta = 0$ (A') calculations and $\cancel{8}^{7}$ for $\eta = 1$ (A'') calculations. This basis-set gives 144 functions for both symmetry type calculations.
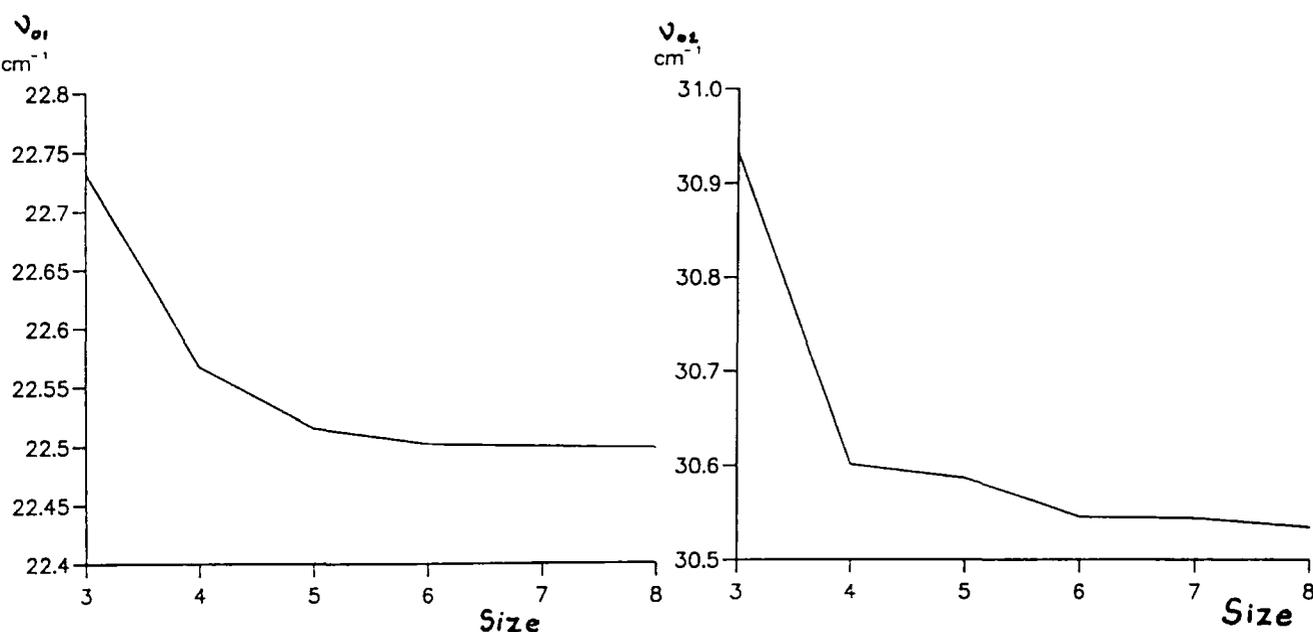
Fig. 20. Convergence of Frequencies with Respect to $\cos \chi$ Basis Set Size for Jacobi II.

$\cos \chi$ basis-set convergence was carried out for 4 functions in ρ by varying q_{max}.

ρ basis-set convergence was carried out for 7 functions in $\cos \chi$ with $q_{max} = 6$.

It is quite apparent that in addition to a much smaller basis-set in ρ and $\cos \chi$ the DGB basis is also much smaller, compared to Jacobi I. Some of the reduction in DGB size is attributable to a smaller range of distribution. This may be attributed in part to a different criterion for assessing convergence and in part to basis functions with different spread in the other two coordinates. In particular the improved shape of the $\Upsilon_w(\rho)$ of the Jacobi method II relative to the harmonic oscillator functions of Method I will have reduced the DGB range required; it is clear from the potential energy surface that R and
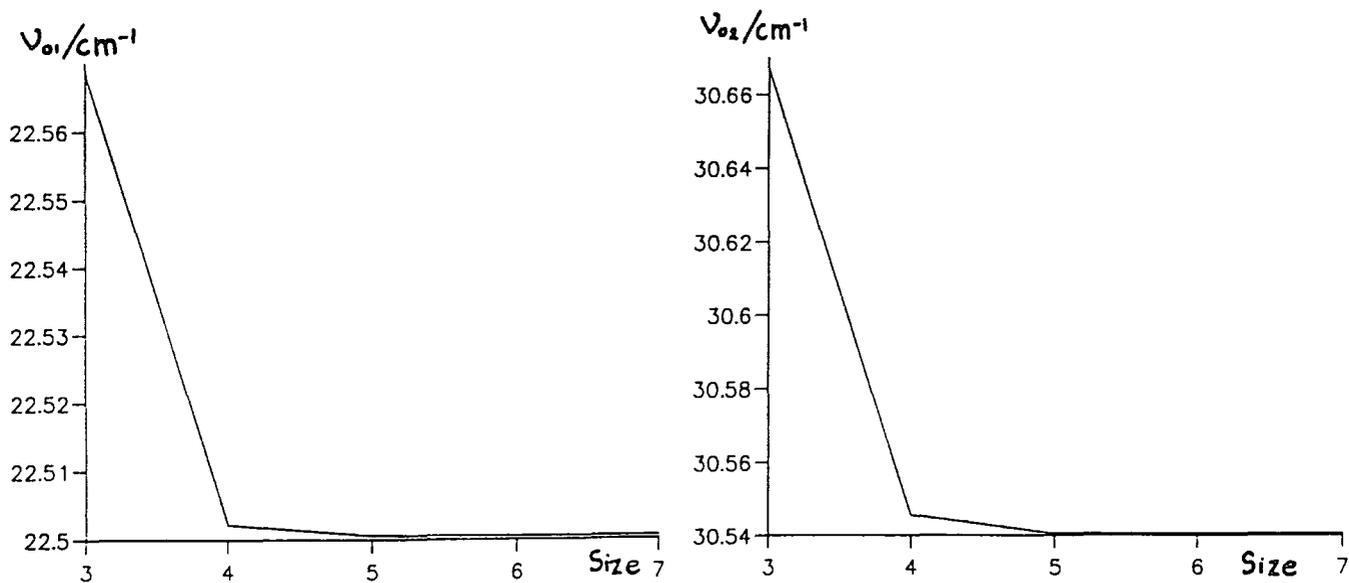
Fig. 21. Convergence of Frequencies with Respect to ρ Basis Set Size for Jacobi II.

Fig. 22. Convergence of Frequencies with Respect to DGB Size for Jacobi II.

ρ motions will couple. Whether this change has caused deterioration of the results is an important question, which is answerable from the results.

8: Triatom Calculations – Ar$_3$.

8.4 Comparison of the Results from the Different Methods.

The bases as described in the preceding sections give matrix problems of dimension 729 for normal mode, 1125 for Jacobi I and 144 for Jacobi II, although the normal mode basis could have been reduced by up to almost 50% by imposing a maximum quantum sum without much loss of accuracy. Clearly if results from Jacobi II are at least as good as the other methods it is much more efficient, particularly bearing in mind that solving matrix problems for all eigenvalues scales as N^3 in time, and for a single eigenvalue roughly as N^2. The results from the different methods are given in tables 26 and 27, where hyperspherical calculations, by the authors of [48]are denoted "HHCC".

Table 26. Comparison of results of A_1 symmetry (A' in S_2) for different methods for Ar$_3$ (HFD-C potential).

	Jacobi I	Jacobi II	Normal mode	HHCC
n	E/cm^{-1}	E/cm^{-1}	E/cm^{-1}	E/cm^{-1}
0	−254.735	−254.736	−254.700	−254.733
2	−224.114	−224.187	−224.075	−224.215
4	−211.364	−211.518	−211.625	−211.846
6	−195.842	−196.350	−195.721	−198.282
7	−191.277	−191.667	−191.941	−193.523

Table 27. Comparison of results of E symmetry ($A' \oplus A''$ in S_2) for different methods for Ar$_3$ (HFD-C potential).

	Jacobi I	Jacobi II		Normal mode		HHCC
		A' in S_2	A'' in S_2	lower	upper	
n	E/cm^{-1}	E/cm^{-1}	E/cm^{-1}	E/cm^{-1}	E/cm^{-1}	E/cm^{-1}
1	−232.223	−232.216	−232.234	−232.235	−232.224	−232.216	−232.231
3	−211.318	−210.637	−211.385	−211.573	−211.494	−211.192	−211.741
5	−204.466	−204.461	−204.566	−205.096	−204.378	−204.327	−204.948

On the whole, the Jacobi method I seems to produce only approximate eigenvalues, compared to the hyperspherical method, which should be more accurate. The deficiencies

of the former are illustrated by the failure of the E symmetry degenerate pairs of states to be degenerate, whereas this degeneracy is embodied in the hyperspherical model. There does indeed seem to have been little advantage in using the Jacobi I method over the normal mode method when a range of eigenvalues are compared. This seems to suggest that at least some of its problems stem from the inappropriate use of H.O.'s, particularly in the ρ coordinate.

In contrast the Jacobi II method is seen to perform rather well, certainly given the small basis-set used. There is still a lack of degeneracy for E symmetry pairs since these now arise from two different calculations of differing symmetry in S_2 (see chapter 3 for a discussion of symmetrisation). There is no doubt that the Jacobi Method II provides a means of modelling the lower states efficiently enough for application to the five-dimensional problems Ar_2HX, for which Ar_3 is a good part-model.

8.5 Jacobi Method II – Further Calculations, Results and Discussion.

It is instructive to examine the forms of the wavefunctions: illustrations of the square of these appear in appendix D. The form of the dynamics is simply seen when individual modes are excited singly or multiply, but becomes hard to see when combination excitation is present. Single quantum excitations display the forms of triatomic normal modes: an antisymmetric stretching mode ($n = 1a$), rocking mode ($n = 1b$) and symmetric stretch ($n = 2$). Due to the reduced symmetry used in the calculation states $n = 3b$ and $n = 4$ arose from one calculation. The closeness of these eigenvalues has probably caused considerable mixing, evidenced by the stretching character introduced into the $n = 4$ level. Of particular interest is $n = 5a$, where there appears to be in phase motion of ρ and $\cos \chi$, $n = 5b$ where a breathing mode seems to have been transformed to almost entirely ρ stretch by the presence of $\cos \chi$ excitation (compare to $n = 2$), and the state at -190.0cm^{-1} where, despite the vibration being close to an inversion path and the energy being above the saddle point, the vibrational mode imposes a dynamical barrier to inversion such that the wavefunction does not extend to near the saddle point nor suffer a great increase in its energy.

Although the Ar_3 molecule has no permanent dipole, a quadrupole produced by the

overlap of two atoms will induce a dipole at the third centre such that for molecular configurations other than equilateral triangular the molecule will possess a multipole moment [98]. Given an expression for this distortion dipole it is possible to evaluate transition dipole moments. A model for the overlap induced quadrupole has been discussed in the chapter on three-body forces, where a table containing overlap induced quadrupole moments may also be found. Table 28 contains values for the Ar_3 cluster instantaneous dipole for various frozen configurations along vibrational coordinates.

Table 28. Some values of the instantaneous dipole for configurations along vibrational paths ($\beta = 0.936\text{Å}^{-1}$).

R	ρ	$\cos\chi$	$\mu_x/$D	$\mu_y/$D
Antisymmetric Stretch ($n = 1a$)				
3.75	3.30	0.0	0.0	1.6×10^{-3}
3.50	3.40	0.0	0.0	9.1×10^{-4}
3.30	3.80	0.0	0.0	4.7×10^{-6}
3.15	4.10	0.0	0.0	1.7×10^{-5}
2.80	4.30	0.0	0.0	9.7×10^{-4}
Ar_2 Rocking ($n = 1b$)				
3.40	3.80	0.00	0.0	6.8×10^{-5}
3.40	3.80	0.08	4.9×10^{-5}	-2.9×10^{-5}
3.40	3.80	0.12	6.6×10^{-5}	-1.5×10^{-4}
3.40	3.80	0.28	-1.3×10^{-5}	-1.2×10^{-3}
Symmetric Stretch ($n = 2$)				
3.00	3.40	0.0	0.0	-2.8×10^{-5}
3.20	3.75	0.0	0.0	-1.8×10^{-5}
3.40	3.95	0.0	0.0	-8.6×10^{-6}
3.50	4.10	0.0	0.0	-1.5×10^{-5}
3.75	4.35	0.0	0.0	-2.7×10^{-6}

Using the expressions of Guillot *et al.* [98], transition dipole moments were evaluated for the basis-set given above, using the Jacobi II method.

The calculated dipole moment of Ar_3 is believed to be too small to be observed using current far infra-red spectroscopic methods. Since the pair quadrupole, and hence the

induced dipole, is dependent on the degree of overlap of atomic orbitals, it will in general be small except for configurations close to the inner turning-points of the vibrational wavefunctions. In general, the quality of the wavefunction at points where one coordinate is extreme will be much more poorly converged than the energy; such points will have the largest trimer-dipole. This explains why only transition dipole moments between the ground state and the lowest three excited states are found to be converged. The distinction between symmetry allowed and symmetry forbidden states is also reduced by mixing; states $n = 3b$ and $n = 4$ show this, the intensity of the symmetry-allowed transition decreasing while the supposed-forbidden state gains intensity. The three results given in table 29 do, however, give a reasonable value of the transition dipole moment for one allowed (between A_1 and E) transition and show an acceptable approximation to zero for a forbidden (A_1 to A_1) transition. The transition dipole is resolved along a unit vector parallel to R, $\mu_{\|}$, and along a unit vector perpendicular to this and in the molecular plane, denoted $\mu_\perp$.

Table 29. Transition dipole moments for Ar_3.

n	$\langle 0|\mu_\perp|n\rangle/D$	$\langle 0|\mu_{\|}|n\rangle/D$
1a	0.0	7.2×10^{-5}
1b	-6.9×10^{-5}	0.0
2	0.0	-1.2×10^{-7}

8.5. 1   An Assessment of a Minimal Basis Set.

A basis-set,

$$\Psi(\eta) = \sum_{v=0}^{4} \sum_{w=0}^{2} \sum_{i=1}^{12} c_a \Psi_a \qquad (152)$$

reduced in size in ρ and $\cos\chi$ functions was investigated, with $q_{max} = 4$ and keeping the same DGB. Such a reduced-size basis-set is probably the smallest that might be admissible for Ar_2HX calculations.

The single-quantum states (see table 30) are much better represented than the rest, the largest change in frequency being $0.17cm^{-1}$ from the ground state to the symmetric stretch. The mode corresponding to Ar_2 rocking is seen to be the best converged at the

Table 30. Comparison of good and reduced (r) basis-sets by the Jacobi II method.

	Frequencies ($\nu_{n \leftarrow 0}/\text{cm}^{-1}$)		
n	Jacobi II	Jacobi II(r)	Visual form of Ψ
1a	22.5022	22.6194	antisymmetric stretch
1b	22.6102	22.6010	Ar_2 rock
2	30.5489	30.7210	symmetric stretch
4	43.2180	43.7836	2 quanta Ar_2 rock (+some stretch)
3a	43.2693	44.2008	antisymmetric stretch+Ar_2 rock (a)
3b	43.3515	45.7407	antisymmetric stretch+Ar_2 rock (b)
5a	50.1117	51.0775	complex
5b	50.1706	52.3770	Ar_2 stretch+Ar_2 rock

'reduced' basis-set level, presumably due to a smaller fractional change in the Φ_v basis-set size. The order of the error in frequencies introduced by truncating the basis-set in the manner above will be relevant to assessing the error in calculations to be performed on Ar_2HX systems; if calculations get to about 0.2cm^{-1} from experiment, we cannot be sure whether the error is due to basis-set incompleteness, Hamiltonain approximations, or potential surface errors.

8.6 A Comparison of Frequencies for Different Potentials.

Using the Jacobi II method with the basis-set given in section 8.3, which is of size 144, results were obtained for two similar pair-wise-additive potentials and for the inclusion of some trial three-body components. The pairwise-only potentials have the Φ and Υ tailored to the potential in question. The three-body calculations use the Φ and Υ tailored for the appropriate pairwise potential. The pairwise potentials are described in the section on two-body potentials. The three-body terms V_{ddd} and V_{ddq} are as previously described and use the Bell and Zucker values for parameters, while the V_{Jansen} term uses the parameters $S_{Jansen} = 430000.0\text{Åcm}^{-1}$ and $\beta = 1.23\text{Å}^{-1}$.

From the results of the two- and three-body calculations in table 31, it can be seen that the changes in frequencies due to inclusion of three-body energy components are sufficiently larger than spectroscopic errors to affect an experimental spectrum. In

Table 31. Frequencies ($\nu_{n\leftarrow 0}/\text{cm}^{-1}$) for trial three-body potentials compared to the two-body only.

Potential	$V_{\text{HFD-B2}}$	$V_{\text{HFD-C}}$	$V_{\text{HFD-C}} + V_{\text{ddd}}$	$V_{\text{HFD-C}} + V_{\text{ddd}} + V_{\text{ddq}}$	$V_{\text{HFD-C}} + V_{\text{Jansen}}$
n			Excitation energies $(E_n - E_0)/\text{cm}^{-1}$		
$1a$	22.494	22.502	22.163	22.136	22.764
$1b$	22.503	22.501	22.160	22.130	22.759
2	30.556	30.549	30.242	30.222	30.647
4	43.202	43.218	42.620	42.573	43.501
$3a$	42.108	43.163	42.545	42.499	43.570
$3b$	43.345	43.351	42.734	42.686	43.761
$5a$	49.654	49.640	49.058	49.002	49.957
$5b$	50.167	50.171	49.581	49.538	50.493
6	58.400	58.386	57.804	57.764	58.602
7	63.077	63.069	62.302	62.246	63.468
8	64.727	64.843	64.160	64.106	65.230
			Ground-state rotational constants		
A/MHz	1754	1754	1749	1749	1761
B/MHz	1752	1753	1748	1748	1761
C/MHz	872	872	871	871	874

addition it is clear that the changes in frequencies that arise from using an alternative two-body potential are greater than one order of magnitude smaller. Knowing that the differences between two-body potentials are so much smaller is essential if spectroscopy is to be used to probe non-additive potentials through calculations. Three three-body terms were tested. The triple-dipole is clearly the most important term, measured by the change in frequencies, as expected. In contrast, the next-higher dispersion term, the dipole-dipole-quadrupole, is seen to have roughly 10% as much effect. The V_{Jansen} term is apparently almost as important as the triple-dipole in some states, and should not be neglected without good reason in any description of three-body forces in Ar_3.

For a Lennard-Jones (Leitner [50]) potential, V_{LJ}, there are three sets of results available, see tables 32 and 33.

8: Triatom Calculations – Ar_3.

Table 32. Comparison of A_1 eigenvalues (in cm^{-1}) from different workers for V_{LJ}.

n	Leitner *et al.* [50]	Horn *et al.* [49]	HHCC ($\lambda_{max} = 84$)	Jacobi II
0	37.35	37.24	37.369	37.367
2	63.07	64.90	62.751	62.778
4	73.28	74.96	73.123	73.503
6	84.15	90.00	84.037	87.003
7	88.42	–	88.195	–

Table 33. Comparison of E eigenvalues (in cm^{-1}) from different workers for V_{LJ}.

n	Leitner *et al.* [50]		Horn *et al.* [49]		HHCC	Jacobi II	
n	lower	upper	lower	upper	$\lambda_{max} = 78$	A' in S_2	A'' in S_2
1	51.38	56.37	56.35	56.58	56.185	56.190	56.197
3	72.52	73.52	74.16	74.30	73.104	73.453	73.292
5	77.44	85.30	82.46	82.70	78.785	79.173	78.622

It is worth comparing the eigenvalues, referred to zero energy at the potential minimum. The Horn results agree qualitatively with those which I calculate, but show distinct quantitative discrepancies. In particular it is noted that pairs of states which should be degenerate are quite close by my method, taking into consideration that the symmetry used was not the full symmetry of the system, while there are much larger differences between physically degenerate states in the Horn calculations. Horn *et al.* claimed a convergence of $\pm 0.01 cm^{-1}$, but the differences between physically degenerate states show that their calculations have not achieved this. Hyperspherical calculations using the program of Hutson and Jain, referred to earlier and denoted HHCC here, support my values by close agreement of eigenvalues, and the normal mode and Jacobi I calculations agree with the Jacobi II. It is also unexpected that the ground state of Horn *et al.* is about 0.1 cm^{-1} lower than all of the other calculations; their method should be variational. The anomalous ground state and large discrepancy in the energies of physically degenerate states in the Horn *et al.* calculations suggests a programming error of some nature.

The results of Leitner *et al.* are qualitatively different to the others; there is correlation between A_1 states, but there seems to be no sensible correlation between E states,

with apparently spurious eigenvalues present. The appearance of spurious eigenvalues in the Leitner *et al.* calculations seems to imply a programming error of some kind. It is worth noting that, since my calculations are performed in S_2, one of the E pair at 73.45 cm^{-1} is an eigenvalue of the same matrix as that at 73.50 cm^{-1}. The 73.50 cm^{-1} state is assigned as being of A_1 on inspection of the wavefunctions. Although the wavefunctions show mixing between these two states, the overlap integral between them is smaller than expected and equal to 0.002.

Horn [49]has also performed calculations on the HFD-B2 pairwise additive potential. It is useful to compare their results with the HHCC (method [48]) and Jacobi II results, see tables 34 and 35. Such a comparison does not change the conclusions from the V_{LJ} results on the reliability of the four different methods; the HHCC calculations appear to be the best, with the Jacobi II performing comparably for the lower states, while the results of both Leitner and Horn appear to be unreliable on the basis of some serious errors.

Table 34. Comparison of A_1 eigenvalues (in cm^{-1}) from different workers for V_{HFD-B2}.

n	Horn *et al.*	HHCC ($\lambda_{max} = 84$)	Jacobi II
0	43.72	43.816	43.813
2	76.64	74.349	74.370
4	88.90	86.700	87.025
6	106.49	100.329	102.240
7	108.56	105.065	–

Table 35. Comparison of E eigenvalues (in cm^{-1}) from different workers for V_{HFD-B2}.

n	Horn *et al.* lower	upper	HHCC $\lambda_{max} = 78$	Jacobi II A' in S_2	A'' in S_2
1	66.49	66.76	66.311	66.306	66.316
3	87.21	87.76	86.820	87.170	86.921
5	97.61	97.66	93.615	93.988	93.467

It is also interesting to determine to what extent the change in frequencies due to a change in potential depends on the basis-set. This might be a valuable way of reducing

8: Triatom Calculations – Ar₃.

computing times in an analysis of the effect of three-body forces. Calculations were performed with the Jacobi II method, with the two basis-sets detailed above, for the HFD-C potential with and without a trial three-body dispersion term, the exact nature of which is not relevant to this discussion.

Table 36. $\nu_{n \leftarrow 0}(2\text{body}) - \nu_{n \leftarrow 0}(3\text{body})$ for Ar_3 good and reduced basis-sets.

n	Jacobi II(r)	Jacobi II
1a	0.351	0.367
1b	0.361	0.367
2	0.292	0.327
4	1.334	0.645
3a	0.657	0.712
3b	3.179	0.666
5a	0.590	0.669
5b	2.966	0.633

From the results given in table 36, it is clear that for the single quantum modes ($n = 1a, 1b$ and $n = 2$), the quantity $\nu_{n \leftarrow 0}(2 \text{ body}) - \nu_{n \leftarrow 0}(3 \text{ body})$ differs between the good and reduced basis-sets by an order of magnitude less than the change in $\nu_{n \leftarrow 0}(2 \text{ body})$ on reducing the basis-set; the change in $\nu_{n \leftarrow 0}(2 \text{ body})$ on reducing the basis-set is less than 0.2cm^{-1}. It is also very clear that for $n > 2$ there will be very great errors in predicting the effects of a realistic three-body effect from a reduced basis-set. Hence I conclude that the perturbation in frequency due to a small change in potential converges much faster than the frequency, and hence reduced basis-set calculations can be used with caution to estimate the effect of perturbative three-body terms.

Accurate rotational constants can be calculated by performing ro-vibrational Hamiltonian calculations for $J > 0$. However, as mentioned earlier, the Jacobi II calculation is purely vibrational. To obtain good estimates of the rotational constants, the inertia tensor may be inverted and expectation values of the leading diagonal calculated. This gives the equations:

$$A = \left\langle \frac{1}{I_{Ar_2} \sin^2 \chi} + \frac{1}{2\mu R^2 \tan^2 \chi} \right\rangle$$

$$B = \left\langle \frac{1}{2\mu R^2} \right\rangle \tag{153}$$

$$C = \left\langle \frac{1}{2\mu R^2 + 2I_{Ar_2}} \right\rangle.$$

The result of applying these equations to the lowest few states of Ar_3 is given in table 37. The rotational constants show the correct symmetry for a_1 states as well as illustrating the larger average size of Ar_3 in a symmetric stretch.

Table 37. Rotational constants for the lowest few levels of Ar_3, calculated for V_{HFD-C}.

	A/MHz	B/MHz	C/MHz
Ground state	1754	1753	872
First bend (A')	1746	1693	844
First bend (A'')	1740	1700	848
Symmetric stretch	1697	1695	842

In conclusion, it seems clear that the Jacobi II calculations are good and justify the use of Method II in the calculations of one- and two-quantum states, although the HHCC method is better for higher energies. I am confident that discrepancies between the results of both Horn and Leitner and my calculations do not cast doubt upon the validity of Method II, or its results, since there appear to be serious physical deficiencies in the Horn and Leitner results.

A basis-set of a size suitable for calculations on Ar_2HCl was compared against the chosen Jacobi II basis-set, and found to be adequate.

9: Calculations on Ar$_2$HX Systems.

This chapter begins with an explanation of the significance of the expectation values that have been calculated. An account of some convergence tests is then followed by a key to the acronyms used in discussing and tabulating the results. The discussion is divided into three main sections: calculations on Ar$_2$H/DCl using pairwise potentials, calculations on Ar$_2$HCl including trial three-body terms, and preliminary calculations on Ar$_2$HF. Comparisons with experiment are made where this is possible

9.1 Calculated Parameters and Spectroscopic Observables.

Once a calculation has yielded an eigenvalue and eigenvector a host of expectation values can be calculated. Of particular interest are the trimer rotational constants and parameters that indicate the type of motion the HX molecule executes. In the latter category I choose to calculate expectation values of two parameters:

$$P_2(\cos\theta) = \frac{1}{2}(3\cos^2\theta - 1)$$
$$\Delta(\theta, \phi) = \sin^2\theta\cos 2\phi. \tag{154}$$

These are chosen since they correlate with the nuclear quadrupole coupling constants resolved along the principal inertial axes, χ_{xx}, χ_{yy} and χ_{zz}. In particular:

$$\chi_{xx} = \chi_{HX}\langle P_2(\cos\theta)\rangle$$
$$(\chi_{yy} - \chi_{zz}) = \chi_{HX}\frac{3}{2}\langle\Delta(\theta, \phi)\rangle, \tag{155}$$

where χ_{HX} is the quadrupole coupling constant of the uncomplexed hydrogen halide.

The values of these two expectation values can also be used in guiding the assignment of eigenstates to vibrational modes and in judging the degree of freedom of HX motion:

- $\langle P_2(\cos\theta)\rangle$ is

    1 if HX is fixed at $\theta = 0°$ or $180°$,

    $-\frac{1}{2}$ if fixed at $\theta = 90°$ and

0 in the free rotor limit.

• $\langle \Delta(\theta, \phi) \rangle$ is

1 if HX is fixed at $\theta = 90°, \phi = 0°$(co-planar Ar$_2$ and HX),

−1 if $\theta = 90°, \phi = 90°$ (crossed Ar$_2$ and HX) and

0 in the free rotor limit.

Large amplitude motion will result in expectation values with a wide variation between the rigid limits; a rigid analysis cannot be applied to the expectation values. In addition, expectation values of close to zero should not be regarded as highly numerically significant; a small change in the dynamics can cause large fractional changes, or even a change of sign. The same caution applies to the experimental quantities with which these expectation values correlate; the hyperfine splittings used in their calculation are very much smaller than the vibrational or rotational energy intervals. More specifically, it is those states which have quadrupole coupling constants close to that of the ground state which are worst defined: the spectra are in the ground-to-excited vibrational transition energy region. The best determined experimental values of $\langle P_2(\cos\theta) \rangle$ and $\langle \Delta(\theta, \phi) \rangle$ are probably accurate to about 1 part in 100.

The evaluation of rotational constants is more difficult; *a priori*, one might expect to perform a series of calculations for various J, K and calculate the rotational constants from the eigenvalue differences. However, this means a lot of computing and it is impractical to compute A, B and C in this way. There are also theoretical problems in the total-internal angular momentum coupling, which was noted in the chapter discussing the theory.

Alternatively, the inertia tensor may be inverted and expectation values of the leading diagonal calculated. The expressions obtained by such an inversion are prohibitively long and some approximation is appropriate. Neglect of terms in HX inertia, I_{HX}, gives the

rigid limit rotational constants:

$$B_x \approx \left\langle \frac{1}{I_{Ar_2} \sin^2 \chi} + \frac{1}{2\mu R^2 \tan^2 \chi} \right\rangle$$

$$B_y \approx \left\langle \frac{1}{2\mu R^2} \right\rangle \tag{156}$$

$$B_z \approx \left\langle \frac{1}{2\mu R^2 + 2I_{Ar_2}} \right\rangle,$$

where the rotational constants have been labelled with cartesian, rather than principal inertial, axis labels to avoid confusion in the case of axis switching.

In a free-rotor limit, treating the HX as structureless in this way is valid. For real systems, however, there needs to be a correction applied to the above terms to take account of neglecting I_{HX}. For Ar_2HCl corrections of -6 MHz to B_y and -1.5 MHz to B_z have been estimated [21]; I_{HCl} is a factor of about 200 less than the other inertial terms. Non-rigidity of the complex, accounted for in the above corrections, causes the HCl to be perturbed in its bending coordinate as the complex rotates (Coriolis perturbation) and further reduces the contribution from I_{HCl} by a factor of about 0.65. The greater rigidity of Ar_2DCl will to increase the error introduced by assuming that the HX is free-rotor.

In practice, the expectation values of the functions given above were calculated using Gaussian quadrature in all coordinates except R, where a trapezium-rule integration was used. The orthogonality of basis functions was used where the argument of the integral depended on only a subset of the five coordinates.

9.2 Convergence of Ar_2H/DCl Basis Set.

For Ar_2HCl, various convergence tests were performed and the following basis-set chosen:

- A product of $\Upsilon_w(\rho)$ basis functions, with $0 \leq w \leq 2$, and $\Phi_v(\cos\chi)$, with $0 \leq v \leq 4$, was used with a maximum of 4 quanta in the product ($q_{max} = 4$).

- 16 equally spaced Gaussians distributed on $(2.500\text{Å}, 4.600\text{Å})$, 'c' parameter $= 0.7$.

- $j_{HCl} < 6$. $k > 1$ for $j = 5$ and $k = 4$ for $j = 4$ are not used.

The Υ and Φ basis-set size is the same as the 'reduced' basis in the Ar_3 calculations, from which it was found that the worst error in frequency was less than 0.2 cm^{-1}; in

particular the changes in frequency for Ar_3 were: 0.12 cm^{-1} (antisymmetric stretch), 0.009 cm^{-1} (Ar_2 rock) and 0.17 cm^{-1} (symmetric stretch). The results from Ar_3 are taken as adequate indicators of the level of convergence of these modes in Ar_2HCl, although θ–χ coupling will probably exaggerate the Ar_2 rock (χ bend) convergence error slightly. Υ and Φ basis-set error is by far the largest contributor to basis-set error, and has most effect on the experimentally undetectable states. Convergence tests for j_{max} (table 38) and N_{DGB} (table 39) were performed with $q_{max} = 0$, and results for the ground state, Σ bend and R stretch (no excitation possible in ρ) examined as being representative of the system dynamics.

9: Calculations on Ar_2HX Systems.

Table 38. Convergence (for Ar_2HCl) with respect to j_{max}. $k_{max} = j_{max}$, except †, where $k_{max} = 3$ and only $k = 0,1$ for $j = 5$ are used. $q_{max} = 0$ was used, with other parameters as given at the start of this section.

j_{max}	Ground state Energy/cm^{-1}	Σ bend Energy/cm^{-1}	$\langle P_2(\cos\theta)\rangle$	$\langle\Delta(\theta,\phi)\rangle$
4	−315.54452	−272.97236	0.289626	0.047440
5†	−315.56424	−272.98983	0.290525	0.047420
5	−315.57401	−272.99233	0.290318	0.047402
6	−315.57785	−272.99419	0.290378	0.047404
7	−315.57835	−272.99586	0.290382	0.047404

Table 39. Convergence (for Ar_2HCl) with respect to N_{DGB}. $q_{max} = 0$ was used, with other parameters as given at the start of this section.

N_{DGB}	Ground state Energy/cm^{-1}	Stretch Energy/cm^{-1}	B_y/MHz	B_z/MHz
12	−315.55701	−280.09491	1605.793	843.216
14	−315.56394	−280.16382	1608.975	844.131
16	−315.56424	−280.17974	1609.697	844.319
18	−315.56432	−280.18036	1609.717	844.330
20	−315.56431	−280.18037	1609.571	844.293

The presented tables (38 and 39) show that the basis-set is well converged, with errors in $\langle P_2(\cos\theta)\rangle$ and $\langle\Delta(\theta,\phi)\rangle$ appearing in the fourth significant figure, errors in the rotational constants B_y and B_z of the order of 0.1 MHz, and ground state convergence of better than 0.02 cm^{-1}. These errors are two orders of magnitude smaller than the effects of hypothesised three-body forces. It was remarked above that the basis-set errors arising from the small Υ and Φ basis-set size are by far the largest. Practical computational restrictions preclude the inclusion of more $\Upsilon_w\Phi_v$ functions without reducing the other basis-function sizes.

The HX bending modes have the largest transition dipoles and are the only states, apart from the ground state, which are observable using current experimental techniques.

In consequence, it is believed to be important to ensure that the bending modes were well represented, hence to concentrate on the Y_{jk} and ψ_i basis-set size. An upshot of the small basis-set size in Υ is likely to be large errors in B_z, for all modes, and a contribution to the frequency errors of the order of 0.02 cm^{-1} for the bending states; HX bending states have ρ motion which is very similar to the ground state.

Table 40. Convergence (for Ar$_2$DCl) with respect to j_{max}. $k_{max} = j_{max}$, except †, where $k_{max} = 3$ and only $k = 0, 1$ for $j = 5$ are used. $q_{max} = 0$ was used, with other parameters as given at the start of this section.

j_{max}	Ground state Energy/cm^{-1}	Σ bend Energy/cm^{-1}	$\langle P_2(\cos\theta)\rangle$	$\langle \Delta(\theta,\phi)\rangle$
4	−324.88844	−279.46143	0.253153	0.101277
5†	−325.00325	−279.57735	0.254973	0.102032
5	−325.02608	−279.58202	0.254676	0.102604
6	−325.04680	−279.59314	0.254628	0.102782
7	−325.04969	−279.59722	0.254725	0.102776

The calculations for Ar$_2$DCl do not take account of the centre-of-mass shift in the Ar–DCl potential evaluations. This shift is approximately 0.03 Å, which will lead to an under-estimate in B_y of approximately 30 MHz. The convergence test (table 40) indicates that the $j_{max} = 5^\dagger$ basis set is suitable; the ground state is converged to about 0.05 cm^{-1}. DCl has a smaller rotational constant than HCl, therefore Ar$_2$DCl is more rigid, hence the poorer convergence for Ar$_2$DCl. The isotopic substitution does not affect the suitability of the DGB proposed for Ar$_2$HCl, and the basis-sets in ρ and $\cos\chi$ were determined taking the substitution into account.

9.3 Key to the Results.

In the tables of results and discussion single letters are used to refer to a calculation with a given basis-set and potential and a short abbreviation is used to refer to experimental and previous results.

3. 1 Experimental and Previous Results on Ar$_2$HCl.

Expt. Experiments of Gutowsky [19](ground state) and Saykally [20]groups on Ar$_2$HCl.

HHB. Results of Hutson *et al.*[21]using the H6(3) potential for clamped Ar$_2$. The Ar-Ar energy is taken as zero at the clamped geometry ($\rho = 3.82$ Å, $\cos \chi = 0$).

3. 2 Calculations on Ar$_2$H/DCl with Two-body Potentials.

TWO0 Calculation using the H6(4,3,0) and HFD-C potentials for Ar$_2$HCl [HCl $v = 0$].

Basis used:

- ρ and $\cos \chi$ basis functions are eigenstates of an effective potential in one dimension. This is defined as an adiabatic cut on the potential energy surface.

- A product of three basis functions in ρ and five in $\cos \chi$ was used with a maximum of 4 quanta in the product.

- 16 equally spaced Gaussians distributed on $(2.500\text{Å}, 4.600\text{Å})$, '$c$' parameter $= 0.7$.

- $j_{HCl} < 6$. $k > 1$ for $j = 5$ and $k = 4$ for $j = 4$ are not used.

TWO1 Calculation using the H6(4,3,0) and HFD-C potentials for Ar$_2$HCl [HCl $v = 1$].

The basis used is identical to **TWO0**.

TWOD0 Calculation using the H6(4,3,0) and HFD-C potentials for Ar$_2$DCl [DCl $v = 0$].

The basis uses the same method as **TWO0**, but in this case the adiabatic cut is on the Ar$_2$DCl potential surface. No diatom centre-of-mass shift was applied.

TWO(3) Calculation using H6(3)+HFD-C potentials for Ar$_2$HCl.

The basis used is identical to **TWO0**.

3. 3 Three-body Calculations on Ar$_2$HCl.

In all cases the H6(4,3,0)+HFD-C two-body potentials were used, as was the same basis-set as the two-body calculation **TWO0**.

Idd Three-body induction term (up to hexadecapole on HCl), using the multipole strengths and polarisabilities given by Bulanin *et al.*.

AT Three-body Axilrod-Teller term with $\nu_{123} = 1060420\text{cm}^{-1}\text{Å}^9$.

DDD Three-body anisotropic dispersion term with $\nu_{123} = 1060420 \text{cm}^{-1}\text{Å}^9$ and using the polarisabilities given by Bulanin *et al.*.

DDD† Three-body anisotropic dispersion term with $\nu_{123} = 1060420 \text{cm}^{-1}\text{Å}^9$ and using the polarisabilities given by Bulanin *et al.*, damped with a product of D_3 functions with $\beta(\text{Ar} - \text{Ar}) = 4.348\text{Å}^{-1}$ and $\beta(\text{HCl} - \text{Ar}) = 3.577\text{Å}^{-1}$.

JAN Three-body Jansen term, with $\beta_{\text{Jansen}} = 1.24\text{Å}^{-1}$, $S_{\text{Jansen}} = 2 \times 10^5 \text{cm}^{-1}\text{Å}$ and $\delta_{\text{Jansen}} = 0.15\text{Å}$.

iQd Three-body HCl dipole–overlap induced quadrupole energy, with $\beta_{\Theta-\text{def}} = 0.965\text{Å}^{-1}$ and the dipole strength given by Bulanin *et al.*.

iQdq Three-body (HCl dipole + quadrupole)–overlap induced quadrupole energy, with $\beta_{\Theta-\text{def}} = 0.965\text{Å}^{-1}$ and the multipole strengths given by Bulanin *et al.*.

MOD1 Three-body terms from calculations **Idd**, **DDD†**, **JAN** and **iQdq** summed (i.e. Model # 1).

MOD2 Model # 2 three-body potential: induction as for **Idd**, dispersion as **DDD†**, otherwise $\beta_{\Theta-\text{def}} = 1.000\text{Å}^{-1}$, $\beta_{\text{Jansen}} = 1.31\text{Å}^{-1}$, $S_{\text{Jansen}} = 7.5 \times 10^5 \text{cm}^{-1}\text{Å}$ and $\delta_{\text{Jansen}} = 0.15\text{Å}$.

9.3. 4 Notes Appearing in the Results.

Note 1. Ar$_2$ separation fixed at value based on Gutowsky result $B_z = 1733.86$MHz.

Note 2. For the fixed Ar$_2$ calculation there is only one stretch, of the R coordinate. These results are entered under the 'Breathing Stretch' heading.

Note 3. This was the first experimentally observed transition and is used as the standardisation for each set of results independently of the others.

9.4 Ar$_2$H/DCl Two-body Results and Analysis.

Atom-atom-diatom trimers, with 'T' equilibrium geometry, such as Ar$_2$HCl/HF, have six vibrational modes. Three modes correspond with the triatomic modes which Ar$_3$ was seen to have in the previous chapter, and show the same correspondence to a normal mode description of the vibrations. I refer to these three modes as 'triatom-like

9: Calculations on Ar$_2$HX Systems.

modes'; they are represented in figure 23. The other three modes correspond with HX vib-rotor states. Plots of the square of some cuts of the wavefunction for Ar_2HCl and Ar_2DCl are given in appendix E. All of the wavefunctions show the kind of large amplitude motion expected for a van der Waals cluster; the HCl bending states are notable in this respect, showing considerable wavefunction density at the $\theta = 90°$ geometry for the in-plane and out-of-plane bends, and at the secondary potential minimum ($\theta = 180°$ and 57.5 cm^{-1} above the primary minimum) for the parallel bend.

Breathing stretch   Wagging stretch x bend
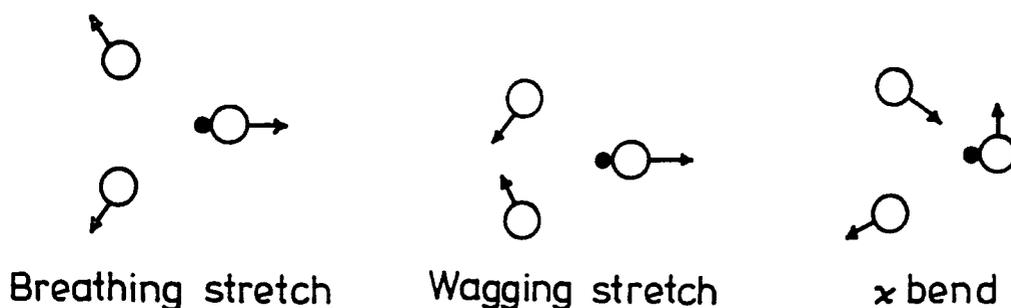
Fig. 23. Pictorial representation of Ar_2HCl triatom-like modes.

A comparison of the energy of the HCl free-rotor states with the bending states of the ArHCl and Ar_2HCl systems is shown in figure 24.

A progressive increase in energy of the HCl motion going from free HCl to ArHCl to Ar_2HCl is observed, correlating with increasing localisation of the wavefunction (i.e. increasing rigidity). The three single-quantum rotational states of HCl are degenerate, but the states with which they correlate in the molecular complexes are split in energy due to both the dynamical and potential effects of the other bodies. In the presence of a single Ar atom the HCl rotation with no angular momentum along the Ar–HCl axis ($k = 0$) is shifted up in energy less than the two rotations which do have angular momentum along the Ar–HCl axis ($k = \pm1$) since there is less interaction for $k = 0$ due to a secondary potential minimum at the Ar–ClH geometry. The ArHCl state which correlates with $k = 0$ has axial symmetry and is termed the Σ, or parallel, bend; the
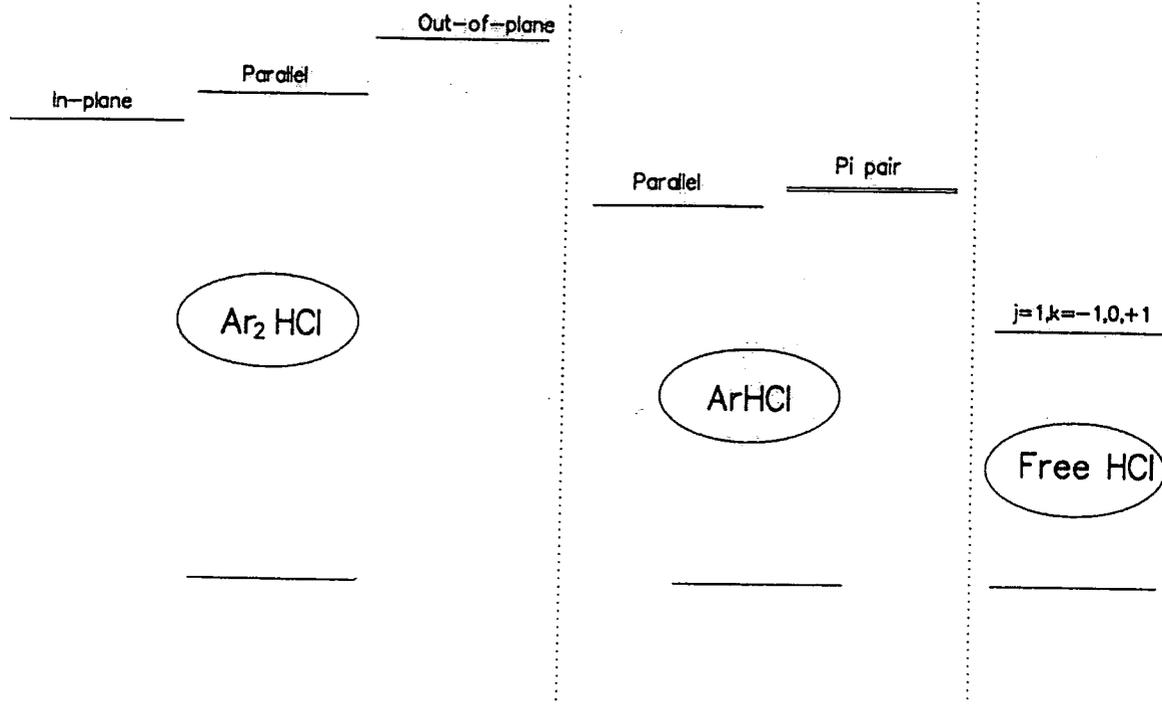
Fig. 24. HCl free-rotor and bending state energy diagrams.

other two states have wavefunction nodes containing the intermolecular axis and so are referred to as Π bend states. The dynamical effects of Coriolis coupling causes a small splitting of the Π states in addition to the Π–Σ splitting due to the potential. In Ar_2HCl, Π state splitting is much larger and is due to quite different potential shapes for the in-plane and out-of-plane bends. The Π pair still have a centre which is higher in energy than the parallel bend, but because the Ar atoms are off-axis, the primary minimum is broader in-plane and the in-plane bend is of lowest energy. Symmetry labels in the group $C_{2v}(M)$, with character table given in the chapter on theory, can be given to the bending states: A_1 for the Σ bend, B_2 for the in-plane bend and B_1 for the out-of-plane bend.

The triatom-like modes no longer show the degenerate states which exist for triatomic systems since the the potential does not have C_{3v} symmetry. There are similarities between the Ar_3 and Ar_2HCl systems, however, as evidenced by the similar energy level structure in the diagram given in figure 25.

The symmetric combination of R and ρ stretches is termed the 'breathing mode', while the asymmetric combination is termed the 'wagging mode'. The Ar_2 rocking motion (which, in Ar_3, is degenerate with the wagging mode) is termed the 'χ bend'. The triatom-

9: Calculations on Ar_2HX Systems.
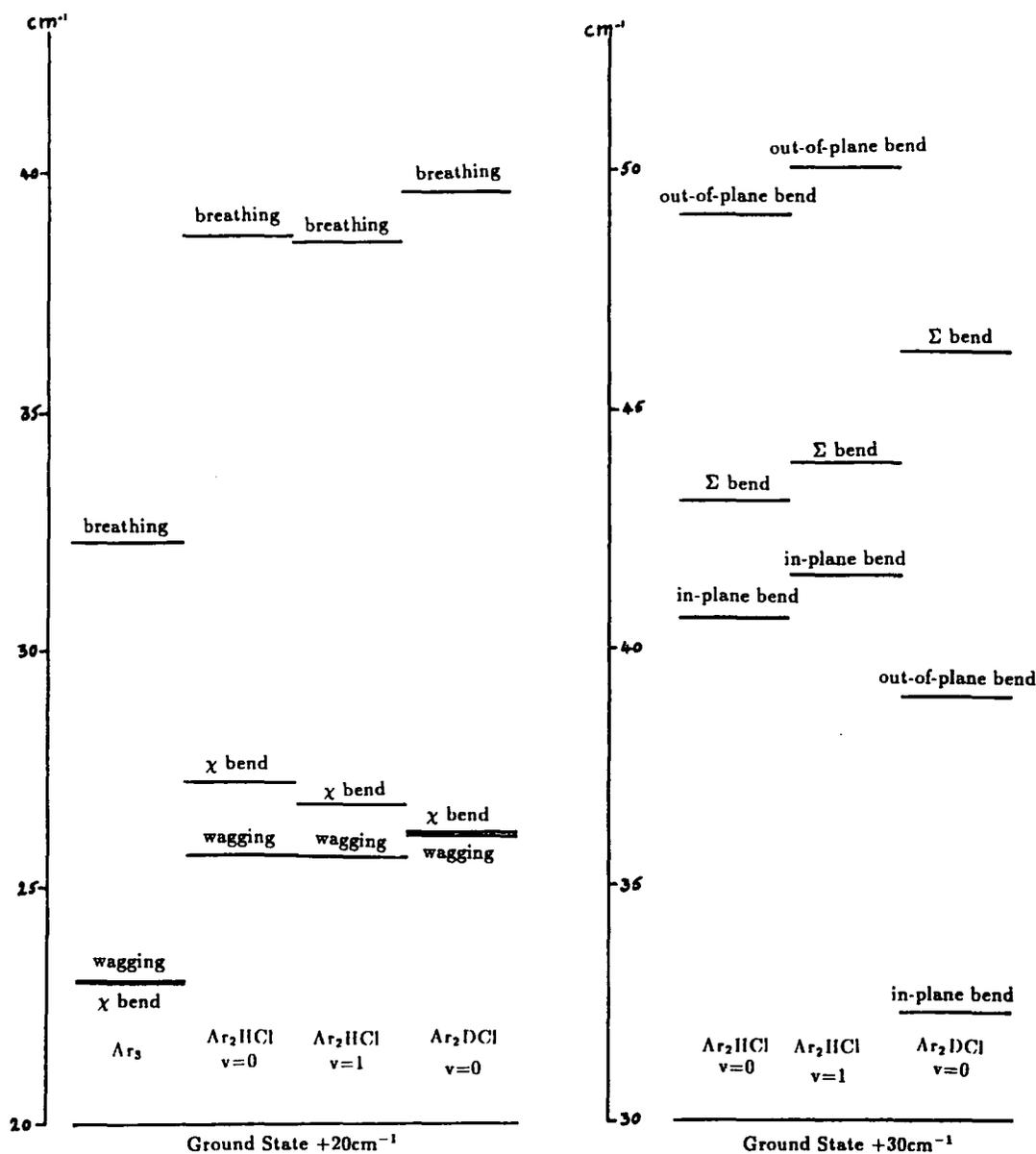
Fig. 25. Energy level diagram for some Ar$_2$Y systems.

like modes are totally symmetric (A_1), except for the χ bend(B_2). A_2 symmetry states only exist for multiple-quantum modes, such as an out-of-plane + χ bend combination.

From the energy level diagram, which is derived from tables 42 and 43, the frequency shift between HCl $v = 0$ and $v = 1$ states can be seen. As expected, excitation of the HCl vibrational motion causes a much smaller shift of the triatom-like modes than of

9: Calculations on Ar$_2$HX Systems.

the HCl bending modes. The observation that the χ bend is shifted the most, out of the triatom-like modes, is evidence of coupling between HCl bending and Ar_2 rocking motions. There is a red-shift of 2.83 cm^{-1} between $v = 0$ and $v = 1$, and calculations are listed in table 43; experimental data is not available, although feasible.

The effect of H/D isotopic substitution is also worthy of note. The greater rotational constant of DCl leads to a great increase in the rigidity of the DCl motion, which can be seen from the plots of Ψ^2 given in appendix E. The effect of this greater rigidity is to reduce the Π state energies and to increase the Σ bend energy. The Π bends decrease in energy because the wavefunction concentrates in the region of the principal potential minimum, while the Σ bend increases in energy because wavefunction density is reduced in the region of the secondary potential minimum (see appendix E). The parallel bend state corresponds with the first overtone of the Π states in the rigid limit; clearly this limit is not being closely approached for Ar_2DCl, even though the trend is apparent. An upshot of the energy shifts is an increase in the energy separation of the parallel bend and breathing state. This reduces the mixing of these two states, as can be seen from the absence of R excitation in plots of the Ar_2DCl parallel bend, while some excitation is seen for Ar_2HCl. More evidence for the mixing in Ar_2HCl is seen from an analysis of potential perturbations, and is discussed in a following section.

Table 41. Ar_2DCl Out-of-plane (Π_c) bend results.

	Experiment	TWOD0
$\nu_{i\leftarrow 0}$/cm^{-1}	36.046	37.712
$\langle P_2(\cos\theta)\rangle$	0.189	0.1983
$\langle \Delta(\theta,\phi)\rangle$	−0.226	−0.2449
B_x/MHz	1788.14	1754.49
B_y/MHz	1662.76	1695.75
B_z/MHz	849.02	855.04

Additional information on the Ar_2HCl potential and dynamics can be deduced from experiments on Ar_2DCl; the data can help to understand mixing phenomena, which will be different for the two systems, as well as providing more information to fit calculations

9: Calculations on Ar_2HX Systems.

to. To-date only the out-of-plane bend has been characterised [103], see table 41; both the experiment and spectrum assignment are difficult.

The theoretical results for Ar_2DCl are, by comparison with experiment for the only characterised state, of suitable quality to aid in the assignment of further states; a full set of one-quantum states is given in tables 42 and 43. Recalling that the neglect of the centre-of-mass shift leads to an under-estimate in B_y of approximately 30 MHz, this quantity is seen to be about 60 MHz higher than experiment. Coriolis mixing is discussed below in more detail, but here I note that the out-of-plane bend has neglected mixing with the breathing stretch, which has $B_y = 1600$ MHz; the effect of mixing will be to decrease the aforementioned 60 MHz discrepancy to a more reasonable value. There are clear discrepancies between experiment and theory, however, with origins in both basis-set and potential error. This problem is addressed more fully below, with reference to Ar_2HCl and plausible three-body forces.

For Ar_2HCl, experimental results exist for the Ground State [19] and the HCl bending modes [20], while previous calculations [21], denoted **HHB**, were performed with the Ar_2 clamped with $\cos \chi = 0$ and $\rho = 3.82$Å, based on the A rotational constant for the ground state. Clamping the Ar_2 reduces the number of modes; there is only a centre of mass stretch, rather than both Wagging and Breathing, and no χ Bend. The centre-of-mass stretch appears to be more like the Breathing mode in my calculations.

In comparing the experimental to theoretical results care must be taken since the property name does not always represent the same quantity. To be specific, the clamped Ar_2 (**HHB**) calculations were performed with $\frac{\hbar^2}{2\mu R^2}(J(J+1) - 2K^2)$ on the Hamiltonian matrix diagonal. In the **HHB** calculation $J = 0$ was always programmed, but for the Π bends $K = 1$ was used so that the energy $-2B_y$ is added to all diagonal elements, hence to the eigenvalues. Taking the values of B_y calculated, there should be 0.115 cm^{-1} added to the in-plane bend and 0.116 cm^{-1} added to the out-of-plane bend energies to bring the predicted frequencies into line with the experimental parameter $\nu_{i \leftarrow 0}$, which is a vibrational transition frequency. My calculations use a vibration-only Hamiltonian so the frequencies are directly comparable with experiment. Both the earlier calculations and my own use the same expressions for evaluating the rotational constants, and as

Table 42. Collected two-body results for Ar_2H/DCl – spectroscopically observed states.

	Expt	HHB	TWO(3)	TWO0	TWO1	TWOD0	TWO(3)–TWO0	Expt–TWO
Name	Ground State $[\epsilon = 0, \eta = 0]$ (A_1)							
Energy/cm^{-1}	–	–253.753	–323.324	–317.931	–320.756	–327.665		
$\langle P_2(\cos\theta)\rangle$	0.4165	0.4540	0.4472	0.4429	0.4520	0.5922	0.0043	–0.0264
$\langle\Delta(\theta,\phi)\rangle$	0.0313	0.0218	0.0222	0.0255	0.0252	0.0227	-0.0033	0.0058
B_x/MHz	1733.86	–^{Note1}	1757.19	1756.99	1757.51	1760.83	0.20	–23.13
B_y/MHz	1667.92	1702.4	1671.10	1668.24	1650.54	1662.99	2.86	–0.32
B_z/MHz	844.45	857.6	849.53	848.73	844.23	848.34	0.81	–4.28
Name	In-plane (Π_b) Bend $[\epsilon = 0, \eta = 1]$ (B_2)							
Energy/cm^{-1}	–	–213.438	–283.737	–278.741	–280.778	–295.694		
$\nu_{i\leftarrow 0}$/cm^{-1}	37.196	40.315	39.587	39.190	39.978	31.971	0.397	–1.994
$\langle P_2(\cos\theta)\rangle$	–0.001	–0.0330	–0.0191	–0.0031	0.0170	0.2551	–0.0160	0.002
$\langle\Delta(\theta,\phi)\rangle$	0.340	0.3673	0.3531	0.3441	0.3319	0.2375	0.0090	–0.004
B_x/MHz	1683.61	–^{Note1}	1744.23	1744.98	1746.24	1757.05	–0.75	–61.37
B_y/MHz	1682.42	1730.8	1694.27	1686.04	1668.90	1641.48	8.23	–3.62
B_z/MHz	826.70	864.6	851.25	849.22	844.64	839.83	2.04	–22.52
Intensity$_{i\leftarrow 0}$	>3	–	5.329	5.350	5.650	14.447		
Name	Parallel (Σ) Bend $[\epsilon = 0, \eta = 0]$ (A_1)							
Energy/cm^{-1}	–	–211.164	–282.590	–276.606	–278.721	–283.557		
$\nu_{i\leftarrow 0}$/cm^{-1}	39.555	42.589	40.734	41.325	42.035	44.108	–0.591	–1.770
$\langle P_2(\cos\theta)\rangle$	0.291	0.2943	0.2772	0.2752	0.2796	0.2622	0.0019	0.016
$\langle\Delta(\theta,\phi)\rangle$	0.062	0.0430	0.0474	0.0591	0.0564	0.1165	–0.0117	0.003
B_x/MHz	1730.70	–^{Note1}	1753.23	1753.72	1754.43	1752.57	–0.48	–23.02
B_y/MHz	1720.89	1793.4	1758.94	1766.59	1759.34	1792.39	–7.65	–45.70
B_z/MHz	883.04	879.2	868.55	870.47	868.49	877.12	–1.93	12.57
Intensity$_{i\leftarrow 0}$	1.0 See Note 3.							
Name	Out-of-plane (Π_c) Bend $[\epsilon = 1, \eta = 1]$ (B_1)							
Energy/cm^{-1}	–	–206.517	–276.638	–271.389	–273.344	–289.953		
$\nu_{i\leftarrow 0}$/cm^{-1}	45.203	47.236	46.686	46.542	47.412	37.712	0.144	–1.339
$\langle P_2(\cos\theta)\rangle$	–0.025	–0.0030	–0.0140	–0.0224	–0.0209	0.1983	0.0084	–0.003
$\langle\Delta(\theta,\phi)\rangle$	–0.295	–0.3098	–0.3146	–0.3197	–0.3181	–0.2449	0.0051	0.025
B_x/MHz	1774.	–^{Note1}	1750.15	1749.94	1750.05	1754.49	0.21	24.5
B_y/MHz	1752.	1740.8	1706.72	1705.52	1698.29	1695.75	1.19	46.5
B_z/MHz	854.6	861.7	856.59	856.21	854.40	855.04	0.38	–1.6
Intensity$_{i\leftarrow 0}$	>3	–	4.972	4.942	5.397	16.282		

explained above these expressions can overestimate B_y by about 6 MHz and B_z by about 1.5 MHz. These corrections are not applied; the numbers quoted are the expectation values of the previously quoted equations.

Both the **HHB** and my own calculations do not include Coriolis coupling, which may significantly affect the physical states. Calculations of this effect would be useful. A preliminary investigation of Coriolis mixing has been undertaken by Elrod [104], who tried to deperturb his experimental data. Elrod's calculations show that the degree of mixing between the parallel and in-plane bends cannot be determined from his data; he calculates deperturbed values for B_z of 843.8 MHz for the in-plane bend and 865.8 MHz for the parallel bend, based on an estimate of Coriolis mixing extended from the known effect for ArHCl.

Evidence of mixing is also found for the out-of-plane bend from the large residuals found when fitting the various spectroscopic parameters to the spectrum; Elrod reports that there seemed to be a crossing with a dark state at about $J = 7$. Candidates for states interacting with the out-of-plane bend are states with two quanta in the χ bend and wagging stretch pair. These states have symmetry A_1 (two quanta in a single mode) or B_2 (one quantum in each mode), hence can only interact through dynamical (Coriolis) coupling. However, because the basis-set used in ρ and $\cos\chi$ is forced to be so small by computational restrictions, the calculation of these two excited states to the same accuracy as the out-of-plane bend is not possible. The accurate calculation of these states, together with a proper treatment of the Coriolis coupling, will be needed to quantify the mixing effect and further understand the spectrum. For now I note that discrepancies between theory and experiment for the out-of-plane bend will have large contributions from neglected dynamical effects, especially in the rotational constants, in addition to possible three-body effects.

For the suggested Coriolis coupling to the out-of-plane bend, symmetry can be applied to find which rotational constants may be perturbed. If two states of symmetry Γ_α and Γ_β are to interact through a component of the total angular momentum operator, the latter must have symmetry $\Gamma_\alpha \otimes \Gamma_\beta$ since the direct product must be totally symmetric. Thus for the out-of-plane bend (B_1) to interact with a two-quanta χ bend or wagging

stretch (both A_1), the perturbation must have symmetry B_1, hence is the $\hat{J}_y$ operator and B_y will be mixed. On the other hand mixing with the χ bend + wagging stretch state (B_2) occurs through $\hat{J}_z$ (symmetry A_2) since $B_1 \otimes B_2 \to A_2$. We can expect the state with two quanta in the wagging mode to have quite a large B_y and I suggest that this is a candidate for Coriolis mixing with the out-of-plane bend since it will bring the predicted value closer to experiment. Reliable estimates of the rotational constants of mixing states are required to address this problem more fully.

In summary, Coriolis mixing is likely to affect B_z in the in-plane and parallel bends and both B_z and B_y in the out-of-plane bend, while the others should not be affected and provide useful probes of proposed three-body effects.

A clamped Ar_2 calculation determines the more easily experimentally observable HX bending states, and so is potentially useful. The χ bend, and what is effectively the wagging stretch, are not part of the clamped model and so possible coupling of these modes to bending states cannot be assessed. The results presented in tables 42 and 43 allow a quantitative assessment of the errors arising in a clamped Ar_2 calculation. The calculation **TWO(3)** was performed using the same potential as the **HHB** results. From a comparison of these results is is clear that the clamped Ar_2 calculation is better than might, at first, be estimated; the θ, ϕ expectation values are generally good estimates. As expected, from noting the R–ρ coupling in the potential surface, there is more effect on the B_y rotational constant (which is a measure of R excitation) when vibrations in ρ are allowed. This coupling is evident in the wavefunction plots presented in appendix E. More importantly, the extra two degrees of freedom in **TWO(3)** cause a drop of almost 2 cm^{-1} in $\nu_{i \leftarrow 0}$ for the parallel bend, indicating rather more effect than might be deduced from purely the expectation values. A clamped calculation is clearly only suitable for broad characterisation of the dynamics, and is inappropriate for an analysis of the two- and three-body potential energy surface.

Only recently [66] the ArHCl potential was improved in the light of fitting calculations to spectroscopic states which had not been observed at the time the H6(3) potential was derived. Significant improvements were possible since the Legendre series used could be determined to more terms. Calculations were performed with the older, H6(3), potential

9: Calculations on Ar_2HX Systems.

Table 43. Collected two-body results for Ar_2H/DCl – spectroscopically unobserved states.

	HHB	TWO(3)	TWO0	TWO1	TWOD0	TWO(3)–TWO0
Name	Wagging Stretch $[\epsilon = 0, \eta = 0]$ (A_1)					
Energy/cm^{-1}	$-Note2$	-298.349	-292.983	-295.825	-302.354	
$\nu_{i \leftarrow 0}$/cm^{-1}	$-Note2$	24.975	24.948	24.931	25.310	0.027
$\langle P_2(\cos\theta)\rangle$	$-Note2$	0.4334	0.4297	0.4367	0.5821	0.0036
$\langle\Delta(\theta,\phi)\rangle$	$-Note2$	0.0253	0.0280	0.0281	0.0247	-0.0027
B_x/MHz	$-Note2$	1679.05	1679.19	1680.30	1685.12	-0.14
B_y/MHz	$-Note2$	1703.12	1700.11	1682.15	1693.07	3.01
B_z/MHz	$-Note2$	831.40	830.68	826.58	830.62	0.72
Intensity$_{i \leftarrow 0}$	–	0.014	0.014	0.016	0.016	
Name	χ Bend $[\epsilon = 0, \eta = 1]$ (B_2)					
Energy/cm^{-1}	–	-296.819	-291.655	-294.924	-302.323	
$\nu_{i \leftarrow 0}$/cm^{-1}	–	26.505	26.276	25.832	25.342	0.228
$\langle P_2(\cos\theta)\rangle$	–	0.4278	0.4230	0.4264	0.5164	0.0048
$\langle\Delta(\theta,\phi)\rangle$	–	0.0296	0.0342	0.0388	0.0755	-0.0046
B_x/MHz	–	1788.68	1788.23	1787.92	1784.94	0.45
B_y/MHz	–	1613.33	1613.25	1602.79	1635.40	0.08
B_z/MHz	–	834.67	834.55	831.75	840.82	0.12
Intensity$_{i \leftarrow 0}$	–	0.175	0.237	0.432	4.883	
Name	Breathing Stretch $[\epsilon = 0, \eta = 0]$ (A_1)					
Energy/cm^{-1}	-217.784	-287.095	-281.724	-284.648	-290.678	
$\nu_{i \leftarrow 0}$/cm^{-1}	35.969	36.229	36.207	36.108	36.987	0.021
$\langle P_2(\cos\theta)\rangle$	0.3891	0.3967	0.3985	0.4004	0.5670	-0.0017
$\langle\Delta(\theta,\phi)\rangle$	0.0266	0.0275	0.0302	0.0292	0.0247	-0.0027
B_x/MHz	$-Note1$	1742.77	1742.90	1741.85	1748.88	-0.13
B_y/MHz	1670.6	1636.08	1628.88	1617.72	1606.64	7.20
B_z/MHz	846.7	834.35	832.42	829.42	827.86	1.93
Intensity$_{i \leftarrow 0}$	–	0.120	0.091	0.123	0.030	

(**TWO(3)**) and the more recent, H6(4,3,0) potential (**TWO0**) in order to quantify the effect of the two-body potential surface improvements on the dynamics, as well as allowing comparison with the **HHB** calculations. Most fundamentally, as shown in table 44, the H6(4,3,0) potential has deeper primary and secondary potential wells and higher

Table 44. Comparison of H6(3) and H6(4,3,0) ArHCl potential surfaces.

	H6(3)	H6(4,3,0)
primary well depth/cm^{-1}	174.7	176.0
secondary well depth/cm^{-1}	139.5	148.3
barrier height/cm^{-1}	67.1	71.0

rotational barrier height, as well as a more anisotropic repulsive wall.

The overall effect of the deeper, steeper-sided, potential wells is to push up the energy levels; the Σ bend rises 6.0 cm^{-1}, and the ground state by 5.4 cm^{-1}. The more precise description of the angular ArHCl potential is seen to affect the bending states most, including the χ bend, causing changes in frequencies of from 10% to 30% of the discrepancy from experiment. This underlines the importance of having a reliable two-body potential. The H6(4,3,0) potential is fitted to so many observables that I believe that, for bound-state geometries, its errors are less than 20% of the H6(3) errors; the H6(4,3,0) is reliable. Of the expectation values, the rotational constant estimates are mostly negligibly affected, although the higher rotational barrier and greater anisotropy shift B_y by up to 8 MHz in both directions. On the other hand some of the angular expectation values are rather more affected, although these tend to be those with smaller magnitudes and little information can be deduced from the changes.

The need for a reliable two-body potential in a model with full vibrational freedom has been argued for, above. These criteria are met by calculation **TWO0** such that discrepancies between the theoretical and experimental results for Ar$_2$HCl may be ascribed to one of:

1. basis-set incompleteness,

2. dynamical approximations in the form of neglected angular momentum coupling terms, or

3. the presence of a physically significant three-body potential.

Basis set incompleteness was addressed in the section on convergence, where it was noted that errors in B_x are likely to be large, and states excited in ρ will be worst converged. The

9: Calculations on Ar$_2$HX Systems.

effect of some neglected angular momentum terms in the Hamiltonian has been qualitatively discussed in the preceding paragraphs dealing with Coriolis mixing; a quantitative theoretical treatment remains to be developed. The magnitude and form of three-body effects has been addressed in a previous chapter, while the effect of these effects on the dynamics is addressed in the following section.

The difference between experiment and calculation TWO0 is tabulated, in this section, in order to assess the effect of items (1) to (3), above. Having a qualitative assessment of the effects of (1) and (2), it is possible to deduce the effect of (3). In all cases, the differences in the frequencies between a two-body potential calculation and experiment are greater by two orders of magnitude than the inferred basis-set derived errors. Coriolis coupling is likely to have a similarly small effect on the frequencies, hence the experimental frequencies provide a good test of proposed three-body effects, and indicate that these forces are highly significant by the magnitude of the discrepancies (greater than 1.3 cm^{-1}). Basis-set errors in expectation values of P_2 and Δ are also much smaller than the observed discrepancies, although the inferred three-body effects on these values are less significant than on the frequencies, particularly in the light of the neglect of some $\hat{j}_{\mathrm{HX}}$ terms in the Hamiltonian. In the cases where the theoretical values are not close to zero, and the experimental values are not very close to the ground state, expectation values of P_2 and Δ provide an important test of the angular dependence of proposed three-body effects. The rotational constant B_y is also converged to well within the observed deviations, although B_x, and to a lesser extent B_z, are less well converged due to basis-set unconvergence. Perhaps more importantly, the rotational constants are perturbed by Coriolis mixing; an estimated deperturbation of the Σ and in-plane bends changes B_z from 827 MHz to 844 MHz for the in-plane bend, and from 883 MHz to 866 MHz for the Σ bend. In both cases this effect drastically reduces the inferred three-body effect on B_z.

9.5 Ar$_2$HCl Three-body Results and Analysis.

. 1 Analysis and Results for Trial Dispersion Forces.

Table 45. Three-body Dispersion Calculations – HCl Bending Modes.

	AT	DDD	DDD†	TWO0
Name	In-plane (Π_b) Bend $[\epsilon = 0, \eta = 1]$ (B_2)			
Energy/cm^{-1}	−272.102	−272.197	−272.203	−278.741
$\nu_{i \leftarrow 0}$/cm^{-1}	39.226	38.859	38.859	39.190
$\langle P_2(\cos\theta) \rangle$	−0.0036	−0.0071	−0.0071	−0.0031
$\langle \Delta(\theta, \phi) \rangle$	0.3452	0.3469	0.3469	0.3441
B_x/MHz	1734.76	1734.76	1734.77	1744.98
B_y/MHz	1679.82	1680.14	1680.16	1686.04
B_z/MHz	845.03	845.13	845.14	849.22
Intensity$_{i \leftarrow 0}$	5.189	5.080	5.080	5.350
Name	Parallel (Σ) Bend $[\epsilon = 0, \eta = 0]$ (A_1)			
Energy/cm^{-1}	−269.129	−268.950	−268.960	−276.606
$\nu_{i \leftarrow 0}$/cm^{-1}	42.199	42.105	42.103	41.325
$\langle P_2(\cos\theta) \rangle$	0.2506	0.2468	0.2468	0.2752
$\langle \Delta(\theta, \phi) \rangle$	0.0596	0.0616	0.0616	0.0591
B_x/MHz	1741.97	1741.80	1741.84	1753.72
B_y/MHz	1761.81	1759.71	1759.75	1766.59
B_z/MHz	866.28	865.68	865.70	870.47
Intensity$_{i \leftarrow 0}$	1.0 See Note 3.			
Name	Out-of-plane (Π_c) Bend $[\epsilon = 1, \eta = 1]$ (B_1)			
Energy/cm^{-1}	−264.512	−264.444	−264.451	−271.389
$\nu_{i \leftarrow 0}$/cm^{-1}	46.816	46.612	46.611	46.542
$\langle P_2(\cos\theta) \rangle$	−0.0227	−0.0250	−0.0250	−0.0224
$\langle \Delta(\theta, \phi) \rangle$	−0.3201	−0.3201	−0.3201	−0.3197
B_x/MHz	1740.01	1739.83	1739.84	1749.94
B_y/MHz	1697.36	1697.40	1697.43	1705.52
B_z/MHz	851.57	851.54	851.55	856.21
Intensity$_{i \leftarrow 0}$	4.733	4.615	4.615	4.942

From the results in tables 45 and 46, it is clear that the use of an Axilrod-Teller triple-dipole term (**AT**) is generally not a good approximation to the real triple-dipole term which takes into account the anisotropic polarisability of the HCl (**DDD**). To be more precise, there is a division of suitability of such an approximation between HCl

9: Calculations on Ar$_2$HX Systems.

Table 46. Three-body Dispersion Calculations – Triatom-like Modes.

	AT	DDD	DDD†	TWO0
Name	Ground State $[\epsilon = 0, \eta = 0]$ (A_1)			
Energy/cm^{-1}	−311.328	−311.056	−311.062	−317.931
$\langle P_2(\cos\theta)\rangle$	0.4443	0.4412	0.4412	0.4429
$\langle\Delta(\theta,\phi)\rangle$	0.0252	0.0260	0.0261	0.0255
B_x/MHz	1747.88	1747.43	1747.44	1756.99
B_y/MHz	1662.02	1661.96	1661.98	1668.24
B_z/MHz	844.83	844.70	844.71	848.73
Name	Wagging Stretch $[\epsilon = 0, \eta = 0]$ (A_1)			
Energy/cm^{-1}	−286.919	−286.673	−286.679	−292.983
$\nu_{i\leftarrow 0}$/cm^{-1}	24.409	24.383	24.383	24.948
$\langle P_2(\cos\theta)\rangle$	0.4311	0.4281	0.4281	0.4297
$\langle\Delta(\theta,\phi)\rangle$	0.0278	0.0287	0.0287	0.0280
B_x/MHz	1674.19	1674.03	1674.03	1679.19
B_y/MHz	1692.69	1692.54	1692.56	1700.11
B_z/MHz	827.48	827.39	827.40	830.68
Intensity$_{i\leftarrow 0}$	0.011	0.011	0.011	0.014
Name	χ Bend $[\epsilon = 0, \eta = 1]$ (B_2)			
Energy/cm^{-1}	−285.530	−285.298	−285.303	−291.655
$\nu_{i\leftarrow 0}$/cm^{-1}	25.798	25.758	25.759	26.276
$\langle P_2(\cos\theta)\rangle$	0.4263	0.4229	0.4229	0.4230
$\langle\Delta(\theta,\phi)\rangle$	0.0315	0.0327	0.0327	0.0342
B_x/MHz	1780.52	1780.13	1780.14	1788.23
B_y/MHz	1604.24	1604.38	1604.40	1613.25
B_z/MHz	830.16	830.10	830.11	834.55
Intensity$_{i\leftarrow 0}$	0.174	0.178	0.178	0.237
Name	Breathing Stretch $[\epsilon = 0, \eta = 0]$ (A_1)			
Energy/cm^{--1}	−275.461	−275.238	−275.245	−281.724
$\nu_{i\leftarrow 0}$/cm^{-1}	35.867	35.818	35.818	36.207
$\langle P_2(\cos\theta)\rangle$	0.4091	0.4048	0.4048	0.3985
$\langle\Delta(\theta,\phi)\rangle$	0.0273	0.0287	0.0287	0.0302
B_x/MHz	1736.81	1736.35	1736.36	1742.90
B_y/MHz	1612.65	1613.39	1613.43	1628.88
B_z/MHz	826.49	826.59	826.60	832.42
Intensity$_{i\leftarrow 0}$	0.045	0.049	0.049	0.091

9: Calculations on Ar_2HX Systems.

bending modes and the triatom-like modes and also between $\langle P_2(\cos\theta)\rangle$, $\langle\Delta(\theta,\phi)\rangle$ and the other observable quantities.

In all cases the values of $\langle P_2(\cos\theta)\rangle$ and $\langle\Delta(\theta,\phi)\rangle$ in **AT** are poor indicators of effect: the error, compared to **DDD**, is of the same order as the anisotropic triple-dipole effect. This is to be expected since it is precisely the θ dependence which is lacking in the Axilrod-Teller term. It is significant to note that even without any θ dependence in the Axilrod-Teller potential, some modes in calculation **AT** display changes in $\langle P_2(\cos\theta)\rangle$ and $\langle\Delta(\theta,\phi)\rangle$, relative to the two-body calculation, of larger magnitude than calculation **DDD**. This must be due to the repulsive nature of the potential causing a slightly different part of the two-body surface to be sampled.

The reliability of the other observable quantities depends on the mode in question. In calculation **AT** the ground state and the triatom-like modes (modes where the structure of the HCl is not dynamically significant) are much closer to **DDD** than the modes which have HCl bending character. This is to be expected since the bending modes will sample much more of the anisotropy of the potential. It is found that the triatom-like modes have values of $\nu_{i\leftarrow 0}$ in error by an order of magnitude less than the effect, while the error is the same order as the effect in the HCl bending modes; the anisotropic triple-dipole should be used in predicting frequencies. The rotational constant predictions show much less sensitivity to the anisotropy of the triple-dipole term; they are principally affected by the overall repulsive nature of the potential and display introduced errors of only a few percent upon using the Axilrod-Teller approximation, and show less distinction between mode types.

In conclusion, the Axilrod-Teller term is not good enough as an approximation to the anisotropic triple-dipole dispersion; only the rotational constants are adequately predicted. As the order of the multipole moments of the dispersion interaction increases, the form of the anisotropic term becomes very complicated and such terms would have to be very important to merit the full form. Higher-order dispersion terms could probably be usefully modelled using atomic forms. The smaller magnitude, and the more complicated angular dependence, of effects of higher-order than the triple-dipole both support use of isotropic terms; a complicated angular dependence is likely to have a near-isotropic effect,

9: Calculations on Ar$_2$HX Systems.

when averaged over vibrations. Currently, it is not thought worthwhile to calculate the effect of such terms at all since so little is known about the three-body potential.

The effect of my trial damping term may be evaluated by comparing the results of calculations **DDD** and **DDD†**. These results show that this damping term is of negligible effect. Certainly, the effect of this damping term is much less than the convergence of the calculation and mostly smaller than the accuracy of experiment. I do not believe that the term I used for damping is more than an order of magnitude inadequate and so conclude that damping of three-body dispersion is not important.

The comment, made above, on the shifts in $\langle P_2(\cos\theta)\rangle$ and $\langle \Delta(\theta,\phi)\rangle$ following addition of the Axilrod-Teller potential (no (θ,ϕ) dependence) suggests further analysis of the effect. If the (θ,ϕ) dependence of the anisotropic triple-dipole term is examined, there is seen to be less repulsion for geometries with $\theta = \pi/2$ and also for $\phi = 0,\pi$. From this, one would naively expect $\langle P_2(\cos\theta)\rangle$ to be more negative and $\langle \Delta(\theta,\phi)\rangle$ to be more positive upon inclusion of the anisotropic dispersion. If the results of calculation **DDD** are examined, this is seen to be largely the case, but prominent discrepancies can be seen in the χ bend, the breathing stretch and the out-of-plane bend. The perturbations in the angular expectation values in calculations **AT** and **DDD** are shown in table 47. If the results of calculation **AT** are now examined and the shifts in these angular expectation values taken to be the second-order effect of the purely repulsive nature of the triple-dipole, acting through the radial-angular coupling in the two-body potential, we may assume first-order perturbation theory and subtract this effect from the perturbations due to the anisotropic dispersion in order to obtain the effect of the angular dependence in the anisotropic dispersion. From table 47 it is seen that the result of this subtraction is changes in $\langle P_2 \rangle$ and $\langle \Delta \rangle$ as predicted from the angular form of the anisotropic potential and remarkably constant across the different modes; the out-of-plane bend is an exception since the fractional change in $V(\phi)$ is smaller than for the other modes, over the range of the wavefunction.

The separation of the effect on $\langle P_2(\cos\theta)\rangle$ and $\langle \Delta(\theta,\phi)\rangle$ due to isotropic repulsion and angular shape was quite successful, and suggests a general method of analysis. However, a similar analysis of the results presented below for different three-body potential

Table 47. Perturbations in the Angular Expectation Values due to Inclusion of an Axilrod-Teller (isotropic) and Anisotropic Triple Dipole terms, and the Difference in the Perturbations.

	Isotropic	Anisotropic	Difference
Ground State			
$\langle P_2(\cos\theta)\rangle$	0.0014	−0.0017	−0.0031
$\langle \Delta(\theta,\phi)\rangle$	−0.0003	0.0006	0.0009
Wagging Stretch			
$\langle P_2(\cos\theta)\rangle$	0.0013	−0.0017	−0.0030
$\langle \Delta(\theta,\phi)\rangle$	−0.0002	0.0007	0.0009
χ Bend			
$\langle P_2(\cos\theta)\rangle$	0.0034	0.0000	−0.0033
$\langle \Delta(\theta,\phi)\rangle$	−0.0027	−0.0016	0.0011
Breathing Stretch			
$\langle P_2(\cos\theta)\rangle$	0.0107	0.0064	−0.0043
$\langle \Delta(\theta,\phi)\rangle$	−0.0029	−0.0015	0.0014
In-plane (Π_b) Bend			
$\langle P_2(\cos\theta)\rangle$	−0.0005	−0.0040	−0.0035
$\langle \Delta(\theta,\phi)\rangle$	0.0011	0.0028	0.0017
Parallel (Σ) Bend			
$\langle P_2(\cos\theta)\rangle$	−0.0247	−0.0285	−0.0038
$\langle \Delta(\theta,\phi)\rangle$	0.0004	0.0024	0.0020
Out-of-plane (Π_c) Bend			
$\langle P_2(\cos\theta)\rangle$	−0.0003	−0.0026	−0.0023
$\langle \Delta(\theta,\phi)\rangle$	−0.0004	−0.0004	0.0000

terms fails. I suggest that this is due to the existence of a mixture of attractive and repulsive zones as θ varies, resulting in a failure of an isotropic average to be an accurate predictor of the effect; even using the rotational constants to indicate the isotropic average, and thus to guide predictions in shift due to radial-angular coupling in the two-body potential, fails.

9.5. 2 Analysis and Results for the Model # 1 Three-body Potential.

9: Calculations on Ar$_2$HX Systems.

The changes in the various calculated quantities on the addition of various three-body potentials are given in tables 48 and 49, denoted $P_\dagger$, where the subscript $\dagger$ represents a calculation code-name. ΣP is the result of summing the four perturbations due to calculations **Idd** (the interaction of dipoles induced on the argon atoms), **DDD†** (the damped anisotropic triple-dipole), **JAN** (the exchange-overlap equations of Jansen) and **iQdq** (the overlap-quadrupole interacting with HCl multipoles). The tables of perturbations show the relative importance of the various model contributions to the three-body potential quite clearly; comparison with spectroscopic data is made later.

Table 48. Three-body Perturbations – HCl Bending Modes.

	P_{Idd}	$P_{\text{DDD†}}$	P_{JAN}	P_{iQdq}	P_{MOD1}	ΣP
In-plane (Π_b) Bend [$\epsilon = 0, \eta = 1$] (B_2)						
$\nu_{i \leftarrow 0}/\text{cm}^{-1}$	−0.636	−0.331	0.047	−3.114	−3.785	−4.033
$\langle P_2(\cos\theta) \rangle$	−0.0045	−0.0040	−0.0012	−0.0316	−0.0318	−0.0414
$\langle \Delta(\theta,\phi) \rangle$	0.0016	0.0028	−0.0001	0.0132	0.0135	0.0175
B_x/MHz	−0.27	−10.21	2.29	−1.58	−9.74	−9.77
B_y/MHz	−0.35	−5.88	0.93	2.83	−3.87	−2.47
B_z/MHz	−0.14	−4.08	0.77	0.42	−3.40	−3.02
Parallel (Σ) Bend [$\epsilon = 0, \eta = 0$] (A_1)						
$\nu_{i \leftarrow 0}/\text{cm}^{-1}$	−0.504	0.777	0.015	−2.660	−2.414	−2.372
$\langle P_2(\cos\theta) \rangle$	0.0056	−0.0284	−0.0010	0.0525	0.0167	0.0288
$\langle \Delta(\theta,\phi) \rangle$	−0.0024	0.0024	−0.0011	−0.0106	−0.0026	−0.0117
B_x/MHz	−0.06	−11.87	2.76	−4.10	−10.65	−13.27
B_y/MHz	−4.28	−6.85	1.04	−60.25	−48.39	−70.33
B_z/MHz	−1.19	−4.77	0.95	−17.10	−15.63	−22.11
Out-of-plane (Π_c) Bend [$\epsilon = 1, \eta = 1$] (B_1)						
$\nu_{i \leftarrow 0}/\text{cm}^{-1}$	−0.418	0.069	−0.001	−2.370	−2.574	−2.720
$\langle P_2(\cos\theta) \rangle$	−0.0044	−0.0026	−0.0005	−0.0273	−0.0301	−0.0349
$\langle \Delta(\theta,\phi) \rangle$	−0.0011	−0.0004	−0.0007	−0.0053	−0.0048	−0.0076
B_x/MHz	−0.56	−10.10	2.32	−5.18	−13.50	−13.51
B_y/MHz	−0.09	−8.09	1.45	1.84	−4.98	−4.90
B_z/MHz	−0.17	−4.67	0.94	−0.85	−4.77	−4.75

It is clear that the larger effects are observed for addition of either the dispersion

Table 49. Three-body Perturbations – Triatom-like Modes.

Ground State Energy	–317.222	–311.062	–318.559	–314.484	–307.713	–317.931
	P_{ldd}	$P_{\mathrm{DDD}\dagger}$	P_{JAN}	P_{iQdq}	P_{MOD1}	ΣP
Ground State $[\epsilon = 0, \eta = 0]$ (A_1)						
$\langle P_2(\cos\theta) \rangle$	–0.0066	–0.0017	0.0000	–0.0303	–0.0375	–0.0387
$\langle \Delta(\theta, \phi) \rangle$	0.0011	0.0006	–0.0008	0.0055	0.0085	0.0064
B_x/MHz	–1.35	–9.55	2.00	–16.30	–24.84	–25.20
B_y/MHz	–0.16	–6.26	1.42	2.64	–2.35	–2.36
B_z/MHz	–0.38	–4.01	0.84	–3.33	–6.80	–6.88
Wagging Stretch $[\epsilon = 0, \eta = 0]$ (A_1)						
$\nu_{i \leftarrow 0}/\mathrm{cm}^{-1}$	–0.083	–0.565	0.055	–0.557	–1.086	–1.150
$\langle P_2(\cos\theta) \rangle$	–0.0068	–0.0017	–0.0003	–0.0249	–0.0314	–0.0336
$\langle \Delta(\theta, \phi) \rangle$	0.0011	0.0007	–0.0006	0.0041	0.0069	0.0054
B_x/MHz	–0.68	–5.16	1.04	–8.04	–11.49	–12.83
B_y/MHz	–0.30	–7.55	1.58	–0.29	–7.04	–6.56
B_z/MHz	–0.27	–3.28	0.65	–2.25	–4.89	–5.15
χ Bend $[\epsilon = 0, \eta = 1]$ (B_2)						
$\nu_{i \leftarrow 0}/\mathrm{cm}^{-1}$	–0.087	–0.517	–0.004	–0.437	–1.100	–1.047
$\langle P_2(\cos\theta) \rangle$	–0.0073	0.0000	–0.0008	–0.0337	–0.0412	–0.0419
$\langle \Delta(\theta, \phi) \rangle$	0.0014	–0.0016	–0.0006	0.0084	0.0115	0.0076
B_x/MHz	–1.24	–8.09	1.90	–14.29	–21.17	–21.72
B_y/MHz	0.13	–8.85	1.94	3.24	–2.18	–3.54
B_z/MHz	–0.26	–4.43	0.96	–2.51	–5.73	–6.26
Breathing Stretch $[\epsilon = 0, \eta = 0]$ (A_1)						
$\nu_{i \leftarrow 0}/\mathrm{cm}^{-1}$	–0.152	–0.390	0.002	–1.370	–1.527	–1.909
$\langle P_2(\cos\theta) \rangle$	–0.0120	0.0064	–0.0011	–0.0964	–0.0806	–0.1032
$\langle \Delta(\theta, \phi) \rangle$	0.0013	–0.0015	–0.0016	0.0220	0.0190	0.0202
B_x/MHz	–1.21	–6.55	1.85	–6.43	–14.84	–12.34
B_y/MHz	4.20	–15.45	1.72	58.94	28.32	49.40
B_z/MHz	0.86	–5.82	0.90	14.43	4.20	10.36

term (DDD†) or the overlap-induced quadrupole term (iQdq). In all cases the greater

θ, ϕ dependence of the overlap-induced quadrupole interacting with the HCl dipole and

quadrupole causes the greatest effect on $\langle P_2(\cos\theta) \rangle$ and $\langle \Delta(\theta, \phi) \rangle$ to arise in calculation

9: Calculations on Ar$_2$HX Systems.

iQdq. In general there appears to be slightly more effect on the rotational constants in calculation **DDD†**, indicating a largely repulsive effect in both calculations **DDD†** and **iQdq**. It is noticeable that for the HCl bending modes a greater perturbation of B_x is seen in calculation **DDD†**: but **iQdq** for the other modes. Since B_x is controlled by the moment of inertia of the Ar_2 fragment, the results of **iQdq** should be interpreted as showing that it is the exponential dependence of the overlap-induced quadrupole on Ar–Ar separation which is in control, rather than the R^{-n} multipole interaction; the smaller effect of the overlap-quadrupole in the bending modes arises since the bending samples attractive as well as repulsive regions.

The large change in B_y for the parallel bend is noteworthy; this is presumably due the the secondary potential minimum being at smaller R.

An assessment of the degree to which first-order perturbation theory holds for the expectation values, where the perturbation is a given model three-body component, can be made by comparing ΣP and P_{MOD1}. If the first-order régime was applicable then $\Sigma P = P_{\text{MOD1}}$; failure will be due either to the potential perturbation being too large (i. e. large enough to change the character of the wavefunction) or to interaction of states. In practice first-order perturbation theory is seen to provide quite a good description, although insufficient for giving precise results. The inadequacy of first-order perturbation theory is probably largely attributable to the potential terms being too large; frequencies are changing by $\sim 10\%$. For the breathing stretch and the parallel bend I believe there to be breakdown due to coupling of these two states, since $\Sigma P - P_{\text{MOD1}}$ is substantially larger for these two states. Addition of $\Sigma P - P_{\text{MOD1}}$ for the two states for each expectation value gives a result close to zero, consistent with an interaction of these states (which are only 5 cm^{-1} apart). After taking mixing into account, the remaining discrepancies are well within the range of differences for the non-interacting states.

. 3 Comparison of Experiment and Three-body Calculations.

Calculations (**MOD1**) were performed using the Model # 1 potential, which has parameters chosen to match the model to *ab-initio* results, as described in the chapter on three-body potentials. These results are compared (table 50) to the two-body calculation,

experiment, and an alternative three-body model (Model # 2), which is discussed below.

It is apparent that the Model # 1 potential changes the frequencies in the correct direction, but over-corrects the discrepancy between two-body calculations and experiment. The frequencies are probably the most important single test of a model, but the expectation values provide important additional information. In particular, all of the expectation values for the ground state agree quite well with experiment, although the effect of three-body forces is more significant on the rotational constants: but is rather indeterminate on the P_2 and Δ expectation values.

For the in-plane bend, while the value of $\langle P_2 \rangle$ is rather too small to draw many conclusions, the value of $\langle \Delta \rangle$ should be well defined both experimentally and theoretically. The effect of the three-body potential on $\langle \Delta \rangle$ is in the wrong direction, however, and an inspection of the perturbations due to the independent contributions does not suggest that there is under-representation of any term causing this discrepancy; the angular dependence of one or more terms in the three-body model must be deficient, although not seriously. The B_x rotational constant is seen to be a great deal different to experiment. As explained in the section on convergence, the basis-set in ρ is rather small, and tailored to a two-body potential, so that perturbations to a ground-state character ρ-motion are poorly modelled. In addition, neglected $\hat{j}_{Ar}\hat{j}_{HX}$ terms might be important, acting through the $\tan^2 \chi$ term in the expression for B_x. I do not consider B_x to be a good indicator of the accuracy of three-body forces, therefore. B_y, on the other hand, is quite close to experiment with a two-body potential, and changes little on addition of three-body components. The Coriolis mixing of the in-plane and parallel bend, through the $\hat{J}_z$ operator, has already been discussed; this has the effect of mixing the B_z so that the sum of the perturbation for both modes should be compared with the sum of the deviations of the two-body calculation from experiment. Such a comparison shows an over-estimate of three-body effect.

The parallel bend shows rather good agreement between calculation MOD1 and experiment, excepting B_x, as before, although here the effect is probably less, due to smaller $\hat{j}_{Ar}\hat{j}_{HX}$ coupling terms.

The out-of-plane bend suffers from Coriolis mixing such that B_x and B_y are unre-

Table 50. Ar_2HCl Model Three-body Results Compared With Experimental Data.

	Expt	MOD1	MOD2	MOD1—TWO0	MOD2–TWO0	Expt–TWO0
Name	Ground State $[\epsilon = 0, \eta = 0]$ (A_1)					
Energy/cm^{-1}	–	–307.713	–308.976			
$\langle P_2(\cos\theta)\rangle$	0.4165	0.4054	0.4170	–0.0375	–0.0259	–0.0264
$\langle \Delta(\theta,\phi)\rangle$	0.0313	0.0340	0.0314	0.0085	0.0059	0.0058
B_x/MHz	1733.86	1732.15	1737.62	–24.84	–19.37	–23.13
B_y/MHz	1667.92	1665.89	1665.26	–2.35	–2.98	–0.32
B_z/MHz	844.45	841.93	843.12	–6.80	–5.61	–4.28
Name	In-plane (Π_b) Bend $[\epsilon = 0, \eta = 1]$ (B_2)					
Energy/cm^{-1}	–	–272.309	–272.471			
$\nu_{i \leftarrow 0}$/cm^{-1}	37.196	35.405	36.505	–3.785	–2.685	–1.994
$\langle P_2(\cos\theta)\rangle$	–0.001	–0.0348	–0.0256	–0.0318	–0.0225	0.002
$\langle \Delta(\theta,\phi)\rangle$	0.340	0.3576	0.3540	0.0135	0.0099	–0.004
B_x/MHz	1683.61	1735.24	1735.92	–9.74	–9.06	–61.37
B_y/MHz	1682.42	1682.17	1681.92	–3.87	–4.12	–3.62
B_z/MHz	826.70	845.82	845.90	–3.40	–3.32	–22.52
Intensity$_{i \leftarrow 0}$	>3	5.178	4.904			
Name	Parallel (Σ) Bend $[\epsilon = 0, \eta = 0]$ (A_1)					
Energy/cm^{-1}	–	–268.803	–269.152			
$\nu_{i \leftarrow 0}$/cm^{-1}	39.555	38.911	39.824	–2.414	–1.501	–1.770
$\langle P_2(\cos\theta)\rangle$	0.291	0.2919	0.2717	0.0167	–0.0036	0.016
$\langle \Delta(\theta,\phi)\rangle$	0.062	0.0565	0.0594	–0.0026	0.0002	0.003
B_x/MHz	1730.70	1743.07	1745.03	–10.65	–8.68	–23.02
B_y/MHz	1720.89	1718.20	1739.02	–48.39	–27.58	–45.70
B_z/MHz	883.04	854.84	860.89	–15.63	–9.59	12.57
Intensity$_{i \leftarrow 0}$	1.0 See Note 3.					
Name	Out-of-plane (Π_c) Bend $[\epsilon = 1, \eta = 1]$ (B_1)					
Energy/cm^{-1}	–	–263.745	–264.161			
$\nu_{i \leftarrow 0}$/cm^{-1}	45.203	43.968	44.814	–2.574	–1.728	–1.339
$\langle P_2(\cos\theta)\rangle$	–0.025	–0.0525	–0.0431	–0.0301	–0.0207	–0.003
$\langle \Delta(\theta,\phi)\rangle$	–0.295	–0.3245	–0.3231	–0.0048	–0.0033	0.025
B_x/MHz	1774.	1736.44	1738.40	–13.50	–11.54	24.5
B_y/MHz	1752.	1700.54	1700.20	–4.98	–5.32	46.5
B_z/MHz	854.6	851.44	851.85	–4.77	–4.36	–1.6
Intensity$_{i \leftarrow 0}$	>3	4.625	4.394			

9: Calculations on Ar_2HX Systems.

liable indicators. Again $\langle P_2 \rangle$ is rather too small to draw many conclusions and, like the in-plane-bend, $\langle \Delta \rangle$ shifts the wrong way by a small degree.

In conclusion, it is clear that the Model # 1 three-body potential is an over-estimate of three-body effects (manifested through the frequency errors) as well as containing some imprecision of angular form (manifested through contrary shifts of the expectation values). An examination of the perturbations due to individual components of the Model # 1 three-body potential suggests that reducing the overlap-quadrupole will reduce the experiment-theory discrepancies. Since $\widetilde{V}_{\text{Jansen}}$, $V_{\Theta-\text{def}\mu}$, $V_{\Theta-\text{def}\Theta}$ and V_{dd} were summed and then matched to the *ab-initio* data, it is not sensible to tamper with one component alone. Instead I choose to generate an alternative model (Model # 2) by retaining the match with the *ab-initio* data as far as possible by keeping V_{DDD} and V_{dd} the same, choosing the Ar_3 parameters for $\widetilde{V}_{\text{Jansen}}$ (Ar_3 and Ar_2HCl are isoelectronic) and adjusting the value of $\beta_{\Theta-\text{def}}$ to fit the potential, concentrating on the region of the potential minimum.

The Model # 2 potential is identical to the Model # 1 potential advanced in the chapter on the physics of three-body forces, except: $\beta_{\Theta-\text{def}} = 1.000\text{Å}^{-1}$, $\beta_{\text{Jansen}} = 1.31\text{Å}^{-1}$, $S_{\text{Jansen}} = 7.5 \times 10^5 \text{cm}^{-1}\text{Å}$ and $\delta_{\text{Jansen}} = 0.15\text{Å}$. As before, the sum $V_{\text{Jansen}} + V_{\Theta-\text{def}\mu} + V_{\Theta-\text{def}\Theta} + V_{dd}$ correlates with the sum $\Delta E^{\text{SCF}} + \Delta E^{(2)}$. It is found that at close range Model #2 significantly under-estimates the *ab-initio* data; the breakdown of Model #2 appears in table 51, with a comparison with the unpublished results of Chałasiński *et al.* [79]. The close-range breakdown is not very surprising; the SCF results presented in the chapter on three-body potentials show that the simple induced-quadrupole model is poor at short range. This is not a problem in the calculations of single-quantum modes which I present here, since the poorly modelled region is hardly sampled by the wavefunctions.

Having advanced an alternative model for the Ar_2HCl three-body potential, it can be tested against experiment by examining the results of calculation **MOD2**. Applying the same analysis as was used for the **MOD1** results it can be seen that the Model #2 performs much better on the comparison of frequencies, and generally better for the expectation values; only the value of B_y for the parallel bend gets worse. In view of

9: Calculations on Ar_2HX Systems.

Table 51. Breakdown of Non-dispersive Contributions to the Revised Model Three-body Potential for Ar_2HCl ($\cos\chi = 0$, $\phi = 0$).

$R/\text{Å}$	$\rho/\text{Å}$	$\cos\theta$	V_{Jansen}	$V_{\Theta-\text{def}\mu}$	$V_{\Theta-\text{def}\Theta}$	V_{dd}	$\Sigma^{(\text{model})}$	$\Delta E^{\text{SCF}} + \Delta E^{(2)}$
3.640	3.175	1.0	−7.224	7.414	12.840	3.847	16.877	28.83
3.605	3.332	1.0	−3.596	5.079	8.882	3.294	13.658	20.04
3.472	3.861	1.0	−0.543	1.179	2.140	1.996	4.771	5.39
3.290	4.458	1.0	−0.260	0.163	0.312	1.150	1.364	1.44
3.083	5.021	1.0	−0.154	0.019	0.038	0.672	0.575	0.71
2.795	5.664	1.0	−0.057	0.001	0.003	0.342	0.289	0.42
2.869	5.664	−1.0	−0.016	−0.001	0.002	0.020	0.006	0.12
3.157	5.021	−1.0	−0.026	−0.017	0.034	0.019	0.009	0.21
3.546	3.861	−1.0	−0.169	−1.083	1.926	0.022	0.695	0.59
3.5009	3.861	0.984808	−0.479	1.123	1.945	1.687	4.275	4.80
3.5009	3.861	0.939693	−0.466	1.071	1.633	1.124	3.361	3.26
3.5009	3.861	0.866025	−0.446	0.987	1.155	0.468	2.164	1.47
3.5009	3.861	0.766044	−0.420	0.873	0.569	−0.048	0.974	0.00
3.5009	3.861	0.642788	−0.392	0.733	−0.055	−0.314	−0.027	−0.94

the greater difference between the value of $\beta_{\Theta-\text{def}}$ derived from SCF calculations of the overlap-quadrupole and the Model # 2 value, and of the obvious importance of this term in the three-body interactions, it is likely that a more refined description of the overlap field is required, possibly combined with a consideration of the HCl multipoles up to hexadecapole.

Calculations on the currently unobserved triplet of triatom-like modes are listed for reference in table 52; the χ bend is probably experimentally observable and would probably assist in understanding possible Coriolis mixing of double quantum states with the out-of-plane bend. Inclusion of either the Model # 1 or # 2 three-body terms gives a large increase in the predicted intensity of the breathing mode; this does not reflect a reduction in the intensity of the parallel bend, which it is measured relative to, since the χ bend and wagging stretch are little changed. The increase in breathing mode intensity is most likely due to increased mixing between it and the parallel bend, which was noted in a previous section; the energy difference of these two states, after mixing, decreases

9: Calculations on Ar_2HX Systems.

Table 52. Ar_2HCl Model Three-body Results for Which No Experimental Data Exists.

	MOD1	MOD2	MOD1-TWO0	MOD2-TWO0
Name	Wagging Stretch $[\epsilon = 0, \eta = 0]$ (A_1)			
Energy/cm^{-1}	-283.851	-284.941		
$\nu_{i \leftarrow 0}$/cm^{-1}	23.862	24.035	-1.086	-0.913
$\langle P_2(\cos\theta) \rangle$	0.3983	0.4083	-0.0314	-0.0215
$\langle \Delta(\theta, \phi) \rangle$	0.0349	0.0327	0.0069	0.0047
B_x/MHz	1667.70	1669.96	-11.49	-9.23
B_y/MHz	1693.07	1693.65	-7.04	-6.45
B_z/MHz	825.79	826.53	-4.89	-4.15
Intensity$_{i \leftarrow 0}$	0.008	0.008		
Name	χ Bend $[\epsilon = 0, \eta = 1]$ (B_2)			
Energy/cm^{-1}	-282.537	-283.623		
$\nu_{i \leftarrow 0}$/cm^{-1}	25.176	25.353	-1.100	-0.923
$\langle P_2(\cos\theta) \rangle$	0.3818	0.3957	-0.0412	-0.0273
$\langle \Delta(\theta, \phi) \rangle$	0.0458	0.0411	0.0115	0.0069
B_x/MHz	1767.06	1771.72	-21.17	-16.51
B_y/MHz	1611.07	1609.62	-2.18	-3.62
B_z/MHz	828.82	829.51	-5.73	-5.04
Intensity$_{i \leftarrow 0}$	0.315	0.251		
Name	Breathing Stretch $[\epsilon = 0, \eta = 0]$ (A_1)			
Energy/cm^{-1}	-273.033	-273.818		
$\nu_{i \leftarrow 0}$/cm^{-1}	34.681	35.157	-1.527	-1.050
$\langle P_2(\cos\theta) \rangle$	0.3178	0.3530	-0.0806	-0.0455
$\langle \Delta(\theta, \phi) \rangle$	0.0492	0.0404	0.0190	0.0102
B_x/MHz	1728.06	1730.23	-14.84	-12.68
B_y/MHz	1657.20	1637.49	28.32	8.62
B_z/MHz	836.61	831.75	4.20	-0.67
Intensity$_{i \leftarrow 0}$	0.378	0.193		

upon addition of either three-body model.

9: *Calculations on Ar$_2$HX Systems.*

9.6 Preliminary calculations on Ar_2HF.

Using the same method as for Ar_2HCl, calculations were performed on Ar_2HF with the HF in $v = 0$ (denoted **TWOF0**) and $v = 1$ (denoted **TWOF1**).

The basis set was generated using the same procedure as for calculation **TWO0**, using the H6(4,3,2) and HFD-C potentials for Ar_2HF for the determination of Υ and Φ as well as in the Hamiltonian. No convergence testing was performed, so these are preliminary calculations. The only differences between the basis specification for **TWO0** and **TWOF0**, or **TWOF1**, are that the potential used to generate Υ and Φ was the $v = 0$ surface and the DGB centres were evenly spaced on the range (2.200Å,4.200Å). The DGB range was chosen on the basis of an inspection of the potential.

The results appear in tables 53 and 54, with a selection of wavefunction plots provided in appendix F. Despite the larger rotational constant of HF, compared with HCl, the potential energy is more anisotropic in θ. This results in rather similar amplitude of θ motion. The smaller size of the HF is apparent from a noticeably larger amplitude in $\cos\chi$ motion. Plots of the χ bend on a $\cos\theta$ vs. $\cos\chi$ cut, to be found in appendices E and F illustrate these two points. The similarity of the anisotropy/rotational constant ratio between the HF and HCl cases is apparent in the spread of wavefunctions in ϕ also; a similar pattern in the expectation values $\langle P_2 \rangle$ and $\langle \Delta \rangle$ is also seen in both Ar_2HCl and Ar_2HF. The greater anisotropy of potential energy with θ is, perhaps also, the reason for the much greater observed couping of χ and θ motions in the in-plane bend.

Table 53. Preliminary results for Ar_2HF for $v = 0, 1$ - ground state and HF bending states.

Name	TWOF0	TWOF1	TWOF0	TWOF0	TWOF1
	Ground State		In-plane (Π_b) Bend	Out-of-plane (Π_c) Bend	
Energy/cm^{-1}	−284.592	−298.809	-220.498	−199.373	−206.206
$\nu_{i\leftarrow 0}$/cm^{-1}			64.093	85.218	92.603
$\langle P_2(\cos\theta)\rangle$	0.3771	0.4078	-0.0253	−0.0955	−0.0764
$\langle \Delta(\theta,\phi)\rangle$	0.0520	0.0556	0.3530	−0.3379	−0.3271
B_x/MHz	1786.25	1790.75	1761.25	1770.80	1771.77
B_y/MHz	3575.17	3574.52	3604.67	3525.65	3526.66
B_z/MHz	1172.65	1174.99	1161.41	1158.44	1159.32

Table 54. Preliminary results for Ar_2HF for $v = 0, 1$ - triatom-like modes.

	TWOF0	TWOF1	TWOF0	TWOF0
Name	Breathing	Stretch	Wagging Stretch	χ Bend
Energy/cm^{-1}	−242.830	−255.693	−256.666	−253.690
$\nu_{i\leftarrow 0}$/cm^{-1}	41.761	43.116	27.926	30.902
$\langle P_2(\cos\theta)\rangle$	0.3451	0.3769	0.3654	0.3507
$\langle\Delta(\theta,\phi)\rangle$	0.0524	0.0561	0.0555	0.0563
B_x/MHz	1806.71	1811.35	1738.99	1852.17
B_y/MHz	3336.10	3340.58	3637.33	3328.68
B_z/MHz	1139.51	1141.99	1148.87	1145.75

Some experimental data for Ar_2HF is already available, and some spectra for $v = 1$ have been obtained, but not assigned. Microwave spectroscopy was used by the Gutowsky group [22] to characterise the ground state. The values they obtained values for the rotational constants, $A \equiv B_y = 3576.51$ MHz, $B \equiv B_x = 1739.14$ MHz and $C \equiv B_z = 1161.05$ MHz, support the theoretical values; the errors are similar to the Ar_2HCl two-body case.

The HF vibrational red-shift in Ar_nHCl has also been studied [26] For Ar_2HF they observe a red-shift of 14.827 cm^{-1}, which compares favourably with the theoretical value of 14.22 cm^{-1}.

The calculated values given here, despite their preliminary nature, provide a base upon which assignment of spectra can be approached. The parallel bend for HF in $v = 0$ and $v = 1$ is very close to at least one other state of the same symmetry, and is believed to lie at about −216 cm^{-1} for $v = 1$. Computational difficulties, arising from a method of finding eigensolutions based on iterations from an initial energy guess, have hindered calculations on both the parallel and ip-plane bends. The large energies of the HF bending states, compared to Ar_2HCl, is likely to cause greater unaccounted-for mixing due to a greater density of states.

10: Conclusions.

An account of an efficient method for calculating the lower bound states of van der Waals trimers, with up to five degrees of freedom, has been described in the preceding chapters. This method has been successfully applied to Ar_3 and Ar_2HCl in a study of some two- and three-body potential functions and some new information has been produced. The main conclusions were:

- The most important three-body effects in atom-atom-diatom systems can be cast in four physically-based mathematical forms. The four terms described arose from:

  1. dispersion effects consisting of triple-dipole and higher order terms,

  2. the interaction between dipoles induced on the argon atoms by HX permanent multipoles,

  3. orbital deformation due to exchange and overlap repulsion,

  and

  4. the interaction of HX permanent multipoles with the electrostatic field which results from the overlap effects of the two argon atoms.

- A damped sum of triple-dipole and dipole-dipole-quadrupole dispersion terms, using established coefficients, reproduced *ab-initio* calculations of three-body dispersion in Ar_3. The model proposed for the three-body exchange and overlap effects (Jansen) in Ar_3 adequately reproduced *ab-initio* calculations, although exhibited some differences, especially for non-equilateral geometries. The coefficients used were somewhat different to those previously suggested, however.

- The calculated far infrared dipole of Ar_3, approximately $7 \times 10^{-5}D$, is believed to be too small to be observed using current far infra-red spectroscopic methods.

- Two realistic argon pair potentials were examined, the HFD-C and HFD-B2 potentials. The changes in frequencies in Ar_3 between using these two potentials were an order of magnitude smaller than obtained on inclusion of the examined three-body terms. A Lennard-Jones pair potential gave very different results to both the HFD-C

and HFD-B2 calculations, as expected from its unrealistic shape.

• Three completely independent methods were used in the present work on Ar_3, all of which mutually agreed. Discrepancies with previous calculations were found:

1. The results of Horn *et al.* agree qualitatively with my calculations, but show physically degenerate states with energy differences of up to 400 times their claimed convergence. Their ground state is also about 0.1 cm^{-1} lower than all of the other calculations, which should not occur for a variational calculation. The anomalous ground state energy and large discrepancy in the energies of physically degenerate states suggests a programming error of some nature.

2. The results of Leitner *et al.* are qualitatively different to the others; there is agreement between their results and mine for A_1 states, but there seems to be no agreement between E states, with apparently spurious eigenvalues present, also implying a programming error of some kind.

• In Ar_3, the triple-dipole dispersion energy is the most important three-body term, measured by the change in frequencies, as expected. In contrast, the next-higher dispersion term, the dipole-dipole-quadrupole term, has roughly 10% as much effect. The exchange and overlap (Jansen) term is almost as important as the triple-dipole term in some states, and should not be neglected without good reason in any description of three-body forces in Ar_3.

• For Ar_2HCl, variation of model parameters gave an approximate fit to *ab-initio* data, but left noticeable discrepancies, although the literature value for the triple-dipole dispersion coefficient was half the size required to reproduce the *ab-initio* dispersion effects.

• Calculations were performed with the older, H6(3), ArHCl potential and the more recent H6(4,3,0) potential. The refinements incorporated in the H6(4,3,0) were found to have significant effects on the bound states.

• The difference between experiment and theory, using a pairwise-additive Ar_2HCl potential indicated three-body effects on the vibrational transition energies of about 1.5 cm^{-1}.

10: Conclusions.

- The Axilrod-Teller triple-dipole term is a poor approximation to the Ar_2HX triple-dipole term, which takes into account the anisotropic polarisability of the HX molecule.

- Damping of three-body dispersion is not important in the states calculated.

- The dominant three-body effects are the triple-dipole term or the overlap-induced quadrupole term; which is the most important differs between vibrational states. The importance of the effects arising from the overlap-induced quadrupole marks this part of the model for refinement; the overlap-induced field was rather crudely modelled and improvements in the HCl multipole arrangement are possible.

- Perturbation calculations suggest a coupling between the breathing stretch and the parallel bend in Ar_2HCl, which was increased by the model three-body potentials used, but almost absent in Ar_2DCl.

- A three-body potential matched to *ab-initio* calculations for Ar_2HCl (Model # 1) showed changes in the frequencies in the correct direction, but over-estimated the discrepancy between two-body calculations and experiment.

- A modified three-body potential (Model # 2), which also matches the *ab-initio* data to a large extent, was found to give broad agreement between experiment and theory. The remaining discrepancies are believed to be due to inadequacies in the model used, rather than serious physical flaws. A theoretical consideration of Coriolis mixing was found to be necessary for a more precise analysis of the intermolecular potential.

- A red-shift of 2.83 cm^{-1} between $v = 0$ and $v = 1$ is predicted for Ar_2HCl. The experimental determination of this parameter is feasible.

- A red-shift of 14.827 cm^{-1} between $v = 0$ and $v = 1$ is observed for Ar_2HF, which compares favourably with the theoretical value of 14.22 cm^{-1}.

Appendix A— Ar_3 Potential Plots.

Fig. 1 . HFD-C Pairwise Additive Cut on $R = 3.255$Å.
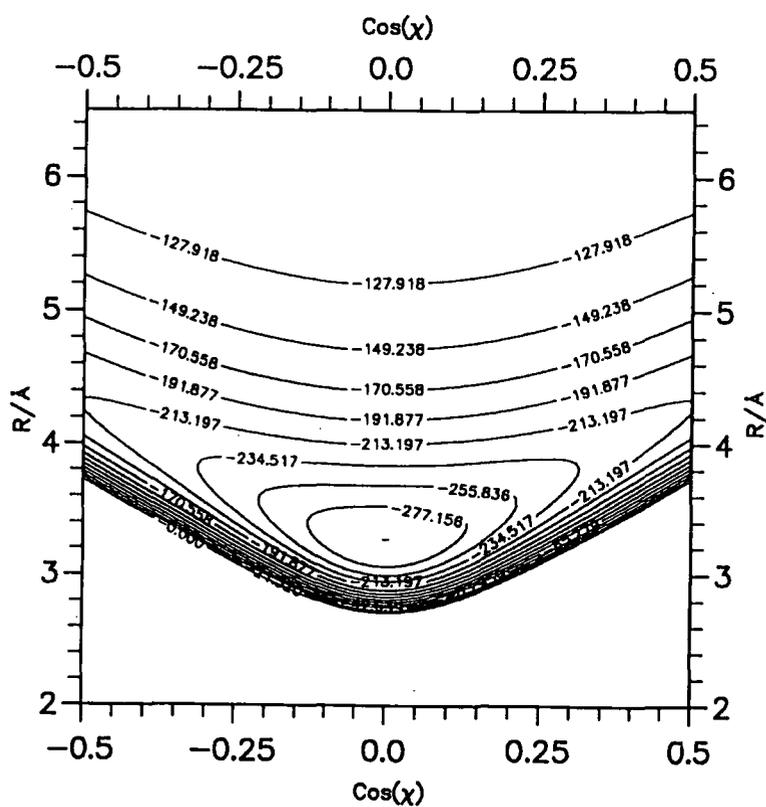
Fig. 2 . HFD-C Pairwise Additive Cut on $\rho = 3.759$Å.

Fig. 3 . HFD-C Pairwise Additive Cut on $\cos \chi = 0$.

Fig. 4 . Angular Features of Triple Dipole Surface for $\rho = 3.759 \text{Å}$
$(\nu_{123} = 3.786 \times 10^5 \text{Å}^9 \text{cm}^{-1})$.
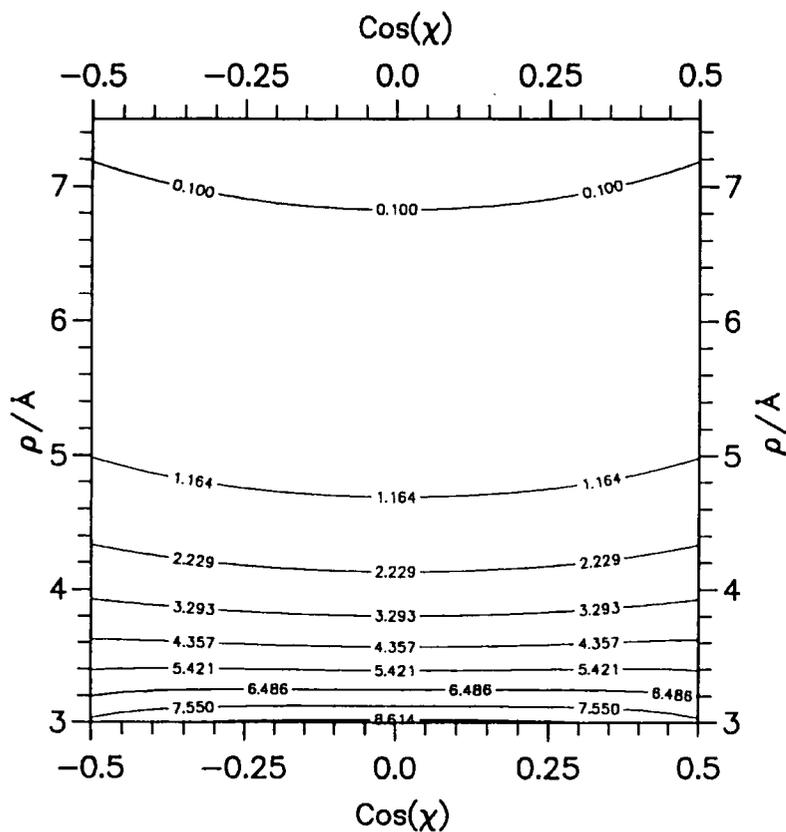
Fig. 5 . Triple Dipole Surface for $R = 3.255\text{Å}$
$(\nu_{123} = 3.786 \times 10^5 \text{Å}^9 \text{cm}^{-1})$.
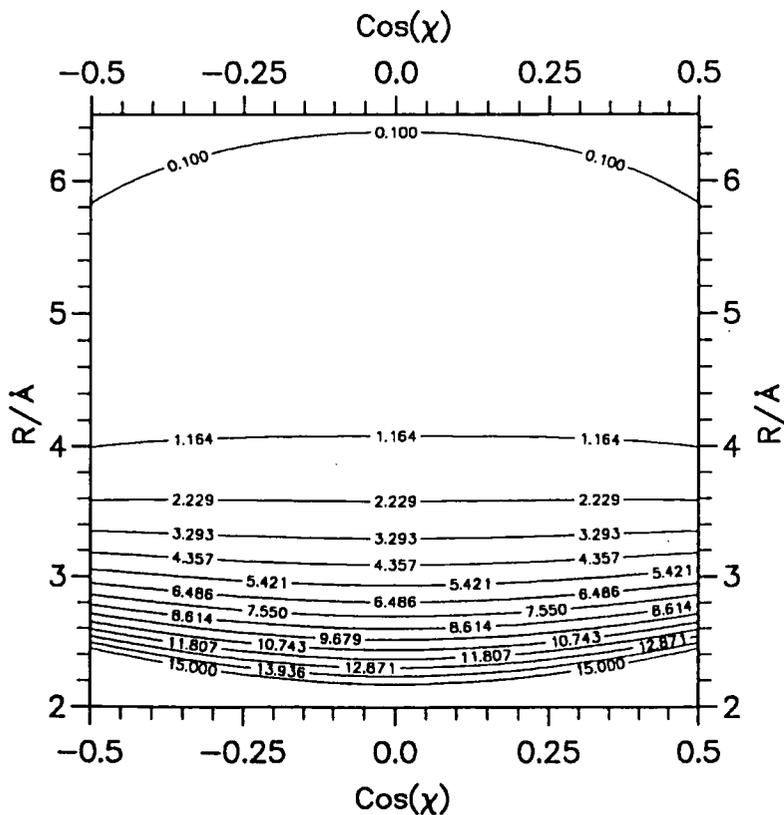
Fig. 6 . Triple Dipole Surface for $\rho = 3.759\text{Å}$
$(\nu_{123} = 3.786 \times 10^5 \text{Å}^9 \text{cm}^{-1})$.
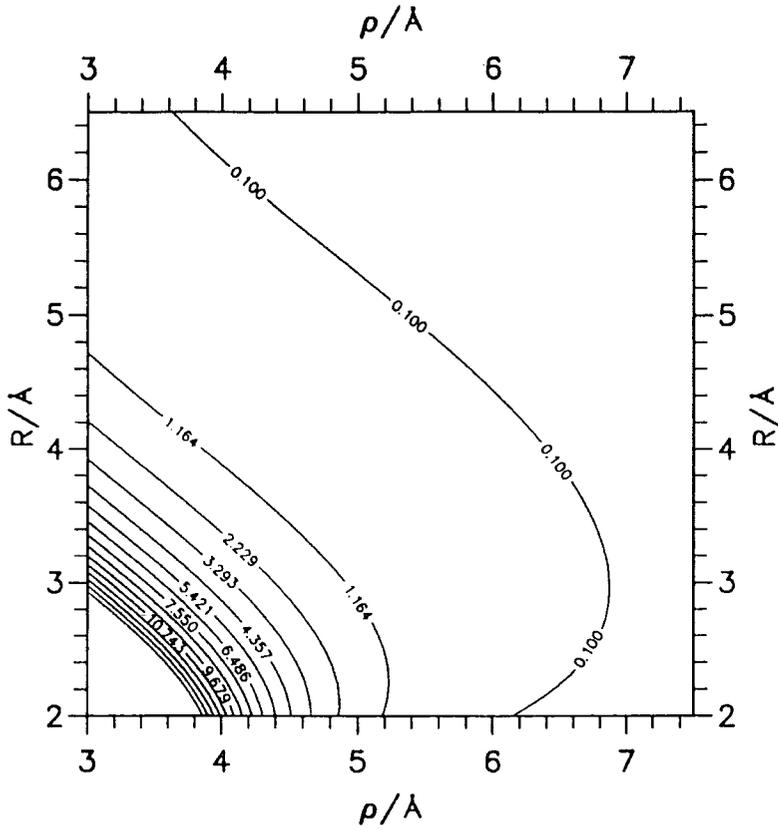
Fig. 7 . Triple Dipole Surface for $\cos \chi = 0$
$(\nu_{123} = 3.786 \times 10^5 \text{Å}^9 \text{cm}^{-1})$.
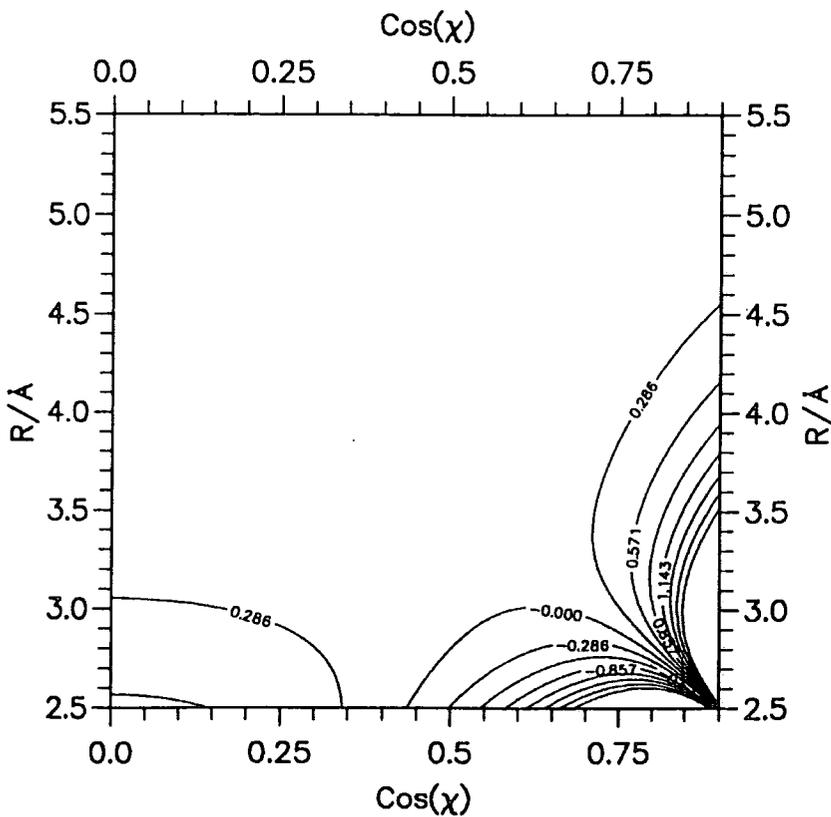
Fig. 8 . Angular Features of Dipole-dipole-quadrupole Surface for $\rho = 3.759\text{Å}$
$(Z_{\text{ddq}}^{(3)} = 1.352 \times 10^5 \text{Å}^1 1 \text{cm}^{-1})$.
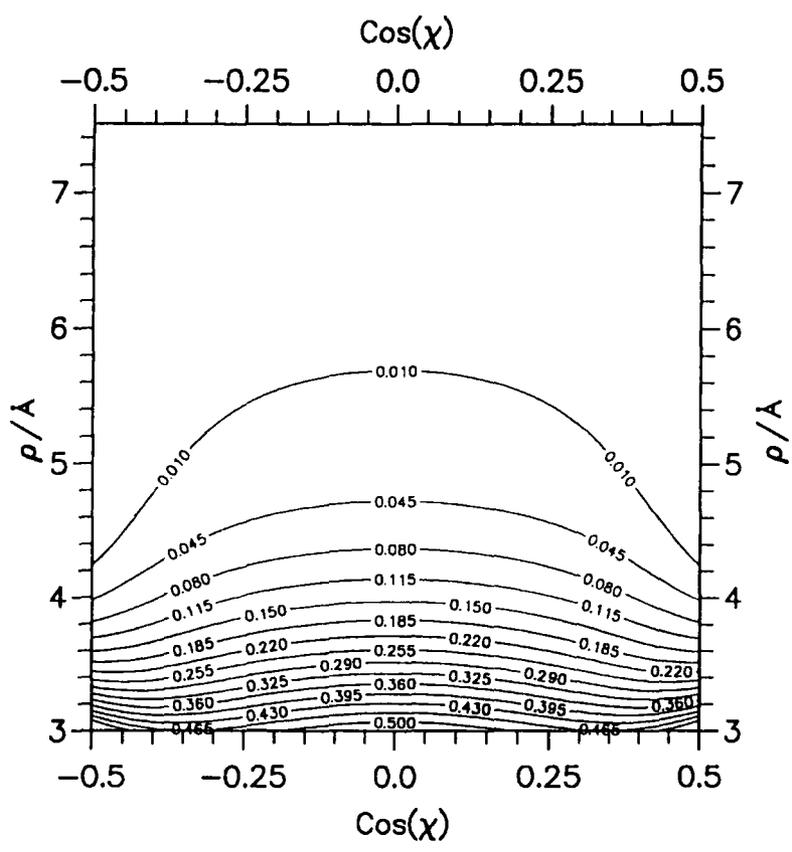
Fig. 9 . Dipole-dipole-quadrupole Surface for $R = 3.255$Å $(Z_{ddq}^{(3)} = 1.352 \times 10^5 \text{Å}^1 1 \text{cm}^{-1})$.
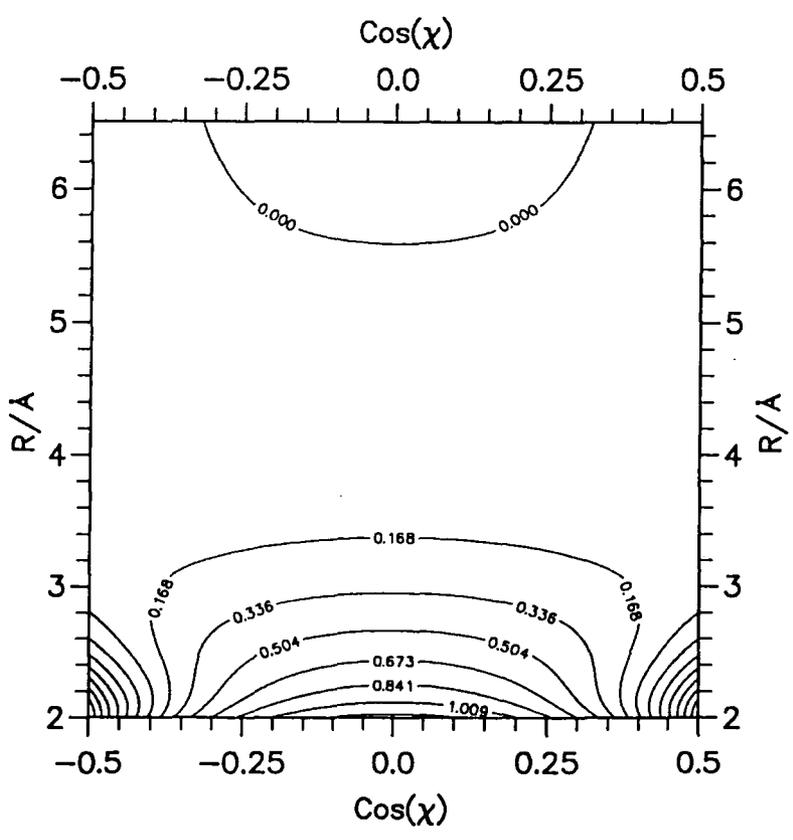
Fig. 10 . Dipole-dipole-quadrupole Surface for $\rho = 3.759$Å $(Z_{ddq}^{(3)} = 1.352 \times 10^5 \text{Å}^1 1 \text{cm}^{-1})$.
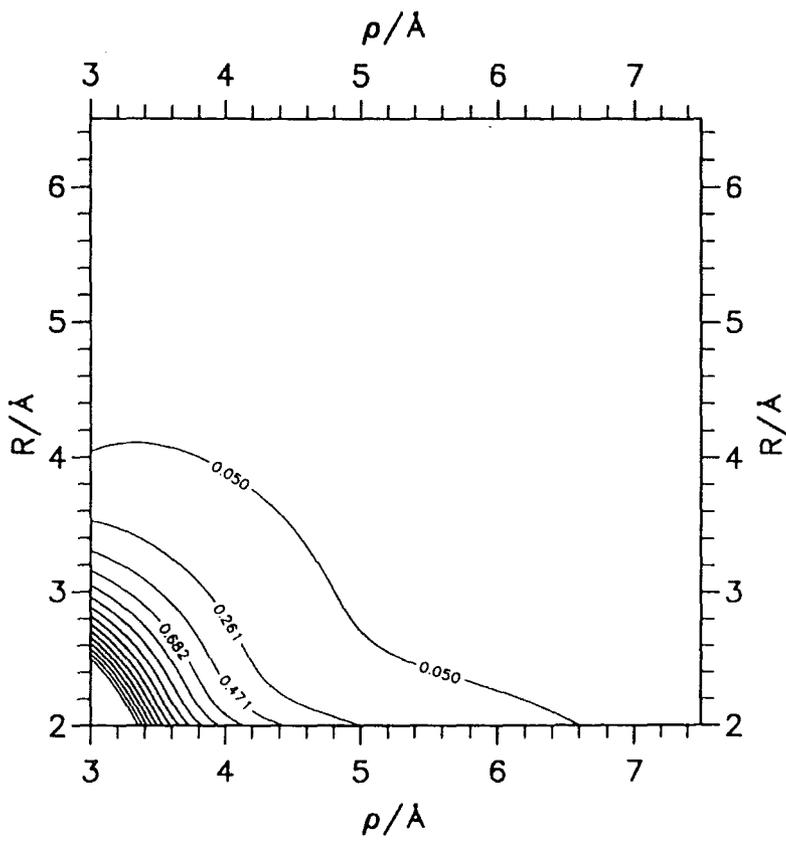
Fig. 11 . Dipole-dipole-quadrupole Surface for $\cos\chi = 0$
$(Z^{(3)}_{\mathrm{ddq}} = 1.352 \times 10^5 \mathring{A}^1 1\mathrm{cm}^{-1})$.
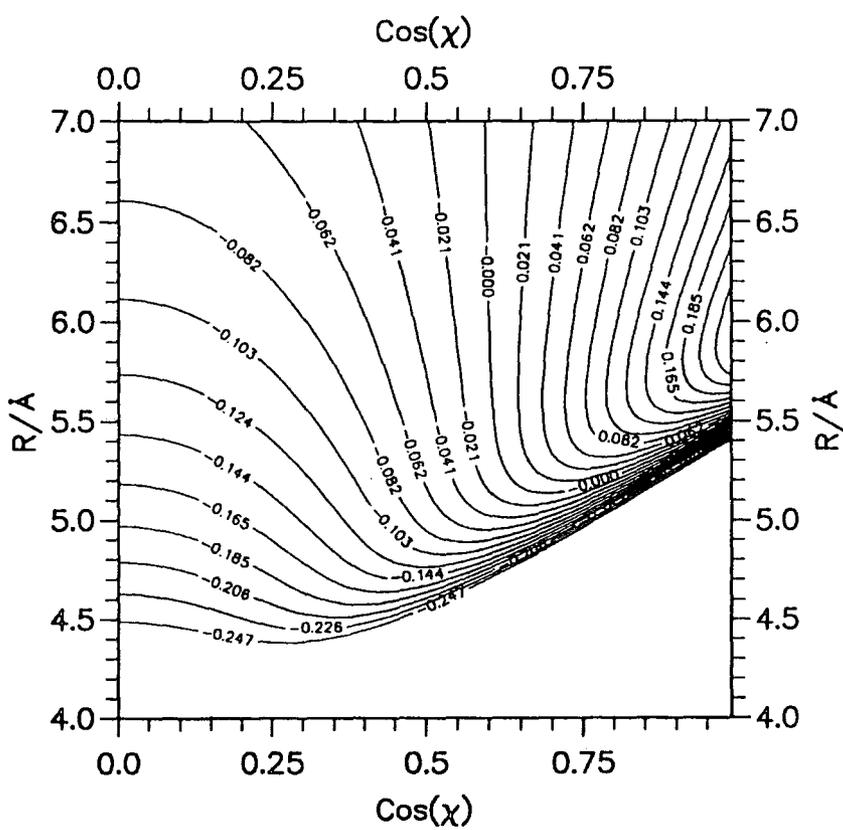
Fig. 12 . Angular Features of Jansen Term for $\rho = 3.759\mathring{A}$
$(S_{\mathrm{Jansen}} = 4.3 \times 10^5 \mathring{A}\mathrm{cm}^{-1}, \beta = 1.23\mathring{A}^{-1})$.

Appendix A– Ar₃ Potential Plots.

Fig. 13 . Jansen Term for $R = 3.255$Å
$(S_{\mathrm{Jansen}} = 4.3 \times 10^5 \, \text{Åcm}^{-1}, \beta = 1.23\text{Å}^{-1})$.

Fig. 14 . Jansen Term for $\rho = 3.759$Å
$(S_{\mathrm{Jansen}} = 4.3 \times 10^5 \, \text{Åcm}^{-1}, \beta = 1.23\text{Å}^{-1})$.

Appendix A– Ar$_3$ Potential Plots.
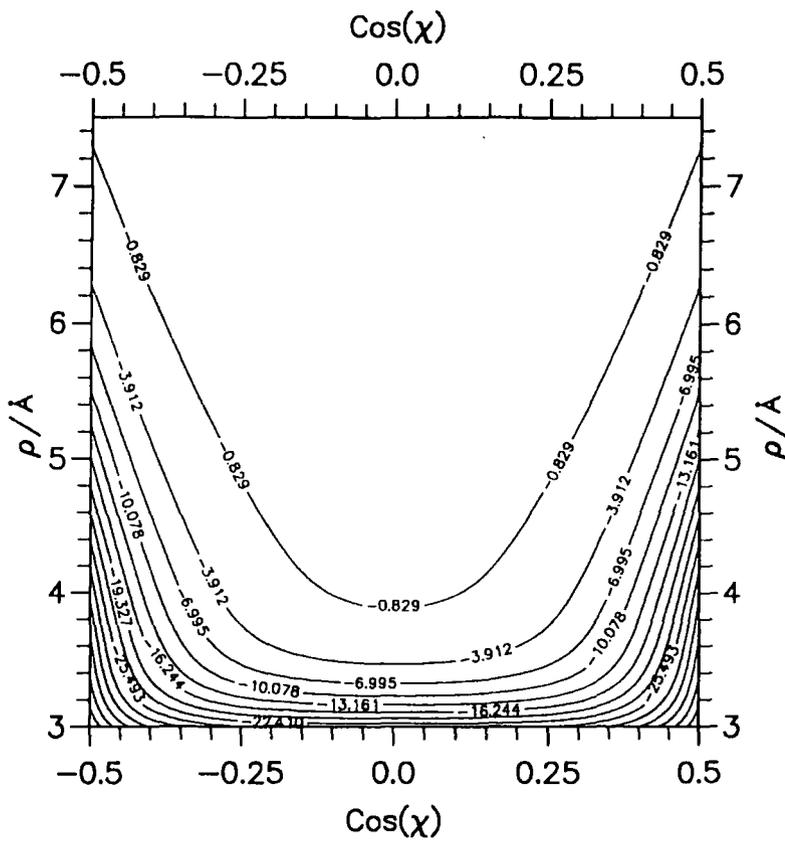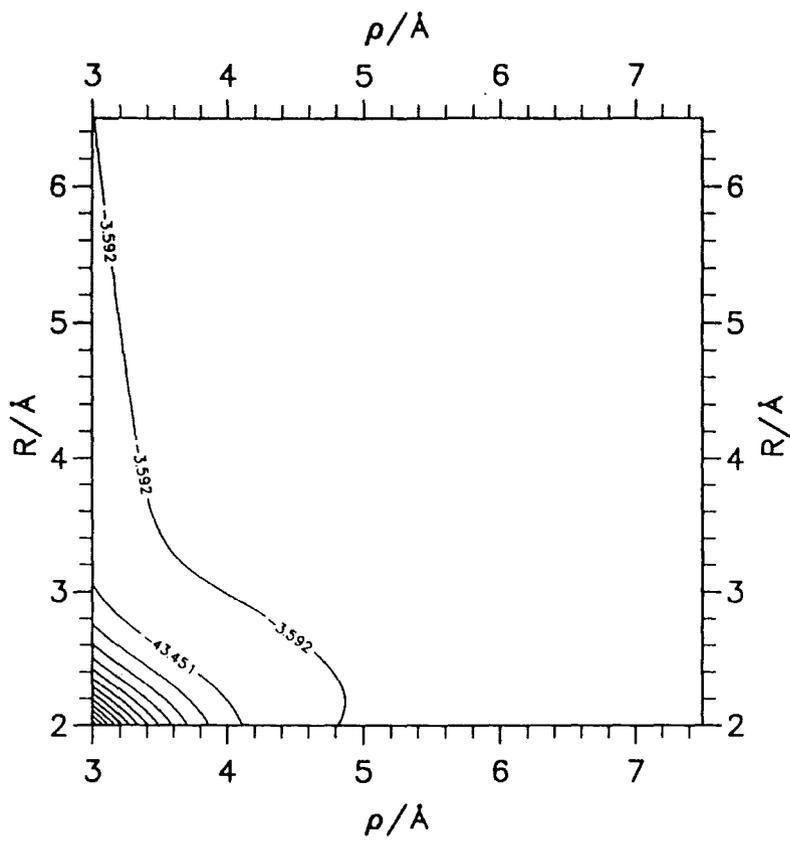
Fig. 15 . Jansen Term for $\cos \chi = 0$
$(S_{\text{Jansen}} = 4.3 \times 10^5 \text{Åcm}^{-1}, \beta = 1.23\text{Å}^{-1})$.

Appendix A– Ar$_3$ Potential Plots.

Appendix B– Ar$_2$HCl Potential Plots.

All cuts have fixed parameters according to $R = 3.45\text{Å}$, $\rho = 3.82\text{Å}$, $\cos\chi = 0$, $\cos\theta = 1$ and $\phi = 0$.

Appendix B– Ar$_2$HCl Potential Plots.

Fig. 1. H6(4,3,0) $v = 0$ Potential for ArHCl Dimer.
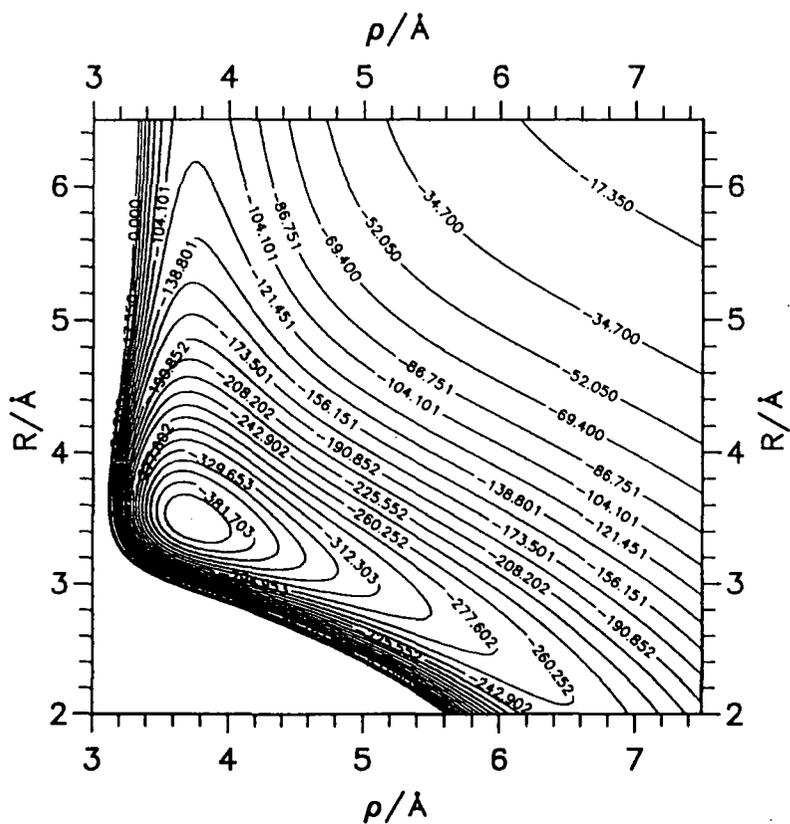
Fig. 2. HFD-C + H6(4,3,0) $v = 0$ Pairwise Additive Cut for R vs. ρ.
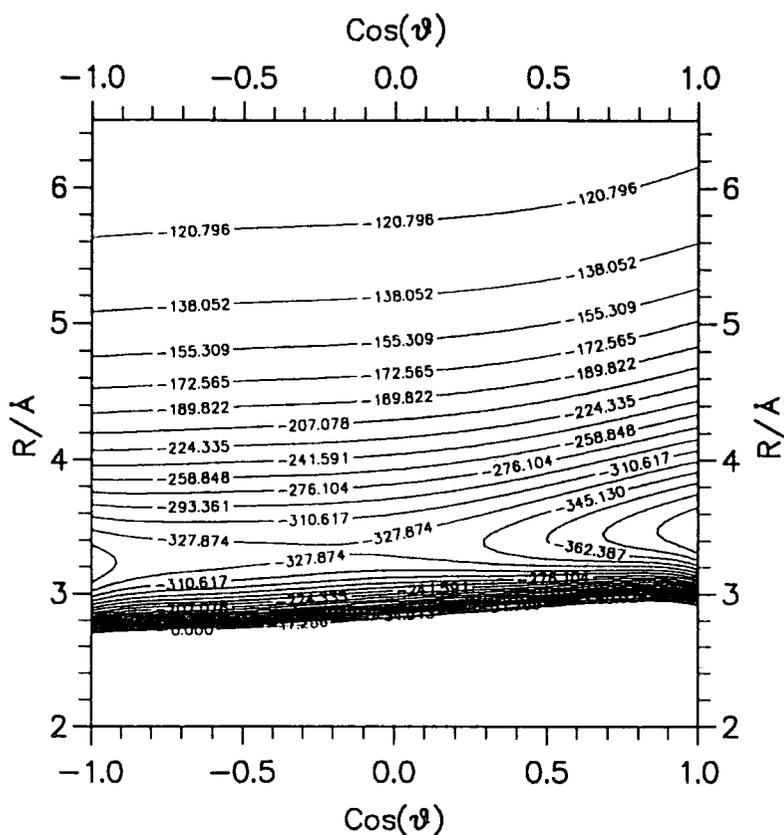
Fig. 3. HFD-C + H6(4,3,0) $v = 0$ Pairwise Additive Cut for R vs. $\cos\theta$.

Fig. 4. HFD-C + H6(4,3,0) $v = 0$ Pairwise Additive Cut for ρ vs. $\cos\chi$.

Appendix B– Ar_2HCl Potential Plots.
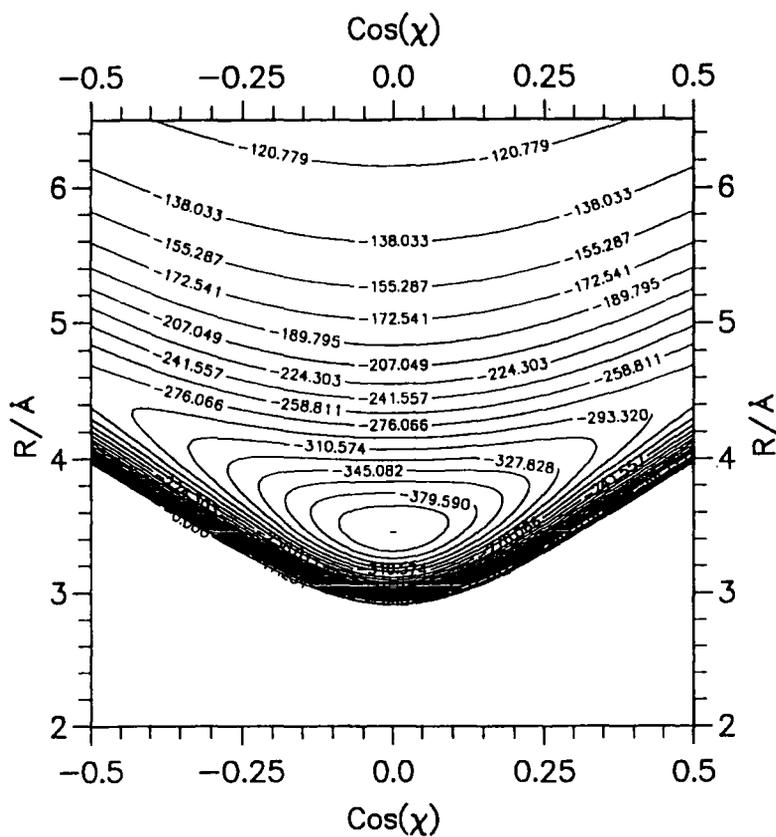
Fig. 5. HFD-C + H6(4,3,0) $v = 0$ Pairwise Additive Cut for R vs. $\cos\chi$.
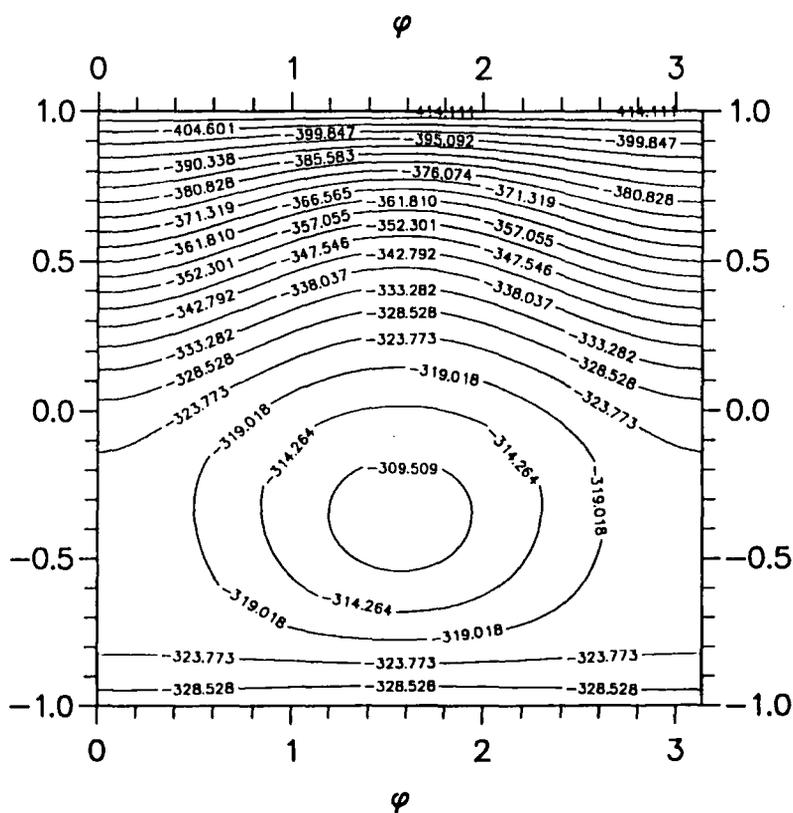
Fig. 6. HFD-C + H6(4,3,0) $v = 0$ Pairwise Additive Cut for $\cos\theta$ vs. ϕ.

Fig. 7. Angular Features of Triple Dipole Surface for R vs. ρ
$(\nu_{123} = 5.4155 \times 10^5 \mathring{A}^9 cm^{-1})$.

Fig. 8. Triple Dipole Surface for R vs. $\cos\theta$
$(\nu_{123} = 5.4155 \times 10^5 \mathring{A}^9 cm^{-1})$.

Appendix B– Ar$_2$HCl Potential Plots.
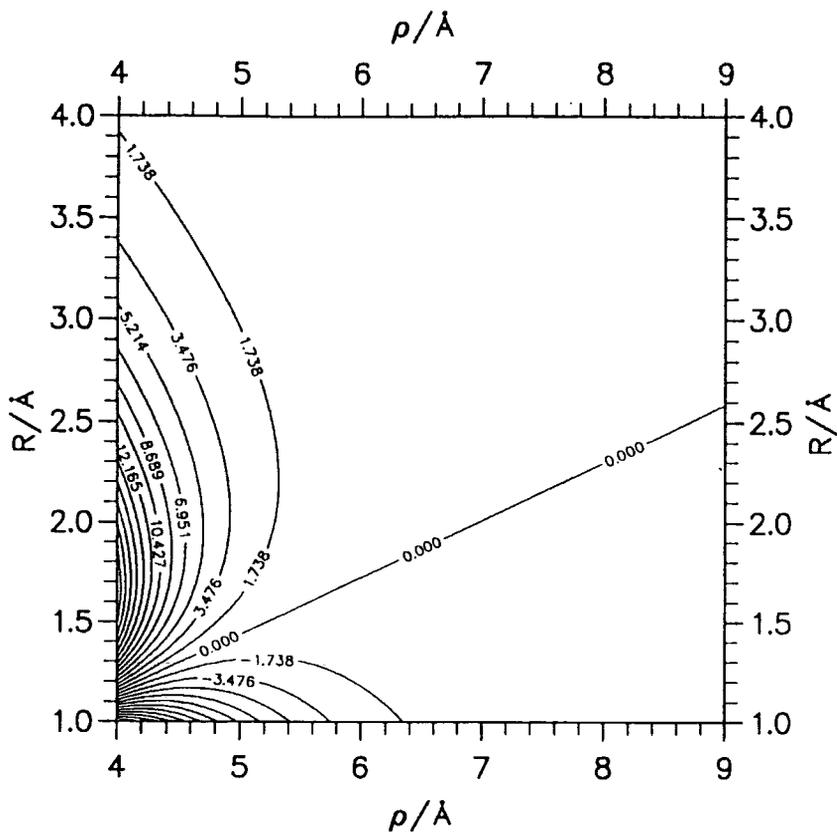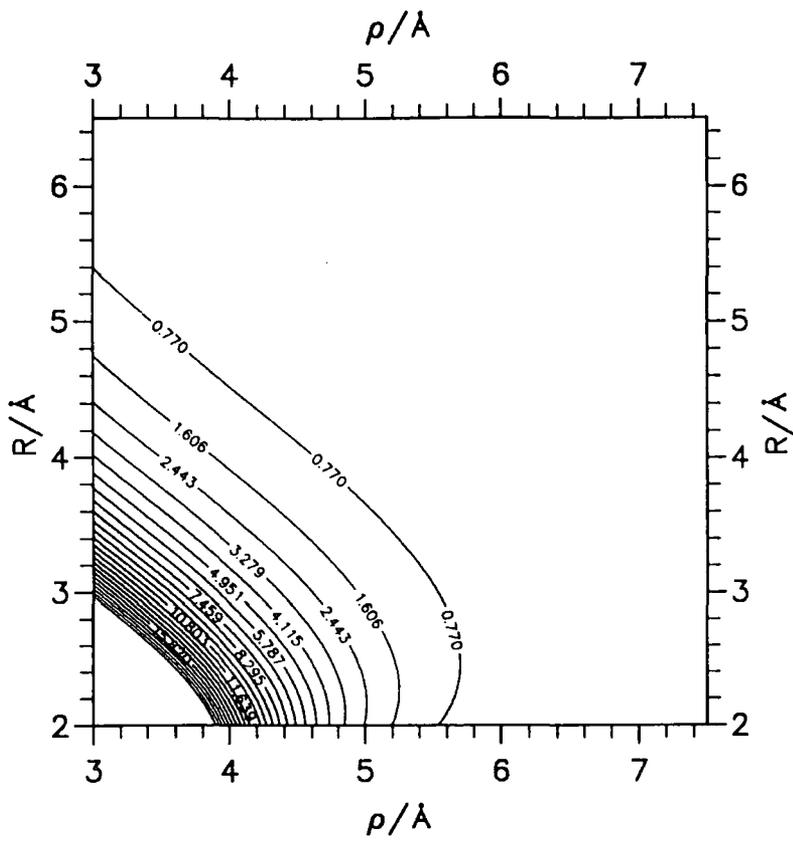
Fig. 9. Axilrod-Teller Surface for R vs. ρ
$(\nu_{123} = 5.4155 \times 10^5 \mathring{A}^9 cm^{-1})$.

Fig. 10. Triple Dipole Surface for R vs. ρ
$(\nu_{123} = 5.4155 \times 10^5 \mathring{A}^9 cm^{-1})$.

Appendix B– $Ar_2 HCl$ Potential Plots.
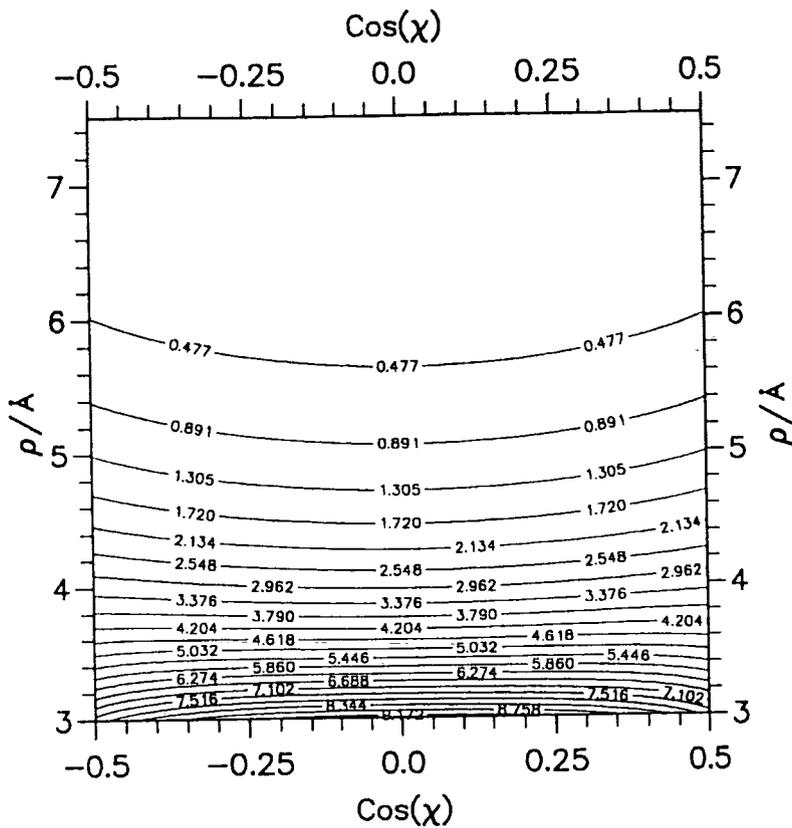
Fig. 11. Axilrod-Teller Surface for ρ vs. $\cos \chi$
$(\nu_{123} = 5.4155 \times 10^5 \text{Å}^9 \text{cm}^{-1})$.

Fig. 12. Triple Dipole Surface for ρ vs. $\cos \chi$
$(\nu_{123} = 5.4155 \times 10^5 \text{Å}^9 \text{cm}^{-1})$.

Appendix B– Ar$_2$HCl Potential Plots.
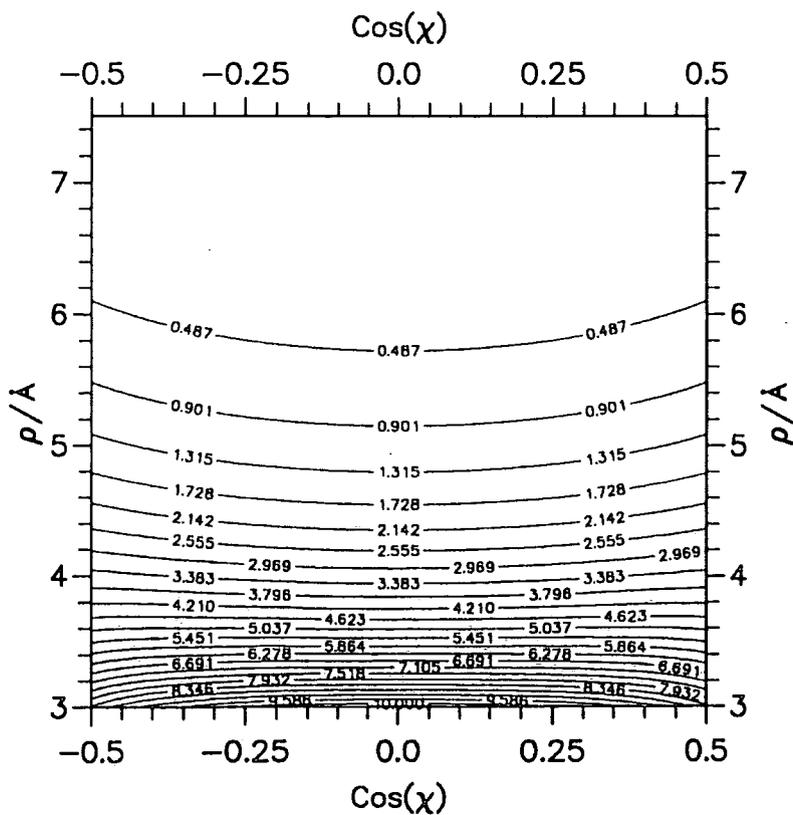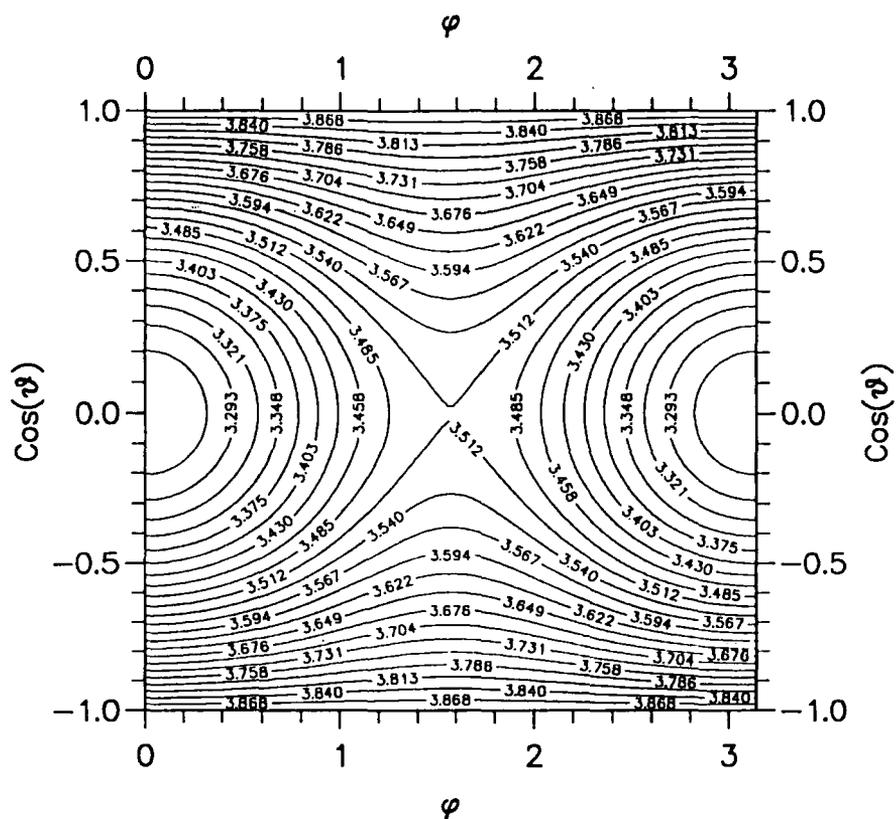
Fig. 13. Triple Dipole Surface for $\cos\theta$ vs. ϕ
($\nu_{123} = 5.4155 \times 10^5 \text{Å}^9\text{cm}^{-1}$).
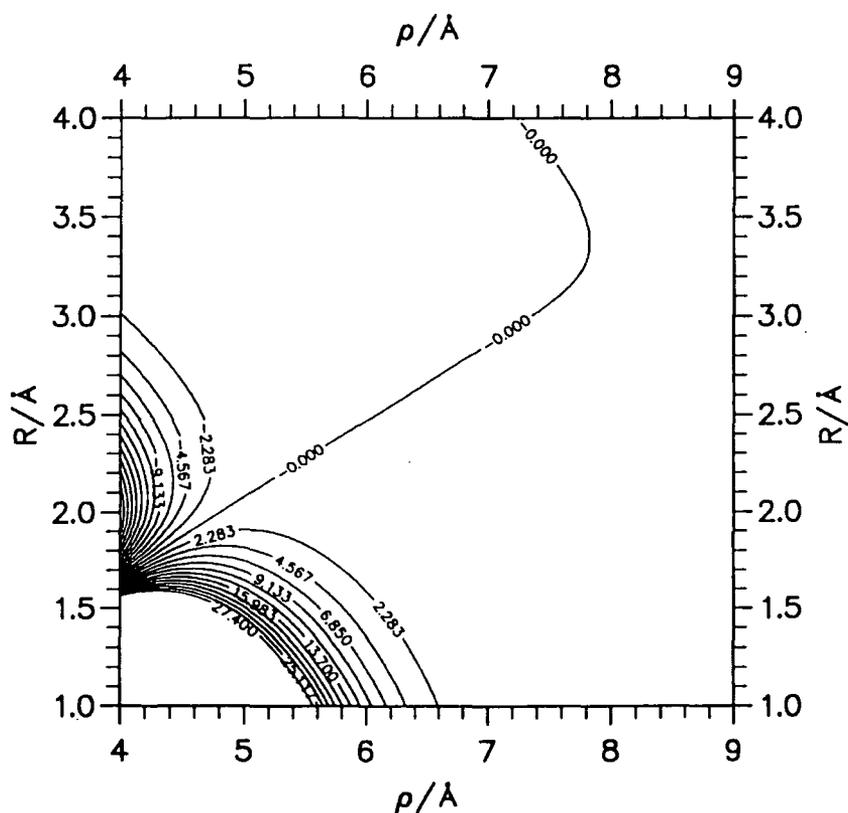
Fig. 14. Angular Features of Jansen Term for R vs. ρ
($S_{\text{Jansen}} = 2.0 \times 10^5 \text{Å}\text{cm}^{-1}, \beta = 1.24\text{Å}^{-1}, \delta_{\text{Jansen}} = 0.15\text{Å}$).

Fig. 15. Jansen Term for R vs. ρ
$$(S_{\text{Jansen}} = 2.0 \times 10^5 \text{Åcm}^{-1}, \beta = 1.24\text{Å}^{-1}, \delta_{\text{Jansen}} = 0.15\text{Å}).$$

Fig. 16. Jansen Term for R vs. $\cos\theta$
$$(S_{\text{Jansen}} = 2.0 \times 10^5 \text{Åcm}^{-1}, \beta = 1.24\text{Å}^{-1}, \delta_{\text{Jansen}} = 0.15\text{Å}).$$

Appendix B– Ar$_2$HCl Potential Plots.
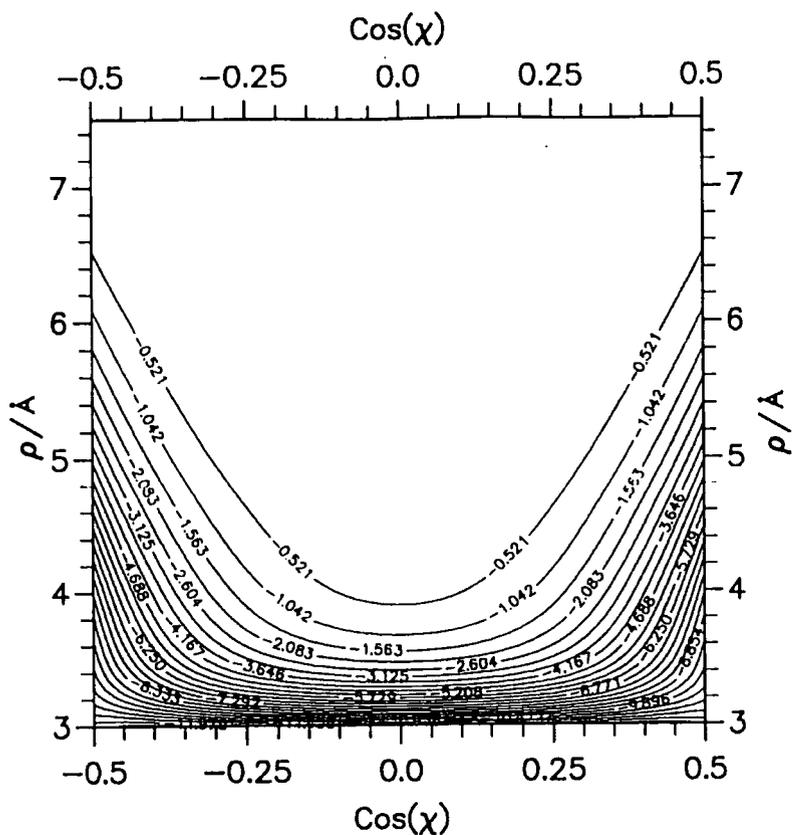
Fig. 17. Jansen Term for ρ vs. $\cos \chi$
$(S_{\mathrm{Jansen}} = 2.0 \times 10^5 \,\mathring{A}\mathrm{cm}^{-1}, \beta = 1.24 \mathring{A}^{-1}, \delta_{\mathrm{Jansen}} = 0.15 \mathring{A}).$

Fig. 18. Jansen Term for $\cos \theta$ vs. ϕ
$(S_{\mathrm{Jansen}} = 2.0 \times 10^5 \,\mathring{A}\mathrm{cm}^{-1}, \beta = 1.24 \mathring{A}^{-1}, \delta_{\mathrm{Jansen}} = 0.15 \mathring{A}).$

Appendix B– Ar$_2$HCl Potential Plots.
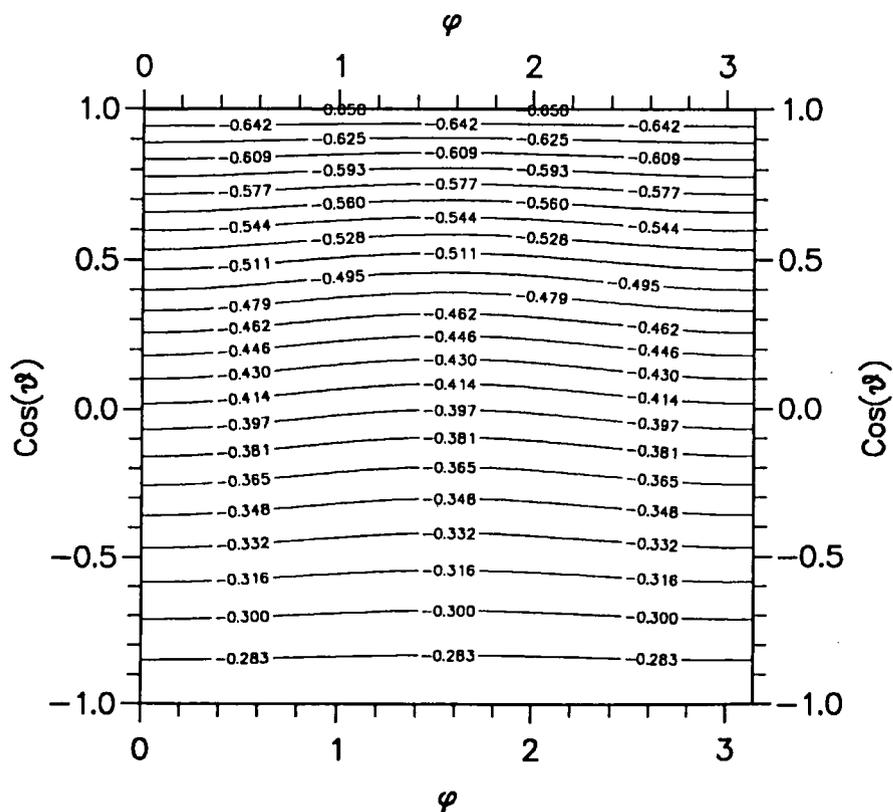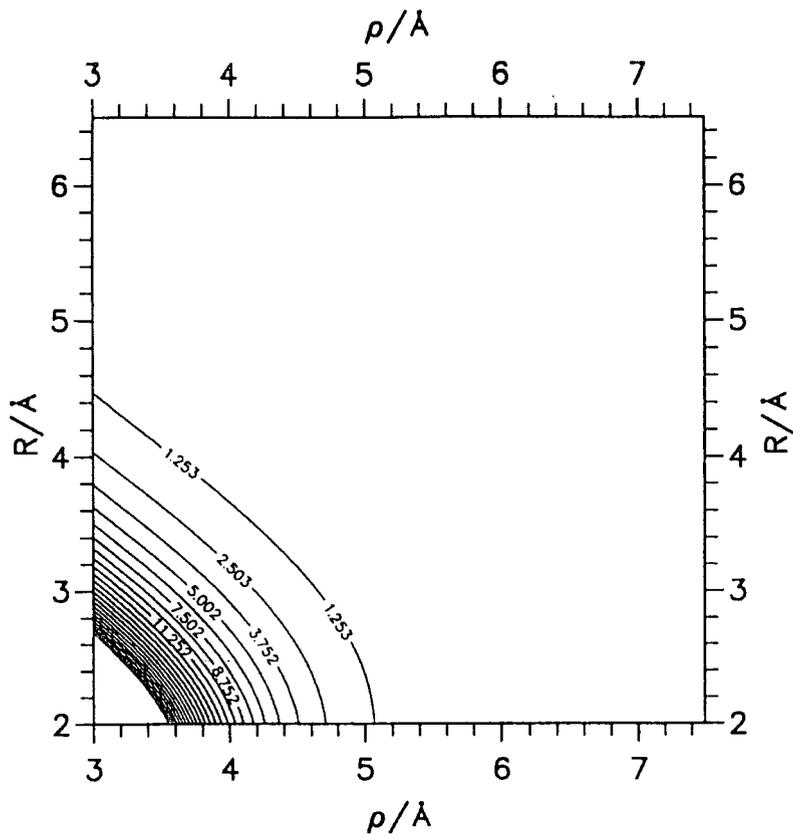
Fig. 19. Induced Dipole Interaction for R vs. ρ
(up to hexadecapole on HCl inducing dipoles on Ar).

Fig. 20. Induced Dipole Interaction for R vs. ρ
(only HCl dipole inducing dipoles on Ar).

Appendix B– Ar_2HCl Potential Plots.

Fig. 21. Induced Dipole Interaction for R vs. $\cos\theta$
(up to hexadecapole on HCl inducing dipoles on Ar).
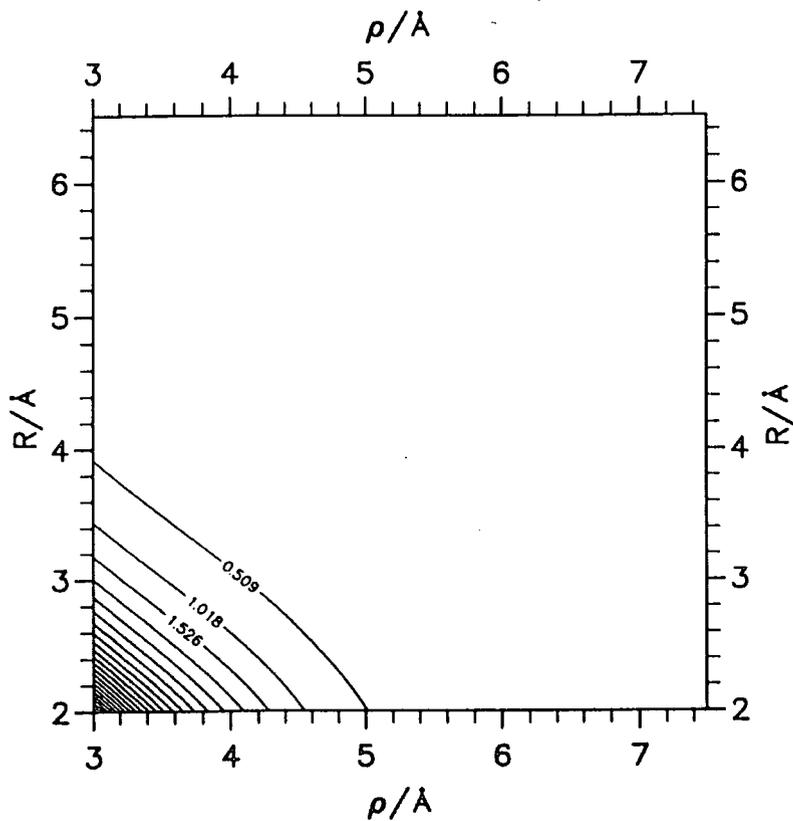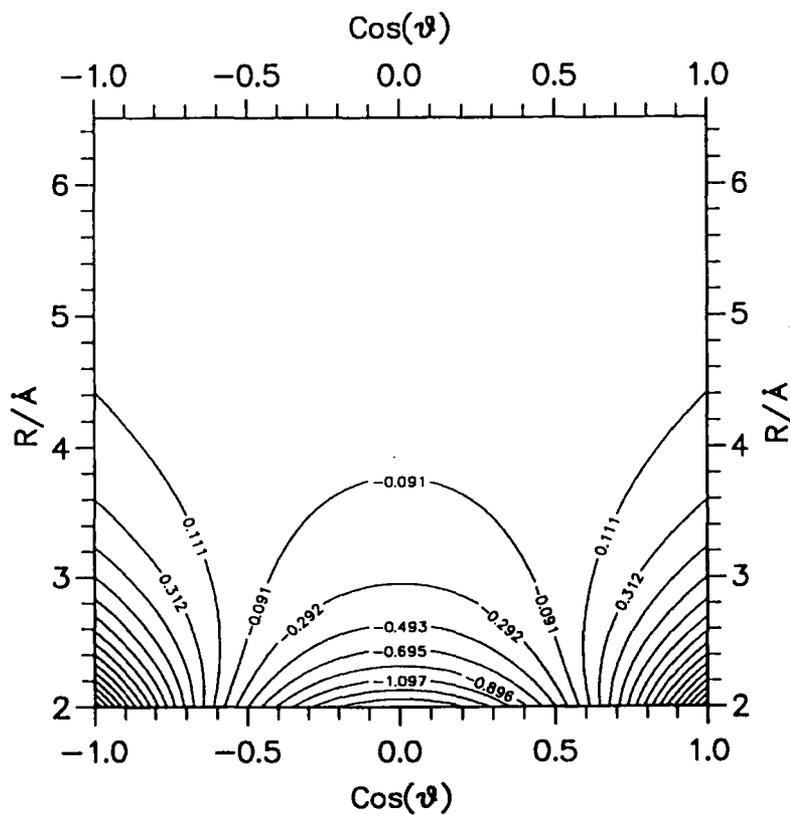
Fig. 22. Induced Dipole Interaction for R vs. $\cos\theta$
(only HCl dipole inducing dipoles on Ar).

Appendix B– Ar₂HCl Potential Plots.
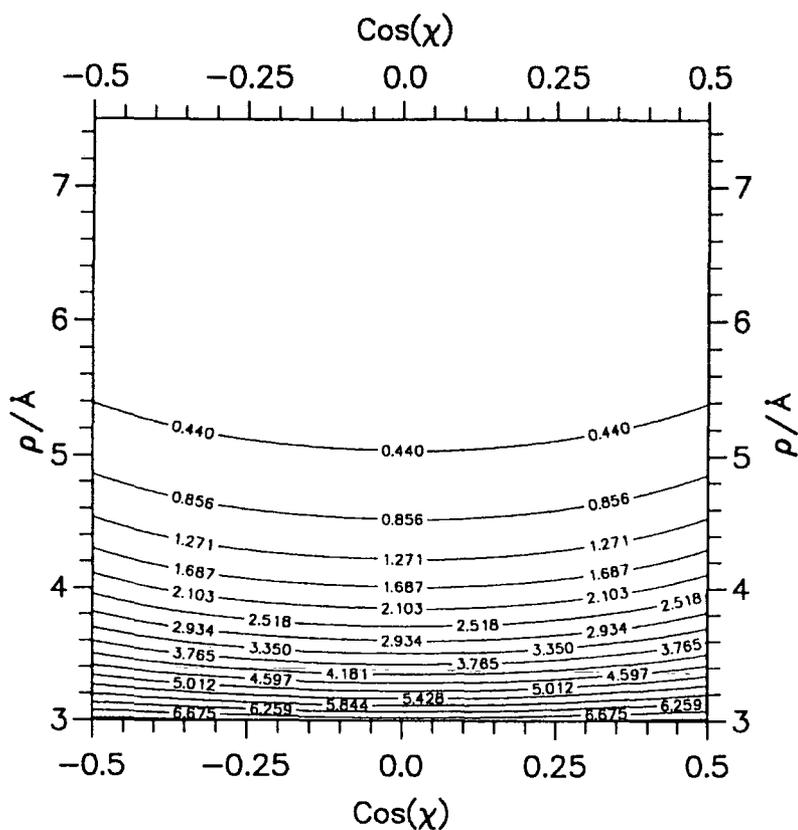
Fig. 23. Induced Dipole Interaction for ρ vs. $\cos\chi$
(up to hexadecapole on HCl inducing dipoles on Ar).

Fig. 24. Induced Dipole Interaction for ρ vs. $\cos\chi$
(only HCl dipole inducing dipoles on Ar).

Appendix B– Ar$_2$HCl Potential Plots.
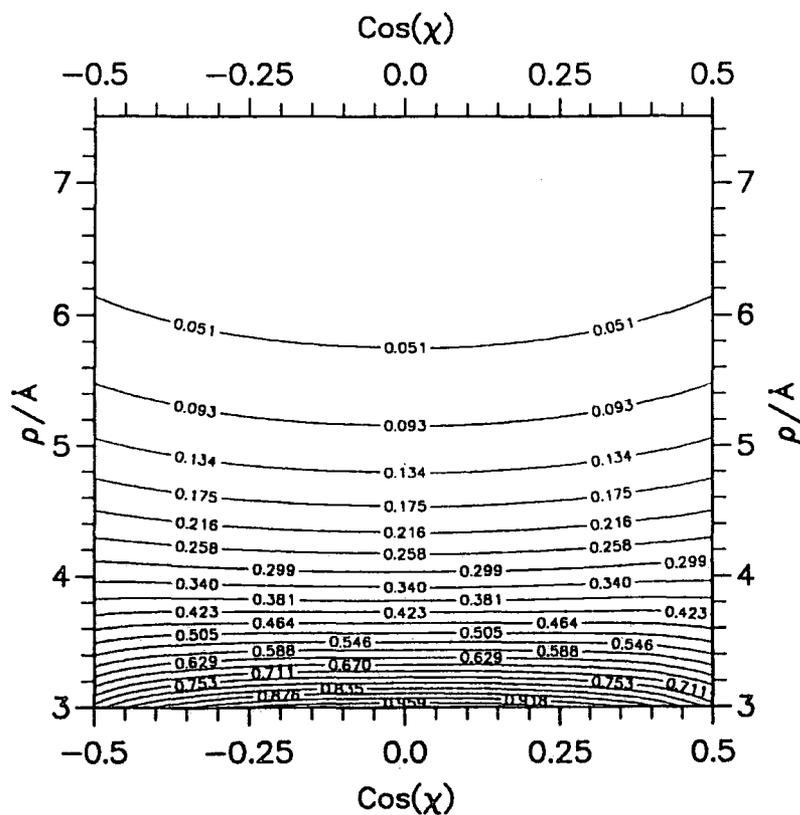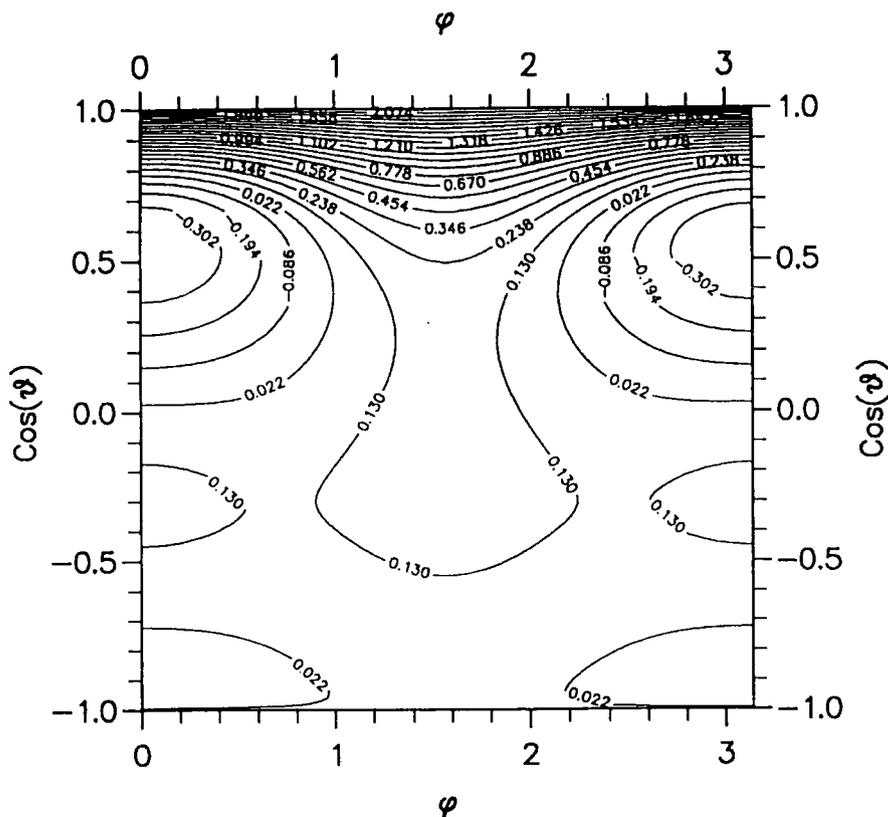
Fig. 25. Induced Dipole Interaction for $\cos\theta$ vs. ϕ
(up to hexadecapole on HCl inducing dipoles on Ar).
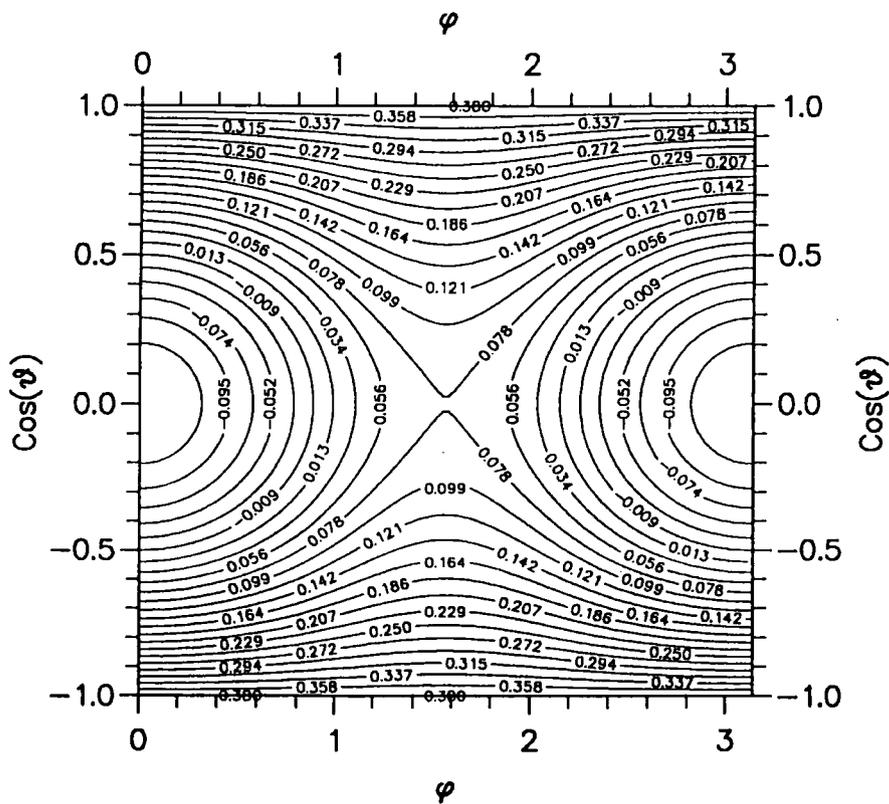
Fig. 26. Induced Dipole Interaction for $\cos\theta$ vs. ϕ
(only HCl dipole inducing dipoles on Ar).
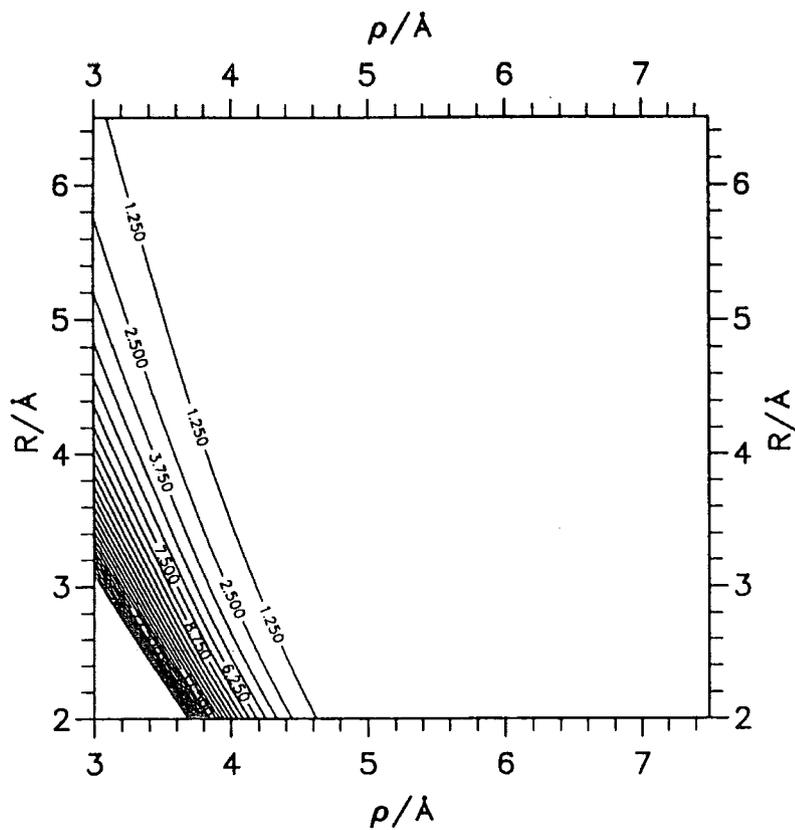
Fig. 27. Overlap Induced Quadrupole – HX Dipole for R vs. ρ $(\beta_{\Theta-\mathrm{def}} = 0.965\text{Å}^{-1})$.
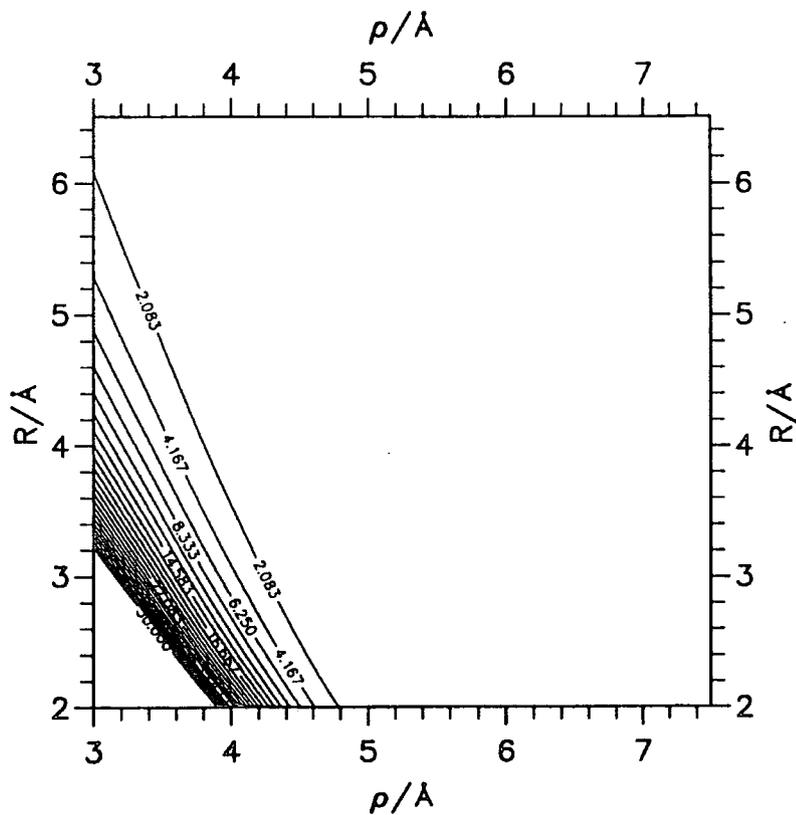
Fig. 28. Overlap Induced Quadrupole – HX Quadrupole for R vs. ρ $(\beta_{\Theta-\mathrm{def}} = 0.965\text{Å}^{-1})$.

Appendix B– Ar$_2$HCl Potential Plots.
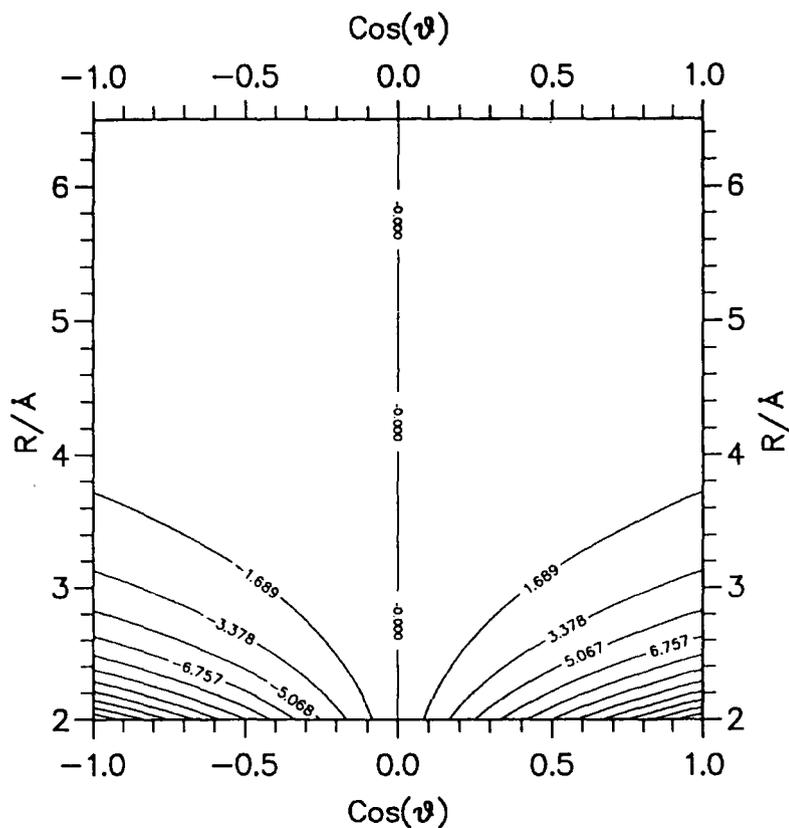
Fig. 29. Overlap Induced Quadrupole – HX Dipole for R vs. $\cos\theta$ $(\beta_{\Theta-\mathrm{def}} = 0.965\mathrm{\AA}^{-1})$.

Fig. 30. Overlap Induced Quadrupole – HX Quadpole for R vs. $\cos\theta$ $(\beta_{\Theta-\mathrm{def}} = 0.965\mathrm{\AA}^{-1})$.

Appendix B– Ar$_2$HCl Potential Plots.
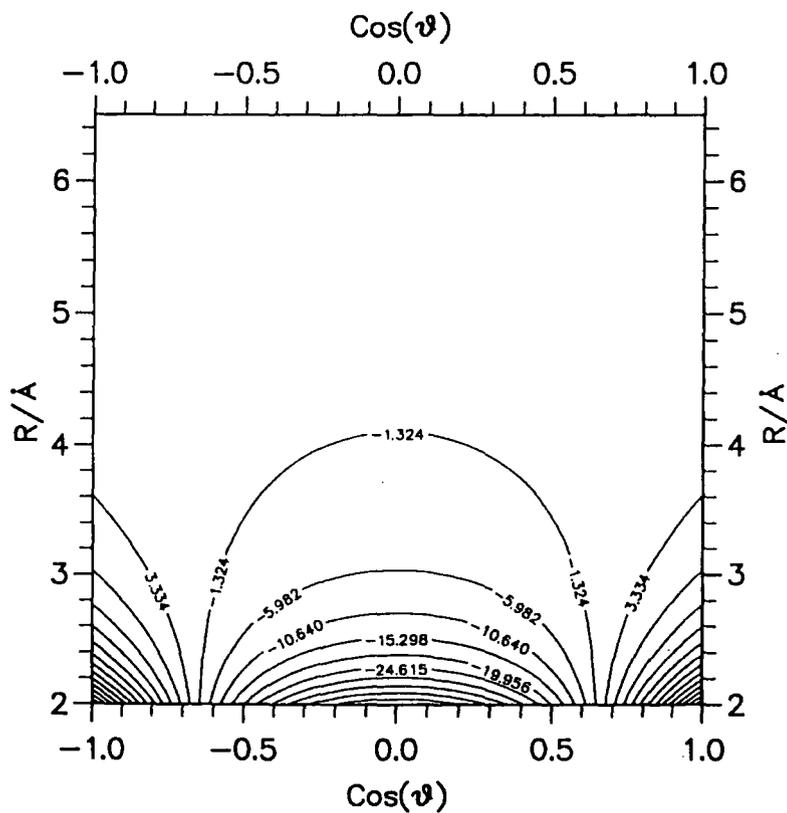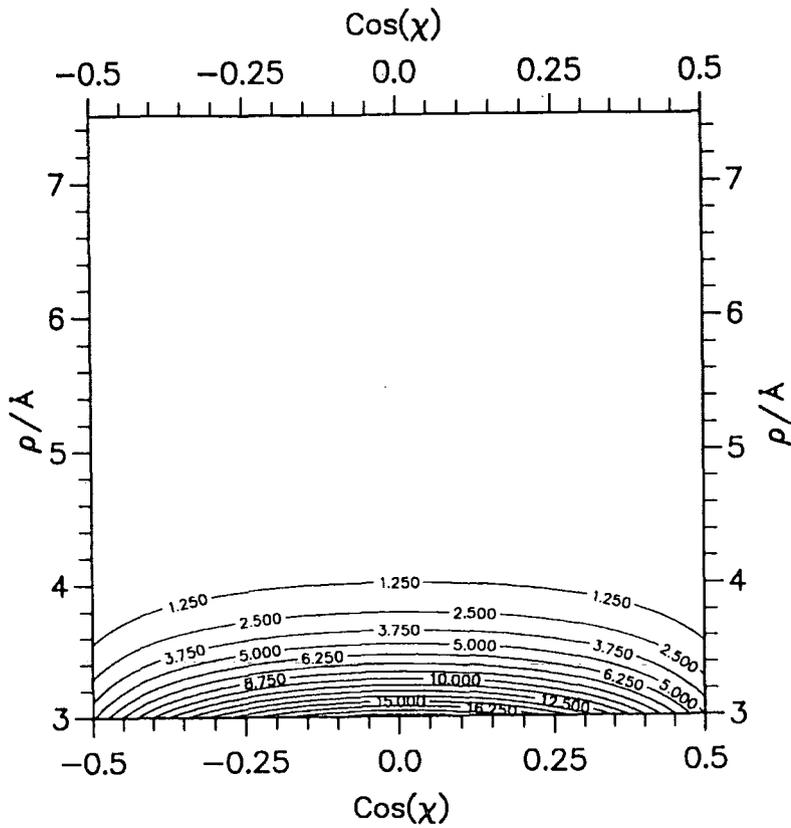
Fig. 31. Overlap Induced Quadrupole – HX Dipole for ρ vs. $\cos \chi$ $(\beta_{\Theta-\text{def}} = 0.965\text{Å}^{-1})$.

Fig. 32. Overlap Induced Quadrupole – HX Quadrupole for ρ vs. $\cos \chi$ $(\beta_{\Theta-\text{def}} = 0.965\text{Å}^{-1})$.

Appendix B– Ar$_2$HCl Potential Plots.
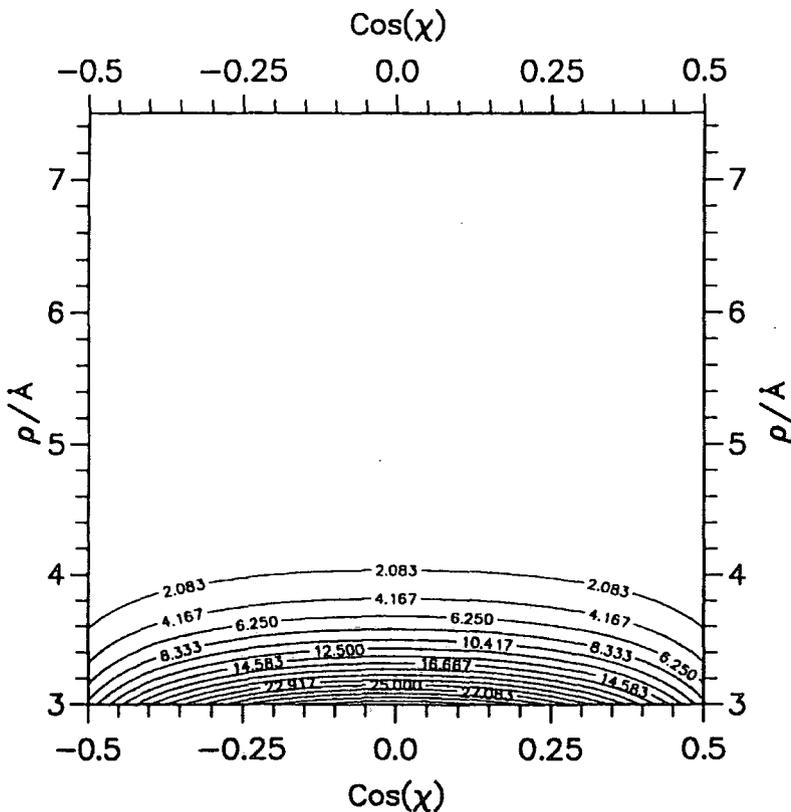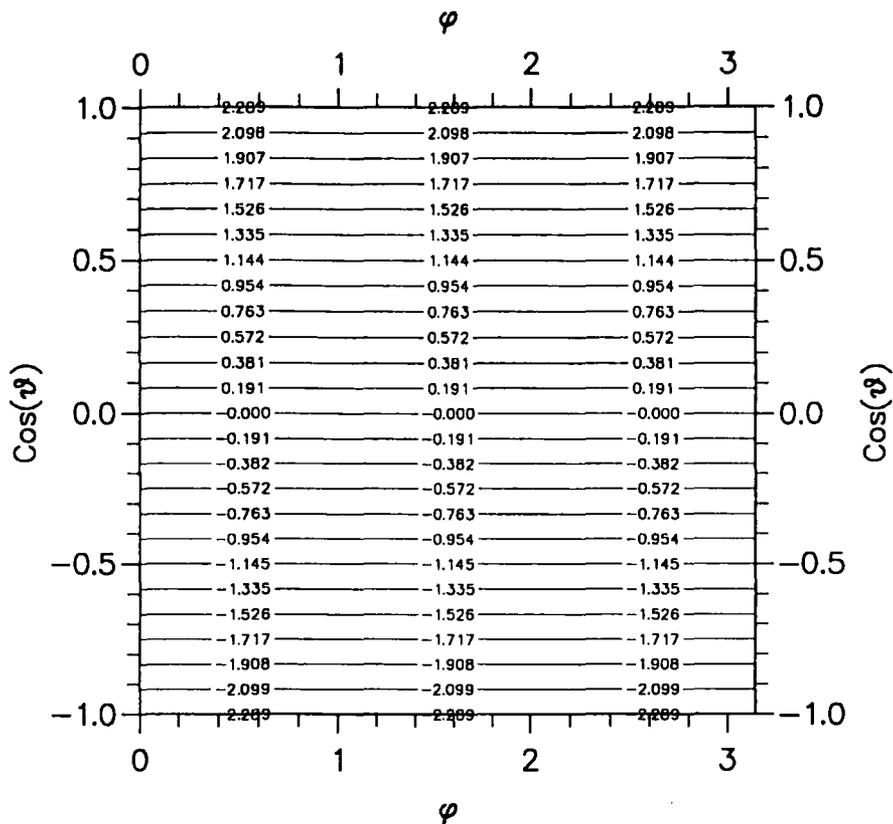
Fig. 33. Overlap Induced Quadrupole – HX Dipole for $\cos\theta$ vs. ϕ $(\beta_{\Theta-\mathrm{def}} = 0.965 \text{Å}^{-1})$.

Fig. 34. Overlap Induced Quadrupole – HX Quadpole for $\cos\theta$ vs. ϕ $(\beta_{\Theta-\mathrm{def}} = 0.965 \text{Å}^{-1})$.

Appendix B– Ar$_2$HCl Potential Plots.
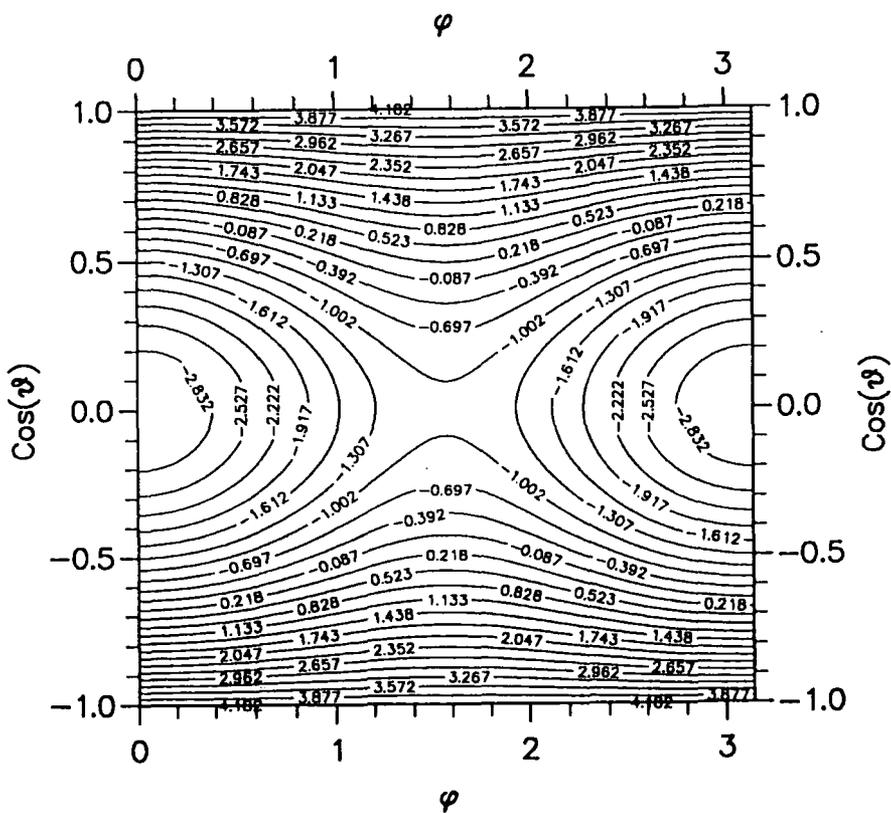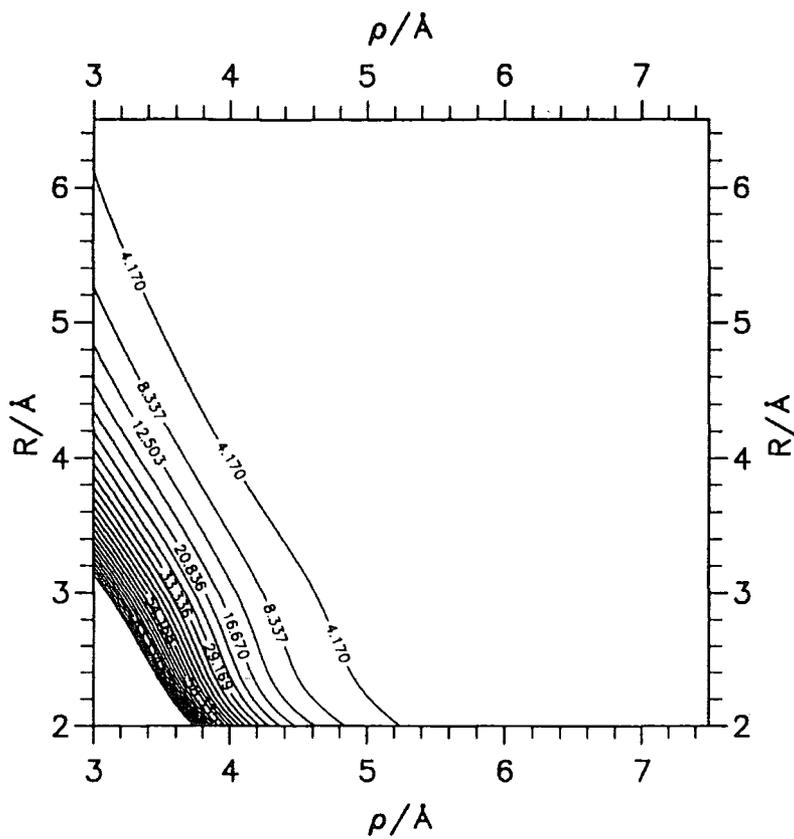
Fig. 35. Sum of Three Body Terms Above for R vs. ρ.

Fig. 36. Sum of Three Body Terms Above for R vs. $\cos\theta$.
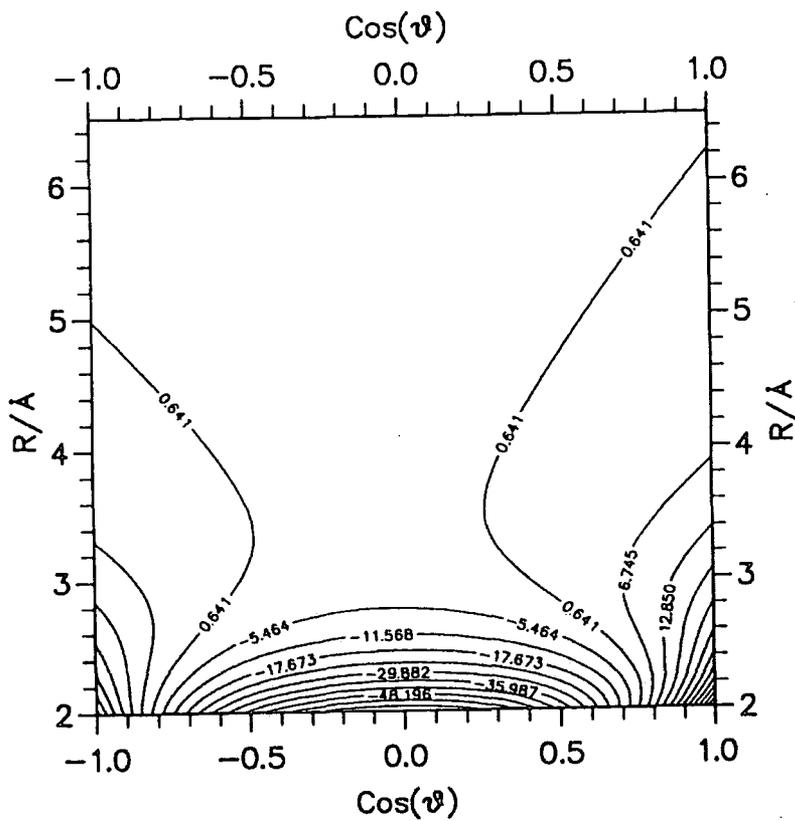
Appendix B– Ar₂HCl Potential Plots.
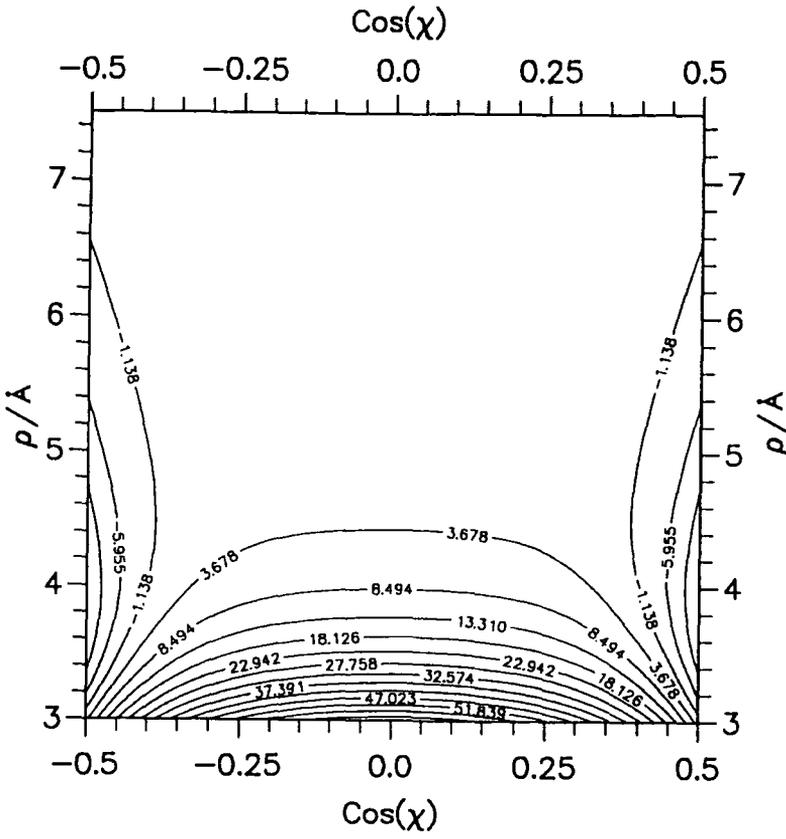
Fig. 37. Sum of Three Body Terms Above for ρ vs. $\cos\chi$.
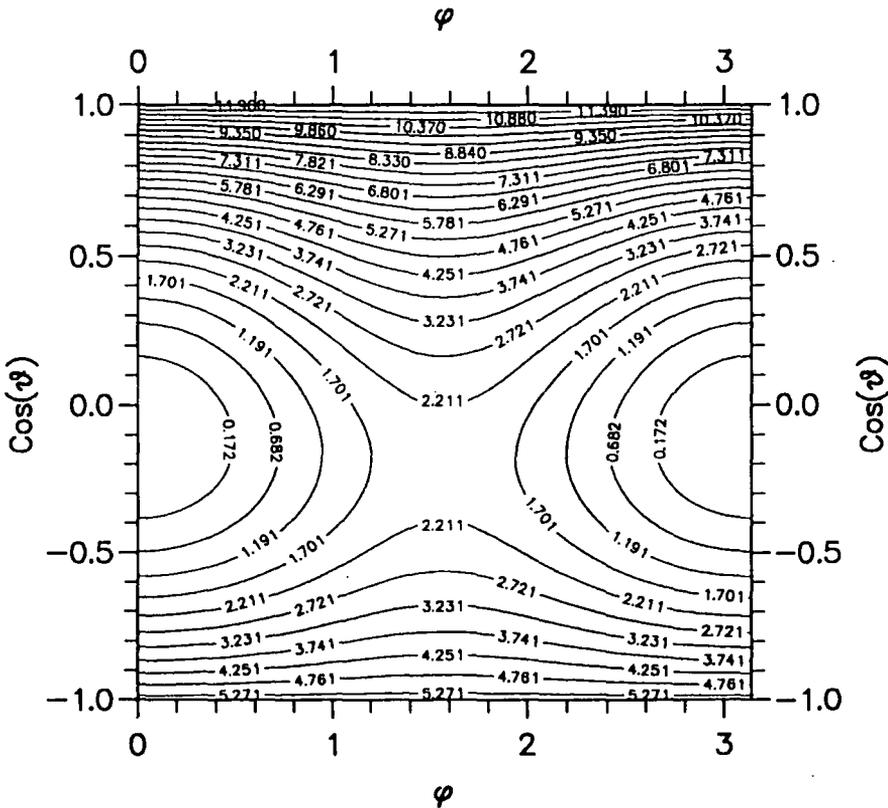
Fig. 38. Sum of Three Body Terms Above for $\cos\theta$ vs. ϕ.

Appendix C– Ar₂HF Potential Plots.

All cuts have fixed parameters according to $R = 3.94\text{Å}$, $\rho = 3.68\text{Å}$, $\cos \chi = 0$, $\cos \theta = 1$ and $\phi = 0$.

Fig. 1. H6(4,3,2) $v = 0$ Potential for ArHF Dimer.

Fig. 2. HFD-C + H6(4,3,2) $v = 0$ Pairwise Additive Cut for R vs. ρ.

Appendix C– Ar$_2$HF Potential Plots.
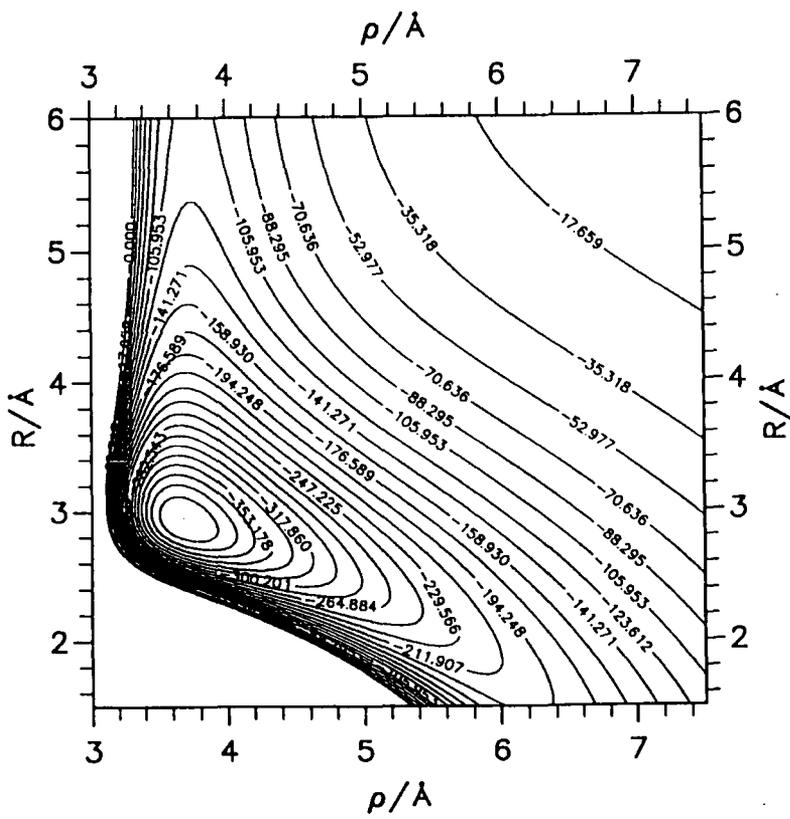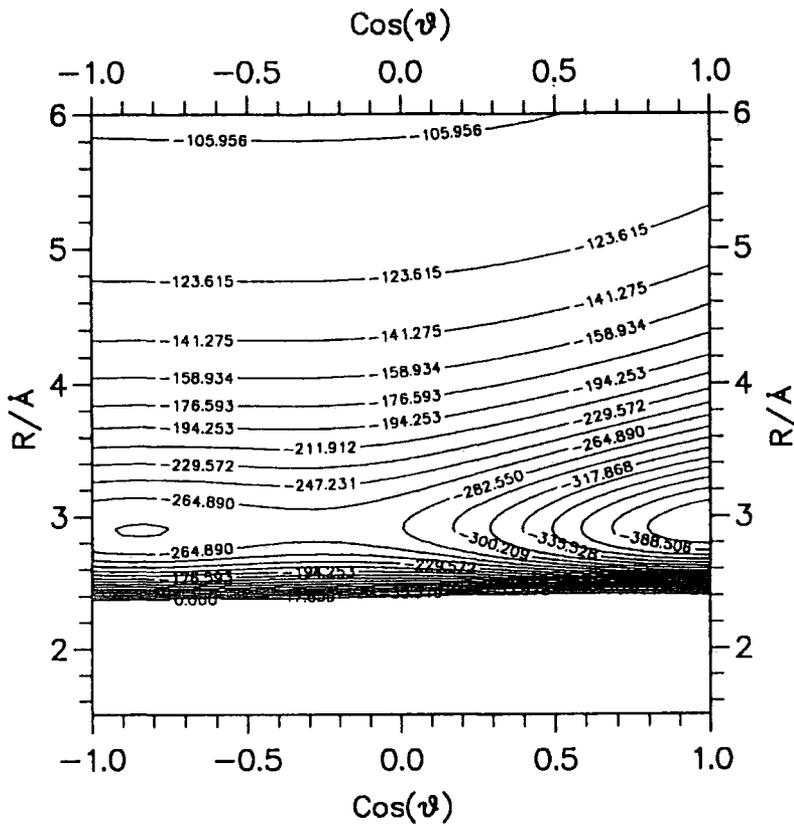
Fig. 3. HFD-C + H6(4,3,2) $v = 0$ Pairwise Additive Cut for R vs. $\cos\theta$.

Fig. 4. HFD-C + H6(4,3,2) $v = 0$ Pairwise Additive Cut for ρ vs. $\cos\chi$.

Appendix C– Ar$_2$HF Potential Plots.

Fig. 5. HFD-C + H6(4,3,2) $v = 0$ Pairwise Additive Cut for R vs. cos θ.

Fig. 6. HFD-C + H6(4,3,2) $v = 0$ Pairwise Additive Cut for cos θ vs. ϕ.

Appendix C– Ar$_2$HF Potential Plots.

Appendix D– Ar$_3$ Wavefunction Plots.

Fig. 1. $\Psi^2_{n=1a}$ for $\cos \chi = 0.0$.

Fig. 2. $\Psi^2_{n=1b}$ for $R = 3.4$Å.

Appendix D– Ar$_3$ Wavefunction Plots.

Fig. 3. $\Psi^2_{n=2}$ for $\cos \chi = 0.0$.

Fig. 4. $\Psi^2_{n=3a}$ for $\cos \chi = 0.1$.

Appendix D– Ar₃ Wavefunction Plots.

Fig. 5. $\Psi^2_{n=3a}$ for $R = 3.3\text{Å}$.

Fig. 6. $\Psi^2_{n=3b}$ for $\cos \chi = 0.0$.

Fig. 7. $\Psi^2_{n=3b}$ for $R = 3.3\text{Å}$.

Fig. 8. $\Psi^2_{n=4}$ for $\cos\chi = 0.0$.

Appendix D– Ar₃ Wavefunction Plots.

Fig. 9. $\Psi^2_{n=4}$ for $R = 3.5$Å.

Fig. 10. $\Psi^2_{n=5a}$ for $R = 3.1$Å.

Appendix D– Ar₃ Wavefunction Plots.

Fig. 11. $\Psi^2_{n=5a}$ for $\cos \chi = 0.12$.

Fig. 12. $\Psi^2_{n=5a}$ for $R = 3.4$Å.

Fig. 13. $\Psi^2_{n=5b}$ for $\cos\chi = 0.1$.

Fig. 14. $\Psi^2_{n=5b}$ for $R = 3.35\text{Å}$.

Appendix D– Ar₃ Wavefunction Plots.

Fig. 15. $\Psi^2_{n=6}$ for $\cos\chi = 0.14$.

Fig. 16. $\Psi^2_{n=6}$ for $R = 3.4$Å.

Appendix D– Ar₃ Wavefunction Plots.

Fig. 17. $\Psi^2_{n=6}$ for $\cos\chi = 0.0$.

Fig. 18. $\Psi^2_{n=6}$ for $R = 3.2\text{Å}$.

Appendix D– Ar$_3$ Wavefunction Plots.

Fig. 19. The Excited State at -190.9cm^{-1} for $\cos\chi = 0.0$.

Appendix E– Ar₂H/DCl Wavefunction Cuts.

All plots in this appendix are of the square of the wavefunction, without any R^2 volume element weighting, and are generated using the H6(4,3,0) and HFD-C potential surfaces. All of the cuts are made for fixed coordinates of $R = 3.5\text{Å}$, $\rho = 3.82\text{Å}$, $\cos\chi = 0$, $\cos\theta = 1$ and $\phi = 0$, unless the excitation is out of plane, when $\phi = \pi/2$.

Fig. 1. Ar_2HCl Ground State for R vs. ρ.

Fig. 2. Ar_2HCl Ground State for ρ vs. $\cos \chi$.

Appendix E– Ar_2H/DCl Wavefunction Cuts.
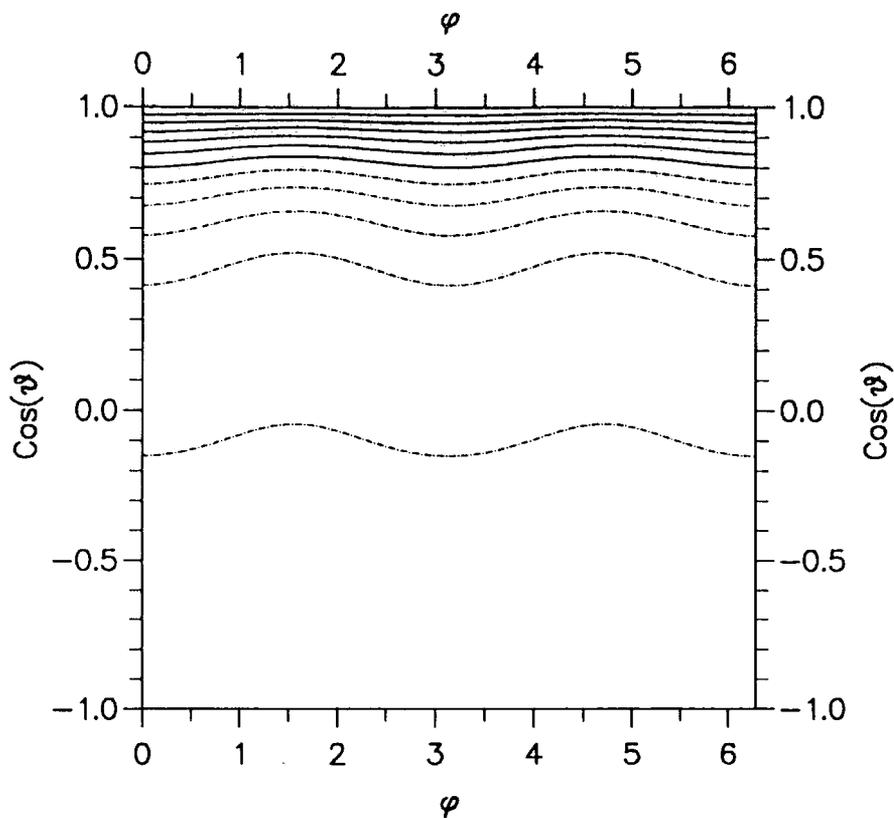
Fig. 3. Ar$_2$HCl Ground State for $\cos\theta$ vs. ϕ.
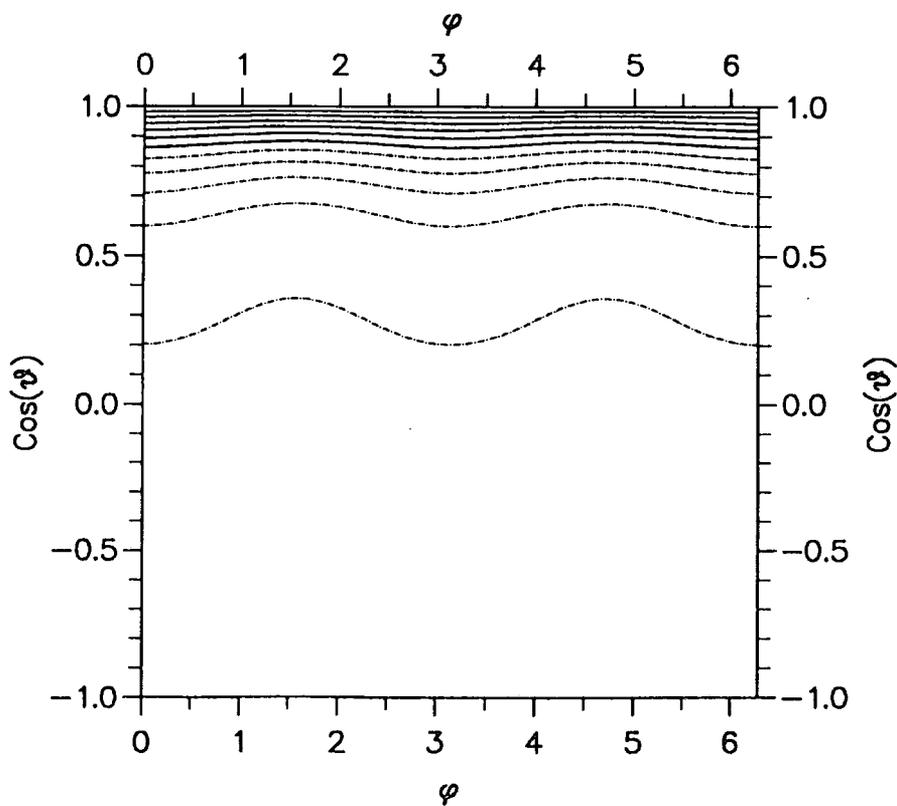
Fig. 4. Ar$_2$DCl Ground State for $\cos\theta$ vs. ϕ.
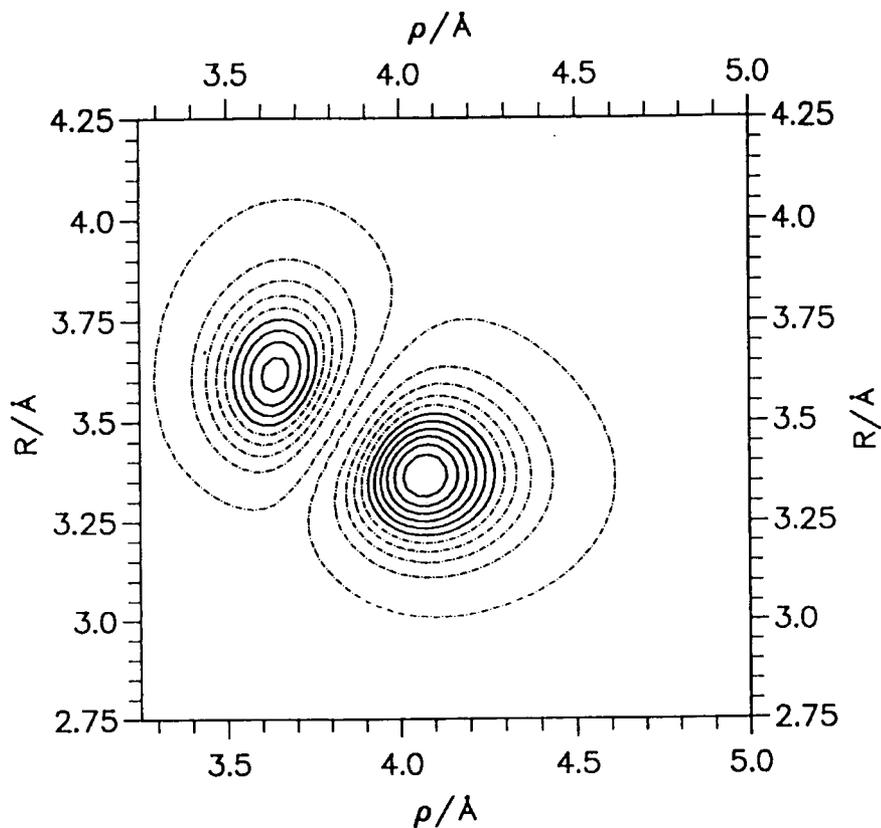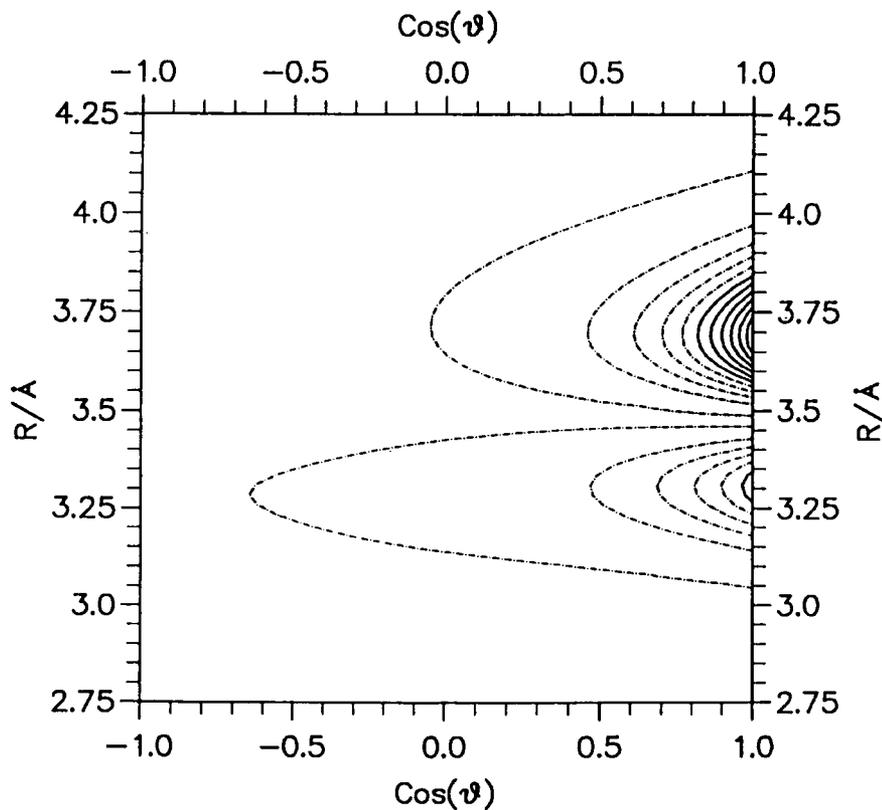
Appendix E– Ar$_2$H/DCl Wavefunction Cuts.

Fig. 5. Ar$_2$HCl Wagging (antisymmetric) Stretch for R vs. ρ.

Fig. 6. Ar$_2$HCl Wagging (antisymmetric) Stretch for R vs. $\cos\theta$.

Appendix E– Ar$_2$H/DCl Wavefunction Cuts.

Fig. 7. Ar$_2$HCl χ Bend for $\cos\theta$ vs. $\cos\chi$.

Fig. 8. Ar$_2$DCl χ Bend for $\cos\theta$ vs. $\cos\chi$.

Appendix E– Ar$_2$H/DCl Wavefunction Cuts.
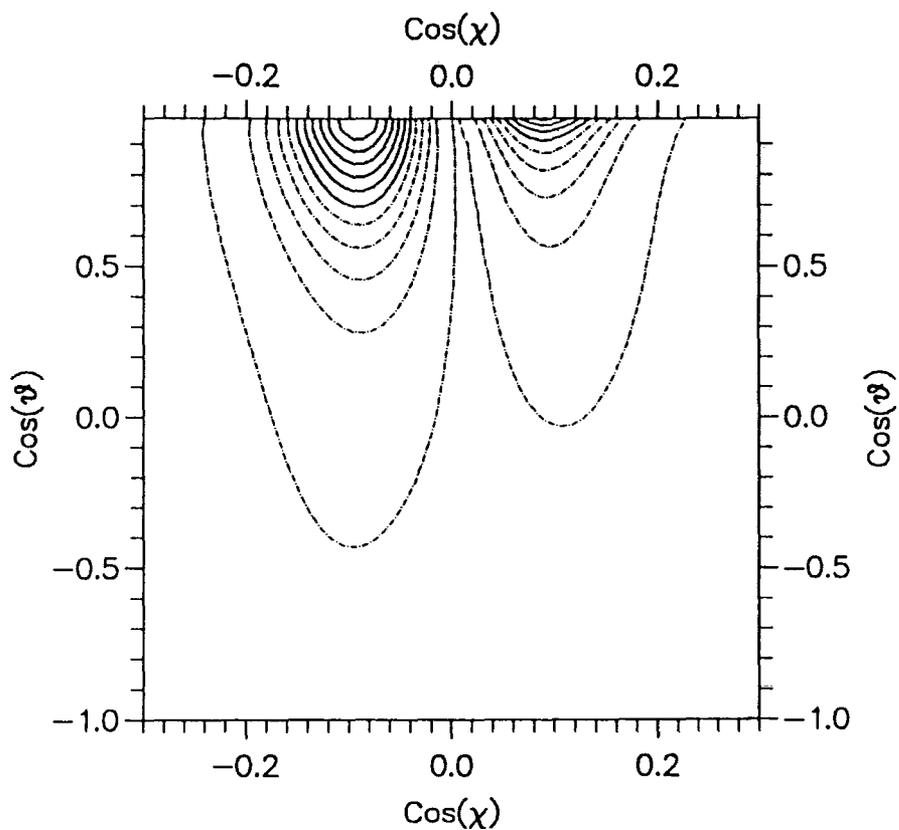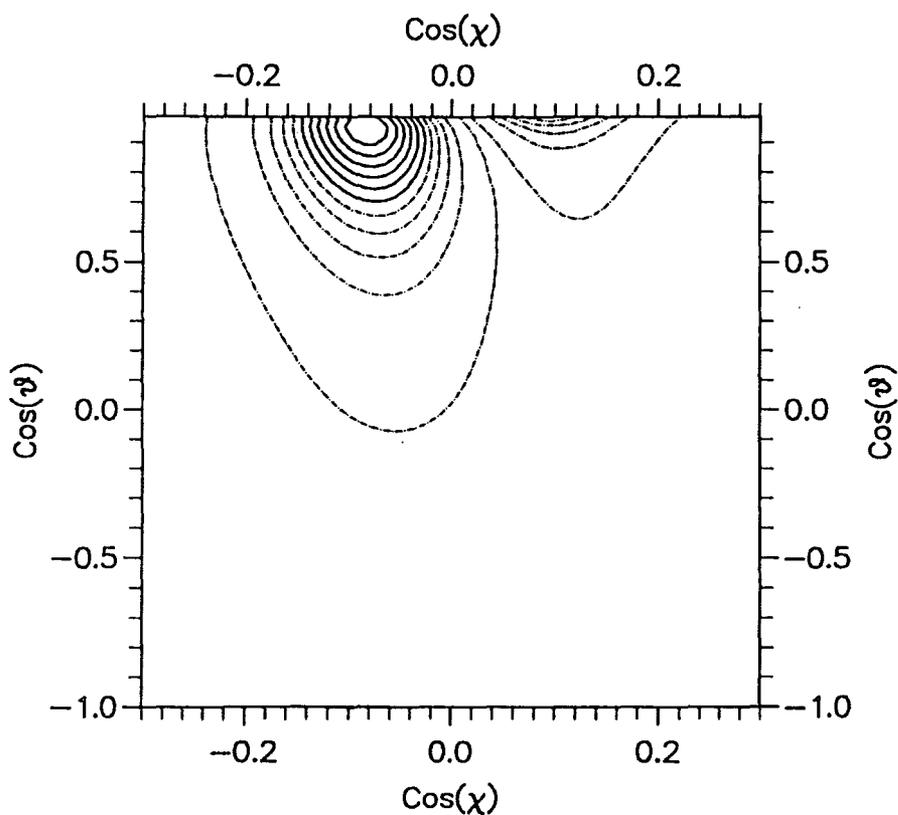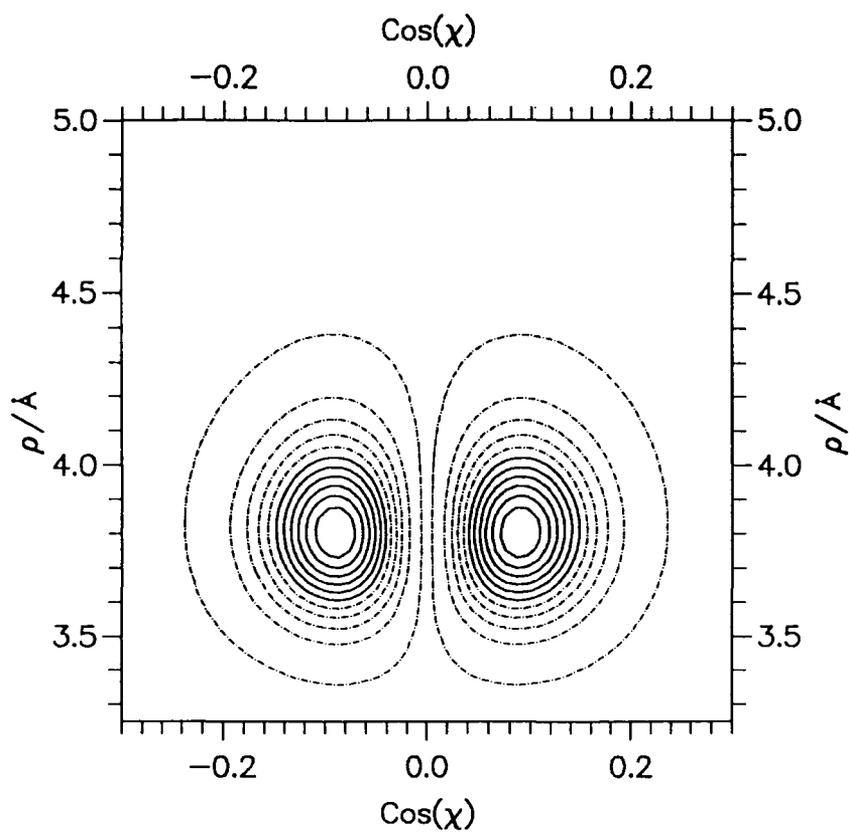
Fig. 9. Ar_2HCl χ Bend for ρ vs. $\cos\chi$.
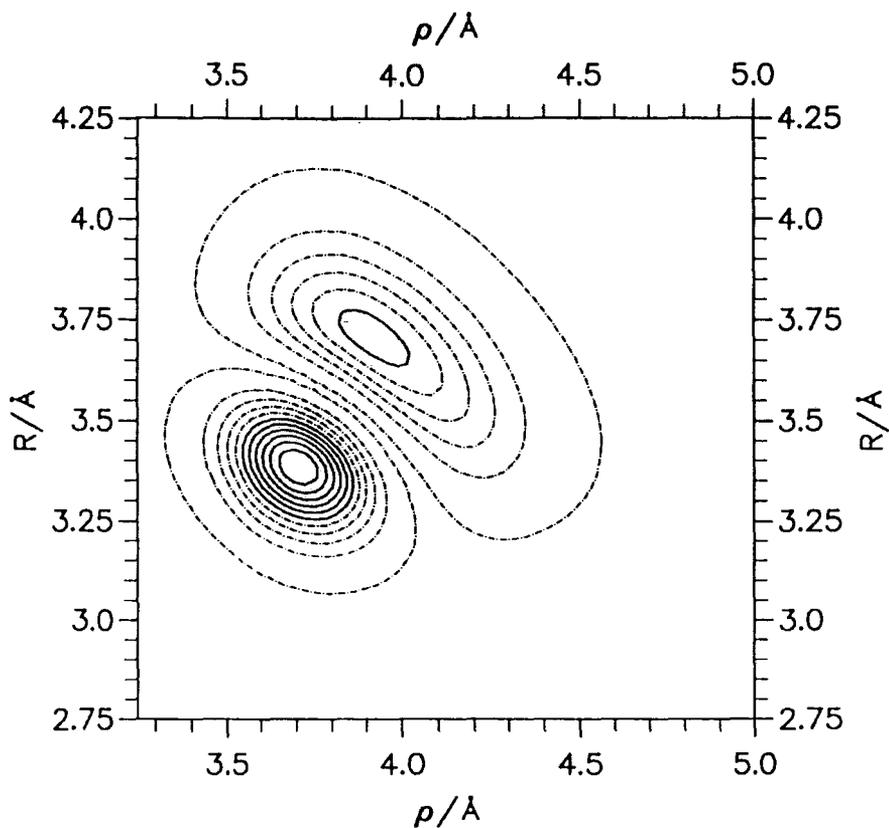
Fig. 10. Ar_2HCl Breathing (symmetric) Stretch for R vs. ρ.
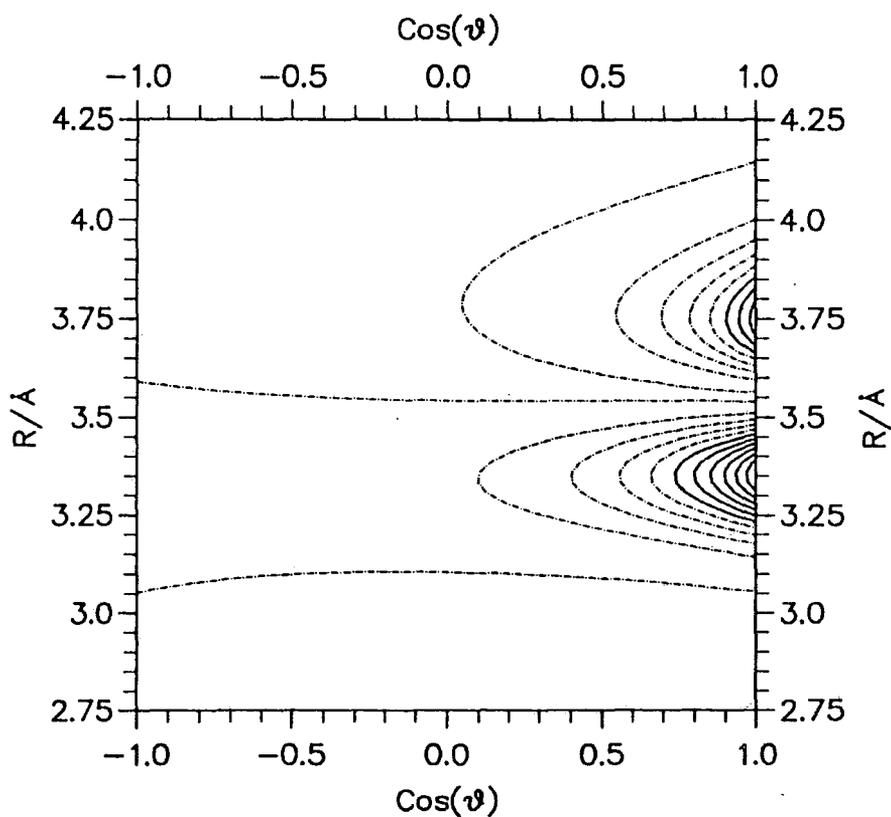
Fig. 11. Ar_2HCl Breathing (symmetric) Stretch for R vs. $\cos\theta$.
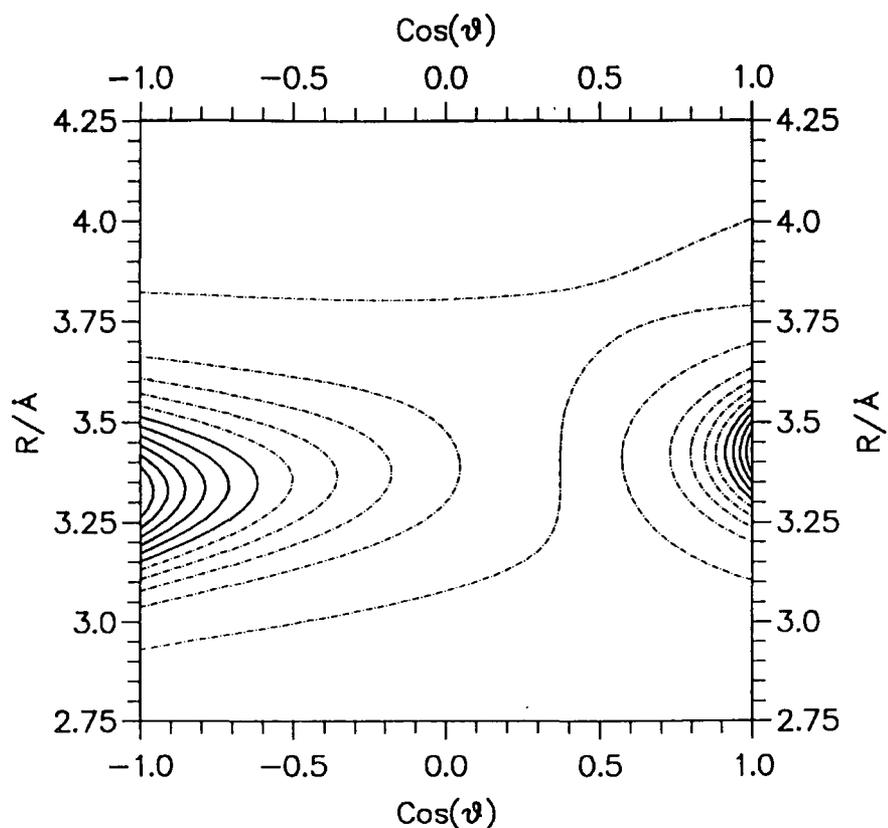
Appendix E– Ar_2H/DCl Wavefunction Cuts.

Fig. 12. Ar_2HCl Σ (parallel) Bend for R vs. $\cos\theta$.

Fig. 13. Ar_2DCl Σ (parallel) Bend for R vs. $\cos\theta$.
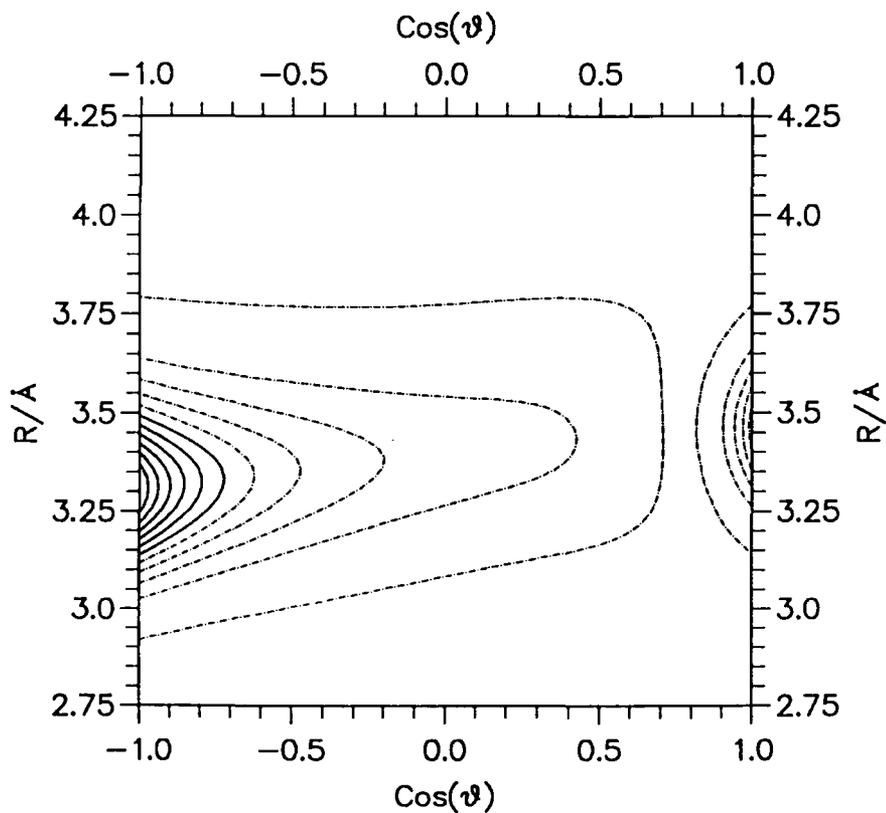
Appendix E– Ar_2H/DCl Wavefunction Cuts.
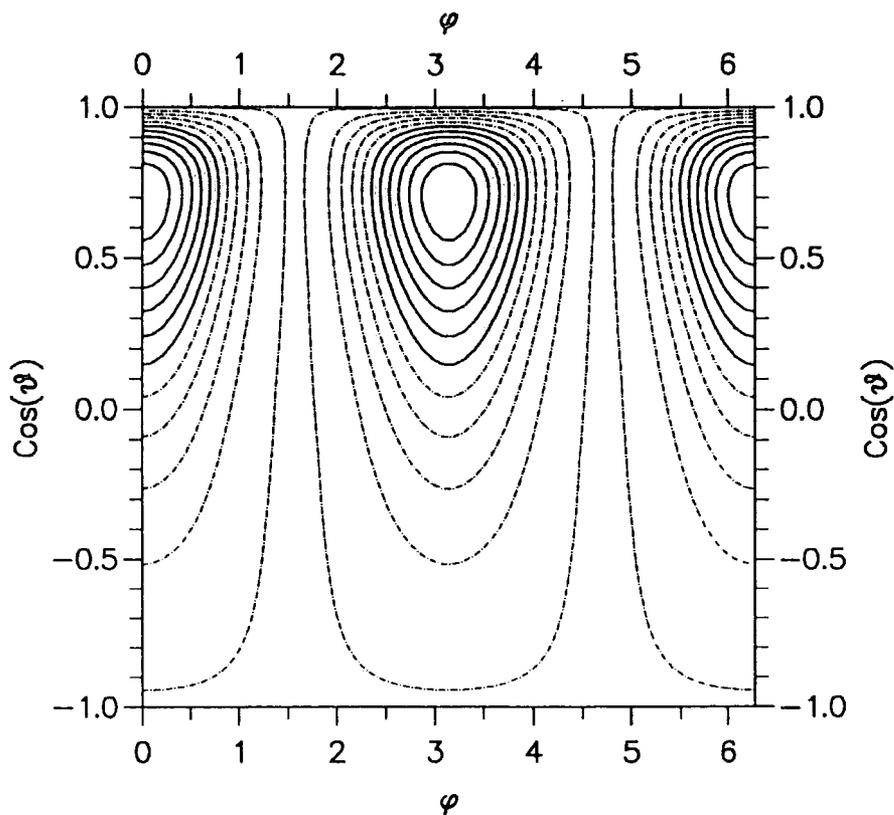
Fig. 14. Ar$_2$HCl In-plane Bend for $\cos\theta$ vs. ϕ.
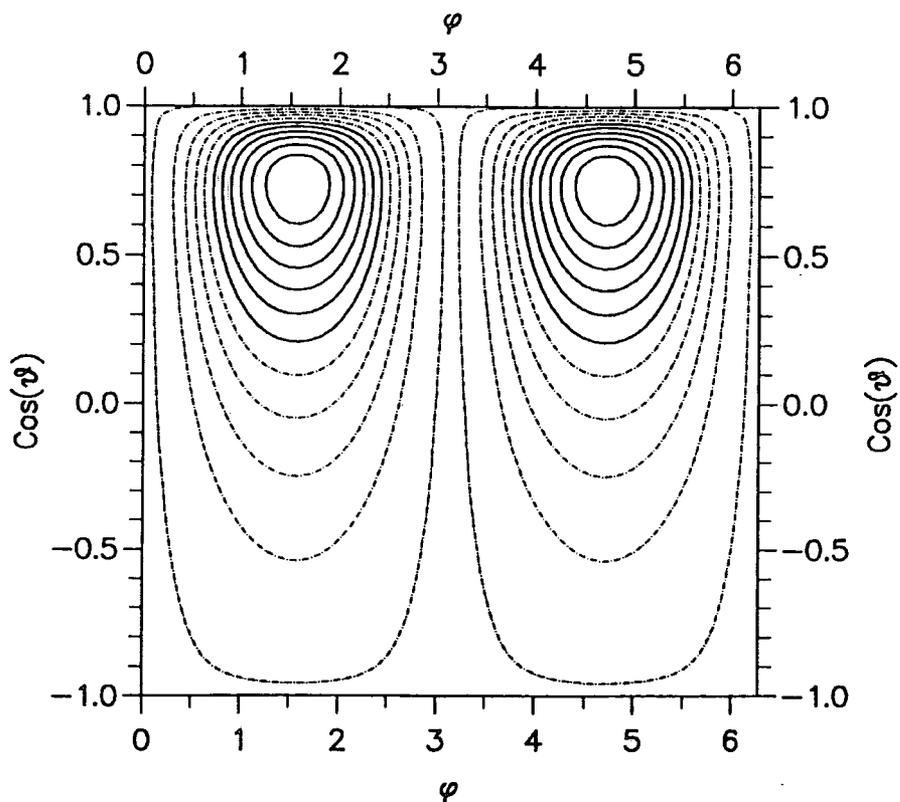
Fig. 15. Ar$_2$HCl Out-of-plane Bend for $\cos\theta$ vs. ϕ.

Appendix E– Ar$_2$H/DCl Wavefunction Cuts.

Fig. 16. Ar$_2$DCl Out-of-plane Bend for $\cos\theta$ vs. ϕ.
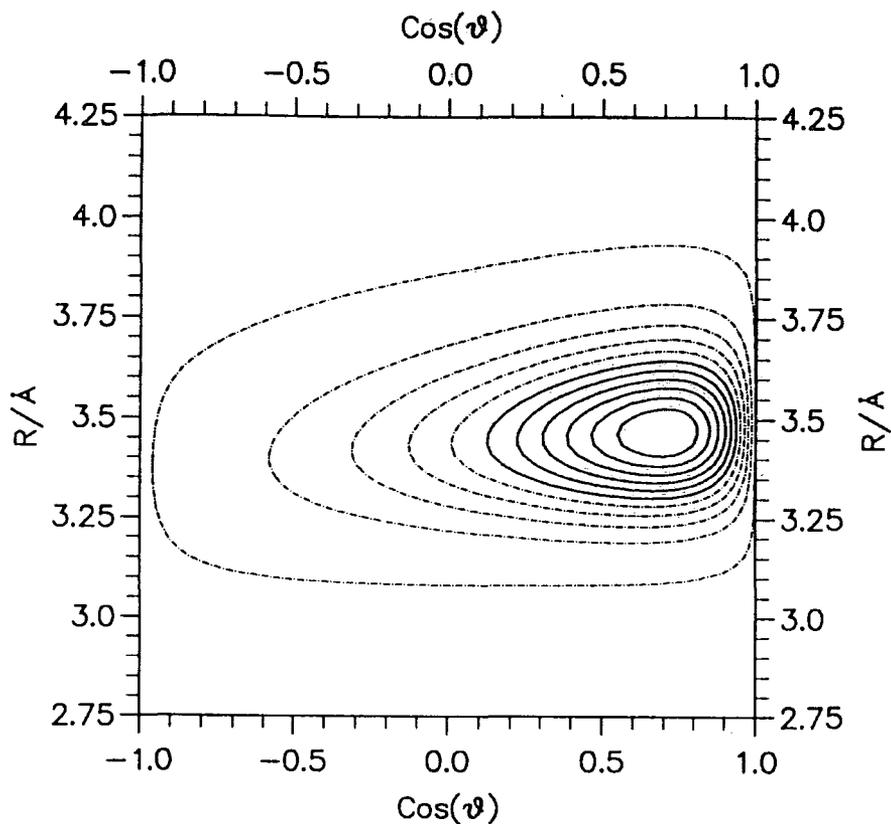
Fig. 17. Ar_2HCl In-plane Bend for R vs. $\cos\theta$.

Fig. 18. Ar_2HCl Out-of-plane Bend for R vs. $\cos\theta$.
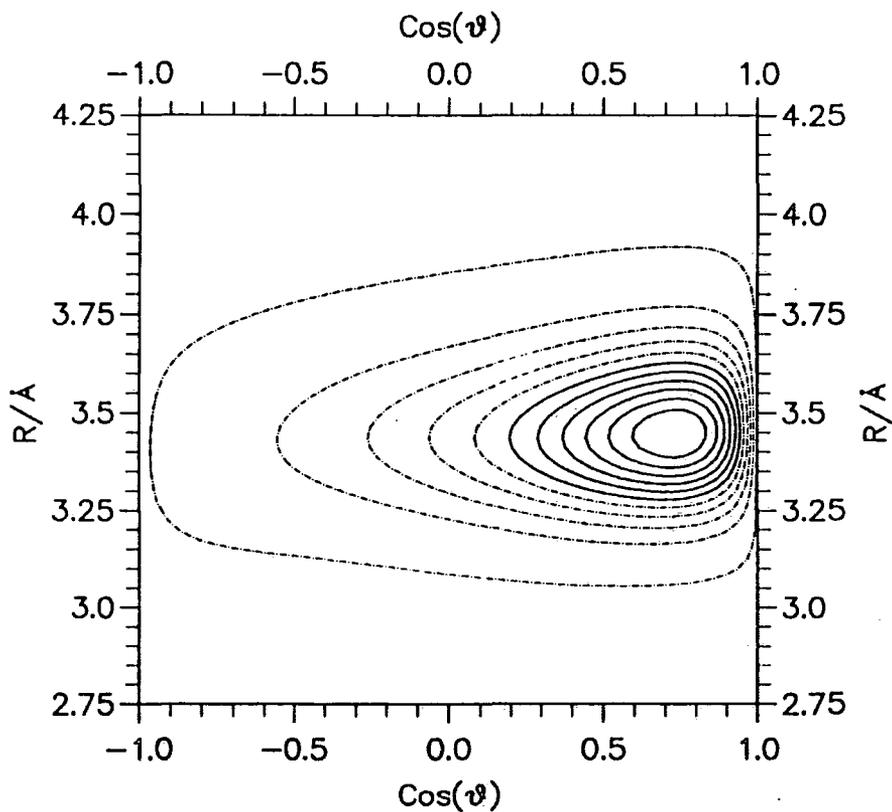
Appendix E– Ar_2H/DCl Wavefunction Cuts.
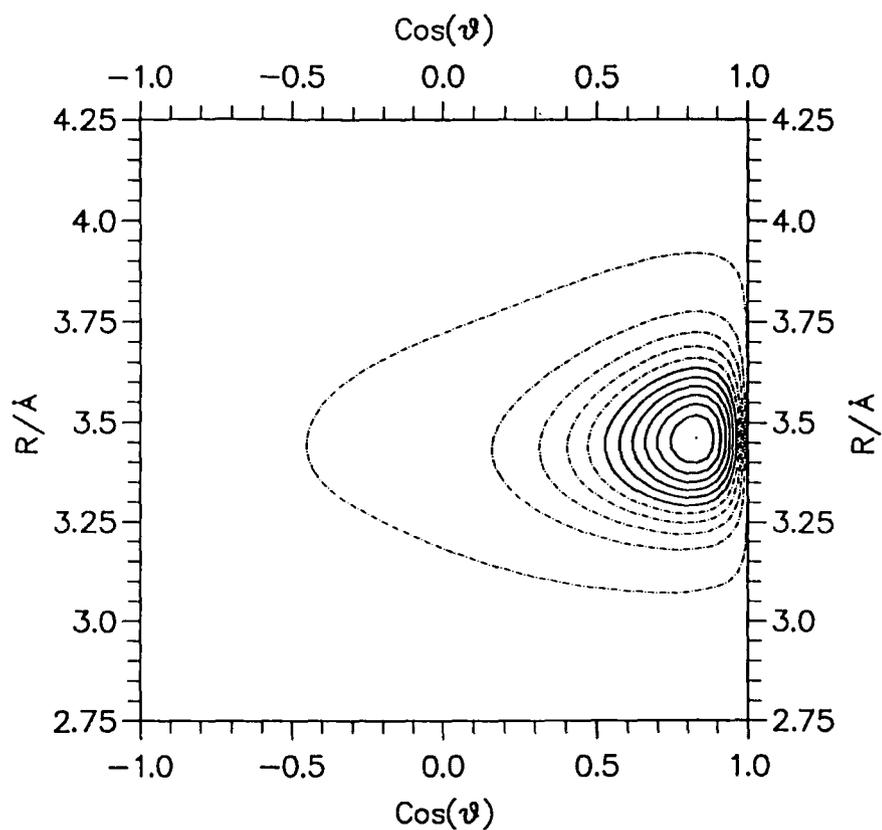
Fig. 19. Ar$_2$DCl Out-of-plane Bend for R vs. $\cos\theta$.
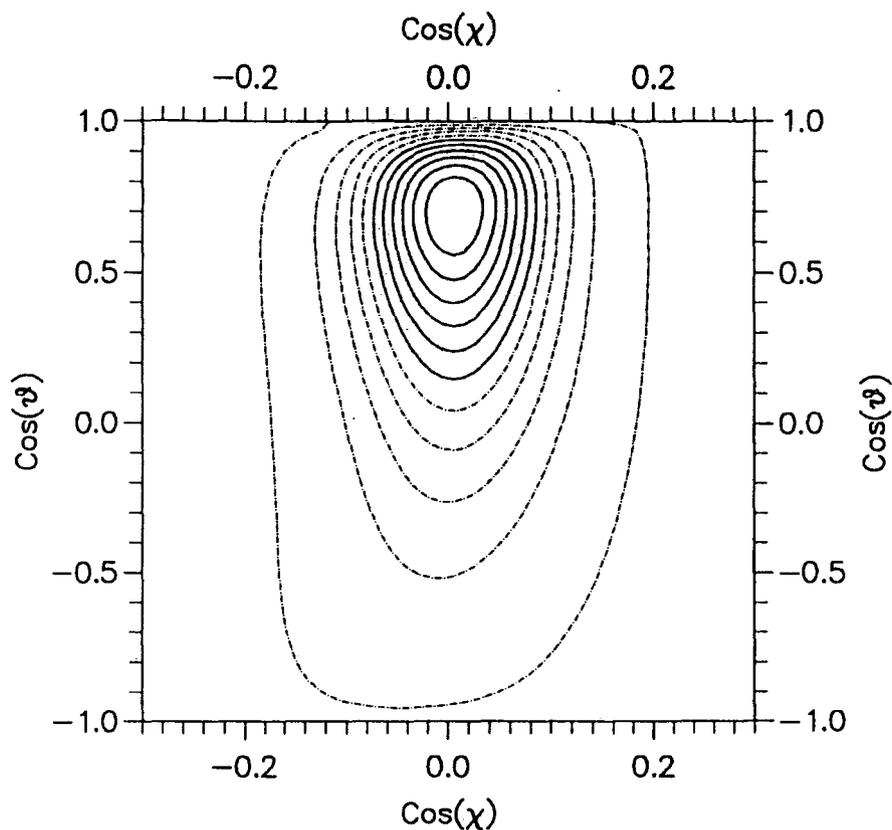
Fig. 20. Ar$_2$HCl In-plane Bend for cosθ vs. cosχ.
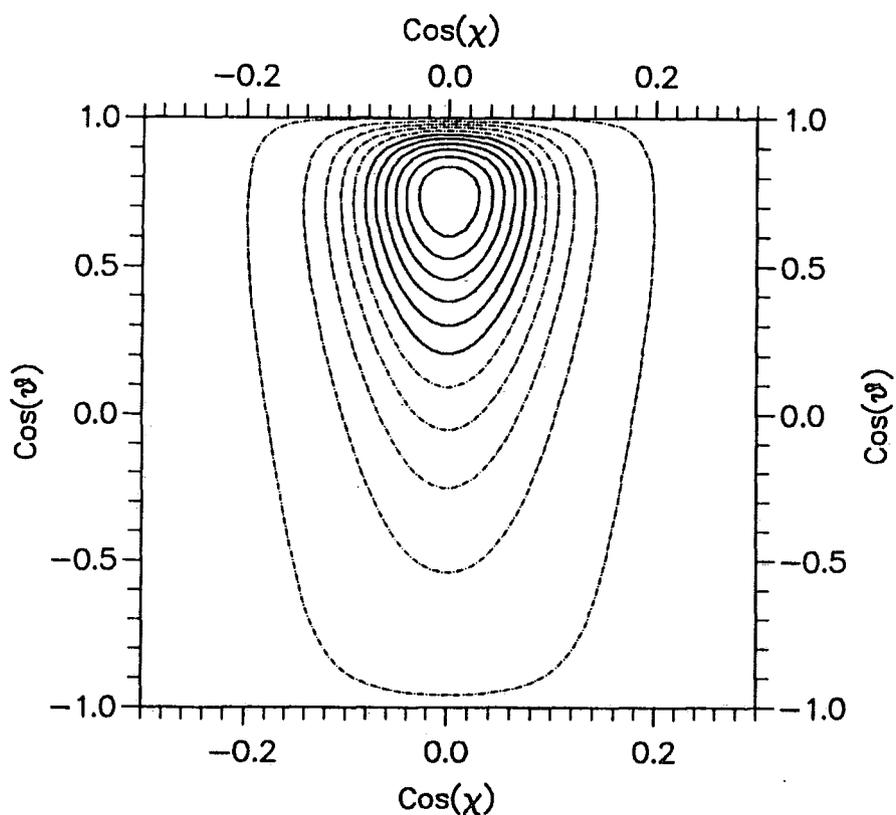
Fig. 21. Ar$_2$HCl Out-of-plane Bend for cosθ vs. cosχ.

Appendix E– Ar$_2$H/DCl Wavefunction Cuts.

Appendix F– Ar₂HF Wavefunction Cuts.

All plots in this appendix are of the square of the wavefunction, without any R^2 volume element weighting, with HF in its $v = 0$ state, and are generated using the H6(4,3,2) and HFD-C potential surfaces. All of the cuts are made for fixed coordinates of $R = 3.0$Å, $\rho = 3.70$Å, $\cos\chi = 0$, $\cos\theta = 1$ and $\phi = 0$.

Fig. 1. Ar$_2$HF Ground State for R vs. ρ.

Fig. 2. Ar$_2$HF Ground State for $\cos\theta$ vs. ϕ.

Appendix F– Ar$_2$HF Wavefunction Cuts.
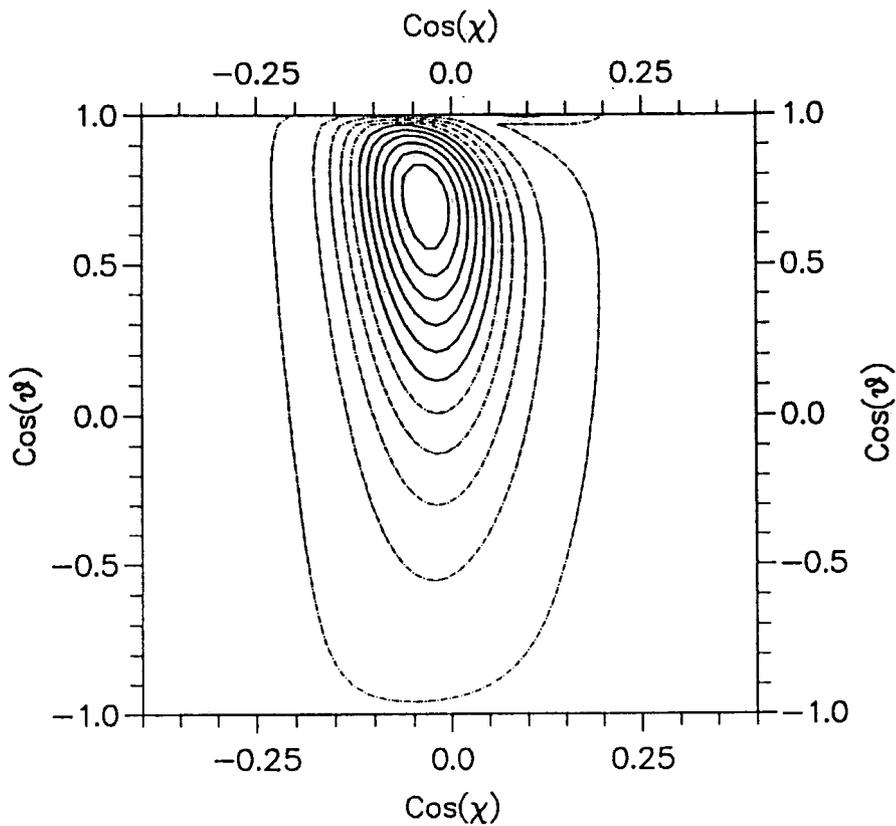
Fig. 3. Ar_2HF In-plane Bend for $\cos\theta$ vs. $\cos\chi$.

Fig. 4. Ar_2HF In-plane Bend for R vs. $\cos\theta$.

Appendix F– Ar_2HF Wavefunction Cuts.

Fig. 5. Ar_2HF In-plane Bend for $\cos\theta$ vs. ϕ.

Fig. 6. Ar_2HF Out-of-plane Bend for $\cos\theta$ vs. ϕ.

Appendix F– Ar_2HF Wavefunction Cuts.

Fig. 7. Ar_2HF χ Bend for $\cos\theta$ vs. $\cos\chi$.

Fig. 8. Ar_2HF $(v = 1)$ Out-of-plane Bend for R vs. $\cos\theta$.

Appendix F– Ar_2HF Wavefunction Cuts.

Appendix G– List of Figures.

Appendix H– List of Tables.

Appendix H– List of Tables.

Appendix H– List of Tables.

Appendix H– List of Tables.

Appendix I– List of References.

[1]. A. C. Legon, Ann. Rev. Phys. Chem. **34**, 275 (1983).

[2]. A. C. Legon, and D. J. Millen, Chem. Rev. **86**, 635 (1986).

[3]. D. J. Nesbitt, Chem. Rev. **88**, 843 (1988).

[4]. R. J. Saykally, Acc. Chem. Res. **22**, 295 (1898).

[5]. R. E. Miller, J. Chem. Phys. **90**, 3301 (1986).

[6]. J. M. Hutson, Advances in Molecular Vibrations And Collision Dynamics 1, 1 (1991).

[7]. A. D. Buckingham, P. W. Fowler & J. M. Hutson, Chem. Rev. **88**, 963 (1988).

[8]. M. Rigby, E. B. Smith, W. A. Wakeham & G. C. Maitland, The Forces Between Molecules, Oxford Univ. Press (1896).

[9]. C. G. Gray & K. E. Gubbins, Theory of Molecular Fluids, Volume 1, Oxford (1984).

[10]. J. M. Hutson, Ann. Rev. Phys. Chem. **41**, 123 (1990).

[11]. B. R. Johnson & W. P. Reinhardt, J. Chem. Phys. **85**, 4538 (1986).

[12]. J. Tennyson, Comp. Phys. Reports 4, 1 (1986)

[13]. Z. Bačić & J. C. Light, Ann. Rev. Phys. Chem. **40**, 469 (1989).

[14]. J. M. Hutson, Dynamics of Polyatomic Van der Waals Molecules, ed N. Halberstadt & K. C. Janda, Plenum, New York (1990).

[15]. D. J Nesbitt, and R. Naaman, J. Chem. Phys. **91**, 3801 (1989).

[16]. M. H. Alexander and D. E. Manolopoulos, J. Chem. Phys. **86**, 2044 (1987).

[17]. J. M. Hutson, BOUND Computer Code, distributed via the Collaborative Computation Project No.6 of the UK Science and Engineering Research Council.

[18]. J. M. Hutson, Chem. Phys. Lett. **151**, 565 (1988).

[19]. T. D. Klots, C. Chuang, R. S. Ruoff, T. Emilsson and H. S. Gutowsky, J. Chem. Phys. **86**, 5315 (1987).

[20]. M. J. Elrod, D. W. Steyert and R. J. Saykally, J. Chem. Phys. **94**, 58 (1991); M. J. Elrod, D. W. Steyert and R. J. Saykally, J. Chem. Phys. **95**, 3182 (1991).

[21]. J. M. Hutson, J. A. Beswick and N. Halberstadt, J. Chem. Phys. **90**, 1337, (1989).

[22]. H. S. Gutowsky, T. D. Klots, C. Chuang, C. A. Schmuttenmaer, T. Emilsson, J. Chem. Phys. **86**, 569, (1987).

[23]. T. D. Klots, R. S. Ruoff, C. Chuang, T. Emilsson and H. S. Gutowsky, J. Chem. Phys. **87**, 4383, (1987).

[24]. H. S. Gutowsky, T. D. Klots, C. Chuang, J. D. Keen, C. A. Schmuttenmaer, T. Emilsson, J. Am. Chem. Soc. **109**, 5633, (1987).

[25]. H. S. Gutowsky, T. D. Klots, C. Chuang, C. A. Schmuttenmaer, T. Emilsson, J. Chem. Phys. **88**, 2919, (1988).

[26]. A. McIlroy, R. Lascola, C. M. Lovejoy & D. J. Nesbitt, J. Phys. Chem. **95**, 2636 (1991).

[27]. M. Rigby, E. B. Smith, W. A. Wakeham & G. C. Maitland, The Forces Between Molecules, Oxford Univ. Press (1896).

[28]. F. L. Pilar, Elementary Quantum Chemistry, Mc.Graw-Hill (1968).

[29]. W Yang & A. C. Peet, Chem. Phys. Lett. **153**, 98 (1988).

[30]. B. R. Johnson, and W. P. Reinhardt, J. Chem. Phys. **85**, 4538 (1986).

[31]. Numerical Algorithms Group Subroutine Manuals.

[32]. J. P. Chesick. J. Chem. Phys. **49**, 3772 (1968).

[33]. B. W. Shore, J. Chem. Phys. **59**, 6450 (1973).

[34]. I. P Hamilton, and J. C. Light, J. Chem. Phys. **84**, 306 (1986).

[35]. Z. Bačić, and J. C. Light, J. Chem. Phys. **85**, 4594 (1986).

[36]. Z. Bačić, and J. C. Light, J. Chem. Phys. **86**, 3065 (1987).

[37]. A. C. Peet, J. Chem. Phys. **90**, 4363 (1989).

[38]. Z. Bačić & J. Z. H. Zhang, Chem. Phys. Lett. **184**, 513 (1991).

[39]. I. P Hamilton, and J. C. Light, J. Chem. Phys. **84**, 306 (1986).

Appendix I– List of References.

[40]. D. C. Clary & P. J. Knowles, J. Chem. Phys. **93**, 6334 (1990).

[41]. D. C. Clary, C. E. Dateo & T. Stoeklin, J. Chem. Phys. **93**, 7666 (1990).

[42]. I. P Hamilton, and J. C. Light, J. Chem. Phys. **84**, 306 (1986).

[43]. D. M. Brink & G. R. Satchler, "Angular Momentum", Oxford University Press (1968).

[44]. M. Abramowitz, and I. A. Stegun, "Handbook of Mathematical Functions", 9th printing, Dover Publications Inc., (1972).

[45]. E. B. Wilson, J. C. Decius and P. C. Cross, "The Theory of Infrared and Raman Vibrational Spectra", Dover Publications Inc., (1955).

[46]. R. J. Whitehead & N. C. Handy, J. Mol. Spectrosc. **55**, 356 (1975)

[47]. S. Carter & N. C. Handy, Mol. Phys. **47**, 1445 (1982).

[48]. J. M. Hutson and S. Jain, J. Chem. Phys. **91**, 4197 (1989).

[49]. T. R. Horn, R. B. Gerber, J. J. Valentini & M. A. Ratner, J. Chem. Phys. **94**, 6728 (1991).

[50]. D. M. Leitner, R. S. Berry & R. M. Whitnell, J. Chem. Phys. **91**, 3470 (1989).

[51]. A. R. Cooper, S. Jain & J. M. Hutson, J. Chem. Phys. xx, xxxx (199x).

[52]. M. Karplus and R. N. Porter, "Atoms & Molecules", Benjamin/Cummings Publishing, (1970).

[53]. E. B. Wilson, J. C. Decius and P. C. Cross, "The Theory of Infrared and Raman Vibrational Spectra", Dover Publications Inc., (1955).

[54]. Collected Algorithms from ACM, Volume II, The Association for Computing Machinery Inc., New York (1979).

[55]. D. A. Varshalovich, A. N. Moskalev & V. K. Khersonskii, Quantum Theory of Angular Momentum, World Scientific Publishing (1988).

[56]. E. U. Condon & G. H. Shortley, Theory of Atomic Spectra, CUP 1935.

[57]. P. R. Bunker, "Molecular Symmetry and Spectroscopy", Academic Press (1979).

[58]. R. A. Aziz, Interatomic Potentials for Rare Gasses: Pure and Mixed Interactions,

from Springer Series in Chemical Physics No.34, Inert Gasses.

[59]. R. A. Aziz and H. H. Chen, J. Chem. Phys. **67**, 5719 (1977).

[60]. J. Hepburn, G. Scoles & R. Penco, Chem. Phys. Lett. **36**, 451 (1975).

[61]. C. Douketis, G. Scoles, S. Marchetti, M. Zen & A. J. Thakkar, J. Chem. Phys. **76**, 3057 (1982).

[62]. R. A. Aziz and M. J. Slaman, Mol. Phys. **58**, 679 (1986).

[63]. J. M. Hutson and B. J. Howard, Mol. Phys. **43**, 493 (1981).

[64]. J. M. Hutson and B. J. Howard, Mol. Phys. **45**, 769 (1982).

[65]. J. M. Hutson, J. Chem. Phys. **89**, 4550 (1988).

[66]. J. M. Hutson, J. Phys. Chem. **96**, 4237 (1992).

[67]. J. M. Hutson, J. Chem. Phys. **91**, 4448 (9).

[68]. J. M. Hutson, J. Chem. Phys. **91**, 4455 (1989).

[69]. K. T. Tang and J. P. Toennies, J. Chem. Phys. **80**, 3726 (1984).

[70]. J. M. Hutson, J. Chem. Phys. **96**, 6752 (1992).

[71]. S. F. Boys & F. Bernardi, Mol. Phys. **19**, 553 (1970).

[72]. K. Szalewicz & B. Jeziorski, Mol. Phys. **39**, 191 (1979).

[73]. S. Rybak, K. Szalewicz, B. Jeziorski & M. Jaszuński, J. Chem. Phys. **86**, 5652 (1987).

[74]. G. Chałasiński & M. M. Szczęśniak, Mol. Phys. **63**, 205 (1988).

[75]. S. M. Cybulski, G. Chałasiński & R. Moszyński, J. Chem. Phys. **92**, 4357 (1990).

[76]. G. Chałasiński, M. M. Szczęśniak & S. M. Cybulski, J. Chem. Phys. **92**, 2481 (1990).

[77]. G. Chałasiński, S. M. Cybulski, M. M. Szczęśniak & S. Scheiner, J. Chem. Phys. **91**, 7814 (1989).

[78]. G. Chałasiński, S. M. Cybulski, M. M. Szczęśniak & S. Scheiner, J. Chem. Phys. **91**, 7048 (1989).

[79]. G. Chałasiński, M. M. Szczęśniak & B. Kukawska-Tarnawska, J. Chem. Phys. **94**,

Appendix I– List of References.

6677 (1991).

[80]. B. M. Axilrod and E. Teller, J. Chem. Phys. **11**, 299 (1943).

[81]. R. J. Bell, J. Phys. B **3**, 751 (1970).

[82]. M. L. Klein & J. A. Venables (Editors), Rare Gas Solids Volume 1, 122, (Academic Press 1976).

[83]. W. J. Meath & M. Koulis, J. Mol. Struct. **226**, 1 (1991).

[84]. P. Piecuch, Mol. Phys. **59**, 1085 (1986).

[85]. P. Piecuch, Mol. Phys. **66**, 805 (1989).

[86]. P. Piecuch, Chem. Phys. Lett. **110**, 496 (1984).

[87]. A. D. Buckingham, Adv. Chem. Phys. **12**, 107 (1967).

[88]. D. E. Stogryn, Phys. Rev. Lett. **28**, 971 (1970).

[89]. D. E. Stogryn, Mol. Phys. **22**, 81 (1971).

[90]. M. O. Bulanin, V. P. Bulychev & K. K. Tokhadze, J. Mol. Struct. **161**, 321 (1987).

[91]. A. Kumar and W. J. Meath, Mol. Phys. **54**, 823 (1985).

[92]. K. T. Tang & J. P. Toennies, J. Chem. Phys. **80**, 3726 (1984).

[93]. A. J. Stone, Chem. Phys. Lett. **83**, 233 (1981); A. J. Stone and M. Alderton, Mol. Phys. **56**, 1047 (1985).

[94]. M. W. Schmidt & K. Ruedenberg, J. Chem. Phys. **71**, 3951 (1979).

[95]. B. H. Wells, Mol. Phys. **61**, 1283 (1987).

[96]. R. D. Amos and J. E. Rice, *CADPAC: the Cambridge Analytic Derivatives Package*, issue 5.0, Cambridge (1992).

[97]. L. Jansen, Adv. Quantum Chem. 2, 119 (1965).

[98]. B. Guillot, R. D. Mountain & G. Birnbaum, Mol. Phys. **64**, 747 (1988).

[99]. A. D. Buckingham, Quart. Rev. (London) **13**, 189 (1959).

[100]. M. Bulski & G. Chałasiński, Chem. Phys. Lett. **89**, 450 (1982).

[101]. D. R. Williams, L. J. Schaad and J. N. Murrell, J. Chem. Phys. **47**, 4916 (1967).

[102]. V. Magnasco and G. F. Musso, J. Chem. Phys. **60**, 3744 (1974).

Appendix I– List of References.

[103]. M. J. Elrod, personal communication.

[104]. M. J. Elrod, personal communication.